Superconductors and High Magnetic Fields

Richard P. Lewin

The Queen's College

University of Oxford

A thesis submitted for the degree of

Doctor of Philosophy

Trinity 2012

For my grandparents.

Superconductors and High Magnetic Fields

Richard P. Lewin
The Queen's College
Oxford

A thesis submitted for the degree of Doctor of Philosophy
Trinity Term 2012

Abstract

This thesis describes a portfolio of work aimed at the high field applications of superconductors and can be split into four main topics:

The thermal stability of technical superconductors. This section investigates the effects of thermal perturbations on technical superconducting wire used in MRI scanner construction. The ultimate aim of this section is to predict how the architecture of the wire may affect its thermal stability. To this end a detailed finite element analysis model was constructed, verified by detailed experimental data, which could then be used to quickly and easily vary the wire's parameters.

Design of a high field pulsed electromagnetic coil for flux trapping in superconductors. This section details the design, construction and testing of a novel pulsed high field magnet. The design uses finite element analysis to predict the electromagnetic, thermal and structural properties of the coil.

Explosive testing of high tensile fibres used in the construction of the high field coil. This section describes the refinement and use of a novel method for testing the mechanical properties of high tensile fibres in cylindrical geometries by using highly pressurized copper vessels.

Pulsed field magnetization of bulk high temperature superconductors. This section discusses the process of magnetizing bulks of high temperature superconductors by using pulsed magnetic fields. It investigates how the trapped field varies with the magnitude and rise-time of the magnetizing field, sample temperature and time after magnetization.

Acknowledgments

This thesis describes research undertaken in the Clarendon Laboratory of the University of Oxford, Department of Physics. It took place between October 2008 and July 2012. The work was funded by the EPSRC[1] and by Siemens Magnet Technology[2] as an industrial case studentship for which I am grateful.

First and foremost I must thank Harry Jones for his supervision, guidance and knowledge over the course of this thesis. I must also thank M'hamed Lakrimi of Siemens Magnet Technology for his help and boundless enthusiasm and interest in my work.

I am very grateful for all of the assistance that I have received from the technical staff in the Physics department with a special mention to Tony Hickman as without his skill and knowledge much of the work detailed here would have been impossible to achieve.

Finally I must thank my family and, last but by no means least, Joelle Mauger for putting up with me and reading through reams of work which, in her words, "makes no sense at all".

[1] Engineering and Physical Sciences Research Council, Polaris House, North Star Avenue, Swindon, SN2 1ET, UK
[2] Siemens plc. Eynsham, Witney, Oxon, OX29 4BP, UK

List of Symbols

$\mathbf{A}$	Magnetic vector potential
A	Area
A_P	Peak magnetic vector potential
A_r	Constant model fit parameter
a_1, a_2	Inner and outer radius of a coil
α	Coefficient of thermal expansion
$\boldsymbol{B}$	Magnetic flux density
B_0	Empirical fitting parameter
B_c	Critical magnetic flux density
B_{c1}, B_{c2}	Lower and upper critical flux densities
B_{irr}	Irreversibility field
b	Half of the length of a coil
C	Capacitance
C_p	Heat capacity at constant pressure
D	Diffusivity
$\boldsymbol{D}$	Electric flux density
E	Energy, Young's modulus
$\boldsymbol{E}$	Electic field strength
E_c	Defined critical electric field strength
ε	Strain
ε_0	Relative permitivity
F	Force, free energy
f_i	Relative fraction by area
G	Gibbs free energy per unit volume, heat generation rate, shear modulus
γ	Empirical factor for fitting critical surface of superconductors
$\boldsymbol{H}$	Magnetic field
H^*	Critical magnetization field
H_c	Critical magnetic field
h	Plank's constant, thickness
$\hbar$	$h/2\pi$
I	Current
I_c	Critical current
i	Index of transition
$\boldsymbol{J}$	Current density
J_c	Critical current density
$\boldsymbol{J_i}$	Induction current density

J_m	Applied current density
J_P	Peak current density
k_B	Boltzman constant
L	Lorenz ratio, inductance
l	Length
λ	Penetration depth, thermal conductivity
M	Mutual inductance
$\boldsymbol{M}$	Magnetization
M_R	M-ratio giving shape of flux trapped in a superconductor
m	Mass
n	Empirical factor for fitting critical surface of superconductors, number of turns in a coil
Φ	Flux
Φ_0	Quantum of flux
P	Power
Ψ	Superconducing order parameter
Q	Laten heat, power dissipation
q	Charge on electon
R	Resistance
RRR	Residual resistivity ratio
ρ	Resistivity
ρ_d	Density
S	Entropy
σ	Electrical conductivity, stress
T	Temperature
T_c	Critical temperature
t	Time
θ	Normalised current density
u	Solid displacement
μ_0	Permeability of free space
V	voltage
v	Poisson's ratio
$\boldsymbol{v}$	Velcoity
W	Energy stored in magnetic coil
ω	Frequency
ξ_0	Coherence length
r, ϕ, z	Cylindrical polar coordinates

Contents

1 Introduction

1.1 Overview of superconductivity

The field of superconductivity was born in 1911 when Heike Kamerlingh Onnes was investigating the electrical properties of metals at temperatures close to absolute zero using liquid Helium [1]. He discovered that at 4.1K mercury suddenly lost all resistance. He originally attributed the loss of resistance to a short circuit across the sample but this was ruled out when the sample was allowed to warm slightly and the resistance returned. In his own words "*Mercury has passed into a new state, which on account of its extraordinary electrical properties may be called the superconductive state*" [2]. His ground-breaking work led to him receiving the Nobel Prize in Physics in 1913 for "his investigations on the properties of matter at low temperatures which led, inter alia, to the production of liquid helium".

There have, over the years, been some very accurate experiments conducted into the upper bound of the resistivity of superconductors. They worked by inducing supercurrents in thin film superconducting rings and measuring the decay of the magnetic field produced by the circulating current. One experiment by Crow stands out as the decay was measured for two and a half years [3] and in this time there was no measurable decay in the persistent current! Improvements in the measurement techniques including changing from Hall probes to highly sensitive pickup coils and reducing the inductance of the ring so that any loss of energy was more measurable put the upper bound of the resistivity of a superconductor to be $10^{-23}\Omega$cm [4]. This is very low, even when compared to the best normal electrical conductor, high purity silver, which has a resistivity of around $10^{-9}\Omega$cm in liquid helium.

The other defining property of superconductors was discovered in 1933 [5]. It was discovered that a superconductor, when cooled to below its critical temperature, acts like a perfect diamagnet in that it will actively expel all applied magnetic flux from the superconducting bulk. This is achieved by the formation of supercurrents in the surface of the superconductor which create a field which is exactly equal to and opposite from the applied field. This effect, known as the Meissner effect, separates a superconductor from a material with just zero resistivity as a perfect conductor would trap the flux rather than expelling it.

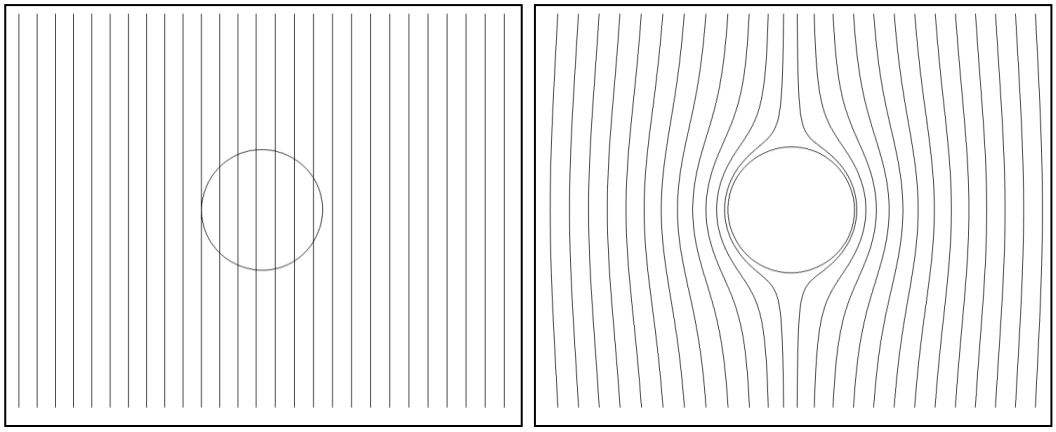

$T>T_c$ $T<T_c$

Figure 1.1. Illustration showing the magnetic field lines around a superconductor above and below its critical temperature.

1.1.1 Critical parameters

In materials which exhibit superconductivity the superconducting state can only exist below a critical temperature, as Onnes discovered by allowing his sample to warm up. Above the critical temperature the material will revert to a 'classical' material, losing its superconducting properties. The transition temperature is not a constant; it varies from material to material and with environmental factors such as pressure, applied magnetic field and current density. Due to the effects of magnetic fields and currents the critical temperature, $T_{c,}$ is defined as the transition temperature with no applied fields or currents.

Applied magnetic fields and applied currents are the environmental factors which are most relevant to this thesis. As the level of applied magnetic field or current density is increased, the temperature at which superconductivity can be observed in a particular material decreases [6]. There comes a point when the applied field or current density is so strong that superconductivity cannot occur, even at absolute zero. This magnetic field is called the critical magnetic field, B_{c0} and the current density is known as the critical current J_{c0}. The critical magnetic field can be related to the critical temperature by the following equation [7]:

$$B_c(T) = B_c(0)\left[1 - \left(\frac{T}{T_c}\right)^n\right] \qquad 1.1.$$

where n=1.7 is a reasonable fit for most practical superconductors.

The three critical parameters can be combined to form a three dimensional graph with one parameter on each axis. The superconducting transition can be displayed on this BJT (Field, Current and

Temperature) graph as a surface also known as the critical surface. A superconductor exposed to conditions which lie above this surface will be in the normal phase and one exposed to conditions which lie below it will be superconducting.

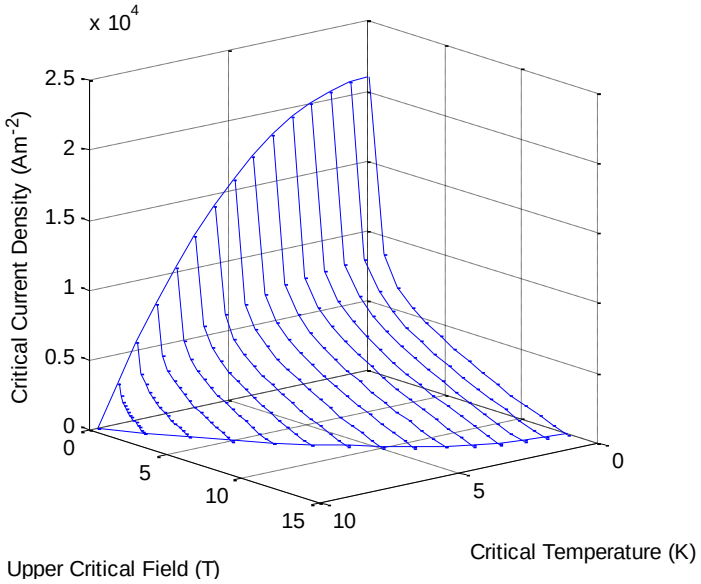

Figure 1.2. Graph showing the critical surface of a typical NbTi wire.

1.1.2 Type I and Type II superconductors

The ability to make wires without a measurable resistance would have been very useful in fields such as the creation of high field electromagnets and power transition. However, all the early superconductors which were discovered were Type I superconductors which are typically pure metals. The type I superconductors all have very low critical magnetic fields, for example mercury has a B_c of just 40mT, which would rule out their use in magnets. To make matters worse, due to the Meissner effect, the magnetic field inside the superconductor is zero and so $\nabla \times \boldsymbol{H} = 0$ for a superconducting region. By Ampere's law, in the steady state, if there is no magnetic field the current density, $\boldsymbol{J}$, must also be zero. Put another way, for current to flow in a type I superconductor, there must be an electric field and so must be subject to dissipative processes. Therefore a type I superconductor will only have zero resistance if there is no current flowing!

The problem of having dissipative superconducting materials seemed to be intractable until the late 1930's when a new class of superconductor, the type II superconductivity, was discovered in lead-bismuth (PbBi) [8]. These new type II superconductors (with a few exceptions such as pure niobium) tended to not be pure metals but alloys or ceramics. They were discovered to have two critical magnetic fields B_{c1} and B_{c2}. With an applied field up to B_{c1} a type II superconductor behaves

exactly like a type I one. When the applied field is greater than B_{c2} then the superconductivity is destroyed. However, between the two critical fields there is a region in which the magnetic flux partially penetrates the superconducting material. The ability of magnetic flux to penetrate a type II superconductor means that $\nabla \times \boldsymbol{H} \neq 0$ inside the superconductor and so it can carry bulk currents.

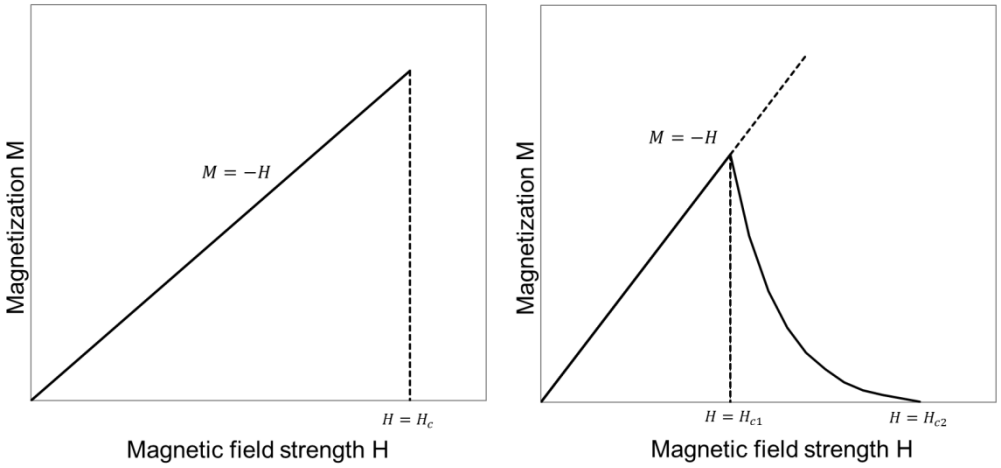

Figure 1.3. Graph showing magnetization of type I and type II superconductors.

In the late 1950's the first practical type II superconductors were discovered with the most important being niobium-titanium (NbTi) and niobium-tin (Nb_3Sn). These superconductors, along with the ability to carry bulk currents, had relatively high critical temperatures and magnetic fields (9.3K and 14.4T for NbTi [9] [10] and 17.8K and 29.5T for Nb_3Sn [11]).

1.2 Other properties of superconductors

1.2.1 Energy gap

Over the years there has been a lot of evidence produced that suggests that there is a difference in the energy of the electrons between the superconducting state and the normal state. This is called the energy gap and is an important property of superconductors which any complete theory of superconductivity must account for. Some of the important experiments which have documented the energy gap are:

Thermal conductivity measurements (1953) – Goodman performed experiments to measure the thermal conductivity of superconducting tin well below its transition temperature [12]. He discovered that the electronic thermal conductivity had an exponential term which was "characteristic of a certain type of physical assembly, for which an energy gap exists between the ground state and

the lowest excited state". In a superconductor the superconducting state is the ground state and the normal state is the excited one.

Specific heat (1956) – Corak measured the specific heat capacity of vanadium above and below its transition temperature [13] and he found that below $0.7T_c$ the electronic component of the specific heat capacity, like Goodmen in the thermal conductivity, had an exponential term consistent with a material where there is an energy gap $\sim k_B T_c$.

Microwave absorption (1957) – By measuring the transition of microwaves through thin films of superconducting tin and lead Glover discovered that there was a sharp absorption peak at microwave frequencies corresponding to an energy of $\sim 3k_B T_c$ [14] and that the energy of this peak varied with temperature. This again indicates that there are two states separated by an energy gap as when the microwave energy matches the gap energy the microwaves readily excite electrons to the higher state and hence the sharp absorption peak.

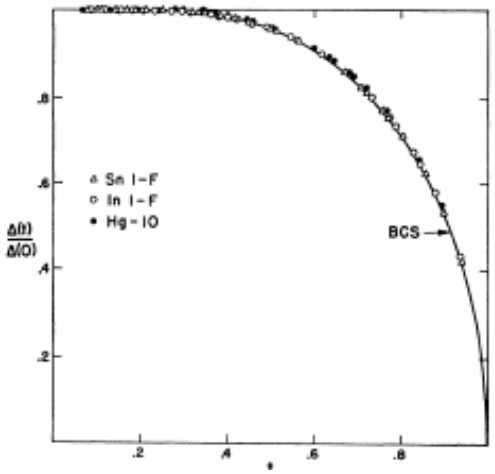

Figure 1.4. Graph showing the variation of the energy gap in a superconductor with temperature [15].

Electron tunnelling (1960) – In work which led to him sharing the 1973 Nobel prize in physics, Giaever investigated the properties of junctions between normal and superconducting material separated by a thin insulating layer [16]. He discovered that in a junction with two normally conductive materials separated by an insulator (NIN) the tunnelling current would vary linearly with applied voltage. However in the superconductor/insulator/normal conductor (NIS) junction the tunnelling current was very much lower at low voltages tending to the behaviour of a NIN junction at a specific critical voltage; V_c. This can be explained by the existence of an energy gap in the

superconductor with the gap being equal to twice the critical voltage. Figure 1.5 shows a more complete explanation of this behaviour.

A detailed graph showing the dependence of the energy gap as a function of temperature taken from [15] is shown in Figure 1.4.

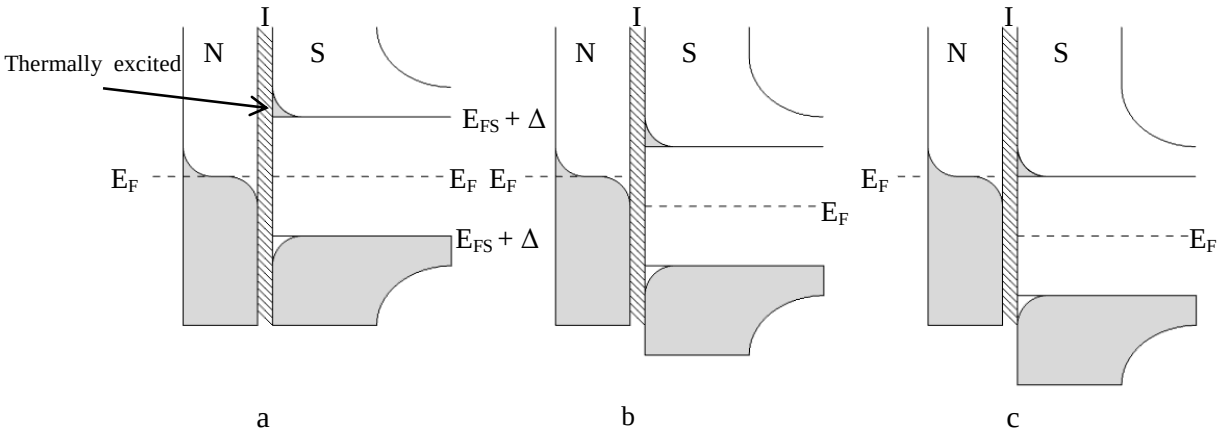

Figure 1.5. Effect of voltage on a NIS junction. a) V=0: A few electrons are thermally excited in the superconductor and the Fermi surface of both materials lie in equilibrium with no current flowing. b) V<V_c. A small current can flow as the voltage shifts the relative positions of the Fermi surfaces and a few of the highest energy quasi-particles can tunnel across the barrier. c) V=V_c. The Fermi energy of the normal material is level with one of the bands in the superconductor so quasi-particles are free to tunnel.

1.2.2 Isotope effect

In 1950 Maxwell [17] and Reynolds [18] both reported that the critical temperature of mercury varied with the atomic mass, M. Shortly after this discovery it was shown that this relation could be expressed as [19] [20]:

$$M^{\frac{1}{2}}T_c = const. \tag{1.2.}$$

Further work showed that exponent of M was close to ½ for a range of superconductors. This was an important discovery as it gave the first direct evidence that phonons were directly linked to the superconducting state. This is because phonons modelled as simple harmonic oscillators have energies which are proportional to $1/\sqrt{M}$ and there is no other known mechanism by which the neutron number of an element could affect the superconducting properties.

1.3 Theories of superconductivity

So far we have just looked at the basic properties of superconductors and have not considered any theories as to what causes this effect. This section will attempt a brief introduction to some of the

important theories which have helped to advance the knowledge of superconductivity over the past hundred years.

1.3.1 Two fluid model

The two fluid model of superconductivity was the first model to try to explain the phenomenon. Proposed by Gorter and Casimir [21], the phenomenological model was inspired by the two fluid model of superfluid helium and was based on the assumption that there were two types of electron in a superconductor. It assumed that below the transition temperature a number of electrons became super-electrons, n_s, which could flow without being subject to dissipative processes. The rest of the electrons, n_n, in the material were assumed to remain in the 'normal' resistive state. As the total number of electrons in the material is constant the electron density can be divided into:

$$n = n_n + n_s \tag{1.3.}$$

At absolute zero all of the electrons in the superconductor would be in the super state. As the temperature approaches the transition temperature the number of super-electrons falls until, at the transition temperature, all electrons are in the normal state. The model offered no theories as to why this would happen but it does explain the zero resistance of superconductors as the super-electrons flow preferentially to the resistive electrons and so the flow of current is resistanceless.

Another assumption of the model is that the two states are separated by condensation energy [22]. For an electron to move into the lower (superconducting) state it must give up this condensation energy.

1.3.2 Thermodynamics of condensation into superconducting state

All phase changes in any material be it solid to liquid, liquid to gaseous or in this case normal to superconducting, have an associated latent heat. This latent heat is the difference in the internal energies between the initial and final state. As was stated in the previous section on the two fluid model: it was assumed that at any given temperature below the transition temperature there would be some normal electrons and some super-electrons with a constant number of total electrons (equation 1.3). At the superconducting transition, if the Gibb's free energies (G_N and G_S are the Gibb's energies of the normal and superconducting states respectively) of each state were different, one state would have more energy and this would allow some electrons to change from one state to the other and a

steady state would not exist. Therefore at the transition boundary the Gibb's energies must be in equilibrium:

$$G_s(T, H_c) = G_N(T, H_c) \tag{1.4.}$$

If we consider a long cylindrical sample in a uniform field then the change in Gibb's energy with field is [20]:

$$G_s(T, H) - G_s(T, 0) = \int dG = -\mu_0 v \int_0^H \boldsymbol{M} \cdot d\boldsymbol{H} \tag{1.5.}$$

We know from the Meissner effect that the magnetization of a superconducting sample is always exactly equal and opposite from the applied field $\boldsymbol{M} = -\boldsymbol{H}$. Therefore the change in Gibb's energy from a sample with no applied field caused by applying the critical field is:

$$G_s(T, H_c) - G_s(T, 0) = \mu_0 v \int_0^{H_c} \boldsymbol{H} \cdot d\boldsymbol{H} \tag{1.6.}$$

Therefore

$$G_s(T, H_c) = G_s(T, 0) + \frac{1}{2}\mu_0 v H_c^2 \tag{1.7.}$$

If any paramagnetic or diamagnetic moments of the normal state are ignored then its magnetic susceptibility is zero. Thus:

$$G_N(T, H_c) = G_N(T, 0) \tag{1.8.}$$

By using equation 1.4 we can see that if there is no applied field then:

$$G_N(T, 0) = G_s(T, 0) + \frac{1}{2}\mu_0 v H_c^2 \tag{1.9.}$$

It is clear from this equation that, below the critical temperature, the energy of the superconducting state is lower. This tells us that the superconducting state is energetically favourable to the normal state below the critical temperature and is therefore the stable state.

There are some other useful things which can be derived from equation 1.9. The transition between the two states is reversible and so its entropy can be found simply from:

$$S = -\left(\frac{\partial G}{\partial T}\right)_{p,H} \tag{1.10.}$$

This gives the entropy difference between the two states as:

$$S_N(0) - S_s(0) = -\mu_0 H_c \frac{dH_c}{dT} \qquad 1.11.$$

We know from equation 1.1 that at the transition temperature the critical field is zero and therefore the difference in entropy given by equation 1.11 is also zero. This tells us that the function of entropy, the first derivative of the Gibb's function, is continuous through the transition between the two states. However the specific heat capacity which is defined by:

$$C_p = T\left(\frac{\partial S}{\partial T}\right)_p = -T\left(\frac{\partial^2 G}{\partial T^2}\right)_p \qquad 1.12.$$

i.e. the second derivative of the Gibb's function, is discontinuous. This is due to the sharp change in the slope of the entropy function between the two states. Due to this discontinuity in the second derivative the superconducting phase change is known as a second order phase change [24].

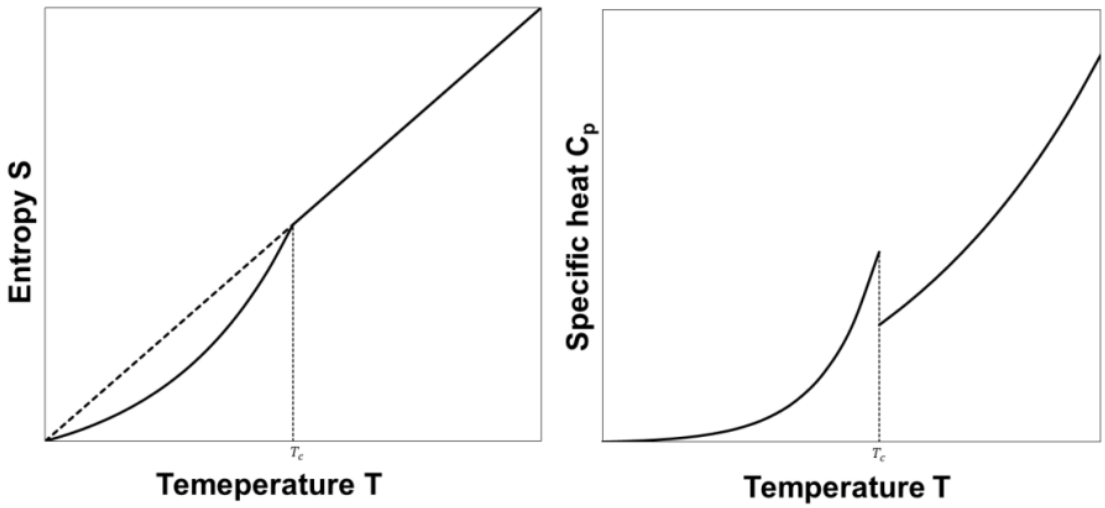

Figure 1.6. The entropy and specific heat of a superconductor vary around the transition temperature with no applied background field. The dashed line shows how the entropy would vary if there were no transition at T_c.

If we again refer back to equation 1.1 it is clear that $\frac{dH_c}{dT}$ is always negative for a superconducting material. When this result is applied to equations 1.11 it is apparent that the superconducting state has lower entropy. This tells us that the superconducting state is less disordered than the normal state. This is due to the electrons condensing in momentum state, giving fewer possible states which the electrons can occupy, increasing their order.

1.3.3 London Model

The London model was a theory proposed by the London brothers in 1935 [25] and more completely by F London in 1950 [26] which tried to put the resistanceless flow of electrons in a mathematical framework. In the absence of a magnetic field the Lorentz force on an electron with charge q is:

$$\boldsymbol{F} = q\boldsymbol{E} \tag{1.13.}$$

As we are dealing with a superconductor we can assume that the electrons within the superconductor are free to move without dissipative forces and so the equation of motion becomes:

$$\frac{d\boldsymbol{v}}{dt} = \frac{q\boldsymbol{E}}{m} \tag{1.14.}$$

where m is the mass of the electron. The supercurrent is the flow of charge so is:

$$\boldsymbol{J} = nq\boldsymbol{v} \tag{1.15.}$$

where n is the number density of electrons. This gives:

$$\frac{d\boldsymbol{J}}{dt} = \frac{nq^2\boldsymbol{E}}{m} \tag{1.16.}$$

The Maxwell-Faraday equation is:

$$\nabla \times \boldsymbol{E} = -\frac{d\boldsymbol{B}}{dt} \tag{1.17.}$$

Therefore

$$\frac{d}{dt}(\nabla \times \boldsymbol{J}) = -\frac{nq^2}{m}\frac{d\boldsymbol{B}}{dt} \tag{1.18.}$$

and so

$$\frac{d}{dt}\left(\nabla \times \boldsymbol{J} + \frac{nq^2}{m}\boldsymbol{B}\right) = 0 \tag{1.19.}$$

Using Ampere's law:

$$\frac{d}{dt}\left(\nabla \times \nabla \times \boldsymbol{B} + \frac{nq^2}{m}\boldsymbol{B}\right) = 0 \tag{1.20.}$$

If we use the formula which applies to any vector:

$$\nabla \times \nabla \times \boldsymbol{B} = \nabla(\nabla \cdot \boldsymbol{B}) - \nabla^2\boldsymbol{B} \tag{1.21.}$$

And Gauss' Law of magnetism:

$$\nabla \cdot \boldsymbol{B} = 0 \tag{1.22.}$$

We get:

$$\frac{d}{dt}\left(\nabla^2\boldsymbol{B} - \frac{nq^2}{\mu_0 m}\boldsymbol{B}\right) = 0 \tag{1.23.}$$

The solution to this equation could either be one of a constant magnetic field within the superconductor or one with a magnetic field which decays exponentially with time. However these solutions are not compatible with the observations of the Meissner effect which has the result that $\boldsymbol{B} = 0$ throughout the bulk of the material, not a constant but finite field or a decaying field. The London brothers recognized this and postulated that not only does the above equation have to equal zero but also the part contained within the bracket must also be equal to zero. Using this postulate and Ampere's law you end up with the London equation:

$$\nabla \times \boldsymbol{J} + \frac{1}{\mu_0 \lambda_L^2} \boldsymbol{B} = 0 \qquad 1.24.$$

where

$$\lambda_L = \left(\frac{m}{\mu_0 n q^2}\right)^{\frac{1}{2}} \qquad 1.25.$$

This can be written more simply by expressing the magnetic field in terms of a gauged vector potential using:

$$\boldsymbol{B} = \nabla \times \boldsymbol{A} \qquad 1.26.$$

Where the gauge is chosen as $\nabla \cdot \boldsymbol{A} = 0$. This is known as the London gauge and leads to the simplified London equation of:

$$\boldsymbol{J} = -\frac{1}{\mu_0 \lambda_L^2} \boldsymbol{A} \qquad 1.27.$$

For the simple situation where we have a flat boundary between superconducting and normal materials with the x-vector being perpendicular to the surface the solution to the London equation is simply of the form:

$$B = B_0 e^{\frac{-x}{\lambda_L}} \qquad 1.28.$$

where x is the distance from the surface of the superconductor to a point inside the material. From this equation we can see that λ_L is the depth to which any magnetic field and hence current will penetrate into the superconductor. Due to this λ_L is known as the London penetration depth and is one of the most important results to come out of the London theory. The penetration depth of lead at absolute zero is $3 \times 10^{-8} m$ [24] and is similar for other type I superconductors. The penetration depth varies with temperature as it is dependent on the number of electrons in the superconducting state which varies from a maximum at absolute zero to none at the transition temperature. At distances much

greater than λ_L the magnetic field will be zero. This shows that the London theory is compatible with the observations of zero resistance and the Meissner effect.

1.3.4 Pippard coherence length

Pippard's work on the penetration depth and surface energy of superconductors [28], [29] led him to start developing the concept of a 'range of coherence', ξ, of the order of 1μm. This range of coherence is the length over which superconducting properties could change.

In 1951 Pippard presented some work which demonstrated that the penetration depth of tin varied markedly when doped with a small amount of indium without any correspondingly large change in the thermodynamic properties [30]. As the thermodynamic properties were almost unchanged the number of charge carriers must also have remained very similar however in the London model the penetration depth depends only on the carrier density so could not account for this discovery. His earlier concept of a range of coherence along with the new discovery motivated him to propose a modification of the London theory [31]. He pointed out that the London model was a 'local' theory of superconductivity as the supercurrent density, $\boldsymbol{J}$, at a particular point within the superconductor depends only on the magnetic vector, $\boldsymbol{A}$, at that specific point. He proposed that a magnetic perturbation would affect all charge carriers at all points within a distance ξ_0, known as the coherence length, of the perturbation. This led to a modified London equation of the form:

$$\boldsymbol{J} = -\frac{n_s q^2}{m_e}\frac{3}{4\pi\xi_0}\int \frac{\boldsymbol{r}(\boldsymbol{r}\cdot\boldsymbol{A})e^{-\frac{\vec{r}}{\xi}}}{r^4} \qquad 1.29.$$

With:

$$\frac{1}{\xi} = \frac{1}{\xi_0} + \frac{1}{\ell} \qquad 1.30.$$

Where the coherence length, ξ_0, is a constant with the dimension of length and ℓ is the mean free path of the superelectrons, a concept analogous to the mean free path of electrons in a normal metal. Thus ξ is the distance over which an applied field will affect the supercurrent in a superconductor. From equation 1.30 it can be seen that in the 'clean limit' where there are few scattering centres so that ℓ is large the range of coherence tends to the coherence length but in a dirty superconductor with a small ℓ the range of coherence will be reduced. This has the consequence that as impurity is added an applied field will be able to penetrate the sample more easily and hence it predicts the correct form of the variation of penetration depth with impurities that was seen. By matching the theory to the results a

figure for ξ_0 of around 10^{-4}cm was found. This figure matched other experimental data well [28] [29]. A similar figure can also be found by simple quantum mechanical considerations: as many theories of superconductivity (for example Pippard quoted [32] [33]) consider that the effect is primarily due to the ordering of electrons in momentum space with an energy within $K_B T_c$ of the Fermi surface. Thus the superelectrons with a velocity, v_f, will have a range of possible values of momentum, P, of the order of:

$$dP = \frac{2dE}{v_f} \approx \frac{2k_b T_c}{v_f} \quad 1.31.$$

As the Heisenberg uncertainty states that $dx \cdot dP \geq \frac{\hbar}{2}$ then:

$$dx \geq \frac{\hbar v_f}{4k_b T_c} \approx 10^{-4} cm \quad 1.32.$$

Put together this evidence gave a good indicator that superconductors had a coherence length and that superconductivity was a 'non-local' phenomenon.

1.3.5 Ginzburg-Landau theory

In 1950 Ginzburg and Landau published a phenomenological model of superconductivity [34] that was based on the thermodynamics of the second order phase change between the normal and superconducting state. The theory expanded upon Landau's earlier work on other second order phase changes [35] such as the ferromagnetic phase change. In the other second order phase changes there is an order parameter of the system which is zero at temperatures above the transition temperature in the normal, disordered, phase but is none-zero below the transition where the system has become more ordered. In superconductivity this parameter was Ψ which represents the wave function of the superelectrons so $\Psi = 0$ when $T \geq T_c$ and $\Psi = \Psi(T) \neq 0$ when $T < T_c$. It was assumed that Ψ was a complex parameter which varied smoothly with temperature and that all the properties of the superconductor would therefore depend on $|\Psi|$. In the theory of second order transitions the free energy is dependent on $|\Psi|^2$ and as $|\Psi|$ tends to zero at T_c we can expand the function of the free energy, F, in a uniform superconductor near to the transition temperature as:

$$F_{s0} = F_{n0} + \alpha|\Psi|^2 + \frac{\beta}{2}|\Psi|^4 \quad 1.33.$$

where orders higher than the forth power have been ignored as $|\Psi|$ is small and so the higher orders will have a negligible effect on the free energy. For the system to be in equilibrium the free energy must be minimized, therefore:

$$\frac{\partial F_{so}}{\partial|\Psi|^2} = 0, \qquad \frac{\partial^2 F_{so}}{(\partial|\Psi|^2)^2} > 0 \tag{1.34.}$$

From this it is easy to see that $\beta_c > 0$ and that $\alpha < 0$ for $T < T_c$. If we assume that the coefficients α and β vary smoothly with temperature and that we work at a temperature close to, but below, T_c then we can express these coefficients as a Taylor series:

$$\begin{gathered}\alpha(T) = (T - T_c) \cdot \left(\frac{d\alpha}{dT}\right)_c + \cdots \\ \beta(T) \approx \beta_c + \cdots\end{gathered} \tag{1.35.}$$

By combining equations 1.33, 1.34 and 1.35 we find that the minimum free energy occurs at:

$$|\Psi| = \left(\frac{\dot{\alpha}}{\beta_c}\right)^{\frac{1}{2}} \cdot (T_c - T)^{\frac{1}{2}} \tag{1.36.}$$

$$F_{s0} = F_{n0} - \frac{\dot{\alpha}^2}{2\beta_c}(T_c - T)^2 \tag{1.37.}$$

where $\dot{\alpha}$ has replaced $\left(\frac{d\alpha}{dT}\right)_c$. By taking into account the difference in energies between the superconducting and normal states given by 1.9 we find the critical field:

$$H_c = \frac{\dot{\alpha}}{\sqrt{\mu_0 \beta_c}}(T_c - T) \tag{1.38.}$$

So far we have just considered spatially uniform superconductors in the absence of applied magnetic fields. If we now apply a magnetic field we must take into account the energy required to expel the field from the bulk of the superconductor along with any energy due to gradients in Ψ. For small values of $|\nabla\Psi|^2$ we can use a series expansion of the energy associated with the gradient and the result, $|-\mathrm{i}\nabla\Psi|^2$, looks like a kinetic energy density in quantum mechanics. Here we introduce a new constant m^* which can be seen as the 'effective mass' and it determines the energy cost of having gradients in Ψ. As the equation should be gauge invariant we will use the usual quantum mechanics gauge replacement of $-i\hbar\nabla \rightarrow -i\hbar\nabla - \mathrm{q}\mathbf{A}$ where $\boldsymbol{A}$ is the magnetic vector potential. q is the charge of the 'particle' which Ψ describes. This was originally assumed to be the charge on an electron but after

BCS theory was developed it became apparent that q was the charge on the cooper pair so $2e$. The energy to set a gradient in Ψ is then:

$$\left(\frac{\hbar^2}{2m}\right)|\nabla\Psi|^2 = \left(\frac{1}{2m}\right)|-\mathrm{i}\hbar\nabla\Psi|^2 = \left(\frac{1}{2m}\right)|-\mathrm{i}\hbar\nabla\Psi - 2\mathrm{e}\mathbf{A}\Psi|^2 \qquad 1.39.$$

When we include the energy required to expel the applied field from the bulk superconductor we get the free energy of the superconductor to be:

$$F_{s0} = F_{n0} + \left(\frac{1}{2m}\right)|-\mathrm{i}\hbar\nabla\Psi - 2\mathrm{e}\mathbf{A}\Psi|^2 + \alpha|\Psi|^2 + \frac{\beta}{2}|\Psi|^4 \qquad 1.40.$$

By minimizing equation 1.40 with respect to the magnetic vector and by using the fact that the supercurrents are equal to $-\partial F_s/\partial A$ [20] the following equation is obtained:

$$\boldsymbol{J}_s = \nabla^2\boldsymbol{A} = -\frac{e\hbar i}{m^*}(\Psi^*\nabla\Psi - \Psi\nabla\Psi^*) - \frac{4e^2}{m^*}|\Psi|^2\boldsymbol{A} \qquad 1.41.$$

An interesting point to note is that in the absence of gradients in the vector field then equation 1.41 reduces to a form very similar to the London equation 1.27:

$$\boldsymbol{J} = -\frac{1}{\mu_0\lambda^2}\boldsymbol{A} \qquad 1.42.$$

Where $\lambda = \lambda_L$ if $|\Psi|^2 = n_s$ i.e. that the magnitude of the order parameter squared is equal to the density of superelectrons. Using equation 1.36 we get the penetration depth:

$$\lambda(T) = \left(\frac{m^* b}{2\mu_0 e^2 \dot{\alpha}(T_c - T)}\right)^{\frac{1}{2}} \qquad 1.43.$$

Another key result of GL theory is found by minimizing the free energy in zero applied field. By considering the equation in one dimension and by using the result in equation 1.33, the following equation is obtained:

$$\frac{\partial F_s}{\partial \Psi} = -\frac{\hbar^2}{2m^*}\frac{d^2\Psi(x)}{dx^2} + a(T)\Psi(x) + b(T)\Psi^3(x) = 0 \qquad 1.44.$$

which has the solution:

$$\Psi(x) = \Psi_0 \tanh\left(\frac{x}{\sqrt{2}\xi(T)}\right) \qquad 1.45.$$

where $$\xi(T) = \left(\frac{\hbar^2}{2m^*\dot{\alpha}(T_c - T)}\right)^{\frac{1}{2}}$$ 1.46.

The parameter ξ is known as the Ginzburg-Landau coherence length and, in a similar manner to the Pippard coherence length earlier, gives the length scale over which the properties of the superconductor can change and is, like the penetration depth, a function of temperature. The coherence length and penetration depth can be combined to give a dimensionless parameter:

$$k = \frac{\lambda}{\xi}$$ 1.47.

The importance of this factor will become apparent later in this chapter as it can be used to classify different types of superconductor.

1.3.6 BCS microscopic theory of superconductors

So far all the theories considered have been phenomenological or empirical theories and have thus not tried to explain the microscopic behaviour which leads to superconductivity; they have only tried to create self-consistent framework to explain what is observed. This changed in 1957 when Bardeen, Cooper and Schrieffer published the first microscopic theory of superconductivity: BCS theory [36]. This sought to explain how interactions between fundamental microscopic particles could give rise to the complex macroscopic phenomenon witnessed. The theory fully accounted for all the known behaviours of superconductors including zero resistivity, the Meissner effect, the energy gap and the isotope effect. As in 1959 Gor'kov showed that Ginzburg-Landau theory could be derived from BCS theory [37], and the full derivation of the theory is far more complicated than is justified for this thesis, only a very brief explanation is presented here.

The two of the key building blocks for BCS theory were provided by Cooper in his 1956 paper on bound electron pairs [38] and Fröhlich in his 1950 paper on the interaction of electrons in a metal [33] which showed how the attractive force required by Cooper could arise. Fröhlich demonstrated that the interaction between electrons and the crystal lattice can cause an attractive force between two electrons despite the repulsive force caused by the Coulombic charges of the electrons. This is obviously not possible with free, bare, electrons. However when the electrons are contained within a conducting material they are not free so excited electrons need to be treated as a quasiparticle where every electron is paired with a corresponding positively charged hole. The effect of these extra holes is

that the repulsive interaction is greatly reduced, dropping to a negligible amount in very short distances, by a process called charge screening. Along with the screening effect of the holes the electron can interact with the lattice of the material. This electron-phonon interaction exists as a phonon is a periodic displacement of the atoms and hence in the electron charge density of the lattice. As the charge density is shifted this creates a periodic electric potential with a wavelength $2\pi/q$ for a phonon with momentum **q**. This periodic potential can then diffract the electrons passing through it. An electron with an initial momentum of $\mathbf{K_1}$ can create a phonon in the lattice with a momentum **q** leaving the electron with a momentum $\boldsymbol{K_1 \pm q}$. This phonon can then travel through the lattice until it is absorbed by a second electron. This is then an interaction at a distance where one electron has caused a momentum change in a second electron by the exchange of a virtual phonon. This interaction can be expressed as a Feynman diagram as shown in Figure 1.7 and it is worth noting that there is no direction arrow needed on the phonon branch as the effect of the interaction is independent of which electron which created or destroyed the phonon.

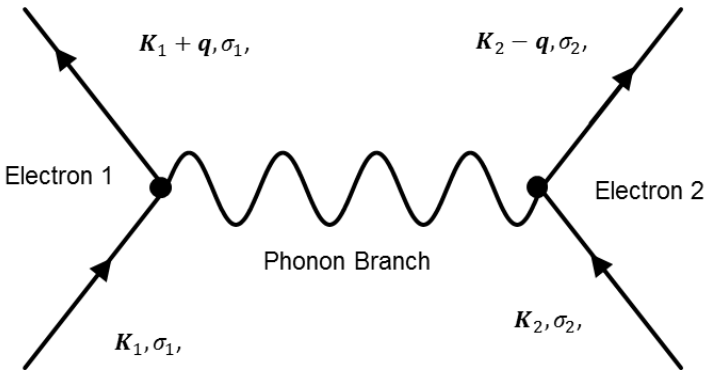

Figure 1.7. Feynman diagram showing how two electrons can interact by the emission/absorption of a virtual photon.

The mathematical analysis of this interaction is beyond the scope of this thesis but the final result for a phonon of momentum $\boldsymbol{q}$ and frequency ω gives an effective force between the two electrons of [20]:

$$V_{eff}(\boldsymbol{q}, \omega) \propto \frac{1}{\omega^2 - \omega_D^2} \qquad 1.48.$$

where ω_D is the Debye frequency of the phonons. It is clear from this equation that the force is attractive for phonons whose frequency is less than the Debye frequency and repulsive for those above it. Hence by combining the greatly reduced Coulombic repulsion due to charge screening and the phonon interaction it is possible for there to exist a net attraction between two electrons in a lattice.

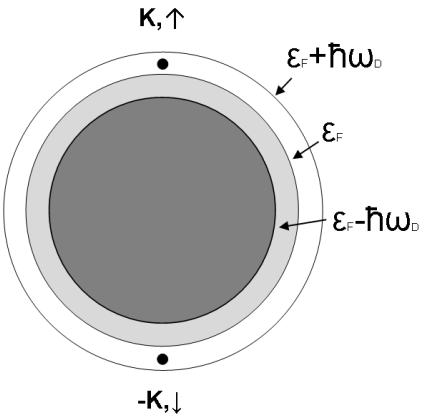

Figure 1.8. A simplified Fermi surface with the $\pm\hbar\omega_D$energy levels which mark the limit of the attractive interaction between two electrons. Also shown is the state of the two electrons considered by Cooper in his paper on bound electron pairs [38].

In the next step towards a full theory of superconductivity Cooper considered the interaction between two electrons with energies which placed them just above a full Fermi surface but below the Debye energy level as shown in Figure 1.8. He showed that two such electrons would have allowable energy levels which lay in a continuous energy spectrum with one, discrete level which was lower than the others by an energy:

$$E = -2\hbar\omega_D e^{-\frac{1}{\lambda}} \qquad 1.49.$$

Were λ is known as the electron-phonon coupling parameter and is assumed to be $\ll 1$ and gives a measure of how likely an electron and a phonon are to interact. Hence for two electrons above a filled Fermi sea there exists a bound state no matter how small the attractive force between them.

BCS realised that with an attractive force the entire surface of the Fermi sea could form bound electron pairs and so the final steps to the full microscopic theory of superconductivity were to produce a coherent state describing the many particle wave function of the Cooper pairs. The resulting wave function predicted a 'gap parameter' or binding energy of the same form as Cooper found in equation 1.49.

This theory was very successful and provided a microscopic explanation to all of the properties of superconductors which had been observed at the time. As the electrons are in a bound state with a net attractive force between them it would take an energy increase to break the pair and hence this gives rise to the energy gap as the bound state is a lower energy state than the free state. The magnitude of the energy gap predicted by BCS was $\sim 3.5 k_B T_c$ or $\Delta = 1.76 k_B T_c$ which agrees very well with the measured data as shown in section 1.2.1. This energy gap then provides an explanation for the

existence of the critical temperature and magnetic field; the critical parameter is just the value of that parameter which will increase the energy of a bound cooper pair by more than the binding energy. The low critical temperatures are explained by the fact that, although the Debye temperature is quite high (~100-300K) for most materials the small electron-phonon coupling constant reduces the relevant temperature range to just a few degrees kelvin. The parameter λ also explains why superconductivity is found primarily in poorly conducting metals as it requires a full Fermi sea (hence the metals at low temperatures) and the better the conductor a metal is the lower the chance of an atom scattering an electron and so the smaller the value of λ becomes. The isotope effect is easily explained within this theory as the superconducting state is a product of the exchange of phonons hence, as stated in section 1.2.2, the energy of the phonons is dependent on the mass of the atoms in the lattice.

By far the hardest common phenomenon to explain with BCS theory is perhaps the most striking: the ability to carry a current with zero resistivity. A reasonably detailed description can be found in relevant text books [39]. However the simple explanation is that with no current flowing the electrons in the Cooper pair have momentum $+k$ and $-k$. When a current is flowing both electrons gain a small extra momentum term δk so the momentums become $\delta k \pm k$ and the average momentum of the pair is δk. As this extra momentum is very small the wavelength of the pair will be very long and as particles are only scattered effectively by features on the same length scale as their wavelength there will be very weak scattering of the pair. This combined with the fact that any scattering event would need to provide enough energy to break the pair before they could be scattered accounts for the infinite conductivity of the superconductor.

The binding energy of the cooper pairs gives a fundamental limit to the current, a so called intrinsic limit, like the critical magnetic field or critical temperature called the depairing current. The depairing current is the current level at which the increase in kinetic energy of the cooper pairs is equal to the energy gap. We can get a good estimate for the depairing current by combining the kinetic energy of the current density with the energy gap per unit volume which is given by $\frac{1}{2}\mu_0 H_c^2$:

$$J_c = \sqrt{\frac{m}{\mu_0 n q^2}} H_c = \frac{H_c}{\lambda} \qquad 1.50.$$

Although the depairing current provides a fundamental limit for the current in superconductors no real material will ever have a critical current of this level. The actual critical current will always be lower due to a process called flux creep and flux flow which will be introduced later in this chapter.

1.4 Type II superconductors

Now that we have explored the various theories which have been created to explain the various fundamental behaviours and properties of superconductors we can look at some of the implications of these behaviours. Perhaps the most fundamental of these is the differentiation between the type I and type II superconductors which has been alluded to earlier in this chapter but we now have the tools needed to explore where this difference comes from.

1.4.1 Surface Energy

In chapter 1.3.2 we saw that the energy associated with expelling a magnetic field from a superconducting volume is $\frac{1}{2}\mu_0 H_c^2$. However implicit in this value is the assumption that the superconducting properties start suddenly and that the external magnetic field will drop sharply to zero at the surface of the superconductor. We have seen in the later sections that this assumption is in fact incorrect as there is the coherence length of the superconducting properties, ξ, and the penetration depth of the magnetic field, λ. The variation of these parameters from the surface of the superconductor for $\lambda \ll \xi$ and for $\lambda \gg \xi$ is shown in Figure 1.9. By using equation 1.47 we can see that these refer to the situations of $k \ll 1$ and $k \gg 1$ respectively.

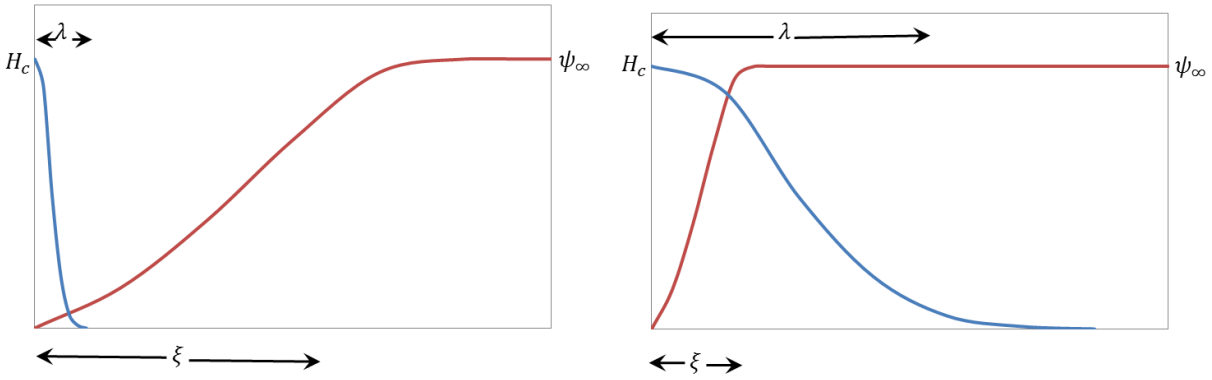

$k \ll 1$ $k \gg 1$

Figure 1.9. Graphs showing the variation of the magnetic field and order parameter from the surface of a superconductor (marked by the left edge of each diagram) in the limits of $k \ll 1$ and $k \gg 1$.

By examining this figure we can see a qualitative difference between the two regimes. For the first case with of $k \ll 1$ the magnitude of the external magnetic flux drops to zero very quickly due to the short penetration depth whereas the long coherence length results in the order parameter only reaching its full value well within the surface of superconductor. Therefore there is distance $\sim\xi - \lambda$ where all of the magnetic flux has been expelled without the full superconducting state existing. This shows that there exists a positive surface energy as the surface is at a higher energy state than the bulk of the material. In the case with $k \gg 1$ the opposite situation is true as there will be a length $\sim\lambda - \xi$ the magnetic field will still exist after the order parameter has reached its maximum value. Thus for this case there is a negative surface energy and it becomes energetically favourable for superconducting/normal surfaces to form throughout the bulk of the material. This then gives the method for classifying the two types of superconductors: type I have positive surface energy and so the formation of surfaces is energetically unfavourable; whereas type II superconductors have negative surface energies and their formation is energetically favourable. It can be shown by numeric integration of the energy using the variation of the order parameter and penetration depth [34] that the critical value for k is:

$$\frac{\lambda}{\xi} = k = \frac{1}{\sqrt{2}} \tag{1.51.}$$

$$\begin{aligned} Type\ I&: k < \frac{1}{\sqrt{2}} \\ Type\ II&: k \geq \frac{1}{\sqrt{2}} \end{aligned} \tag{1.52.}$$

Although Ginzburg and Landau originally derived this criteria they discounted the regime for the type II superconductors as all of the experimental results available to them at the time were from type I superconductors so a $k \gg 1$ seemed unphysical.

1.4.2 Flux quantization

Another key result of the Ginzburg-Landau theory is the phenomenon of flux quantization. This behaviour is simply that the flux passing through a ring of superconductor must take the value of an integer multiple of the base unit of flux. If we recall from chapter 1.3.5 that the order parameter ψ is a complex number and that inside the bulk of a superconductor it has a constant value. Therefore within the bulk material only the phase of the order parameter can vary so it can be written as:

$$\psi = |\psi| e^{i\phi} \tag{1.53.}$$

This allows us to modify the equation for the current within a superconductor given by 1.41:

$$\boldsymbol{J}_s = \left[\frac{q\hbar}{m^*}\nabla\phi - \frac{q^2}{m^*}\boldsymbol{A}\right]|\Psi|^2 \tag{1.54.}$$

If we now integrate the current around a closed loop within the bulk of the superconductor at a distance greater than the penetration depth from the surface, as the magnetic field is zero, the currents will be small and as $|\psi|$ is constant it will play no part in the integral:

$$0 = \oint \boldsymbol{J}_s \,.\, d\boldsymbol{l} = \oint \left[\frac{q^2}{m^*}\boldsymbol{A} - \frac{q\hbar}{m^*}\nabla\phi\right].\, d\boldsymbol{l} \tag{1.55.}$$

$$\oint q\boldsymbol{A} \,.\, d\boldsymbol{l} = \oint \hbar\nabla\phi \,.\, d\boldsymbol{l} \tag{1.56.}$$

If we now recall Stokes' theorem for a general vector **F**:

$$\oint \boldsymbol{F}.\, d\boldsymbol{l} = \int \nabla \times \boldsymbol{F} \,.\, d\boldsymbol{S} \tag{1.57.}$$

Then by using equations 1.26 and 1.57 the left hand side of 1.56 becomes:

$$\oint \boldsymbol{A}.\, d\boldsymbol{l} = \int \nabla \times \boldsymbol{A} \,.\, d\boldsymbol{S} = \int \boldsymbol{B}.\, d\boldsymbol{S} \tag{1.58.}$$

This integral is simply the flux passing through the area encompassed by the original path which we will denote as Φ. As for the right hand side of equation 1.56 since the order parameter cannot vary within the bulk the phase must change by a factor of 2π on the integration around the loop. Therefore we can finally write equation 1.56 as:

$$\Phi = \frac{h}{q}.\, n \tag{1.59.}$$

Where n is an integer. This tells us that the flux passing through the surface of a superconductor must be quantized into discrete levels which are multiples of the base flux quantum:

$$\Phi_0 = \frac{h}{q} \tag{1.60.}$$

Fritz London argued that the charge, q, should be the charge on an electron, e, [26]. However, later experiments [40] [41] showed that the charge is in fact $2e$. This provided direct evidence supporting

BCS theory as the superconducting carrier is a Cooper pair with two electrons and hence twice the electronic charge.

1.4.3 Abrikosov flux lattice

In section 1.1.2 the idea of type II superconductors having two critical fields, without considering the meaning of this fact, was introduced. By referring back to the magnetization curves in Figure 1.3 it can be seen that up to B_{c1} in a type II material the magnetization curve is linear. However above B_{c1} the curve deviates from the linear and the magnetization decays to zero at B_{c2}. This tells us that magnetic flux must be penetrating the bulk of the material. We have subsequently shown in section 1.4.1 that type II superconductors are unstable against the formation of superconducting/normal boundaries within the bulk of the material. Therefore between B_{c1} and B_{c2} we have normal regions within the bulk which carry magnetic flux through the sample thereby reducing its magnetization. We have also shown in section 1.4.2 that the flux passing through these normal regions must be quantized in units of $h/2e$. The first person to consider the form of these normal regions, or fluxons, was Abrikosov [42] in one of the greatest applications of Ginzburg-Landau theory to date. He proposed that the fluxons were thin tubes of flux passing through the bulk. As the energy of the system must be minimized and as a type II superconductor is unstable to the formation of fluxons each fluxon must carry carrying a single unit of quantized flux. This is because if it were larger than the flux quantum it would be energetically favourable for the fluxon to divide into smaller ones until the unitary value was reached and a smaller value is forbidden. The problem is then how the fluxons will be distributed over the surface. As the fluxons are all carrying flux in the same direction they will all be mutually repulsive and the lowest energy state is one in which the distance between each fluxon is maximized and therefore they must be arranged into a regular lattice. In his original derivation of these properties he assumed that the lowest energy state (i.e. the greatest number of fluxons per area with the greatest separation possible) would be given by a square lattice. It was latter shown that a triangular lattice has a lower energy than the square lattice [43] and we can produce a simple argument here to show that this is true. If we have a total flux, B, passing through a unit area then we must have a number of fluxons given by:

$$\frac{n}{A} = \frac{B}{\Phi_0} \tag{1.61.}$$

By looking at Figure 1.10 we can see that the area occupied by one fluxon in a square lattice is simply $A_{sq} = l_{sq}^2$ and for the triangular lattice it is $A_{tri} = \sqrt{\frac{3}{4}} l_{tri}^2$. These can be combined with the number of fluxons per area to calculate the relative fluxons separation which gives:

Square lattice
$$l_{sq} = \sqrt{\frac{B}{\Phi_0}} \tag{1.62.}$$

Triangular lattice
$$l_{tri} = \left(\frac{4}{3}\right)^{\frac{1}{4}} \sqrt{\frac{B}{\Phi_0}} = 1.075 \sqrt{\frac{B}{\Phi_0}} \tag{1.63.}$$

Therefore the larger separation gives a (slightly) lower energy.

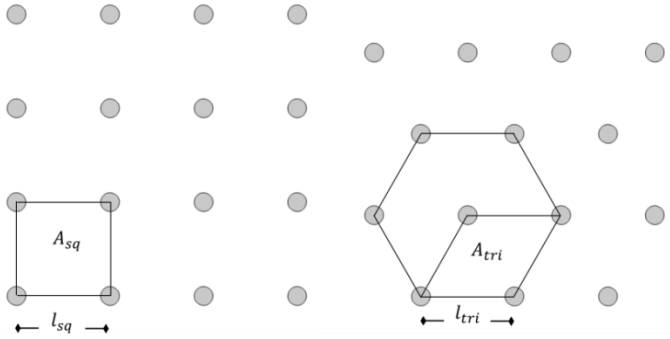

Figure 1.10. Diagram showing the fluxon distribution in a square and triangular lattice.

The Abrikosov flux lattice has been observed experimentally by several different methods from decoration with paramagnetic particles then scanning with an electron microscope [44] to scanning tunnelling microscopy [45]. The original picture of a flux lattice from [44] is shown in Figure 1.11.

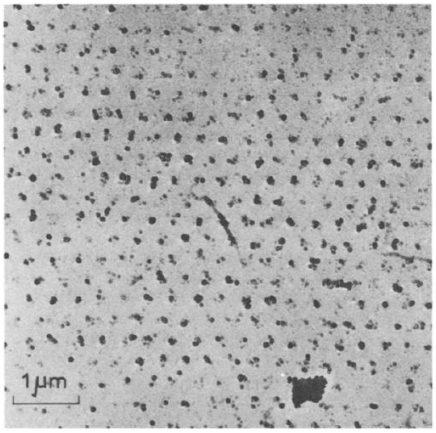

Figure 1.11. Picture showing the original image of an Abrikosov flux lattice taken from [44] which clearly shows the triangular distribution of the fluxons.

1.4.4 Flux flow, flux pinning and flux creep

We have seen so far that, due to Maxwell's equations, no current can flow in a superconductor unless some magnetic field can penetrate the sample and that when a type II superconductor is exposed to a field the flux can pass through the material in discrete fluxons. Thus a type II superconductor can carry a distributed bulk current along its length with, theoretically, zero resistance. However in a wire carrying a bulk current we have fluxons forming perpendicular to the direction of the current flow. Therefore we will have magnetic dipoles interacting with a moving current and so there will be a Lorentz force acting on the fluxons. The magnitude of this force per unit volume is given by [46]:

$$\boldsymbol{F} = \boldsymbol{J} \times \mathbf{B} \tag{1.64.}$$

If this were the only force acting upon the fluxons they would clearly move in a direction perpendicular to both the transport current and the field causing a change in the magnetic field distribution. This in turn will cause an electric field to develop due to the Maxwell-Faraday equation:

$$\nabla \times \boldsymbol{E} = \frac{d\boldsymbol{B}}{dt} \tag{1.65.}$$

or for fluxons moving with a velocity, $\boldsymbol{v}$**:**

$$\boldsymbol{E} = \boldsymbol{v} \times \boldsymbol{B} \tag{1.66.}$$

This electric field will be in a direction anti-parallel to the current and so will oppose any current flow. Thus in a perfect type II superconductor any current flow will still be dissipative despite the zero resistivity; what is needed for a dissipationless current flow is a method to fix the fluxons in place, to stop them from moving. This process is known as flux pinning. Flux pinning can be achieved by the inclusion of non-superconducting normal regions or regions with reduced superconducting properties within the bulk superconductor by creating defects in the crystal lattice. These defects can range from impurities, precipitates, dislocations, strains and grain boundaries. As the fluxons contain a core of normal material there is an associated energy cost in creating them. The same applies for the defect regions and hence the energy cost is minimized when the two regions overlap. Hence a force is required to move a fluxon away from a pinning centre to raise the energy of the system. The critical current of a superconductor is then the current at which the Lorentz force on the fluxons is greater than the pinning force. Above the critical current the fluxons will move freely and this is known as flux

flow. We can find the velocity at which the fluxons will move by considering an equation of motion with a viscous drag coefficient, η, on a single fluxon with a flux density of Φ_0 [39]:

$$J\Phi_0 = \eta v \tag{1.67.}$$

Comparison with equation 1.66 gives the electric field current relation in the flux flow regime as a linear dependence:

$$\boldsymbol{E} = \frac{B\Phi_0}{\eta}\boldsymbol{J} \tag{1.68.}$$

The viscous drag coefficient is thought to be due to the combination of two effects. The first is that the motion of a fluxon will set up electric fields across the normal core which, in turn, will cause a current to flow through a normal, and thus, Ohmic region [47]. The second is that the superconducting waveform cannot react to a perturbation instantly; instead it has a relaxation time which slows any change in superconducting properties [48].

It is worth noting that not all of the fluxons must be pinned for the entire lattice to be fixed as the lattice has a shear strength [49] very similar to the shear strength of solids in solid mechanics (see chapter 5). This means that if one fluxon is pinned then the fluxons around it will also experience a pinning force due to the interaction with the pinned fluxon. This shear modulus can cause the critical current to be reduced even lower than the de-pinning critical current if the Lorentz force exceeds the shear strength of the lattice before the pinning force [50]. In this case the lattice can deform plastically around the pinning centres causing dissipation.

If a current far below the critical current is applied to a pinned superconductor there will still be a small dissipative effect. The cause of this is thermal fluctuations which allow pinned fluxons to jump from one pinning centre to the next, dissipating a small amount of energy as it moves. Figure 1.12 shows the distribution of wells along a highly simplified superconductor assuming periodic pinning. In 1962 Anderson [51] proposed that if the fluxons were pinned in energy wells with an associated depth U then fluxons would 'hop' into adjacent wells, as shown in Figure 1.12A with a frequency:

$$R = R_0 e^{-\frac{U}{k_B T}} \tag{1.69.}$$

where R_0 is a constant which would depend on the specific material properties but it was assumed that $R_0 < 10^{10} s^{-1}$. It was then assumed that the depth of the well would be affected by the presence of a

transport current, raising the barrier to hop against the current but lowering it in the direction of the current as shown in Figure 1.12B. The current would modify the depth so that it would be described approximately by:

$$U \approx U_0 \left(1 - \frac{J}{J_c}\right) \tag{1.70.}$$

and so in the presence of a current there will be a flux creep dissipating energy with a rate:

$$R = R_0 e^{-\frac{U_0}{k_B T}\left(1-\frac{J}{J_c}\right)} \tag{1.71.}$$

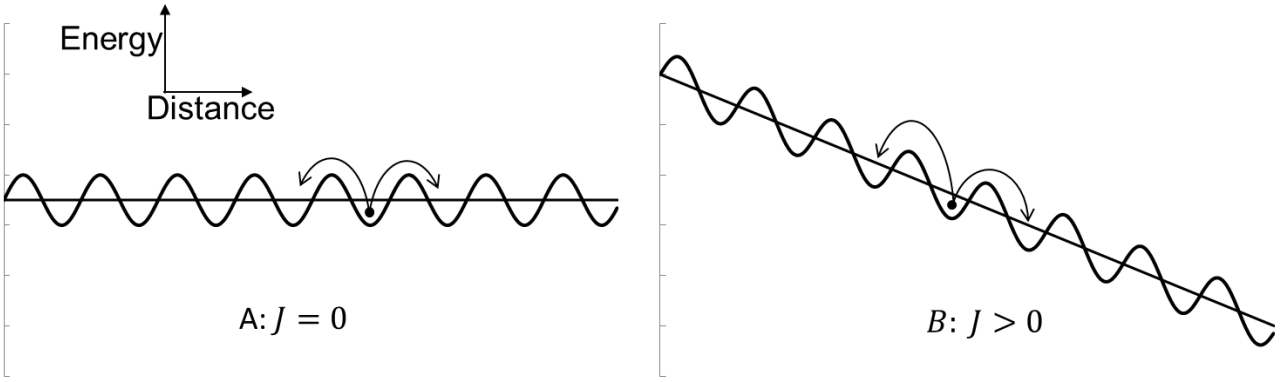

Figure 1.12. Diagram showing the variation of free energy against distance for an idealized periodic flux pinning regime with and without an applied transport current.

1.4.5 E-J characteristics

We have seen that in a perfect, defect free, superconductor that there will still be loses associated with a flowing current due to the movement of fluxons and that this loss is linearly dependant on the current. In a superconductor with perfect uniform pinning at zero temperature so that flux creep is negligible the electric field along the current direction will be zero up to the critical current. At the critical current the pinned flux lattice will instantly and uniformly break and an electric field will suddenly develop and above this value the electric field will have flux flow like an unpinned superconductor. This case of ideal pinning at absolute zero is shown in Figure 1.13 as the case of the ideal superconductor. In reality the superconductor will never be at zero temperature so flux creep will always cause an electric field at any current, even far below the critical current [52]. In theory this should obey the exponential dependence on temperature and current derived by Anderson. However this assumes that the size and depth of the pinning wells is uniform across the material. In a real material neither the critical current nor the pinning potentials are uniform across the material. These variations fall into two broad categories: intrinsic and extrinsic variations. Intrinsic variations are caused by the variation of material properties across the material such as the spatial dependence of

strain and defects and variations in the local stoichiometry of the superconductor and so affect the critical current density J_c. Every physical superconductor will have a geometry, for example they will be incorporated into a wire, and hence has a critical current which is calculated from $I_c = AJ_c$ were A is the cross-sectional area of the material. Variations in A can result in change in the critical current along the superconductor. The modification of the critical current due to geometry is an extrinsic variation. These deviations from a perfect superconductor mean that no theory will perfectly describe the E-J or V-I curve of real material. However it has been found that the curve can be described by the empirical power law [53]:

$$E = E_0 \left(\frac{J}{J_c}\right)^i \qquad 1.72.$$

Or equivalently:

$$V = V_0 \left(\frac{I}{I_c}\right)^i \qquad 1.73.$$

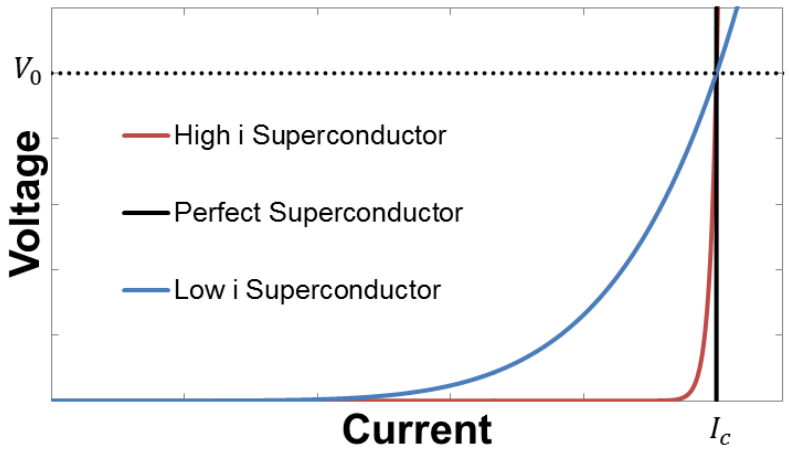

Figure 1.13. V-I curves for a perfect, high i-value and a low i-value superconductor.

Here i is known as the index of transition and describes how 'sharp' the transition from the lossless to lossy regimes. Figure 1.13 shows curves for two different superconductors; one with a high i value and one with a low one. A high i value is indicative of good flux pinning as dissipation is low until quite high current levels and so the fluxons must not be free to move. This is typically observed in low temperature superconductors such as NbTi and Nb_3Sn. Conversely a low i value indicates poor flux pinning and is often observed in high temperature superconductors, particularly at temperatures approaching their T_c. As the transition occurs over such a wide current range, there is no clearly defined level at which a superconductor stops superconducting. This continuous curve gives a problem of how to define the critical current to aid practical comparison of different superconductors; what is

truly needed is a standardised method of defining the critical current level. The criteria which are commonly used to define the critical will be discussed in more detail in the next chapter. However the most common criterion will be introduced briefly here [54]. The criterion is that the critical current is defined as current at which the electric field reaches$100\,\mu V/m$. By measuring the $10\,\mu V/m$ as well as the $100\,\mu V/m$ the i value for the transition can be easily calculated by using:

$$i = \frac{1}{\ln\left(\frac{I_{100\mu V/m}}{I_{10\mu V/m}}\right)} \qquad 1.74.$$

References

[1] H. Kammerlingh-Onnes, *Commun. Phys. Lab. Univ. Leiden,* vol. 120b, 1911.

[2] R. de Bruyn Ouboter, "Heike Kamerlingh Onnes's Discovery of Superconductivity," *Scientific American,* vol. 276, pp. 98-103, 1997.

[3] J. W. Crowe, "Trapped-Flux Superconducting Memory," *Reprinted from IBM J. Res. Devel.,* vol. 1, pp. 1175-1204, 1957.

[4] D. J. Quinn and W. B. Ittner, "Resistance in a Superconductor," *J. App. Phys.,* vol. 33, pp. 748-749, 1962.

[5] W. Meissner and R. Ochsenfeld, "Ein neuer Effekt bei Eintritt der Supraleitfähigkeit," *Naturwiss.,* vol. 21, no. 1933, pp. 787-788, 1933.

[6] H. Kamerlignh Onnes, *Commun. Phys. Lab. Univ. Leiden,* vol. 16, p. 987, 1914.

[7] M. S. Lubell, "Empirical scaling formulas for critical current and critical field for commercial NbTi," *IEEE Trans. Mag.,* vol. 19, no. 3, p. 754, 1983.

[8] W. J. De Haas and J. Voogd, "The influence of magnetic fields on supraconductors," *Comm. Leiden,* vol. 208b, pp. 262-272, 1930.

[9] B. B. Goodman, "The Thermal Conductivity of Superconducting Tin below 1°K," *Proc Phys. Soc. sec. A,* vol. 66, no. 3, pp. 217-227, 1953.

[10] W. S. Corak, B. B. Goodman, C. B. Satterthwaite and A. Wexler, "Atomic Heats of Normal and Superconducting Vanadium," *Phys. Rev.,* vol. 102, no. 3, pp. 656-661, 1956.

[11] R. E. Glover and M. Tinkham, "Conductivity of Superconducting Films for Photon Energies between 0.3 and 40kTc," *Phys. Rev.,* vol. 108, no. 2, pp. 243-256, 1957.

[12] D. K. Finnemore and D. E. Mapother, "Superconducting Properties of Tin, Indium, and Mercury below 1° K," *Phys. Rev.,* vol. 140, no. 2A, pp. 507-518, 1965.

[13] I. Giaever, “Energy Gap in Superconductors Measured by Electron Tunneling,” *Phys. Rev. Lett.*, vol. 5, no. 4, pp. 147-148, 1960.

[14] E. Maxwell, “Isotope Effect in the Superconductivity of Mercury,” *Phys. Rev.*, vol. 78, no. 4, p. 477, 1950.

[15] C. A. Reynolds, B. Serin, W. H. Wright and L. B. Nesbitt, “Superconductivity of Isotopes of Mercury,” *Phys. Rev.*, vol. 78, no. 4, p. 487, 1950.

[16] B. Serin, C. A. Reynolds and L. B. Nesbitt, “Superconductivity of Isotopes of Mercury,” *Phys. Rev*, vol. 78, no. 6, pp. 813-814, 1950.

[17] C. A. Reynolds, B. Serin and L. B. Nesbitt, “The Isotope Effect in Superconductivity. I. Mercury,” *Phys. Rev.*, vol. 84, no. 4, pp. 691-694, 1951.

[18] C. J. Gorter and H. B. G. Casimir, *Physik Z,* vol. 35, p. 963, 1934.

[19] P. M. Marcus and E. Maxwell, “Two-Fluid Models of Superconductivity with Application to Isotope Effects,” *Phys. Rev.*, vol. 91, no. 5, pp. 1035-1042, 1953.

[20] J. F. Annett, Superconductivity, Superfluids and Condensates, Oxford: Oxford University Press, 2004.

[21] P. W. R. Bessonette and M. A. White, “Realistic Thermodynamic Curves Describing a Second Order Phase Change,” *J. Chem. Ed.*, vol. 76, no. 2, pp. 220-223, 1999.

[22] F. London and H. London, “The Electromagnetic Equations of the Supraconductor,” *Proc. Roy. Soc. London A,* vol. 149, no. 866, pp. 71-88, 1935.

[23] F. London, Superfluids I, New York: J. Wiley and Sons Inc., 1950.

[24] A. J. Leggett, “Superconducting Penetration Depth of Lead,” *Rev. Mod. Phys.*, vol. 71, pp. 318-323, 1999.

[25] A. B. Pippard, “Field Variation of the Superconducting Penetration Depth,” *Proc. Roy. Soc. A,*

vol. 203, no. 2, pp. 210-223, 1950.

[26] A. B. Pippard, "The Surface Energies of Superconductors," *Proc. Camb. Phil. Soc.,* vol. 47, pp. 617-625, 1951.

[27] A. B. Pippard, in *Proc. Int. Conf. Low Temp. Phys.*, Oxford, 1951.

[28] A. B. Pippard, "An Experimental and Theoretical Study of the Relation between Magnetic Field and Current in a Superconductor," *Proc. Roy. Soc. Lond. A,* vol. 216, no. 4, pp. 547-568, 1953.

[29] J. Bardeen, "Relation between Lattice Vibration and London Theories of Superconductivity," *Phys. Rev,* vol. 81, no. 5, pp. 829-834, 1951.

[30] H. Frohlich, "Theory of the Superconducting State. I. The Ground State at the Absolute Zero of Temperature," *Phys. Rev.*, vol. 79, no. 5, p. 845, 1950.

[31] D. L. Landau and G. L. Ginzburg, *J. Exper. Phys. USSR,* vol. 20, p. 1064, 1950; reprinted in L. D. Landau Men of Physics vol 2. Pergamon Press, D. T. ter Haar. 1965.

[32] L. D. Landau, *Phys. Z Soviet Un.,* vol. 11, no. 26, p. 545, 1937; reprinted in L. D. Landau and E. M. Lifshitz, Statistical Phys Pergamon Press p343. 1958.

[33] J. Bardeen, L. N. Cooper and J. R. Schrieffer, "Theory of Superconductivity," *Phys Rev.,* vol. 108, no. 5, pp. 1175-1204, 1957.

[34] L. P. Gor'kov, "Microscopic derivation of the Ginzburg--Landau equations in the theory of superconductivity," *JETP (USSR),* vol. 36, no. 6, pp. 1364-1367, 1959; translated by D. ter Haar.

[35] L. N. Cooper, "Bound Electron Pairs in a Degenerate Fermi Gas," *Phys. Rev.,* vol. 104, no. 4, pp. 1189-1190, 1956.

[36] M. Tinkham, Introduction To Superconductivity (second edition), New York: Dover, 2004.

[37] B. S. Deaver and W. M. Fairbank, "Experimental Evidence for Quantized Flux in Superconducting Cylinders," *Phys. Rev. Let,* vol. 7, no. 2, pp. 43-46, 1961.

[38] R. Doll and M. Nabauer, "Experimental Proof of Magnetic Flux Quantization in a Superconducting Ring," *Phys. Rev. Let.,* vol. 7, no. 2, pp. 51-52, 1961.

[39] A. A. Abrikosov, "On the Magnetic Properties of Superconductors of the Second Group," *Sov. Phys. JETP,* vol. 5, pp. 1174-1182, 1957.

[40] W. H. Kleiner, L. M. Roth and S. H. Autler, "Bulk Solution of Ginzburg-Landau Equations for Type II Superconductors: Upper Critical Field Region," *Phys. Rev.,* vol. 133, no. 5A, pp. 1226-1227, 1964.

[41] U. Essmann and H. Trauble, "The direct observation of individual flux lines in type II superconductors," *Phys. Let. A,* vol. 24A, no. 10, pp. 526-527, 1967.

[42] H. F. Hess, R. B. Robinson, R. C. Dynes, J. M. Valles and J. V. Waszcak, "Scanning-Tunneling-Microscope Observation of the Abrikosov Flux Lattice and the Density of States near and inside a Fluxoid," *Phys. Rev. Lett.,* vol. 62, no. 2, pp. 214-216, 1989.

[43] J. E. Evetts, A. M. Campbell and D. Dew-Hughes, "Forces on flux vortices in an arbitrary configuration," *J. Phys. C.,* vol. 1, no. 3, pp. 715-731, 1968.

[44] J. Bardeen and M. J. Stephen, "Theory of the Motion of Vortices in Superconductors," *Phys. Rev.,* vol. 140, no. 4A, pp. A1197-A1207, 1965.

[45] M. Tinkham, "Viscous Flow of Flux in Type-II Superconductors," *Phys. Rev. Let.,* vol. 13, no. 26, pp. 804-807, 1964.

[46] E. H. Brandt, "On the shear modulus of the flux line lattice," *Phys. Stat. Sol. (b),* vol. 77, no. 2, pp. 551-560, 1976.

[47] D. O. Welch, "Concerning factors which determine whether flux-lattice shear or pin breaking limits the critical current density of superconductors," *IEEE Tans. Ap. Sup.,* vol. 3, no. 1, pp. 1476-1478, 1993.

[48] P. W. Anderson, "Theory of Flux Creep in Hard Superconductors," *Phys. Rev. Let.,* vol. 9, no. 7,

pp. 309-311, 1962.

[49] D. T. Ryan, H. Jones, W. Timms and N. Killoran, “Critical current measurements at electric fields in the pV m-1 regime,” *IEEE Trans. Ap. Sup.,* vol. 7, no. 2, pp. 1455-1458, 1997.

[50] T. Onogi, T. Ichiguchi and T. Aida, “Power-law dissipative behavior in high-Tc superconductor,” *Solid State Comm.,* vol. 69, no. 10, pp. 991-993, 1989.

[51] A. F. Clark and J. W. Ekin, “Defining critical current,” *IEEE Trans. Mag.,* vol. 13, no. 1, pp. 38-40, 1977.

2 Finite Element Method

2.1 Introduction

Throughout this thesis there are a number of systems which have required the extensive use of computer modelling in the form of finite element analysis (FEA) to solve a wide range of complex problems. The FEA package primarily used in this thesis is the commercially available Comsol Multiphysics produced by the Comsol Group[3] and has been used for:

- helping to better understand the thermal stability of technical superconductors (chapter 3).
- the design of a high field pulsed coil and understanding its failure (chapter 4)
- extracting material properties from stress-strain data (chapter 5)

As these areas cover a wide range of physics no physics will be presented in this chapter and the physics behind each model will be presented in the relevant chapter. The aim of this chapter is not to fully explain the methods behind FEA (for detailed information on the mathematics behind FEA please consults one of the excellent textbooks on the subject for example [1] [2] [3]), the aim of this chapter is to introduce the reader to the key stages and considerations in FEA along with the relevant terminology used in this thesis.

Within any FEA method there are three main components: The first is the presolver where the geometry and physics of the problem are entered into the computer; the second is the solver where the solution to the problem is calculated; the final on is the post-processing where data is interpreted and extracted from the solution.

2.2 Overview of the method

The core principal of the finite element method is to approximate a continuous differential equation acting over a region with a series of discrete polynomials. If a single polynomial where to be used over the entire region it would have to be of an incredibly high order to adequately approximate the behaviour of the differential equation. Furthermore, as the polynomial would necessarily be a continuous function it would be entirely unable to describe discontinuous behaviour accurately; for example a change in the dielectric strength between two sub-regions. To overcome these obstacles the

[3] COMSOL Ltd, Broers Building, 21 JJ Thomson Avenue, Cambridge, CB3 0FA, United Kingdom

finite element method breaks the region to be modelled into a number of smaller regions, known as elements, which often have either a triangular or rectangular shape and which meet at points known as nodes. The size and number of elements required is dictated by the complexity of the problem and by the degree of accuracy required in the solution. The idea is that the differential equation over each element can then be described accurately by a simple polynomial, often one which is linear or quadratic in nature. The equation describing each element can then be combined to form an accurate description of the original function over the entire region. The form of the assembled equations for a stationary problem will take the form [4]:

$$\boldsymbol{K} \cdot \boldsymbol{U} = \boldsymbol{F} \qquad 2.1.$$

In this equation $\boldsymbol{U}$ is the vector which describes the displacement of each node between elements (e.g. physical displacement in structural mechanics, temperature or electric field), $\boldsymbol{F}$ is the vector of the forces on the nodes and $\boldsymbol{K}$ is a square matrix known as the stiffness matrix. The stiffness matrix is so called because in a simple 1D structural mechanics problem (it was to calculate structural mechanics that FEA was originally developed) equation 2.1 describes the equation of equilibrium for a spring of stiffness K extended by a force F.

The approximate solution to any problem can be calculated from equation 2.1 but in general this is non-trivial as it can contain many thousands of terms and so, over the years, many different solvers have been developed to calculate solutions quickly and easily.

2.3 FEA terminology

During the course of this thesis there will be a lot of discussion about the construction of various FEA models. Most of this discussion will focus on the first stage of the model or the presolver. This is where the details of the model are input and this section will give a brief overview of some of the terminology which will be used repeatedly in later chapters including:

- Model geometry
- Domain properties/physics
- Boundary conditions
- Initial conditions
- Finite element mesh

The first of these steps is to define the geometry of the model. In Comsol this can be done in any number of dimensions between zero and three where the number of dimensions is chosen so that the system to be modelled as accurately as necessary but with the proviso that the computing power required to solve the problem increases dramatically as the number of dimensions increases. Therefore it is usual that the lowest dimension number possible is used while retain enough accuracy to gain meaningful information about the system..

Within the completed geometry there will be a number of separate geometric entities which are known as domains. The properties of each domain can be entered separately and so this is how a complicated system can be modelled as each domain can have differing material properties or loads. When constructing a FEA model it is important that the properties of each domain are considered carefully as accurate domain properties are essential for a FEA model to succeed.

An important consideration is that any model constructed must be of a finite size and so will have boundaries which demarcate the edge of the model. It is very important that to impose boundary conditions on these external boundaries but the exact details of the model will dictate the relevant conditions. For example, in solid mechanics, it is important that the model geometry is constrained in such a way that a force will deform it, not just cause the entire body to displace as a rigid body. Furthermore if the system to be modelled has any planes of symmetry, mirror symmetry boundary conditions can significantly reduce the size of models as it may be that only a fraction of the geometry needs to be modelled to gain a picture of the behaviour of the entire geometry.

The final solution of any differential equation is highly dependent on the bounding conditions. In a stationary model this can be provided by relevant boundary conditions as detailed earlier. For a time dependant model, where the profile of the solution changes with time, this requires initial conditions (for example the starting temperature or stress distribution) from which the evolution can be calculated.

The final stage of the presolver is to create the array of elements over which the model will be solved, this array of elements is known as the mesh. Within commercial FEA packages there are automatic meshers to easily create suitable meshes of varying size or quality. It is the responsibility of the user to ensure that the mesh created is suitable for the model to be solved: finer meshes have smaller elements and hence a greater accuracy but also require greater computational power to solve. There is no hard

and fast rule governing mesh sizes but Figure 2.1 shows two meshes for a simple geometry. It shows a very coarse mesh which would solve quickly but give inaccurate results, and a more suitable mesh which would require more computing power but would give a reasonable solution.

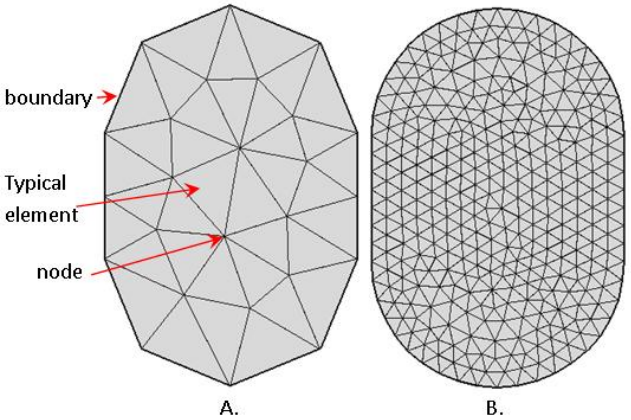

Figure 2.1. A: a coarse mesh and B: a fine mesh used to approximate an oval domain.

Once all of the required information has been input into the presolver and a suitable mesh has been generated the problem can be solved. Within an FEA package there are a number of different solvers [5], each of which has various pros and cons: some are direct solvers which are fast but require a lot of processing power and memory while others are iterative and as such are much slower but are much more memory efficient. The most appropriate solver to use will be dictated by the size and complexity of the problem being considered as well as the computing power available. For more information on solvers please refer to one of the referenced texts.

After a solution to the problem has been calculated the data can be analysed with most commercial FEA packages including some form of post-processing capability. This allows the user to present the data in a variety of formats as well as allowing calculations and analysis such as integration and maximum values to be completed on the data. All of the FEA computational data presented in this thesis is the result of post-processing analysis of the models constructed.

References

[1] A. J. Davies, The Finite Element Method:An Introduction with Partial Differential Equations 2nd edition, Oxford: Oxford University Press, 2011.

[2] M. J. Fagan, Finite element analysis: Theory and practice, London: Prentice Hall, 1992.

[3] D. Braess, Finite Elements: Theory, Fast Solvers, and Applications in Solid Mechanics, Cambridge: Cambridge University Press, 2007.

[4] Comsol Multiphysics Reference Guide version 4.2a, Cambridge: Comsol Ltd, 2011.

[5] Comsol Multiphysics User's Guide version 4.2a, Cambridge: Comsol, 2011.

3 Stability of Technical Superconductors

3.1 Introduction

One of the great successes of superconductors has been to enable the technology of magnetic resonance imaging (MRI). The primary requirement of an MRI scanner is the ability to generate high magnetic fields (~1-3T) in a typical 70cm diameter bore (large enough for a patient to fit inside) with an incredibly large field temporal (1 part in 10^8 per hour) [1] and spatial uniformity (~2ppm in a 45cm diameter spherical volume) [2]. The primary advantage of the use of superconductors is obvious if we consider a simple, hypothetical MRI coil. If we let the coil be 1m long and have an accessible bore diameter of 0.7m wound with 2mm^2 wire carrying 500A (which is fairly typical for an MRI scanner) then to generate a central field of 1T would require around 45km of wire. If this coil was wound using a standard copper wire this would give the resistance of the coil as 300Ω. This would require a power supply capable of producing $75MW$ of power and $150{,}000V$ whilst maintaining the required temporal stability. This system would also require a vast cooling system to help remove the huge amount of energy dissipated in the magnet. By using superconductors the resistance of the coil can be reduced to a negligible value, removing the need for the high power current source and greatly reducing the cooling required to maintain the coil temperature. A further advantage is that the current in the coil can be swept to the required level and the coil can then be placed in persistent mode by using a suitably designed superconducting switch. This removes the need for a permanent power supply; giving the required temporal stability.

There are, as with any technology, technical challenges in the use of superconductors in MRI coils. These challenges include designing a coil that can generate the required field without surpassing the critical current of the wire used and the structural problems associated with containing the high stresses generated within the coil. The problem which will be considered in detail in this chapter is the thermal stability of the wire in the coil and factors which may affect this. This is an issue as there are many potential sources of heat within a superconducting coil varying from resin cracking, wire/coil movement, external vibrations, reduced coolant levels and items dropped onto the coil. Any of these perturbations has the potential to raise the temperature of the wire, driving the critical current level down and, potentially causing the coil to quench and return to the normal state.

3.1.1 Critical current criteria

As was mentioned in section 1.4.5 all superconductors have a critical current density as well as the critical magnetic field and temperature. In a wire a superconductor also has a definable critical current, related to the critical current density by the cross section of the wire, A, by:

$$I_c = AJ_c \tag{3.1.}$$

Using this we can then rewrite equation 1.72, which describes the empirical power law relation between the current density and the electric field, E, induced in the superconductor, in terms of the current in the wire:

$$E = E_0 \left(\frac{I}{I_c}\right)^i \tag{3.2.}$$

where i is known as the index of transition and E_0 is a constant. This electric field/current relation is obviously a continuous curve and so, as mentioned in the introduction, the problem is how to measure the critical current and where to define the critical value on a continuous curve. There are many techniques for measuring the critical current including, amongst others: tube magnetization, static field profile analysis and vibrating sample magnetometry [3]. However as the geometry of the sample in this case is a long wire, by far the simplest method is to pass an increasing current through the sample while measuring the voltage across the sample. More detail of the implementation of this method will be given in section 3.2.3 but the crux of the method is that as the current increases, so will the voltage until a critical current criterion is reached. However the problem remains of how to define the exact superconducting threshold. Three possible methods for defining the threshold are [4]:

- Critical electric field – for short sample measurements it is commonly defined as the current which induces an electric field of either $10\mu V/m$ or $100\mu V/m$ [5] [6] or as $1\mu V/m$ or less in magnet making.
- Critical resistivity – defined as an effective resistivity level often set at $10^{-10}\Omega m$.
- Critical Power – defined as the rate of power dissipation of the current, often set at $1\mu W/m$.

A further method which can be used is known as the offset criterion and it defines the critical current as the level where the gradient of the E-I curve becomes equal to a critical gradient.

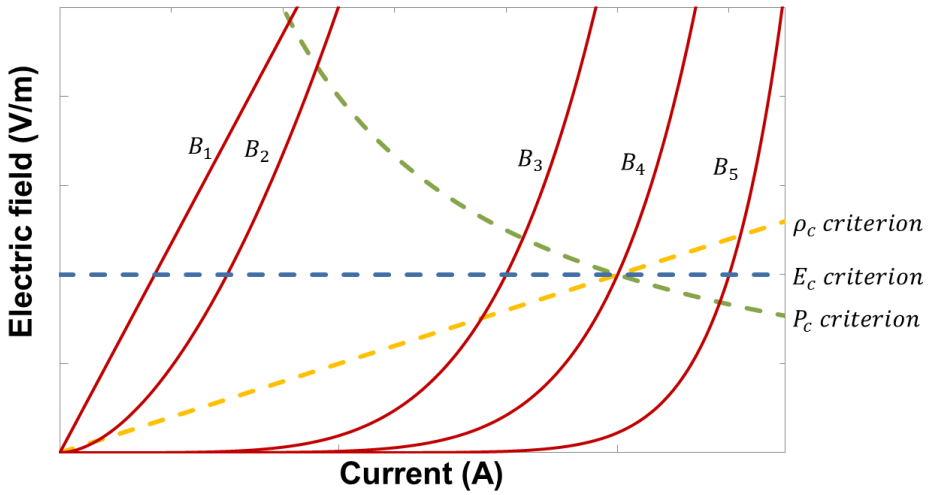

Figure 3.1. The three main criteria for judging critical current shown with curves for a typical superconducting wire in a variety of applied fields from above the upper critical field (B_1) to low field (B_5).

Figure 3.1 shows how the three main criteria vary with current for arbitrary values and E-I curves for an arbitrary superconducting wire in a range of magnetic fields from a high field, above the critical field as demarked by B_1 to a low field marked by B_5. It illustrates some of the strengths and weaknesses of each criterion. The electric field criteria is by far the easiest to implement experimentally but, as is clearly from curve B_1, will give non-zero critical currents even in a wire made purely of a normal conductor. However this is only a problem at very high fields or temperatures where the superconducting properties are weak or non-existent. The resistivity criteria can have the opposite problem in that, as demonstrated by curve B_2, if the resistivity value is set too low the critical current can be given as being zero despite the fact that this curve still has some curvature associated with superconducting properties. However, if the resistivity is set high, it can require very high dissipative voltages to reach the criterion at low applied fields. This could cause a large amount of heating damaging the sample, causing thermal runaway or affecting the results. Therefore, if the resistivity is used several values may be needed for the criterion if it is to be used over a range of applied fields or temperatures. The final criterion is the critical power. This is useful for specific purposes where one is trying to design a system which will dissipate energy below a given threshold but is generally impractical for calculating critical currents.

Due to the ease of implementation the definition which will be used for the rest of this thesis will be the electric field criterion. However one further definition can be useful for determining if a sample has any superconducting properties at high magnetic fields or temperatures and this is the critical index of transition. This involves measuring the index of transition and comparing it to the normal

state value. In the normal state, as the E-I curve will be a straight line, the index is simply $i = 1$ and so the superconducting properties will be said to have been destroyed when the index tends to this value. This will be used to briefly investigate the upper critical magnetic field of the sample in section 3.2.6.

3.1.2 Stabilization, MQE and Minimum Propagating Zones

Early superconducting coils wound with pure niobium titanium (NbTi) wire performed very poorly, quenching at currents much lower than the critical currents predicted by short sample measurements. Part of this problem was due to the flux jump instability in the wire. A good derivation of this can be found in Tinkham [5] but the essence of the problem is that a flux jump within the wire will dissipate a small amount of energy increasing the temperature of the superconductor and reducing its critical current. This reduction in the critical current will cause the current to redistribute causing further heating. If the wire is too thick then the jump in current is larger, thus leading to a higher temperature which in turn leads to a large further decrease in current and the mechanism perpetuates as a feedback [1]; any heat generated cannot conduct out of the wire fast enough and the wire quenches under an adiabatic condition. The maximum thickness of a wire which is stable against such a flux jump event is known as the adiabatic stability criterion and for NbTi it is typically $100\mu m$ but smaller filaments offer increased stability. As a typical critical current density for NbTi is of the order of $1 \times 10^9 A/m^2$ this gives a maximum achievable current of just 8A or so, which would be too low for many applications. The solution to this problem was to create wire with many small filaments so that they would be stable against flux jumps whilst still being able to carry high currents. A related problem for pure NbTi wires, even in filamentary form, can be seen by following a simple derivation from Wilson [1]. The problem considers a long wire of cross-sectional area, A, with a hot spot in the centre. The hot spot has a length ℓ and is at a temperature T_h which is above the critical temperature while the rest of the wire starts at a temperature T_0. The hot part of the wire will be in the normal state and will be generating heat at a rate:

$$G = J^2 \rho \ell A \tag{3.3}$$

If we assume that no heat can flow out of the side of the wire (it can only flow along the wire) and we make the very rough approximation that the temperature gradient along the wire is $\sim(T_h - T_0)/\ell$ then heat will flow away from the hot spot at a rate:

$$C = \frac{2\lambda A(T_h - T_0)}{\ell} \qquad 3.4.$$

where λ is the thermal conductivity and the factor of 2 appears as heat can flow in both directions along the wire. If the wire is in equilibrium then the heat flowing from the hot spot must equal the heat generated in it. Therefore we can combine equations 3.3 and 3.4 to give the critical length:

$$\ell_{crit} = \left[\frac{2\lambda(T_h - T_0)}{J^2\rho}\right]^{\frac{1}{2}} \qquad 3.5.$$

If the hot spot is longer than ℓ_{crit} then the generation will exceed the diffusion and the hot spot will increase in size, propagating down the wire. Conversely a hot spot which is shorter than ℓ_{crit} conduction will exceed generation and it will shrink and the wire will return to stable operation. Therefore this critical length is known as the minimum propagating zone or MPZ. Related to the MPZ is the minimum quench energy or MQE which is simply the amount of energy required to create a hot spot the size of the MPZ. Using typical values for the properties of NbTi at 4.2K (see appendix A) we can calculate the MPZ and the MQE for the wire in this simple model. For example using the data from section 3.2.6 we can see that at 8T the critical current density of the wire is $1.3 \times 10^9 A/m^2$ and from equation 1.1 the critical temperature is 5.7K. Therefore if the wire is carrying 80% of its critical current the MPZ is just $700nm$ long and the MQE for a wire with a diameter of 2mm will be just $14nJ$ of energy! This value is so small due to the relatively large normal state resistivity and very small thermal conductivity of the NbTi causing high heating levels and low conduction away from the hotspot. It is clear then that a coil wound from pure NbTi wire will require very fine filaments, which will be very fragile, and even then will incredibly unstable against the slightest disturbance.

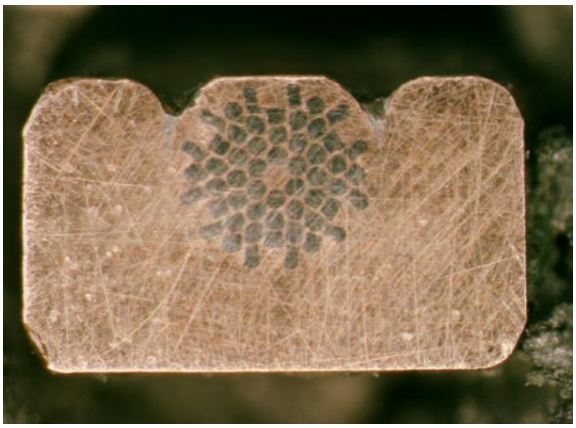

Figure 3.2. A typical superconducting wire with the bundles of NbTi filaments (grey in colour) encased in a copper matrix.

The solution to both the mechanical weakness of fine filaments and the very low MQE is the same: the filaments are encased in a copper matrix. To do this NbTi rods are stacked within a copper billet which is then extruded to a small size. This can then be restacked into a new billet and extruded again [1]. The result of this is that a wire may contain many bundles of filaments with many thousands of small filaments in each bundle all contained in the copper matrix. Figure 3.2 shows a photo of a typical superconducting wire with 54 bundles. The wire shown has been soldered into a copper channel to further increase the ratio of the copper to the superconductor and thus enhance its stability.

The inclusion of the copper has the effect of reinforcing the filaments while greatly increasing the thermal conductivity of the wire and greatly reducing the average resistivity. To illustrate the advantages of using copper we shall briefly consider three hypothetical wires, all carrying 300A, using the simple approximation in equation 3.5. The first wire is a pure NbTi wire with a cross-sectional area of $0.3mm^2$, the second is a pure NbTi with a cross-sectional area of $0.6mm^2$, twice that of the first wire and the third wire is s 50:50 mix of NbTi and copper with a total cross-sectional area the same as the second wire. The results of the calculations for the MPZ and the MQE of these three wires are shown in Table 3.1. It is clear that by replacing half of the superconductor with pure copper, even though the current is far closer to the critical current, you increase the MQE by a factor of around $10{,}000$ making for a wire with greatly increased stability at the loss of engineering current density.

Wire	Fraction of critical current of wire	MPZ (m)	MQE (J)
1	0.8	7.5×10^{-7}	1.4×10^{-9}
2	0.4	15×10^{-7}	5.6×10^{-9}
3	0.8	4.9×10^{-3}	7.2×10^{-6}

Table 3.1. The properties of three different hypothetical wires carrying 300A at 4.2K in an 8T field. The wires are1: $0.3mm^2$ *pure NbTi; 2:* $0.6mm^2$ *pure NbTi; 3:* $0.6mm^2$ *50:50 mix of NbTi and copper.*

It is worth noting that the figures quoted in Table 3.1 are calculated using a very simple one dimensional theory so does not allow for heating of the material around the wire. This means that these figures are the absolute minimum possible for the MQE and MPZ. A more accurate estimate can be gained by completing a three dimensional calculation but these are non-trivial to compute as they require some numeric integration [1] [6].

3.1.3 Aim

As has been explained in section 3.1.2 copper is an essential ingredient when constructing a superconducting wire. The conclusion of the simple derivation is that the greater the fraction of copper used in the wire the greater the stability of the wire and the greater the likelihood that a magnetic coil will be able to achieve its designed maximum field and current. There are, however, downsides to using copper. The first of these is that by increasing the amount of copper the engineering current density (the actual average current density achievable in a particular coil winding) is decreased as, very simply, there is less space for superconductor. Furthermore as the amount of copper increases so does the weight, and crucially, the cost of the wire. If a wire has a copper cross-sectional area of $2mm^2$ then the 45km of wire needed for a single MRI scanner would weigh over 800kg and, going by the peak copper price of 2011 of ~£10,000 per tonne [7], would cost £8,000. As Siemens produce around 1,400 magnets every year reducing the amount of copper by just 20% per magnet could save 220 tonnes of copper and up to £2,200,000 every year. The aim of this chapter is therefore to investigate how much copper is required to achieve a given degree of stability or if any other materials would be an appropriate replacement. Over the years there have been many investigations into the MQE of various wires with methods involving developing experimental [8] - [13] and analytical methods [1] [14] [15]. There have also been attempts to create FEA models [16], [17] to help aid the analysis of these wires but the models and analytical methods have usually used approximations to help avoid the problems associated with modelling the highly non-linear properties of superconductors. Investigating the effect of the copper fraction would be difficult to implement experimentally due to the difficulties of varying the amount of copper in the wire whilst maintaining all the other parameters of the wire (filament number and distribution, critical current etc.). Furthermore analytic methods must all make fairly large approximations to be solvable and so are not necessarily very sensitive to small differences in wire architecture. However FEA modelling programs and computing power have increased greatly in recent years. Therefore it was decided that the best method to progress with the investigation would be to develop a new FEA modelling technique. This FEA model would allow the effect of changing any property of the wire to be tested quickly and easily. As any FEA model is only as good as the data used as validation it was decided that a brief experiment would be conducted before the development of the model would begin.

3.2 Experimental Investigation

As was discussed in the last section, it is very important to have some experimental data against which any computer models built can be compared. This section will focus on describing the design, construction and results obtained from a simple validation experiment. The aim of the experiment was to measure the critical current at a range of magnetic fields before measuring the MQE at a range of fractions of the critical current.

3.2.1 Test sample

The wire that was tested had a standard wire in a channel construction. Figure 3.2 in section 3.1.2 shows a photo of the cross-section of the wire. The details of the wire's composition can be found in Appendix C. As the experiment will be conducted in as close to an adiabatic environment as possible we can use the simple one dimensional theory to gain an estimate of the value of the MQE and its dependence on applied field and current. The various terms in equation 3.5 can be calculated by using the sample properties, the dependence of critical current and critical temperature on applied field [14] and the material properties detailed in Appendix B. The ensuing curves for the MQE are shown in Figure 3.3.

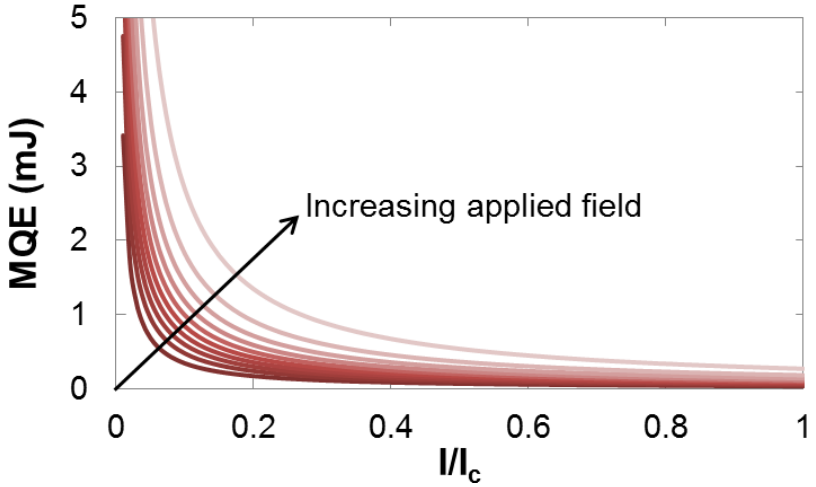

Figure 3.3. The MQE of the sample used at a range of applied magnetic fields for 1T-10T with 1T increments predicted using the simple 1-D analytical model.

It shows that as the applied current decreases the MQE increases as one would expect. Perhaps slightly unexpectedly it predicts that the higher the field the greater the MQE at a given fraction of the critical current. This seems surprising as the higher the applied field the lower the transition temperature of the sample and hence one may think that this would lower the MQE. However, the higher applied field also reduces the critical current, reducing the heating effect and increasing the length of the MPZ and

hence increasing the MQE. This increase in size of the MQE is the dominant effect and hence the higher MQEs at higher fields. It also shows that for this wire we can expect that the MQE will be of the order of a few mJ and that the MPZ is, in general, $> 10mm$ long. This estimate is important as it will help to guide the design of the method for generating the thermal perturbation as detailed in section 3.2.4.

3.2.2 Designing an MQE experiment

An experiment to measure the MQE of a wire at a range of magnetic fields and currents can be divided into two parts. The first part is to measure the critical current of the sample at a range of applied magnetic fields and the second is then to measure the MQE. These two experiments require slightly different experimental set-ups.

For the critical current measurements the electric fields to be measured are in the order of $\sim \mu V/m$ and as the total voltage measured is linearly dependant on sample length it is important to use as long a sample as practicably possible. The other major consideration is that, as there will be dissipation in the wire below the critical current, the sample must be well cooled. If it is not the slight energy dissipation will cause the sample temperature to rise, reducing the critical current and possibly causing run-away heating well below the actual critical current. The techniques used to make these measurements are detailed in section 3.2.3.

The basis of the MQE measurements will be that the current in the sample will be swept to a pre-determined fraction of the critical current, a thermal perturbation will be applied to the sample and then the voltage across the sample will be measured to determine if the sample has quenched or not. If the sample has not quenched the process will be repeated but with a larger perturbation until the sample does quench. The smallest thermal perturbation which can quench the sample is then the MQE of the sample. This measurement requires a method of heating the and, in contrast to the critical current measurements, will require an adiabatic environment so that any energy that is used to disturb the system is not lost to coolant before it can affect the sample. The heating method is described in section 3.2.4 while the technique used to create an approximation to an adiabatic environment is detailed in section 3.2.5.

3.2.3 V-I measurements and the four terminal technique

The basis of the critical current measurement is the four terminal technique for measuring voltages across the sample. The wiring for this technique is shown in Figure 3.4 and consists of attaching the current leads to the ends of the sample and then attaching voltage contacts part way down the sample. The four wire method ensures that (assuming the voltmeter has infinite input impedance) that no current will flow down the voltage leads and so only the resistance of the sample will affect the voltage, not the resistance of the current leads or the voltage contacts. This technique is essential for measuring the critical current as, if you were to use the two wire method, the resistance of the current leads and solder joints would overwhelm the sample signal.

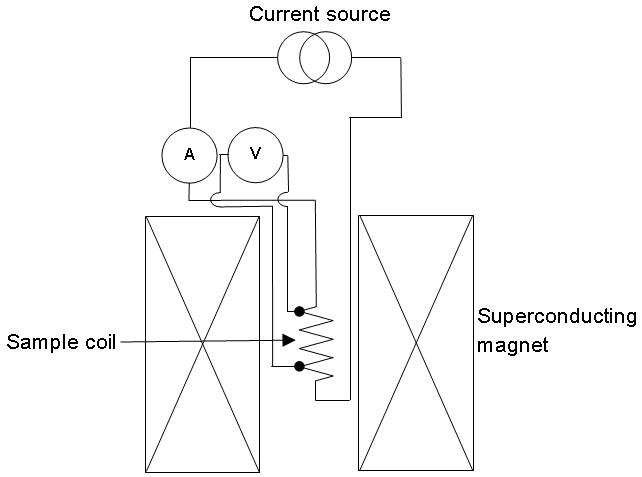

Figure 3.4. Setup used to measure the critical current of the sample at a range of magnetic fields.

When attaching the voltage contacts to a superconducting wire sample there is a very important extra consideration and it is known as the current transfer length [19]. When the current leads are attached to the superconducting wire they are soldered directly onto the outside of the copper sheath. The results of this is that the current enters the wire in the copper and as there will be a thin, slightly resistive, barrier between the copper and the superconductor, the current will flow in the copper for a short distance before entering the superconductor. This distance is the current transfer length. If the voltage measurements include this region a small resistive voltage will be measured along with the superconducting signal. Therefore it is important to place the voltage contacts away from the current contacts with a distance of a few cm usually being considered enough.

As was stated earlier, the longer the sample measured in this experiment, the better the results. As the applied magnetic field was to be produced by a 16T superconducting magnet with a 40mm bore from

Oxford Instruments[4] the longest possible straight sample would obviously be less than 40mm. As the highest electric field to be measured is $100\mu V/m$ this would result in a peak voltage of just $400nV$. This voltage is not immeasurably small [20] but would present significant experimental difficulties. Therefore a longer sample would be useful and the method for implementing this measurement was to form the wire into a small coil on an insulating former (see [21] for details on possible alternative methods). This allows a long length of wire to be placed in the field. In the end two different coils where constructed: one single layer coil which was ideal for the critical current measurements but which could not be well enough insulated for the MQE experiment and a second coil with two layers which might have reduced the contact between the wire and the helium but could be insulated more effectively[5]. The second coil will be explained in section 3.2.5 while photos of the first coil are shown in Figure 3.5. The coil had two copper end contacts separated by a 10G/40 glass composite former. The holder had an insulated length of 80mm and a diameter of 32mm. This allowed for a $3.3m$ length of wire to be measured in the field. Also visible are the heater coils (see section 3.2.4) attached which were used to test the apparatus which would be used for the later MQE experiment.

The prepared sample was inserted into the bore of the magnet and currents of up to 500A were passed through the sample. The current was measured by a high-power calibrated shunt resistor and the sample voltage was amplified using a 10,000 gain low-drift differential amplifier. All data was then recorded on a National Instruments[6] USB-6281 18-bit data logger.

Figure 3.5. The former for the single layer coil and the completed coil constructed for the critical current measurements.

[4] Oxford Instruments, Tubney Woods, Abingdon, Oxfordshire, OX13 5QX, UK.
[5] Winding the samples into coils results in the sample generating a magnetic field along with the background field. This self-field effect is different for both coil geometries and is corrected for in all results shown.
[6] National Instruments Corporation (U.K.) Ltd. Measurement House, Newbury Business Park, London Road, Newbury, Berkshire RG14 2PZ.

3.2.4 Generating a thermal perturbation

For an MQE experiment it is obviously very important to be able to create a thermal perturbation in a controlled and repeatable manner. The total energy input into the system must also be measureable to high degree of accuracy. Over the years there have been many different methods for generating such a perturbation for ceramic heaters [9], laser heaters [8] to induction heating [22] but by far the simplest to implement is a small resistive heater in intimate contact with the sample wire [12]. This method can lead to inaccuracies in the MQE as the thermal timescale associated with heating the sample can be relatively long (~ms) [23]. This allows some of the input energy to flow away from the heated spot, reducing the overall heating effect and increasing the measured MQE. Furthermore, it is important that the heater is shorter than the MPZ as, if it is longer, it will heat a longer length of wire than necessary, increasing the MQE. Despite these problems, as the purpose of this experiment is to provide validation data, it was felt that the simplicity of this method made it the best choice.

Once the heating method had been decided the problems of the construction of the heater and of how to drive a current pulse through the heater still needed to be addressed. The requirements for the pulse generator were that it had to generate a constant current for a short period of time which could be varied if required. Pulses of around 1ms have been shown to be suitable for such an application [23]. For this a cost effective solution proved to be a piece of custom electronics to be used in conjunction with a square-wave signal generator. The signal generator gives a constant series of square voltage pulses with a continuously variable frequency from$10Hz$. By itself though it would not be suitable as it cannot output a high enough power and it gives a constant series of pulses. The electronics which were built solve both of these issues: the first role of the electronic was that, after the signal-generator had been connected via a spring-loaded push switch, it would only let the second positive voltage peak of the series to pass. The first peak and peaks from the third one onwards are all blocked by way of latching flip-flops. The second peak was chosen as the signal generator could be connected part way through the first peak which would give a reduced pulse length. The single voltage peak which was allowed to pass through the electronics was then used to open the gate of a high power transistor. This allowed a voltage to be applied to one end of the heater coil and a current would only be able to flow for the duration that the voltage peak held the transistor gate open. The maximum voltage/current achievable with this setup was $12V/3A$ with a maximum pulse length of 50ms and a minimum of less

than $\sim 5\mu s$ (below this level the data logger used could not record data fast enough to accurately measure the pulse). A simple schematic of the wiring of the control electronic is shown in appendix A.

The material chosen for the heater was constantan wire. Constantan is an alloy of copper and nickel with the specific alloy used being 55:45 copper to nickel. Constantan was chosen as, due to the high mismatch in lattice constants, it is an intrinsic resistor with a resistance value which varies very little between room and cryogenic temperatures (a brief investigation showed that the wire retained about 90% of its room temperature resistance at 4.2K). The wire used had a diameter of 0.1mm and a resistance of $40\Omega/m$ at room temperature or $36\Omega/m$ at 4.2K. Therefore, as the control electronics had a maximum voltage of $12V$ and a maximum current of $3A$, to maximize the possible power dissipation the heater needed to have a resistance of $\sim 4\Omega$. This required $\sim 11cm$ of wire. When this was wrapped tightly around the sample wire it resulted in a heater coil $\sim 2mm$ long. As this length is shorter than the most stringent calculations for the MPZ it should be short enough to provide reasonably accurate measurements of the MQE.

3.2.5 Creating an adiabatic environment

To accurately measure the MQE of the wire it is obviously important to create an environment where the thermal perturbation is not just dissipated into the liquid helium before it can heat the sample. The first sample holder (shown in section 3.2.3) is unsuitable as a sufficient thermal barrier cannot be easily applied to the sample. Therefore, a second holder was designed and constructed in the form of 10G/40 glass composite former capable of holding a two layer coil. The length of the former was $50mm$ with an inner diameter of $21mm$ and an outer diameter of 32mm. An outer case with an inner diameter of 35mm and an out diameter of 38mm was then made out of Tufnol 6F/45. The case had a tight seal around the base of the former so that the volume around the sample wire could be filled with Stycast 2850FT blue with catalyst 23LV from Emerson and Cuming[7]. The Stycast is sold as a thermally conductive, electrically insulating epoxy resin, achieving the improved thermal conductivity through the addition of alumina powder. It was chosen as it has relatively good properties down to very low temperature and, although it is thermally conductive, is not a good conductor with a conductivity of about $0.05W/m \cdot K$ at $4.2K$ [24]. Given the specific heat capacity and density of the

[7] Emerson and Cuming, Nijverheidsstraat 7, B_2260 Westerlo, Belgium.

Stycast (as given in appendix B) then we can calculate the thermal diffusivity, D_{Therm}, which gives a measure of how quickly heat will diffuse through a material [25]:

$$D_{Therm} = \frac{k}{\rho_d c_p} \tag{3.6.}$$

where k is thermal conductivity, ρ_d is the density and c_p the specific heat capacity. The thermal diffusivity is then $1.2 \times 10^{-4} m^2/s$. To gain an estimate of how quickly the temperature will change at the surface of the sample and since the Stycast is approximately 6mm thick above the wire, we can approximate it as a slab 12mm thick. We can then use the solution to the general problem of heat conduction into slab of thickness 2a which tells us that the temperature difference between the surface and centre of the slab will decay at a characteristic time:

$$\tau = \frac{4a^2}{\pi^2 D} \tag{3.7.}$$

Therefore in this case the heat will escape through the Stycast to the liquid helium coolant with a characteristic time of $\sim 30ms$ but, as we have ignored the 6F/45 casing, this time is likely to be much longer in reality. Therefore even the most stringent limiting value for the rate of thermal loss is long when compared to the time scale of the introduction of the heat ($\sim 1ms$) it should not adversely affect the results. Furthermore the small conductivity will allow the sample to cool faster between runs, speeding up the rate at which the experiment can be conducted.

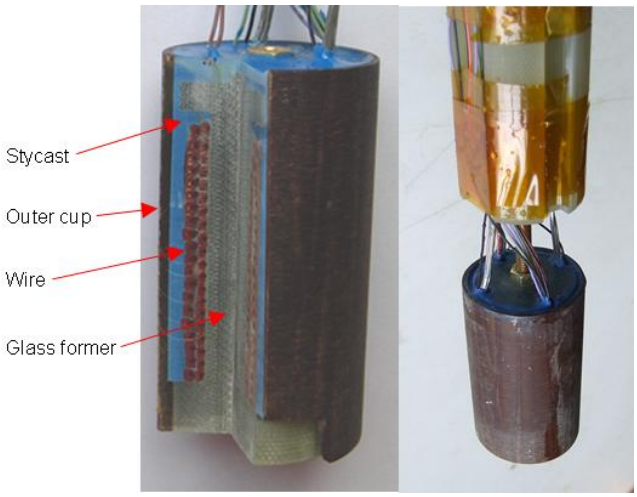

Figure 3.6. The two layer coil sample holder for the MQE measurements and the completed coil mounted on the bottom of the experimental probe.

The final consideration when designing the insulated sample holder is that, due to the resistive nature of the current leads and dissipation in the current transfer length, the wire could be heated in the first

few centimetres of the wire. Therefore, if the contacts were too close to the insulated region the sample could warm unduly, making MQE measurements impossible. To solve this issue the sample holder was mounted a few centimetres from the base of the probe. This allowed the sample wire to be fully surrounded by the cooling helium, hopefully removing any heat generated by current sharing, before entering the insulated region. A photo of the completed holder mounted on the bottom of the probe is also shown in Figure 3.6 with the heater wiring, voltage taps and sample wire clearly visible, bridging the gap between sample holder and probe.

3.2.6 Critical Current Data

Once the sample had been mounted onto a probe, inserted into the bore of the superconducting magnet and cooled to 4.2K the critical current could be measured at a range of applied magnetic fields. The original critical current data was measured using the holder and equipment as described in section 3.2.3. The procedure for the experiment was that the current was increased at a constant rate while the sample voltage was measured. When the voltage across the sample reached the critical value which indicated that the $100\mu V/m$ threshold had been reached the current source was turned off and the sample was allowed to cool for 1 minute before the next data point was taken.

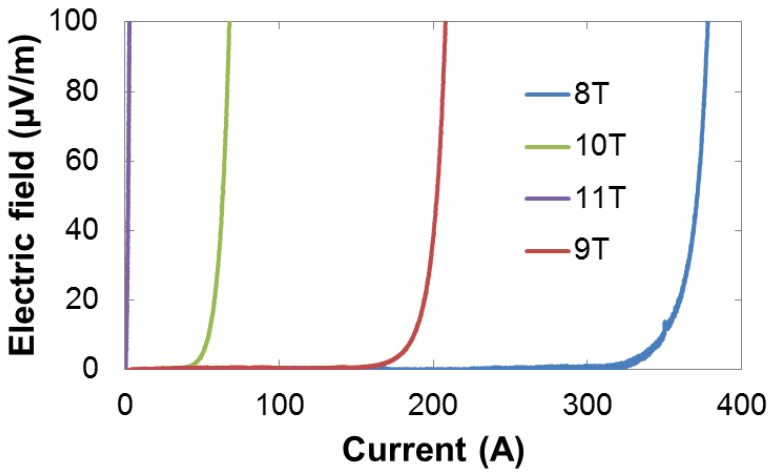

Figure 3.7. Traces for the electric field against applied current for a number of applied magnetic fields.

As the current source available had a maximum current of 500A the critical current could only be measured for applied magnetic field of 7.5T and above. Figure 3.7 shows an example of an electric field/current (E-I) curve for a range of applied fields between 8T and 11T and it shows that the critical current is greatly suppressed as the applied magnetic field increases. Figure 3.8 shows a plot of how the critical current varies with applied field dropping from $470A$ at 7.5T to effectively zero at 11T.

The graph also shows the characteristic 'tail' at high fields caused by the criterion used for judging the critical current although, as we shall see later in this section, that there are still signs of superconductivity to higher fields.

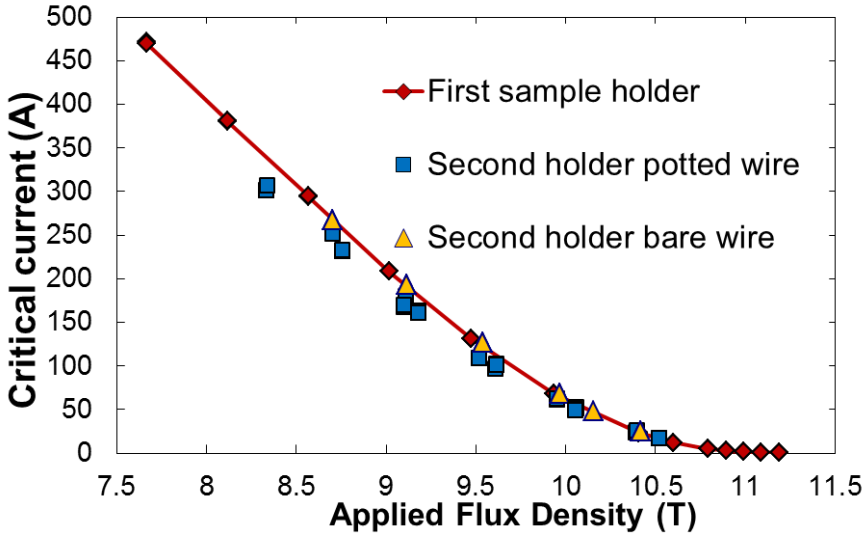

Figure 3.8. The measured critical current for the sample at a range of applied magnetic flux densities for the first sample holder and for the second sample holder both pre and post impregnation.

Once the critical current of the sample had been measured using the first sample a new length of the sample was wound onto the second sample holder. As this sample holder had a significantly smaller winding diameter ($21mm$ compared with $32mm$) it was decided that the critical current of the sample should be re-measured before the sample was potted in the resin. This was to ascertain whether the sample had been damaged by the tighter bend-radius. The results from the unpotted or bare measurements are plotted in Figure 3.8 along with the original data. This plot shows that there was no appreciable degradation in the wire performance. However, once the sample had been potted in the Stycast, the performance of the wire was significantly affected at lower applied fields. At high fields there was negligible difference between the potted and unpotted results but at ~8T (applied background field; the data points are shifted due to self-field correction) the critical current had been reduced by ~50A or 15%. The nature of the E-I curve had also changed significantly as shown in Figure 3.9 which shows a trace of the E-I curve for the same sample on the same holder at 9T before and after impregnation. It shows that the electric field in the potted sample starts to rise at much lower currents before deviating from the smooth curve by increasing incredibly rapidly. What this behaviour illustrates is that the potted wire is in a partially adiabatic environment as any heat dissipated in the wire remains in the wire, increasing the sample temperature and reducing its critical current. This

happens until a certain threshold is reached and the wire quenches, rapidly returning to the normal state and hence the rapid increase in voltage.

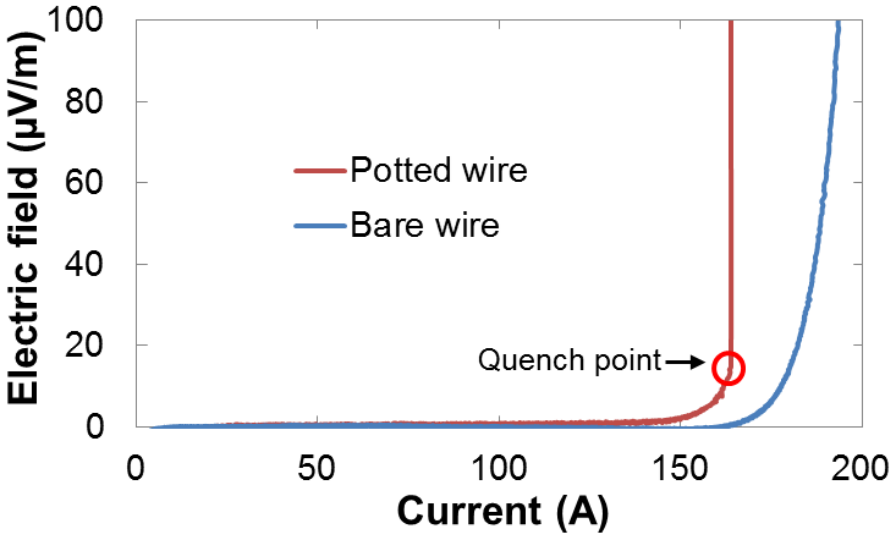

Figure 3.9. Electric field against current plots for the sample at 9T before and after the Stycast impregnation.

Once the data had been recorded the critical current could be read along with the current which gave an electric field of $10\mu V/m$. This second current level is recorded so that the index of transition (as shown in the power law given by equation 3.2) could be calculated by:

$$i = \frac{1}{log\left(\frac{I_{100\mu V/m}}{I_{10\mu V/m}}\right)} \qquad 3.8.$$

The index of transition is an indication of the shape of the transition from superconducting to normal states and can be used as an indicator as to the magnetic field at which the sample stops showing any superconducting properties. It is also well known that, at fixed field intensity, the index transition is also an indication of the quality of the wire manufacturing as sausaging (variation in filament thickness or diameter) leads to lower values. Figure 3.10 illustrates the different shapes that the transition can have at different magnetic fields. It shows the transition traces plotted in Figure 3.7 but with the current axis normalized against the critical current at that field. It shows that at the lower fields the transition is 'sharp' in that the sample changes from a perfect superconductor to a normal material with a relatively small change in current. This is in contrast to higher fields where a dissipative voltage is present even at lower fractions of the critical current. It also shows that at 11T, despite the critical current being effectively zero, the sample still retains some superconducting properties as the E-I line still has a curvature whereas a sample in the normal regime would give a

straight, Ohmic, line. Figure 3.11 shows how the index of transition varies with applied magnetic field and shows that there are still some measureable superconducting properties up to an applied field of 11.2T.

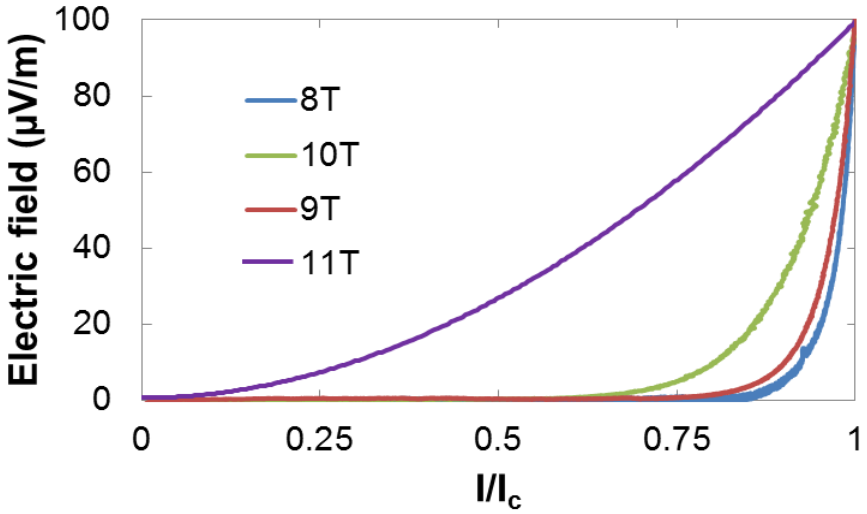

Figure 3.10. *Traces for the electric field against applied current normalized against the critical current for a number of applied magnetic fields.*

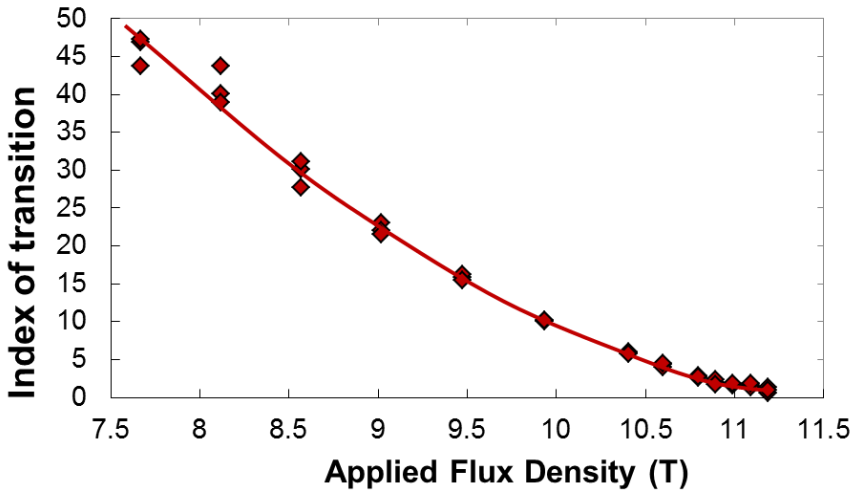

Figure 3.11. *The transition of index as a function of applied magnetic flux density.*

3.2.7 MQE data

Once the critical current had been measured the MQE of the sample could be tested at a range of currents and applied fields. The method used to insulate the sample from the cooling helium is described in section 3.2.5 and the thermal perturbation was created in a controlled manner by the method detailed in section 3.2.4. Once the sample had been mounted in the magnet and had been allowed to cool the actual experimental procedure was:

- The current was rapidly swept up to the required current.

- Once the current had stabilized a current pulse with a duration of $1ms$ was fired through the heater and the voltage across the sample was monitored for 1-2s.
- After the voltage had been monitored, irrespective of whether the sample had quenched or not, the current source was switched off.
- The sample was allowed to cool for 2 minutes before the procedure was repeated.
- If the sample had not quenched the voltage driving the heater current pulse was increased until the smallest current pulse that could quench the sample was found.

As the MQE experiment required the sample current to be held constant for a short period of time (up to 20s) it was decided that the data should be recorded for fields of 9T and above. This is because below 9T the critical currents are very high (over 200A) which could have a few adverse effects. The first is that, although the sample is superconducting and so would not dissipate energy into the helium, the current leads which carry the current to the sample are not. Therefore high currents will cause heating in these, boiling off the liquid helium very quickly, reducing the amount of data which could be collected. The second is that when the sample has quenched it will have a resistance and, as it is well insulated, high sample currents could cause excessive heating, potentially damaging the sample.

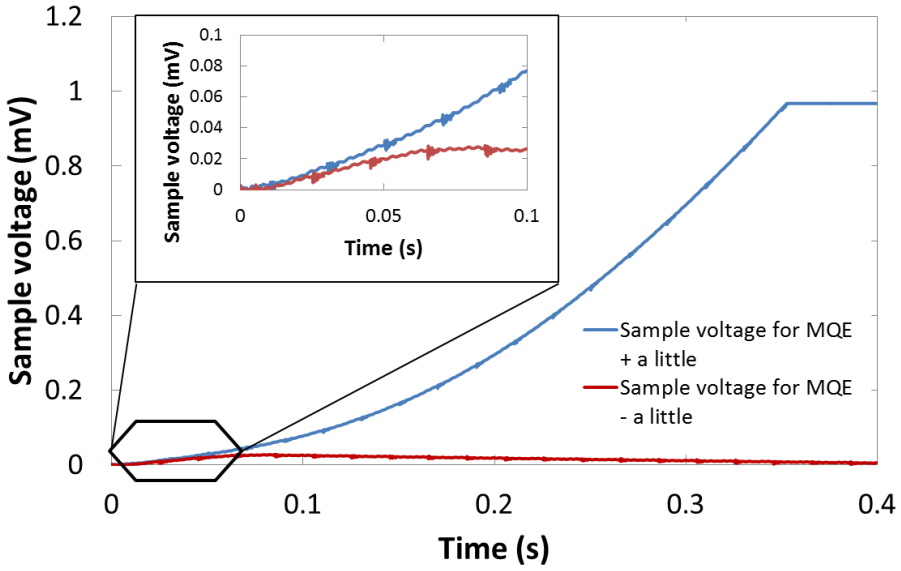

Figure 3.12. The voltage traces recorded after two different thermal perturbations (one just above and one just below the MQE) at 9T and 60A.

Figure 3.12 shows how differently the sample behaves if the thermal perturbation applied is just above or just below the MQE. It shows the voltage trace for two runs at 9T with a 60A sample current after a $3.8mJ$ and a $3.4mJ$ pulse. The voltage after the smaller pulse initially increases, peaking after around $80ms$ before slowly decaying back towards zero. This indicates that the perturbation created a small

normal zone but one which was smaller than the MPZ and so the heat was conducted away faster than it was generated and the normal zone gradually collapsed. On the other hand, the larger pulse, although it was just 10% higher did not peak. The voltage increased in a very similar manner to the voltage after the smaller perturbation but it constantly keeps increasing, the wire never recovers and the normal zone propagates. The flat top to the quenching trace after 320ms is caused by a saturation of the amplifier used to aid the measurement of the signal.

Figure 3.13 shows the results from the MQE measurements and plots them against the fraction of critical current for each magnetic field used. The results showed that, as expected, at a given fraction of critical current the lower fields had a lower MQE but at the same current the lower fields had the higher MQE. In the high current regime the MQE tends towards zero but fractions above 0.8 could not be measured as the sample would spontaneously quench without any extra energy. The low current region (0.2-0.4 depending of field level) shows the MQE increasing rapidly and no data could be obtained in the very low current region as it would have required more energy than the pulse generator could have provided.

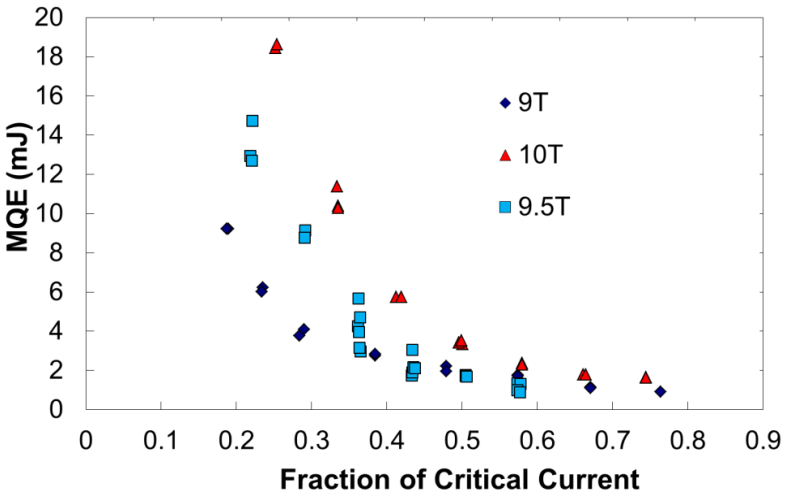

Figure 3.13. *The MQE of the sample against the fraction of critical current at three different applied fields.*

3.2.8 Analysis

The final results show that the experiment to measure the MQE of the sample was reasonably successful and it has provided a wealth of data which can be used to create and tune a computer model describing the thermal stability of superconducting wires. It also showed that the simple one dimensional model provided a reasonable estimate for the values of the MQE at higher currents with the predicted values being about a third of the values measured. This discrepancy is easily accounted

for by the fact that not all of the energy input into the heater coil will reach the wire; due to relatively long time for heat to diffuse from coil to the wire, some heat will have flowed into the insulation, surrounding turns and would have been conducted down the wire before it could cause any significant heating. Furthermore the simple model assumed that the wire was a simple, homogeneous mix but this is far from the case as there is a pure copper sheath surrounding the wire. This may have further increased the measured MQE as it would increase the conduction path between the heater and the wire. Despite producing a good order of magnitude estimate for the MQE and correctly predicting the field dependence the simple model failed to correctly predict the fraction of the critical current where the MQE increased rapidly. It was measured to be between 0.2 and 0.4 for applied fields in the region of 9-10T but the model predicted it to occur at a fraction < 0.1. This is likely due to the simplicity of the model as there are many thermal, superconducting and time-dependant effects which are completely neglected. The aim of constructing the computer models will be to try to incorporate the complicated superconducting behaviour and the internal wire structure which is necessarily omitted from analytical models.

3.3 Computational Investigation

So far in this chapter we have discussed the basis of the MQE, a basic theory to predict it and an experiment conducted to gain some detailed data on how a superconductor responds to thermal perturbations. The aim of all of this has been to gain an understanding of the MQE of superconductors so that a computer model could be generated that could replicate the measured data. A successful model could then make predictions about how different wire architectures may affect the thermal stability of the wire so that cheaper, more stable wires can be made. The rest of this chapter is dedicated to describing the evolution and development of the model before reporting the predictions that the final model made.

3.3.1 Introduction to modelling the MQE of superconductors

The central program which was used for the modelling of the MQE in this thesis is Comsol Multiphysics, a commercially available FEA package from Comsol Ltd[8]. The versions used for this

[8] COMSOL Ltd. Broers Building, 21 JJ Thomson Avenue, Cambridge, CB3 0FA, UK

work were versions 4.0, 4.2 and 4.2A. Matlab R2011b from MathWorks[9] was also used in conjunction with Comsol using an add-on to Comsol known as Comsol Multiphysics with Matlab [26].

As the model was developed it went through many evolutions, increasing in complexity and detail with each newer version. Broadly speaking the versions were:

- Simple 1D model which only considered the thermal aspects of the problem.
- 2D model which again only considered the thermal aspects.
- 2D model which looked at electrical properties of the superconductor with a current flowing in the plane of the model. This model used a constant temperature and ignored magnetic diffusion.
- 2D model which looked at the electrical and thermal properties of the wire with the current in plane again ignoring magnetic diffusion.

Although all of the versions of the model are very different the method used to calculate the MQE from them was very similar. The first stage was that the basic model would be constructed and debugged in the graphical user interface of Comsol. Once the model was behaving in a satisfactory manner it was exported into the Matlab interface where the MQE curves were generated. As the models very quickly got too complicated for analytical solutions a simple trial and error method was developed which could solve for the MQE to any degree of accuracy required. Although the method may not have been the most efficient for all model generations it was applicable to all of them which reduced model development time. The method involved simulating the heat pulse and the response of the wire for up to 5s after the pulse. If the wire had not quenched the energy dissipated by the heater was increased by a set amount and the simulation was repeated. Once the sample had quenched the program returned the to largest energy known to not quench the sample and then started adding a new, smaller, amount to the heater power. This process was repeated until the difference between the largest energy which would not quench the sample and the smallest energy which would quench it reached a predetermined value (it was generally calculated to 3 significant figures). The model would then store the value for the MQE before repeating the entire process for the next current or magnetic field value.

[9] MathWorks, Matrix House, Cambridge Business Park, Cambridge, CB4 0HH, UK

3.3.2 1-D Thermal Model

3.3.2.1 Thermal Diffusion Equation

The starting point for any thermal model is the thermal diffusion equation which describes the evolution of a temperature gradient, ∇T as a function of time, t. For a material with a density, ρ_d, specific heat, c_p, and conductivity, λ, the heat diffusion equation is:

$$\rho_d c_p \frac{dT}{dt} = \nabla \cdot (\lambda \nabla T) + Q \qquad 3.9.$$

where the extra factor, Q, is the power dissipated into the material from another energy source. In the case of a current carrying wire the extra energy will come from electrical energy dissipated into the wire. The equation tells us that the rate of change of thermal energy of a point is dependent on the temperature gradient and the rate of power dissipated at that point. Therefore to build a model we must define each of the three key parameters in turn. The power dissipated will be considered later in this section. Also required is the resistivity of the wire so that the power dissipated can be calculated. The resistivity of the wire in the normal state will be described with the thermal conductivity as these two parameters are very closely related. The superconducting resistivity will be discussed later in this section. Note that the actual values used for each material are contained in Appendix B.

Material Density

The density is perhaps the easiest of the four factors to define accurately. The wire to be modelled is encased in a channel and thus consists of three main materials. These materials are copper, niobium titanium and lead-tin solder used to solder the wire into the sheath/channel. As, in this instance, the model geometry will be one dimensional, it follows that the wire can only be modelled as a homogeneous mixture with its properties being derived from the averaged properties of its constituent materials. Thus if the relative fractions of each material by area are f_{copper}, f_{NbTi} and f_{solder} respectively then the density of the material is simply:

$$\rho_{d\ wire} = f_{copper} \cdot \rho_{d\ copper} + f_{NbTi} \cdot \rho_{d\ NbTi} + f_{solder} \cdot \rho_{d\ solder} \qquad 3.10.$$

Or more generally for a wire with n constituent materials each with a relative fraction f_n:

$$\rho_{d\ wire} = \sum_{i=1}^{n} f_i \rho_{d\ i} \qquad 3.11.$$

With $$\sum_{i=1}^{n} f_i = 1$$

Specific heat capacity [SHC]

The basis for calculating the specific heat capacity for the wire is the same as for the density above except that now the specific heat capacity for each material is function of temperature. The equation for the final specific heat capacity is of the same form as 3.:

$$c_p = \sum_{i=1}^{n} f_i c_{p\,i}(T) \qquad 3.12.$$

Of the three materials the copper is the easiest to define as it is a relatively pure metal and so its properties can be taken directly from the reference literature. All references used, [27] [28] agreed to within a few percent on the low temperature behaviour of the copper and they all showed that the copper followed the classical behaviour expected.

The NbTi superconductor is slightly more complicated as, although the two metals mix fully to form a single alloy with one set of properties, it undergoes a second-order phase change at the critical temperature and field as discussed in the introduction. This phase change leads to the specific heat capacity undergoing a discontinuity at the critical temperature. Therefore the heat capacity must be defined for both regimes with the critical temperature calculated from the equation [14]:

$$T_c(B) = T_c(0)\left[1 - \left(\frac{B}{B_c}\right)\right]^{\frac{1}{n}} \qquad 3.13.$$

where for NbTi [14] $$n = 1.7 \qquad 3.14.$$

where $T_c(B)$ is the critical temperature as a function of applied field B is the applied field and B_c is the critical field at absolute zero. As this function will not be describable using a simple analytical equation like the SHC for copper it must be input into the Comsol model as an interpolation function pre-generated by the Matlab interface. The interpolation function will provide the model with a look-up table for the SHC as the temperature varies.

The most complicated of the materials to define is the lead-tin solder as there is no true alloy phase of the two metals; the solder forms a mixture of nearly pure crystals of lead and tin. This is further complicated by the fact that both elements of the solder are superconducting so will show the same

second order phase transition as the NbTi. However for the model the superconducting transition of both elements can be safely ignored due to their weak superconducting properties. The tin has a critical temperature of 3.7K [29] so is only superconducting outside of the temperature range of the model. Although the lead has a critical temperature of 7.2K [30] it has a critical field of just 50mT at 4.2K which is well below the range of the model and below the ~1.5T field of a standard MRI magnet. Therefore, although the solder has this second order phase shift it will not affect the model to use just the normal state properties [28]. The properties of the solder can then be derived from the ratios of the constituent elements in the normal manner and normal PbSn solder is about 28% lead 72% tin.

Conductivity and Resistivity

The conductivity could be calculated by using an equation of the same form as 3.11 and 3.12. However as the conductivity of the copper is far higher than that of the NbTi or the soft solder the conductivity of the wire is approximated as being the same as that of the copper scaled to the fraction of copper in the wire. Thus the thermal conductivity, λ, is:

$$\lambda = f_{cop}\lambda_{cop} \tag{3.15.}$$

The same argument is used for the calculation of the normal state resistivity of the wire as the resistivity of copper is far lower than that of normal NbTi or PbSn.

To calculate the thermal conductivity of the copper the effects of the applied magnetic field need to be taken into account as well as the effects of the temperature. The thermal conductivity of the copper is calculated from the electrical resistivity using the Wiedemann-Franz law. As copper is a pure metal and a good conductor any applied magnetic field will cause magnetoresistance to increase the resistivity. The transverse resistivity of copper has been shown to increase fairly linearly with applied field and the product of the residual resistivity ratio (RRR) and the applied field is [31]:

$$B_R = B * RRR \tag{3.16.}$$

The residual resistivity ratio, RRR, is the ratio of the resistivity of the copper at room temperature to its value at 4.2K. The increase in resistivity, $\Delta\rho$, is then calculated from the data [31] using:

$$\frac{\Delta\rho}{\rho} = 2.17 \times 10^{-3} \cdot B_R \tag{3.17.}$$

The resistivity of copper at very low temperatures is dominated by the impurities and defects in the lattice and so is fairly constant until about 10-15K depending on the purity of copper [32] and on what heat treatment has been applied to anneal the wire after drawing. Therefore the low temperature resistivity, ρ_{LT}, is modelled as being constant and as being equal to:

$$\rho_{LT} = \frac{\rho_{rT}}{RRR} \tag{3.18.}$$

where ρ_{rT} is the room temperature resistivity of the copper. The final normal state resistivity used in the model is then:

$$\rho_0 = \rho_{Lt}(2.17 \times 10^{-3} \cdot B_R + 1) \tag{3.19.}$$

The thermal conductivity can then be calculated from the Wiedemann-Franz law [33]:

$$\frac{\lambda\rho}{T} = L \tag{3.20.}$$

where L is the Lorenz ratio which is taken to have the value of $2.45 \times 10^{-8}\, W\Omega/K^2$ and is assumed to be independent of temperature. This is a reasonable approximation for the temperature range of the model although, for high purity copper, this is not truly accurate [34]. Equation 3.20 also shows that as the resistivity is constant the thermal conductivity must increase linearly with temperature.

3.3.2.2 Superconducting Properties

The final factor in the heat diffusion equation above was the heat dissipation factor or Q. In a current carrying wire this is simply the electrical power being dissipated into the wire through normal resistivity and superconducting effects such as flux creep or:

$$Q = P = IV \tag{3.21.}$$

As the 1-D model is a uniform homogeneous mix an equation which can describe the power dissipation in the wire for the normal state, the superconducting state and the transition between the two is required. For this the model uses the linear approximation described in [1]. The core of this approximation is that the current is constant with time so the function describes the rate of heat generation as a function of temperature. The first step is to calculate the critical temperature of the superconductor at the magnetic field level being modelled using equation 3.13. Above the critical temperature the current will all be carried by the copper and the resistivity of the copper is assumed to be constant so the rate of heat generation is simply:

$$Q = G_c = J^2\rho \qquad 3.22.$$

The model then defines a secondary critical temperature called the generation temperature, T_G. Below T_G it is assumed that all of the current is carried by the superconductor and so the resistance of the wire, and hence the heat generated, is assumed to be zero. Figure 3.14 shows the dependence of the critical current density as a function of temperature using a linear approximation. This is not truly accurate but as we will see later in section 3.3.4.5 that it is quite a good estimate. It is clear from this graph that a wire which has a critical current density J_{c0} at a temperature T_0 has a generation temperature which varies with applied current density, J_m, as:

$$T_G = T_c - (T_c - T_0)\frac{J_m}{J_{c0}} \qquad 3.23.$$

The rate of heat generation is then assumed to increase linearly between the two critical temperatures from zero to G_c as is shown in Figure 3.15. In the case being modelled here T_0 is simply the temperature of the helium bath, taken to be 4.2K and J_{c0} is the measured critical current density for the magnetic field being modelled.

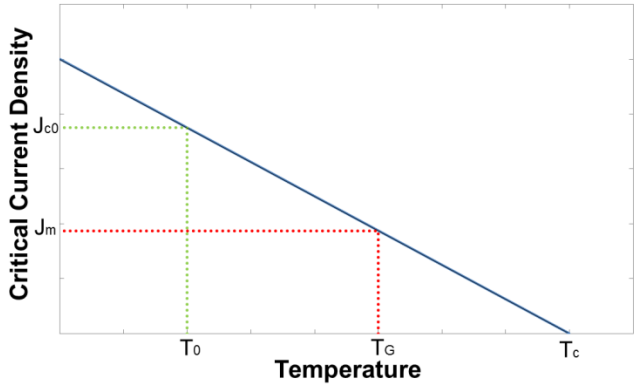

Figure 3.14. *Linear approximation for the dependence of the critical current as a function of temperature.*

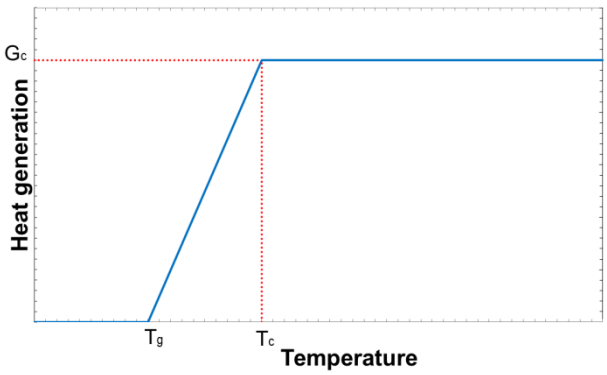

Figure 3.15. *Variation of the rate of heat generation with the wire as a function of temperature.*

3.3.2.3 Model Geometry and Settings

The geometry modelled is simply a line as it is a one dimensional model. The line is assumed to be long enough that the ends of the modelled geometry would not affect the results; that by the time any heat from the pulse reaches the far end of the geometry the wire would have either quenched or recovered. As the model is so simple computational efficiency is not an issue so the model geometry was set to be 10m long. A domain of 1mm is created at one end of the model to signify the heater so that the energy from the heater was created directly in the wire. The boundary condition at the heater end of the model was set to be thermal insulation. As no heat can flow through the thermal insulation boundary this is equivalent to being a mirror plane. The result of this was that the actual length of wire considered by the model was 20m while the heater was 2mm long. The far end of the geometry was held at 4.2K to signify the end of the wire in the helium bath. The model is automatically adiabatic in nature as the one dimension only allows for heat flowing along the length of the wire.

3.3.2.4 Results

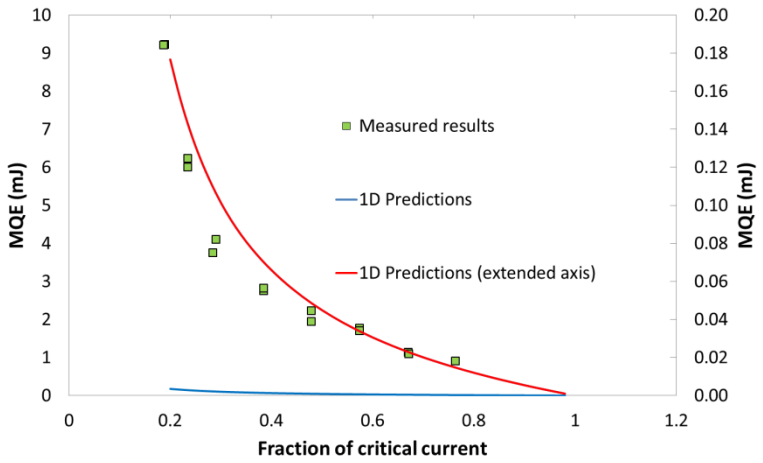

Figure 3.16. Measured and predicted results for 9T with the predicted results plotted twice: once on the same axis as the measured data and once on its own axis.

Once the geometry was set-up and the material properties derived earlier had been entered the model was run in the trial and error program detailed earlier in section 3.3.1. Some of the results from the 1D model are shown in Figure 3.16. The predicted results from the computer model are plotted twice on the same graph as the measured results. The reason for this is so that both the predicted shape and magnitude of the MQE against applied current can be compared to the measured data. The predicted results with the extended axis line are plotted against the right-hand axis. This is so that the shape of the predicted and measured results can be compared directly. It can be seen that the shape of the

predicted curve very closely matches the measured data however when the predicted values are plotted on the same axis as the experimental data it shows that the predicted values are about a factor of fifty too small.

3.3.2.5 Conclusion

It is clear from the results from this simple model is capable of reproducing the trend of the behaviour of the MQE and the wire but it obviously has a large weakness in that the results are far too small. There are two major reasons for this large discrepancy with the first being that the thermal perturbation is induced directly into the superconducting part of the wire. In the experiment the heat was created on the outside of the wire. This means that in the experiment the heat has to flow through the heater insulation, the copper sheath and through the solder layer before it can perturb the supercurrent. This distance will allow any hotspot to spread and thereby reduce the intensity of the perturbation and so a much greater heating effect is required. Also there may not be perfect contact between the heater and the wire so more heat may be lost to the surrounding than can flow into the wire. The second effect is that as the model is assumed to be perfectly adiabatic except for the cold ends once heat has reached the superconductor it can only be conducted away in one dimension along the wire whereas is reality this heat will be able to flow out of the side of the wire as well thereby further reducing the effect of a given thermal pulse.

3.3.3 2-D Thermal Model

The main weaknesses of the 1-D thermal model can easily be improved upon by including a second dimension in the model. This extra dimension will allow the full geometry of the wire and heater to be modelled within certain approximations. The core assumptions of the superconducting properties, material properties and heat generation are all based on the same foundations as the 1-D model with the current only flowing in one direction but now any heat generated will be able to flow in two directions.

3.3.3.1 Model Geometry

The key aspects of the wire geometry which should be included in the model are:

- The wire insert - a homogeneous mix of copper and NbTi
- The copper sheath surrounding the insert
- The solder layer holding the insert into the sheath

- The heater wire and insulation
- Other wire layers surrounding the turn being heated
- Insulation encasing the wire

As the geometry is now 2D and within the x-y plane there needs to be a method for approximating each three dimensional shape which will still retain the properties and material ratios. The initial method for this was to use the average wire width and the ratio of the areas of each constituent of the wire. The average wire width was simply taken to be the average of the wire width and height taken from appendix C. Therefore if the wire has an average width W_A and total area $A_{tot,}$ then the wire constituent with an area A_i will have a width in the model:

$$l_i = \frac{W_A}{2} \cdot \frac{A_i}{A_{tot}} \qquad 3.24.$$

This method leads to the values for the width of each constituent given in Appendix C. The factor of 2 comes into equation 3.24 as a thermal insulation plane is used as a mirror planes so that only half of the transverse geometry needs to be specified. This method ensures that the ratio of the amount of one material to the total of the actual wire is preserved. The length of the wire geometry is 1.5m which is long enough that the cold ends do not affect the results for the MQE but is not so large that the model takes a prohibitively long time to compute the solution. When the thermal insulation boundary at one end of the wire geometry is accounted for the total length of wire considered by the model is 3m.

In this 2-D model it is important to also specify the geometry of the domains around the wire. A complete geometry should include the heater, the turns adjacent to the section of wire of interest and the Stycast insulation both between the turns and encasing the setup. The heater was modelled as a small rectangle with a width equal to the diameter of the constantan wire within a slightly larger rectangle which gave a thin region around the core to denote the heater insulation. The length of the heater region was, like in the 1-D model, 1mm long in the model geometry. When combined with the thermal insulation boundaries this gives a heater geometry 2mm long. The rest of the length of wire which is not surrounded by the heater is modelled as having a thin Stycast casing the same thickness as the heater to model the insulation of the wire. Outside the central wire and casing a region of pure copper is included. This extra region has a width equal to the average wire width and is included to model the effects of heat being lost to the turns surrounding the turn being heated. The final model detail is a thick layer of Stycast to signify the insulation encasing the experiment. The outside of the

Stycast region and the top end of the model are held at a temperature of 4.2K to simulate the helium bath. The modelled geometry is shown in Figure 3.17 although it is important to note that only the very end of the geometry model is shown due to the very high aspect ratio of length to width.

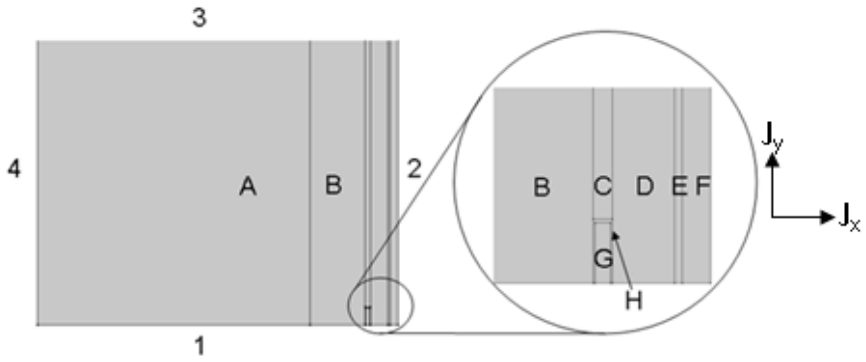

Figure 3.17. Diagram of geometry modelled in 2D thermal model with the key geometrical features being: A/C: Stycast Insulation, B: Secondary Copper Wire, D: Copper Sheath, E: PbSn Solder, F: Copper/NbTi insert, G: Heater, H: Heater Insulation.
Boundaries: 1/2: Thermal Insulation, 3/4 Temperature (held at 4.2K)
J_y indicates the direction parallel to the wire's length while J_x gives direction transverse to the wire.

3.3.3.2 Material Properties

The material properties required in the 2-D model are the same as required for the 1-D in that the model requires the SHC, thermal conductivity and the density of each material. One of the core approximations made by this model is that only the insert will carry current and so only the resistivity of the insert needs to be considered. Although this is a poor approximation it greatly simplifies the complexity of modelling required and will give an idea of what may be happening to the thermal energy within the wire. It will however greatly reduce the predicted MQE as the dissipation in the normal zone will be significantly greater than in reality. As in the last section the insert is considered to be a uniform mixture of NbTi so the properties are derived in the same manner as in 3.3.2.1. The properties of the copper regions, insert and PbSn solder are also the same as derived earlier.

The new materials which need to be defined are the Stycast insulation and the heater region. The Stycast regions are modelled as blue 2850FT hardened with catalyst 23 LV [35] [36] [24]. The final region to be defined is the heater. The core of the heater is made from constantan which is an alloy consisting of 55% copper and 45% nickel. Reference [37] gives the SHC for constantan with 40% and 60% copper. As the values given for these compositions differs by <1% the SHC of the 55% copper constantan is assumed to behave in the same manner as the 60% copper mixture. The thermal

conductivity at 4.2K is calculated from [38] and, as the resistivity is nearly independent of temperature, it is assumed to follow the Wiedemann-Franz law. Once the whole sample is impregnated the heater will be insulated by cotton fibre impregnated with resin. As there is no data in the literature for cotton fibre impregnated in Stycast resin it was assumed to behave in the same manner to the Stycast although this will of course introduce a large error in the rate of heat conduction between the heater and the sample.

3.3.3.3 Superconducting Properties

The superconducting properties used in the 2-D model are exactly the same as detailed in section 3.3.2.2. Again the current isn't modelled directly; the power dissipation at each point is calculated from the temperature of that point. The only assumption which is different is that the current is now entirely carried by the insert so before heat can be generated within the wire the thermal perturbation must diffuse through the sheath and lead-tin solder.

3.3.3.4 Results

The model was again entered into the trial and error solution program to generate the predicted curves for how the MQE would vary with the applied current. The measured and predicted results for 9T are shown in Figure 3.18. Figure 3.19 shows the measured and predicted data after the data had been multiplied by a factor of 10 for ease of comparison between the data sets. Figure 3.20 shows a direct comparison between the predicted curves for all three fields. These results show that the 2D thermal model is more accurate than the 1D model as the predicted values are approximately a factor of 10 too small (compared to 50 for the 1D model). Furthermore, after the factor of 10 is applied, the predicted curve at 9.5T predicts the trend of the data accurately for all current fractions, correctly showing the 'knee' at $\sim 0.3 J_c$. There are, however, there are clearly some flaws in the model's assumptions as shown by the plots of the data at 9T and 10T along with the large multiplication factor required. One problem is the small value predicted for the MQE and also, as shown by Figures 3.19 and 3.20, the model predicts the wrong dependence of the MQE with applied magnetic field. In both the basic theory, the higher magnetic fields have high MQEs at a given fraction of the critical current. The model predicts the opposite of this; giving higher MQEs at lower applied fields.

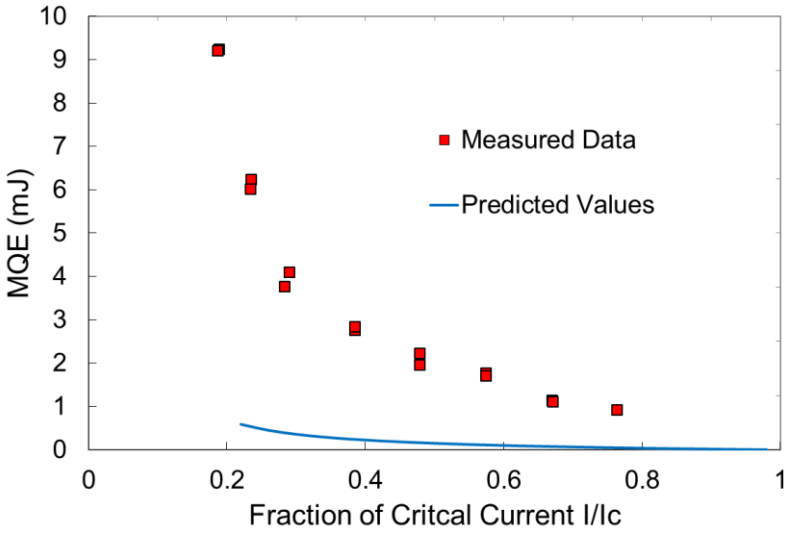

Figure 3.18. *Measured data and the predicted curve for the MQE of EAS T108 against the fraction of critical current applied at 9 T.*

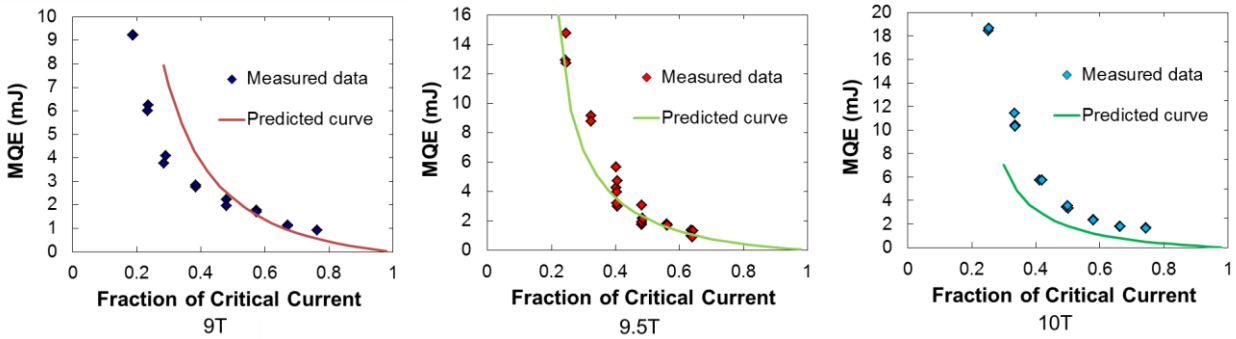

Figure 3.19. *The measured and predicted data with a multiplication factor of 10 applied to the predicted data for 9T, 9.5T and 10T.*

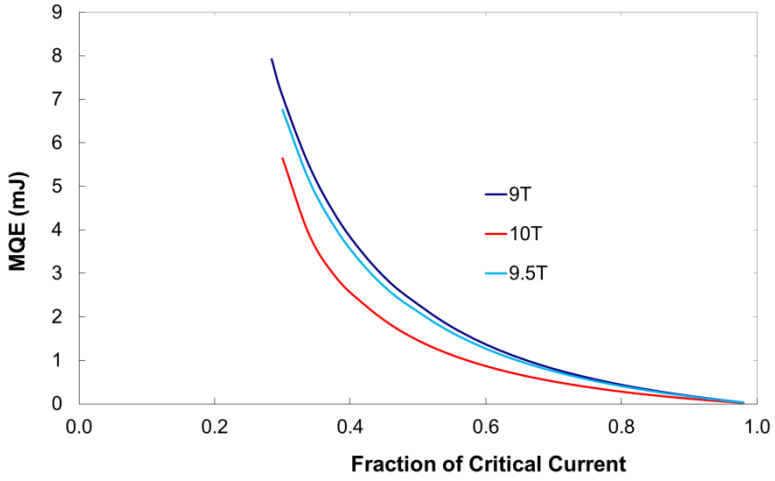

Figure 3.20. *The curves generated by the model for the sample's MQE at all three applied magnetic fields.*

3.3.3.5 Conclusion

It is clear from the results generated by the 2-D thermal model that the core of the model; the dependence of the MQE on the applied current, produces results which can accurately reproduce the

real world data when a multiplication factor is included. However this model clearly does not encompass all the relevant behaviour as the dependence of the MQE curve on the applied magnetic field is wrong. There are several assumptions which could reduce the accuracy of its predictions, the primary of these is that the current is carried entirely by the superconducting insert even after the quench. This assumption is clearly incorrect as some of the current will redistribute into the copper sheath, lowering the heating effect of a given current at any temperature. The method of calculating the power dissipation as a function of temperature at each point also ignores the highly non-linear resistivity of the superconductor as a function of current. These two effects will need to be addressed to improve the accuracy of the model and are likely responsible for the low MQEs predicted.

3.3.4 2-D Current Distribution Model

The obvious refinement to the 2-D thermal model detailed earlier in this chapter is to model the currents in the superconductor and how they are redistributed by a thermal perturbation. Although this seems like it should be a reasonably simple affair as there is a module within Comsol Multiphysics, called the ACDC module [39], dedicated to solving current distribution problems, there are two main difficulties in implementing such a model: The first is that the standard current problem is a linear problem in that the resistivity is independent of the current or voltage. Hence the current and voltage in Ohm's law are simply proportional to each other with the resistance being the constant of proportionality. However in a superconductor the resistivity in a superconductor is dependent on the current density flowing through the superconductor as governed by the power law in equation 3.2 and so the problem is highly non-linear. This non-linearity can cause problems in terms of being expensive in computing power and can lead to convergence problems in a model. These problems are however soluble with computing time and carefully set up solver settings. Unfortunately the first problem also hints at the nature of the second problem which is far more difficult to accommodate; the problem is that as the resistivity is dependent on the current the problem has a circular dependency.

3.3.4.1 Circular dependency difficulties

In any current distribution model the core equation is simply Ohm's law:

$$V = IR \tag{3.25.}$$

Therefore, in a standard current model where the resistance is independent of the current and voltage, the user will define either a voltage or a current and the model will calculate the other variable

accordingly. When superconductors are introduced the problem increases in complexity as the resistivity, and hence the resistance, is now dependent on the applied current density or in general:

$$R \propto f(I) \tag{3.26.}$$

In a model with more than one dimension this leads to difficulties. For arguments sake let us consider a 2-D geometry. If we take a single point in the geometry across which we apply a voltage we can normally calculate the current simply using equation 3.25. However in this situation as R varies with I the model does not have a consistent starting point from which to calculate either the resistance or the current; there is the circular dependency or more simply the current flowing through any given point depends on itself. To get around this problem we must either input a trial solution and allow the model to iterate or to find a separate variable which the model can calculate and then use to derive the values for the resistance and current.

3.3.4.2 Modelling the Current Distribution using the V formulation

The first possible method for calculating the current distribution is to define the voltage manually within the PDE solver within Comsol. We can start by defining the electric potential V and then the electric field in the superconductor is:

$$\boldsymbol{E} = -\nabla V \tag{3.27.}$$

And the current is defined by:

$$\boldsymbol{J} = \sigma \boldsymbol{E} \tag{3.28.}$$

To obtain the equation to be solved in the PDE solver we must consider Ampere's Law:

$$\nabla \times \boldsymbol{H} = \boldsymbol{J} + \frac{d\boldsymbol{D}}{dt} \tag{3.29.}$$

If we take the divergence of the equation 3.29 we obtain:

$$\nabla \cdot (\nabla \times \boldsymbol{H}) = \nabla \cdot \boldsymbol{J} + \frac{d}{dt} \nabla \cdot \boldsymbol{D} \tag{3.30.}$$

Using the general vector identity applicable to any vector:

$$\nabla \cdot (\nabla \times \boldsymbol{A}) = 0 \tag{3.31.}$$

and from Maxwell's first law:

$$\nabla \cdot \boldsymbol{D} = \rho \tag{3.32.}$$

If we assume that there are no free charges in the system then equation 3.30 becomes:

$$\nabla \cdot \boldsymbol{J} = -\frac{d\rho}{dt} = 0 \tag{3.33.}$$

i.e. that the divergence of the current should be zero everywhere within the model so there are no current sources or sinks within the model geometry. The final equation to be solved now comes from combining equation 3.33 with equations 3.27 and 3.28:

$$\nabla \cdot (\boldsymbol{J}) = \nabla \cdot (\sigma \cdot \mathbf{E}) = \nabla \cdot (\sigma \cdot \nabla V) = 0 \tag{3.34.}$$

The superconducting properties can then be introduced using the power law introduced earlier reproduced here for ease of reference:

$$|E| = E_c \left(\frac{|J|}{J_c}\right)^i \tag{3.35.}$$

By re-writing equation 3.35 using equation 3.28 we can obtain the definition of the conductivity of the superconductor as a function of electric field:

$$\sigma = \sigma_c \left(\frac{|E|}{E_c}\right)^{\frac{1}{i-1}} \tag{3.36.}$$

The model can then calculate the current using equation 3.28 and therefore the circular dependence is broken as first a conductance is calculated and then the current. The model will then iterate any solution until a self-consistent solution is found.

Although this method of defining a new solver within the PDE solver of Comsol works well it is computationally expensive and even the simplest calculation of sweeping up the current in the superconducting insert by itself can take around an hour to compute. As this is a very long computation time by the time the full system is modelled the computation time would be prohibitively long to run the program multiple times to generate the MQE curve. Therefore an alternative method with a much shorter computation time was developed by the author.

3.3.4.3 Modelling the Current Distribution using the H formulation

Let us define $\boldsymbol{H}$ as the vector potential to be solved[10]. This can be regarded as the magnet field. In general terms this vector has three components:

$$\boldsymbol{H} = \begin{Bmatrix} H_x \\ H_y \\ H_z \end{Bmatrix} \tag{3.37.}$$

Since $$\nabla \cdot \boldsymbol{J} = 0 \tag{3.38.}$$

We can write: $$\boldsymbol{J} = \nabla \times \boldsymbol{H} \tag{3.39.}$$

$$\boldsymbol{J} = \begin{Bmatrix} J_x \\ J_y \\ J_z \end{Bmatrix} = \begin{Bmatrix} \dfrac{\partial H_z}{\partial y} - \dfrac{\partial H_y}{\partial z} \\ \dfrac{\partial H_x}{\partial z} - \dfrac{\partial H_z}{\partial x} \\ \dfrac{\partial H_y}{\partial x} - \dfrac{\partial H_x}{\partial y} \end{Bmatrix} \tag{3.40.}$$

However as we are working in a 2-D geometry in the x-y plane all the $\partial/\partial z$ terms are all zero and we are not interested in $\boldsymbol{J}_z$ as 3.38 shows that this will play no part in the solution so can be set to equal zero. Therefore we have the equation:

$$\boldsymbol{J} = \begin{Bmatrix} J_x \\ J_y \end{Bmatrix} = \begin{Bmatrix} \dfrac{\partial H_z}{\partial y} \\ -\dfrac{\partial H_z}{\partial x} \end{Bmatrix} \tag{3.41.}$$

Hence we only need to model the out of plane component of the magnetic field H_z. The final equation is found if we assume that any change in magnetic field is very slow then the Maxwell-Faraday equation can be approximated as:

$$\nabla \times \mathbf{E} = 0 \tag{3.42.}$$

and as $$\boldsymbol{E} = \rho \boldsymbol{J} \tag{3.43.}$$

where ρ is the resistivity, we get to the equation:

$$\nabla \times \mathbf{E} = \rho \cdot \nabla \times \boldsymbol{J} = \rho \cdot \begin{pmatrix} 0 \\ 0 \\ \dfrac{\partial J_y}{\partial x} - \dfrac{\partial J_x}{\partial y} \end{pmatrix} = 0 \tag{3.44.}$$

This then leads to the fundamental equation to be solved by the model:

[10] The idea to define the current in terms a vector potential was kindly provided by Prof Archie Campbell: University of Cambridge, Department of Engineering, Trumpington Street, Cambridge, CB2 1PZ, UK.

$$\nabla \times (\rho \cdot \nabla \times \boldsymbol{H}) = 0 \tag{3.45.}$$

This equation requires a little more manipulation before it can be input into the PDE solver in Comsol. The first step requires the use of the divergence of a vector which is defined as:

$$\nabla \cdot \boldsymbol{A} = \frac{dA_x}{dx} + \frac{dA_y}{dy} + \frac{dA_z}{dz} \tag{3.46.}$$

Using equation 3.46 we can write the z component of $\nabla \times \boldsymbol{J}$ in the brackets in equation 3.44 as:

$$\frac{\partial J_y}{\partial x} - \frac{\partial J_x}{\partial y} = \nabla \cdot \begin{pmatrix} J_y \\ -J_x \end{pmatrix} \tag{3.47.}$$

Therefore if we ignore the components of equation 3.44 which are equal to zero it can be written as:

$$\rho \cdot \nabla \times \boldsymbol{J} = \rho \cdot \left\{ \nabla \cdot \begin{pmatrix} J_y \\ -J_x \end{pmatrix} \right\} = \nabla \cdot \begin{pmatrix} E_y \\ -E_x \end{pmatrix} = 0 \tag{3.48.}$$

We can compare this to the form of the equation input which Comsol requires in the partial differential equation module [26]:

$$e_a \frac{\partial^2 V}{\partial t^2} + d_a \frac{\partial V}{\partial t} + \nabla \cdot \boldsymbol{\Gamma} = f \tag{3.49.}$$

Therefore to solve the superconducting properties we set:

$$e_a = d_a = f = 0 \tag{3.50.}$$

And

$$\boldsymbol{\Gamma} = \begin{Bmatrix} \Gamma_x \\ \Gamma_y \end{Bmatrix} = \begin{Bmatrix} E_y \\ -E_x \end{Bmatrix} \tag{3.51.}$$

To complete the basic current model some boundary conditions are required. The boundaries which act as the current source or sink can simply be left as the default condition of zero flux as $\boldsymbol{H}$ has no components perpendicular to any boundaries. Of the remaining two boundaries one should be set to $H_z = 0$. This acts like a symmetry plane for the model so defines the centre of the wire. The remaining boundary is then used to define the current. If the bulk current is flowing in the general direction $\vec{j}$ which is perpendicular to the direction $\vec{k}$ then:

$$J_j = \frac{dH}{dk} \tag{3.52.}$$

$$|J_j| = \frac{\Delta H}{\Delta k} \tag{3.53.}$$

Therefore for a wire with width $\mathcal{L}$ as one boundary (boundary 2 in Figure 3.17) is set to $H = 0$ the average current density in the wire is:

$$|J_j| = \frac{H}{\mathcal{L}} \tag{3.54.}$$

And so if the required current density is J_y this can be achieved by setting the final boundary (boundary 4 in Figure 3.17) to be:

$$H = J_j \cdot \mathcal{L} \tag{3.55.}$$

The current in the domains is then calculated from the magnetic field using equation 3.41 and the resistivity can then be defined using the normal power law:

$$\rho \propto J^{i-1} \tag{3.56.}$$

$$\rho = \rho_c \cdot \left(\frac{J}{J_c}\right)^{i-1} \tag{3.57.}$$

A more accurate method for defining the resistivity of the insert is based on the calculation of the resistance of two parallel resistors[11]. As in the insert we have the superconductor and the copper matrix in intimate contact we can approximate them as being two resistors with resistance R_{sc} and resistivity ρ_{sc} for the superconductor and R_{cop} and ρ_{cop} for the copper. Now the resistance of the insert can be calculated as:

$$\frac{1}{R} = \frac{1}{R_{sc}} + \frac{1}{R_{cop}} = \frac{R_{cop} + R_{sc}}{R_{cop} \cdot R_{sc}} \tag{3.58.}$$

and as $\rho \propto R$

$$\rho = \frac{\rho_{cop} \cdot \rho_{sc}}{\rho_{cop} + \rho_{sc}} \tag{3.59.}$$

By looking at the limits at low and high current densities it becomes apparent why this is more accurate than equation 3.57 in the low current regime:

As $$\lim_{J \to 0} \rho_{sc} = 0 \tag{3.60.}$$

$\therefore$ $$\rho_{cop} \gg \rho_{sc} \tag{3.61.}$$

and so: $$\lim_{J \to 0} \rho = \frac{\rho_{cop} \cdot \rho_{sc}}{\rho_{cop}} = \rho_{sc} \tag{3.62.}$$

[11] Please note that after the results found in sections 3.3.4.4 to 3.3.4.7 and section 3.3.4.9 were generated using this method a more accurate method was found courtesy of Dr Martin Wilson. The newer method and the likely impact on the presented results can be found in section 3.3.4.8.

Therefore in the low current, superconducting, regime the resistivity of the insert is dependent on the resistivity of the superconductor and so obeys the power law given earlier. In the higher current regime:

As $$\lim_{J\to\infty} \rho_{sc} = \infty \qquad 3.63.$$

$\therefore$ $$\rho_{cop} \ll \rho_{sc} \qquad 3.64.$$

and so $$\lim_{J\to\infty} \rho = \frac{\rho_{cop} \cdot \rho_{sc}}{\rho_{sc}} = \rho_{cop} \qquad 3.65.$$

Therefore in the high current regime when $J \gg J_c$ the resistivity becomes dependant solely on the resistivity of the copper and losses its dependence on the power law. This behaviour is what would be expected as in the low current region when $J \ll J_c$ the resistivity of the copper is much higher than the resistivity of the superconductor. Therefore the bulk of the current will be carried by the superconductor and its resistivity will dominate the properties of the wire. However when the current is well above the critical current the resistivity of the wire increases rapidly with current which would, if it was by itself, lead to a wire with infinite resistivity which is obviously unphysical. Therefore in this regime the copper will have a much lower resistivity and the properties of the copper will dominate. A graph showing the E-I and resistivity curves predicted by the model are shown in Figure 3.21 and Figure 3.22. For a comparison E-I and resistivity curves for a pure superconductor and for a normal copper wire of the same dimension were calculated using equation 3.57 and Ohm's law respectively.

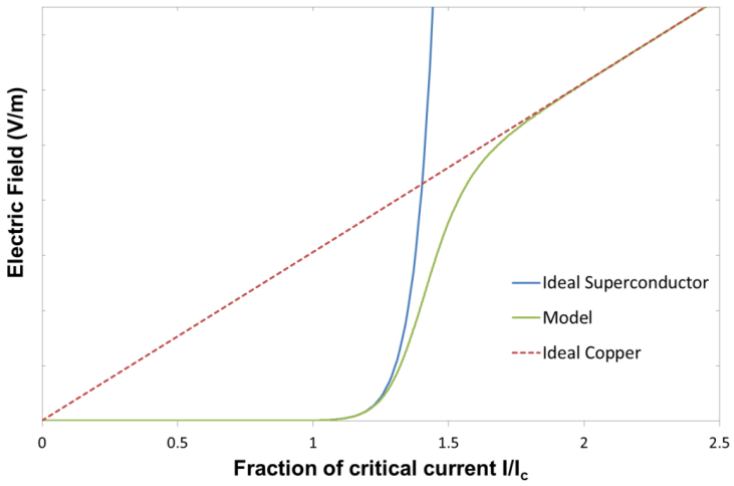

Figure 3.21. *E-I curves for an ideal pure superconductor, copper and the curve used by the computer model.*

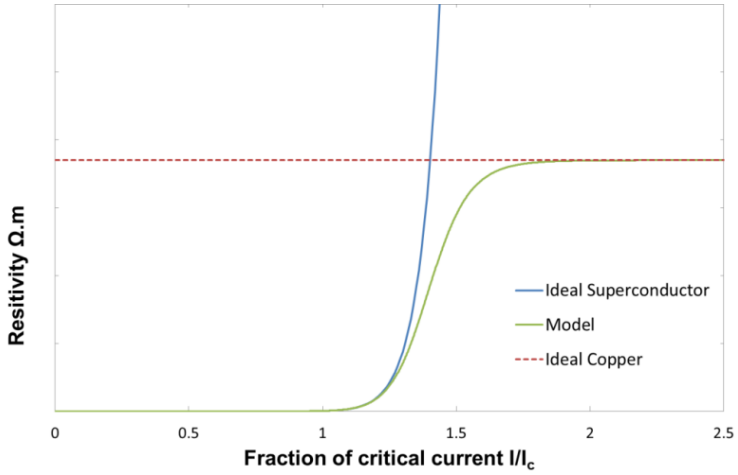

Figure 3.22. *Resistivity as a function of current for an ideal pure superconductor, copper and the curve used by the computer model.*

The next step is to see how the model copes with a superconducting insert with a normal copper sheath. The purpose of this is to see how the current redistributes within the wire as the resistivity of the insert increases. As the current distribution is governed by the relative resistivities in the low current region all the current should be carried by the insert as it will have a much lower resistance. Once the insert starts to develop an appreciable resistance the current should distribute between the copper and the superconductor according to the ratios of the resistances or:

$$\frac{I_{sc}}{I_{cop}} = \frac{R_{cop}}{R_{sc}} \qquad 3.66.$$

Therefore if the insert has and area A_{sc} and the cladding has an area A_{cop} the ratio of currents should be:

$$\frac{I_{sc}}{I_{cop}} = \frac{\rho_{cop} \cdot A_{sc}}{\rho_{eff} \cdot A_{cop}} \qquad 3.67.$$

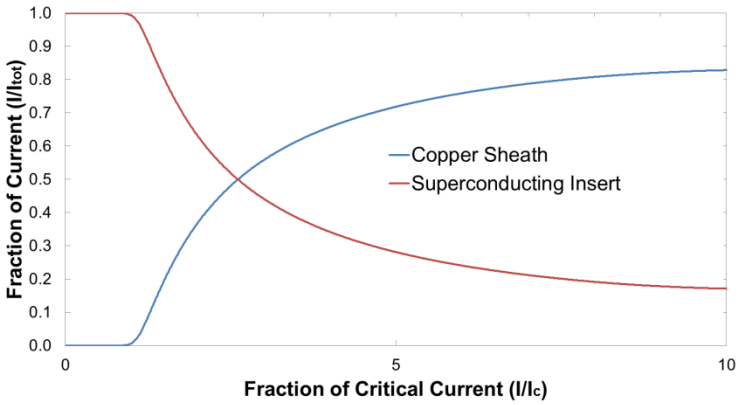

Figure 3.23. *The fraction of the total current carried by the copper sheath and the superconducting insert as a fraction of critical current for a perfectly cooled wire.*

A model was constructed to test the current redistribution in a wire with the same geometry as the wire in the MQE experiment and models. The current in the wire was swept up to twenty times the critical current while the temperature was held fixed at 4.2K to indicate a perfectly cooled conductor. This scenario is clearly unphysical as at these high current levels it would not be possible to remove the heat generated quickly enough, causing the temperature of the superconductor to rise. The results in Figure 3.23 show that, as expected, up to the critical current the entirety of the current is carried in the superconducting insert. Above the critical current the current distributes so that it is shared between the insert and the sheath with the insert carrying a greater fraction at extremely high multiples of the critical current.

3.3.4.4 Validating the 2-D current model

Before the model can be refined into a more complicated form it is a good idea to validate the simple model against measured data. The simplest way of doing this is to compare the E-I curve predicted by the model to the real curves generated for the sample before it was impregnated and so the cooling of the sample would be very good and the sample could be assumed to be at 4.2K for the duration of the run. The model was then used to generate predicted E-I curves for each of 8.5T, 9T, 9.5T and 10T which could be directly compared to the curves measured in section 3.2.6. These curves are shown in Figure 3.24.

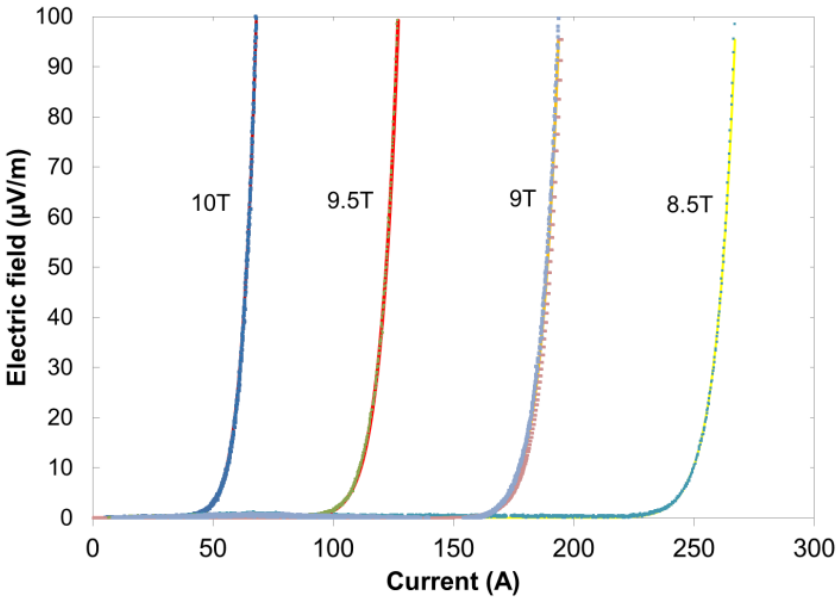

Figure 3.24. The measured (smooth curves) and predicted curves (data points) for the V-I curves for EAST108 at 8.5T, 9T, 9.5T and 10T.

It is clear from Figure 3.24 that the model can produce results which very accurately agree with the measured V-I data for a well cooled superconducting wire with the transition occurring at the correct current for each magnetic field with the correct transition shape. It shows that the model can reproduce to a very high fidelity the measured E-I curves for a well cooled superconductor right through the non-linear transition down to the microvolt scale. However before this model can be used to explain the MQE experiment measurements the current only model must be coupled to a thermal model.

3.3.4.5 2-D Current Distribution and Thermal Model

The equations listed so far describe the superconductor at a constant temperature and magnetic field. For a full model of the MQE the effects of the temperature and applied field need to be taken into account. The simpler of these is the magnetic field as it is considered to be constant during the duration of the model so can be accounted for by using the correct value of J_c and n, both of which, as in earlier sections, are derived from experimental measurements of the wire to be modelled.

Although a linear approximation was used earlier a more accurate method uses the equation from reference [14] which gives the dependence of the critical temperature with magnetic field and an empirically derived factor n:

$$B_c(T) = B_c(0)\left[1 - \left(\frac{T}{T_c}\right)^n\right] \tag{3.68.}$$

where for NbTi: $n = 1.7$

Therefore:

$$T_c(B) = T_c(0)\left[1 - \left(\frac{B}{B_c}\right)\right]^{\frac{1}{n}} \tag{3.69.}$$

The value for $T_c(B)$ can then be entered into the equation from [40] which gives the dependence of J_c as a function of temperature:

$$J_c(T) = J_c(0K)\left[1 - \left(\frac{T}{T_c}\right)^n\right]^\gamma \tag{3.70.}$$

$$\gamma \cong 2 \tag{3.71.}$$

where γ, like n above, is empirically derived. As the actual data was measured at 4.2K we can modify equation 3.70 to use the measured critical current density so it becomes:

$$J_c(T) = J_{c(4.2k)}\left[1 - \left(\frac{T - 4.2}{T_c - 4.2}\right)^n\right]^\gamma \tag{3.72.}$$

Equation 3.72 then leads us to how we can modify the function for the resistivity of the insert. The first step is to replace J/J_c in the power law governing the resistivity of the superconductor with a dimensionless parameter θ:

$$\theta = \frac{J}{J_c(T)} \tag{3.73.}$$

for the range $T_0 \leq T < T_c$, $J_c(T)$. A slight difference is that we now need to add small constant, δ, to help the model to converge. This extra constant has no physical meaning but it is added as:

$$\lim_{J_c(T)\to 0} \theta = \infty \tag{3.74.}$$

Therefore without the added δ constant the model would fail when the temperature of any part of superconductor reached the critical temperature as the θ function would tend to an infinite value. This leads to the variation of $J_c(T)$ with temperature:

$$J_c(T) = \begin{cases} J_{c(4.2k)}\left[1 - \left(\frac{T-4.2}{T_c-4.2}\right)^n\right]^\gamma + \delta \; for \; T < T_c \\ \delta \;\; for \; T \geq T_c \end{cases} \tag{3.75.}$$

The constant δ is of the order $10^{-4}J_{c0}$ to minimise any errors in the model. Currently the index of transition is assumed to be independent of temperature.

The final equation to link the current aspects of the model to the thermal one is to define the equation for heat generation which is simply:

$$P = \rho(\theta)J^2 \tag{3.76.}$$

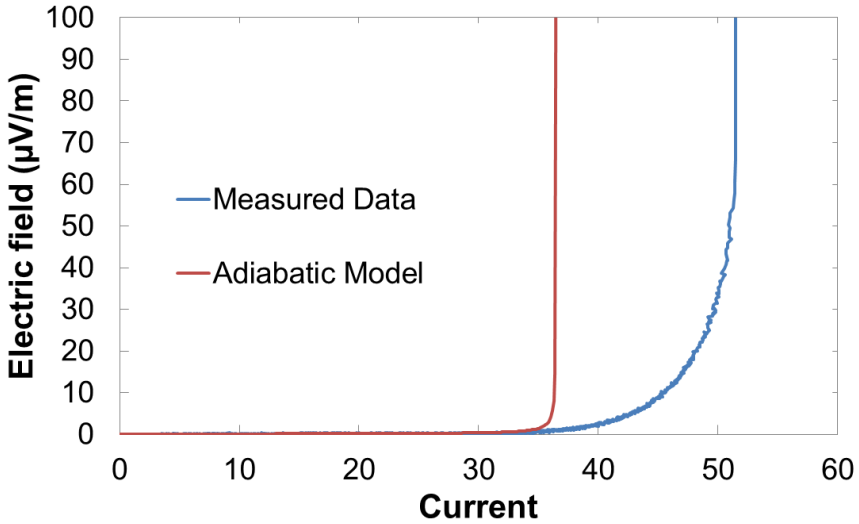

Figure 3.25. Measured V-I curve for impregnated EAS T108 at 10T and the predicted curve at 10T for a fully adiabatic environment.

Although the formulation for the thermal aspects of this model should work there is one more problem to consider. As the superconductor obeys the power law it will always have a finite resistivity and hence there will always be a small amount of heat generated in the wire. If the wire is modelled as being in a fully adiabatic environment any heat generated will cause the temperature of the wire to increase. This increase in temperature will degrade the superconducting properties causing an increase in the rate of heating until the wire quenches. Hence the use of the true power law for the resistivity and a fully adiabatic environment results in the modelled system being dynamically unstable. Figure 3.25 shows a graph for the E-I curve predicted by the computer model if the wire is assumed to be in a fully adiabatic environment while producing realistic amounts of heat. It is clear from this plot that when heat is generated and not removed from the wire at all the wire will quench far earlier than it does in reality. Therefore for a thermal model to accurately replicate the behaviour of the wire either the perfect power law or the fully adiabatic environment must be changed. We can get information about the best method to adopt if we look back to the critical current data we can calculate the rate of power dissipation into the wire as the current increases by simply using the well-known equation:

$$P = IV \qquad 3.77.$$

The curves for power against time can then be used to obtain the power which was being dissipated into the wire at the point at which the wire quenches. We can also use numeric integration to calculate the total amount of energy which had been transferred into the wire during the measurement of the critical current up to the quench point. By comparing the power and total energy dissipation at quench for all the repeats at all applied magnetic fields we can gain information about what is happening to the thermal energy in the wire. If the total energy dissipated at quench is roughly the same for all runs then it is likely that the environment is fairly close to being truly adiabatic. If, however, the power at quench is roughly constant for all runs this will indicate that the wire is being cooled by some means. This comparison is most convincing if two runs at the same magnetic field but where the current is increased at different rates. Table 3.2 shows the data for two runs with an applied field of 9T.

Run	Sweep Rate (A/s)	Power at Quench (mW/m)	Energy Dissipated at Quench (mJ/m)
A.	1.67	2.07	11.3
B.	4.17	2.47	5.1

Table 3.2. Table showing the power and total energy dissipated at quench for wire EAS T108 during two impregnated V-I curve measurements at 9T.

It is clear from Table 3.2 that the power at the quench of the two runs is much closer than the energy dissipated in the wire. This fact by itself indicates that there must be some cooling of the wire as at 4.2K the specific heat capacity of the wire is $\sim 3.44 mJ/m \cdot K$. Thus if the environment was truly adiabatic you would expect the temperature of the wire in run A to have increased to around 7.5K. This is well above the critical temperature of NbTi at 9T which is around 5K and so the superconducting state would have been destroyed much earlier than it was. If the power at quench is averaged over all of the runs a value of $2.45 \pm 0.65 mW/m$ which should give a temperature rise of 0.7K/s. It would, at this stage, be useful to know the temperature of the sample during the impregnated critical current measurements which was not measured during the experiment itself due to the difficulties of thermometry in high magnetic fields. We can however obtain an estimate of the average temperature of the sample by comparing the impregnated E-I curve to the equivalent curve for the well cooled sample. Figure 3.26 shows a graph of two runs for the sample at the same applied field before and after impregnation.

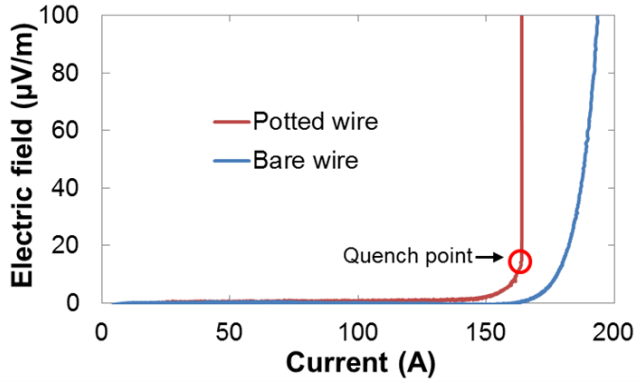

Figure 3.26. *Electric field against current plots for the sample at 9T before and after the Stycast impregnation.*

If we recall the power law governing the superconducting transition is:

$$V = V_o \left(\frac{I}{I_c}\right)^i \qquad 3.78.$$

where the equation has been re-written into a slightly more convenient form for the ensuing calculations. Therefore as we know the current and the voltage at all points on the measured data for the impregnated samples we can infer what the effective critical current must be:

$$I_c = I \cdot \left(\frac{V}{V_0}\right)^{-\frac{1}{i}} \qquad 3.79.$$

If we assume that the index of transition is only dependant on the applied field it will be a constant during each run so can be taken to simply be the value extracted from the well cooled run. Using this equation for the inferred critical current along with equation 3.72 which gives the dependence of the critical current of NbTi on temperature we reach the equation:

$$T = T_0 + (T_c - T_0)\left\{1 - \left(\frac{I_c}{I_{c0}}\right)^{\frac{1}{\gamma}}\right\}^{\frac{1}{n}} \quad 3.80.$$

Or in full:

$$T = T_0 + (T_c - T_0)\left\{1 - \left(\frac{I \cdot \left(\frac{V}{V_0}\right)^{-\frac{1}{i}}}{I_{c0}}\right)^{\frac{1}{\gamma}}\right\}^{\frac{1}{n}} \quad 3.81.$$

Using this equation the temperature against time and the highest temperature of the sample before the quench were estimated. The result was that the final temperature of every run was very similar with a value of $4.29 \pm 0.03K$ with no appreciable trend on this value with critical temperature. It therefore appears that the wire is cooled with a maximum cooling power of ~2.5mW/m at a temperature of 4.29K. By comparing how the temperature rises with time against the power dissipated with time we can calculate the cooling power versus temperature function. Figure 3.27 shows the typical cooling curve calculated for a run. The run shown is a typical 9.5T run with a peak superconducting power dissipation of 2.77mW/m which is well within one standard deviation of the mean. It is possible that the cooling power will continue to increase as the temperature increases past the maximum measured temperature. However the volume of helium cooling the wire is small and so when the heat dissipation gets too high this volume will be driven out or reduced by the gas boiled off by the wire. This means that the cooling power will have a maximum value at some unknown temperature. Therefore the cooling curve was truncated at the maximum measured cooling power as this was the largest cooling power for which there was an experimental basis.

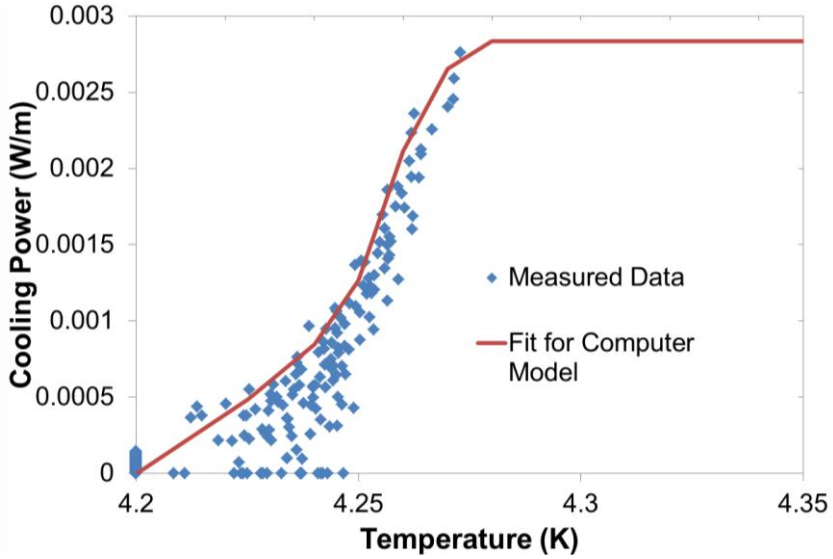

Figure 3.27. Calculated data for cooling power against sample temperature for a typical 9.5T impregnated critical current measurement sweep. Also plotted is the fitted curve used for the cooling curve used in the computer model.

It is clear by now that the sample must be cooled despite the Stycast impregnation process. The most obvious possibility for the nature of this cooling would be conduction cooling with the heat flowing along the length of the wire through the copper to the helium bath. However a quick calculation shows that this cannot be the whole reason: if we consider a rod or wire of length L with constant cross-section, A, with one end held at a temperature T_1 and the other held at T_2 then the heat flow down the wire will be:

$$\frac{dQ}{dt} = \lambda A \frac{dT}{dx} = \lambda A \frac{T_2 - T_1}{L} \qquad 3.82.$$

As for a 3m wire the heat can flow in both directions from the centre the length would be 1.5m and T_1 is simply the temperature of the helium bath so 4.2K. Therefore as the thermal conductivity is $\sim 400 W/(m.K)$ the maximum heat flow for a T_2 of 4.3K is ~55μW or roughly 2% of the actual cooling effect seen. In fact for thermal conduction along the wire to be the sole cooling effect either the thermal conductivity of the copper must be $\sim 22{,}000 W/(m.K)$ or the temperature of the wire must be ~10K. Both of these situations are obviously unphysical and so there must be a cooling effect through the wire's surroundings. Part of this will be heat conduction into the Stycast resin but as the thermal conductivity of this material is so low ($\sim 0.004 W/(m.K)$) so is again unlikely to be the main source of cooling. It seems likely that the Stycast either did not fully bind to the surface of the wire or that the Stycast cracked away from the wire upon exposure to the low temperature environment [41].

Figure 3.28 shows that both of these scenarios were indeed present in the wound sample as it shows a photo of the samples cross-section after it had been machined to expose the wound wire.

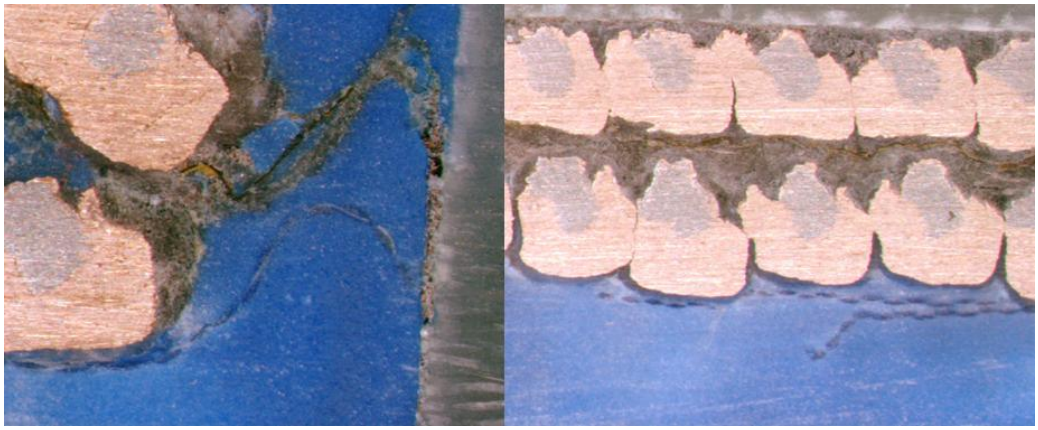

Figure 3.28. A crack in the Stycast insulation and the lack of Stycast resin encasing the individual turns possibly leading to helium seeping into the wire.

Either of the two previous scenarios would lead to a similar effect of the surface of the wire being cooled directly along its length by a small amount of liquid helium. It is not possible to ascertain the exact nature of this cooling effect nor is it necessary for the end aim of this model; the aim is to investigate how the wire reacts to heat, not necessarily how heat flows through the wire's surroundings. Therefore it is more important to know the empirical function of the cooling.

The final problem is how to apply the empirically derived cooling functions to the model. There are two options for this: we can either apply a surface heat flux to the outer boundaries of the wire or we can apply a body heat source to one or more of the domains [26]. By far the simpler of these two is to use the body heat source as the form of empirically derived cooling curve is already in the form of a body cooling averaged over domain of the insert. It is not necessarily obvious why it should be appropriate to apply the cooling to the insert domain as well as the copper domain but looking back at Figure 3.2 which shows the photo of the wire cross-section shows that if the perimeter of the wire is cooled then approximately 1/3 of the insert's perimeter is cooled directly. By making some approximations about conduction path lengths and cooled surface area of the copper and insert areas and by using equation 3.82 it was estimated that approximately $2/3$ of the heat generated in the centre of the insert would exit the wire through the copper and the other 1/3 of the heat would exit directly through the surface of the insert. Therefore the cooling curve was applied so that the total cooling effect over the wire would be equal to the derived cooling curve with the magnitude of the cooling effect in the insert being one third and the copper two thirds of the total.

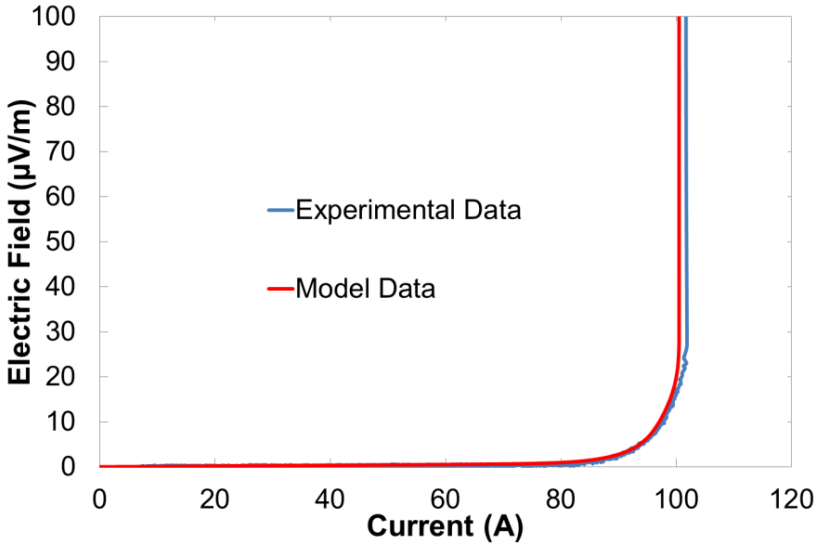

Figure 3.29. Experimental data and the predicted curve for an E-I curve for an impregnated sample at 9.5T.

Figure 3.29 shows the V-I curve predicted by the computer model when a body cooling term of the form shown in Figure 3.27 is added to the thermal and current model. The model curve follows the measured curve very closely predicting a quench current of 101A which is an error of just 1% on the original data. This is a very good fit especially considering that the error on each data point in the calculated cooling curve is $\pm 40\%$. This model also is very successful at predicting the temperature rise of the sample with time as well. The calculated curve and the model's prediction are both plotted in Figure 3.30. The calculated data for times below 52s are manually set to be 4.2K for clarity as the noise on the signal is larger than the signal which is being measured. The reduction in the error on the calculated values as the temperature increases is clearly visible as the spread of the data points greatly reduces as the time and hence temperature increases. The difference in the final temperature and the time taken to quench between the model and experiment are both <1% (reduced from ~10% before the cooling curves were modified).

Although the model was very successful in reproducing the E-I curve for one specific run, each run of the impregnated sample is slightly different. This is probably due to the fact that the exact form of each run will be governed by the starting state of the sample and the samples surroundings. If the sample was left for slightly longer for one run (this could easily have happened as the time between runs was manually timed and the first run at each field level occurred after the magnet had been ramped which takes ~10mins) then there would be a slightly larger store of 'coldness' to aid the

cooling of the sample. Therefore it is impossible to create a model which will accurately predict the behaviour of the sample for every run.

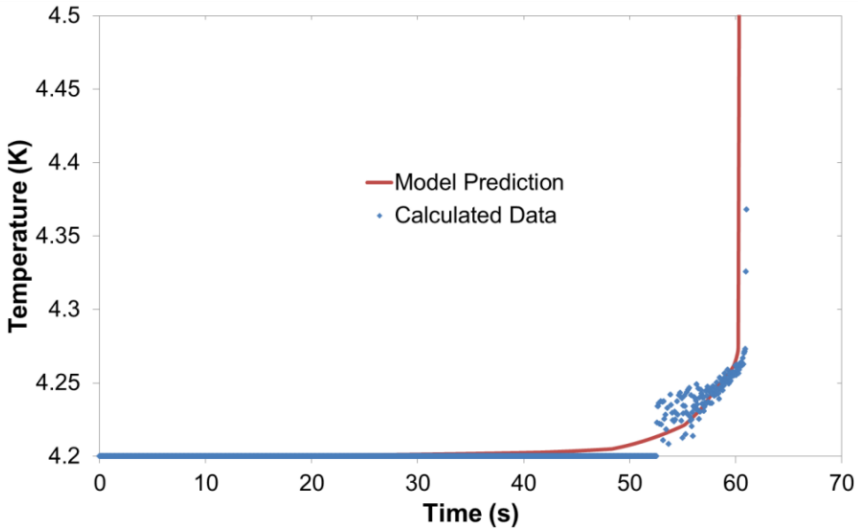

Figure 3.30. Calculated and predicted temperature as a function of time during a critical current measurement run at 9.5T for the wire EAS T108.

Once the proof of principle of the model had been demonstrated using the specific cooling curve already presented the cooling curve for each applied magnetic field level was calculated. These curves were then used to generate averaged E-I curves for all the field levels 9T-10T which are shown in Figure 3.32. It was not possible to calculate a cooling curve for 8.5T runs as the small measured voltages made it impossible to extract meaningful information from the data so the curve extracted from the 9T data was used. The generated curves were then adapted slightly via trial and error to improve the fit of the predicted curve to the measured data although no data point on the curve was varied by more than 10% from the calculated curves. This extra modification was done as the generated curves are subject to large errors due to the noise on the data and the uncertainties on the actual critical field at absolute zero. The predicted curves generated by the model using these empirical cooling curves are shown in Figure 3.31 along with the calculated data. Figure 3.32 and Figure 3.33 show the predicted and measured voltages and temperatures of the sample at each field level. These plots show that by using the empirically derived cooling curves the model can reproduce the basic thermal and current interaction within the superconductor to a very high accuracy.

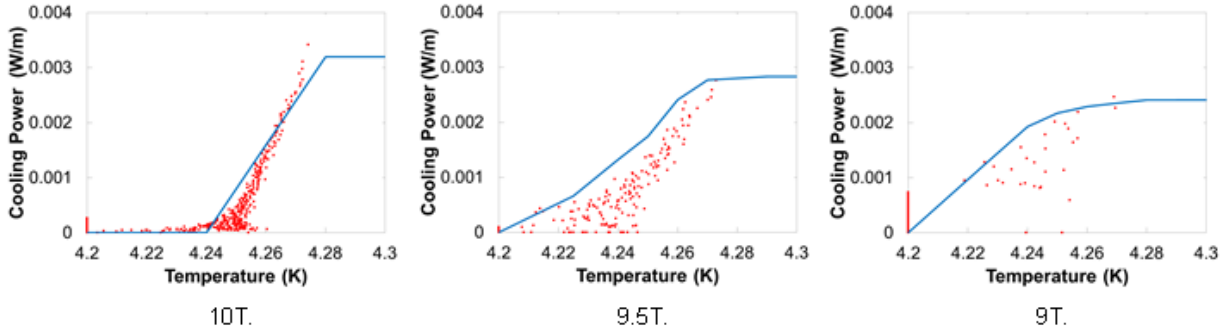

Figure 3.31. *Calculated cooling curves (red data points) and the adjusted curves (blue curves) used for each field level in the model.*

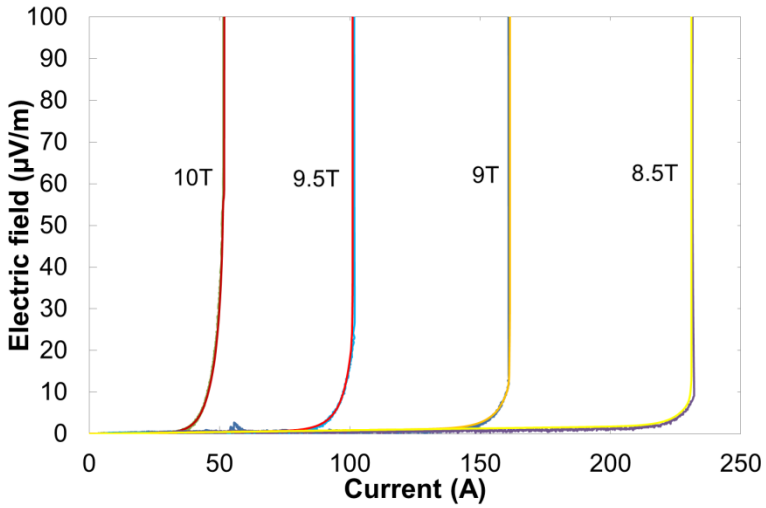

Figure 3.32. *Measured and predicted E-I curves for EAS T108 impregnated in Stycast.*

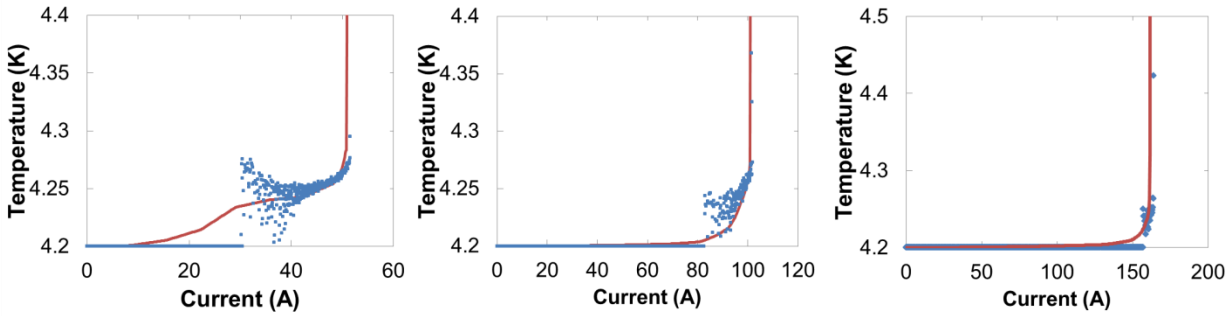

Figure 3.33. *Variation of temperature of the sample with time calculated from measured data (blue data points) and from the model (red curve) for each field level.*

3.3.4.6 Full 2-D Thermal and Current Model of the MQE Experiment

In the last section the model was shown to be able to accurately reproduce the behaviour of the sample during current sweeps up to the critical current. The final step in validating this model is to ascertain whether it can reproduce the MQE measurements as accurately. To this end the geometry of the model was created to be identical to that used in section 3.3.3.1 for the purely thermal model and the same trial and error algorithm was used to calculate the MQE values. Despite the success of the model to this point obtaining solutions to point-like thermal perturbation proved to be difficult. The difficulties

arose from the fact that the heating effect causes high thermal gradients which cause the superconducting properties to vary rapidly over short distances. As the properties can change so rapidly, if the model's mesh is too coarse, the properties could change markedly over a single mesh element. The result of this is that the simple polynomials used by the computer model cannot approximate the result accurately which leads to small fluctuations in the solution of a time step. As these small fluctuations are then used as the starting point for the next time step they have a tendency to increase in size with every iteration. This causes the model solution to diverge from the true solution until a singularity is reached and the model cannot continue. The solution for the results at 9.5T and 10T was to refine the mesh until the model would solve. However, as this problem is compounded by increasing the index of transition or the magnitude of the current, no solution to the problem at 9T could be found which would have generated the entire MQE curve in a reasonable time with the computing power which was available.

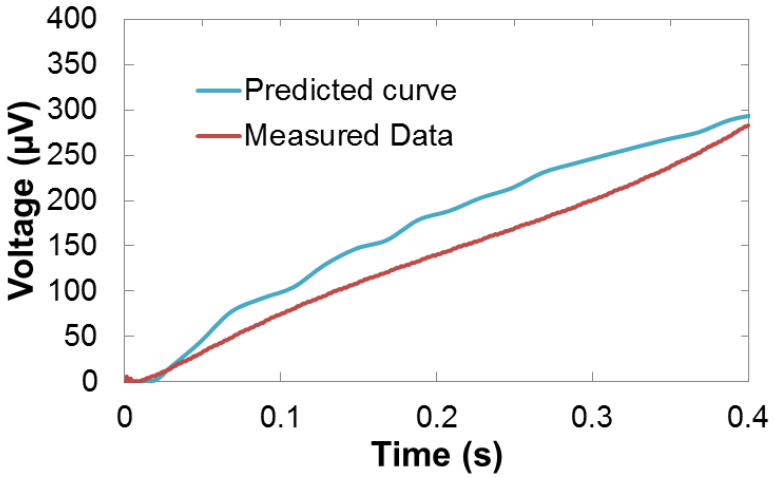

Figure 3.34. *The measured and predicted voltage after an initiated quench at 9.5T and 40A sample current.*

Figure 3.34 shows a plot of the measured and predicted voltage rise as the sample quenches at 9.5T while carrying 40A and Figure 3.35 shows the predicted curves for the MQE at 10T and 9.5T along with all measured data. Figure 3.36 shows that data once it had been fitted to the measured data by dividing the predicted values by 1.55. Figure 3.35 shows that the predictions from this model are, in general, quite accurate and are much more accurate than the purely thermal model earlier. The unfitted data is of the order of 50% too large which, although it is disappointing that the much improved model still has a relatively large error, this is a large improvement on the thermal model which was a factor of 10 too small. Furthermore it is clear that the accuracy of the underlying assumptions has been greatly improved by adding the current distribution model. Furthermore, after scaling, the model

correctly predicts the correct dependence of the MQE on applied field for the 9.5T and 10T plots. The model also gives very detailed predictions for what may be occurring within the wire during a quench. Figures 3.37, 3.38 and 3.39 which show how the current distribution parallel and transverse to the wire and the temperature of the wire are predicted to evolve in the 180ms after the thermal perturbation.

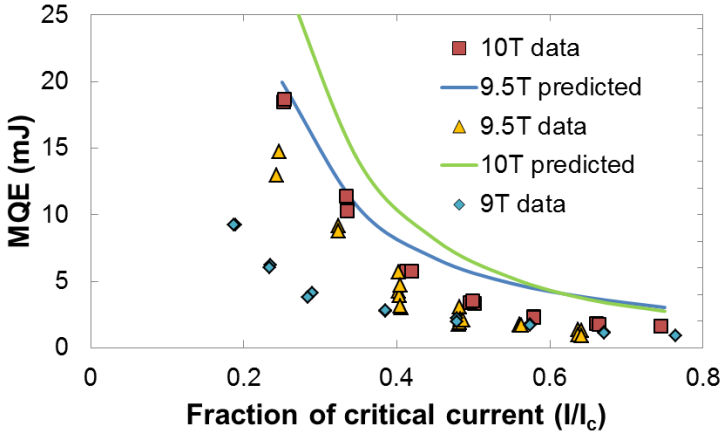

Figure 3.35. The measured data and the curves predicted using the 2D thermal, current model for the MQE at 9.5T and 10T and the data at 9T.

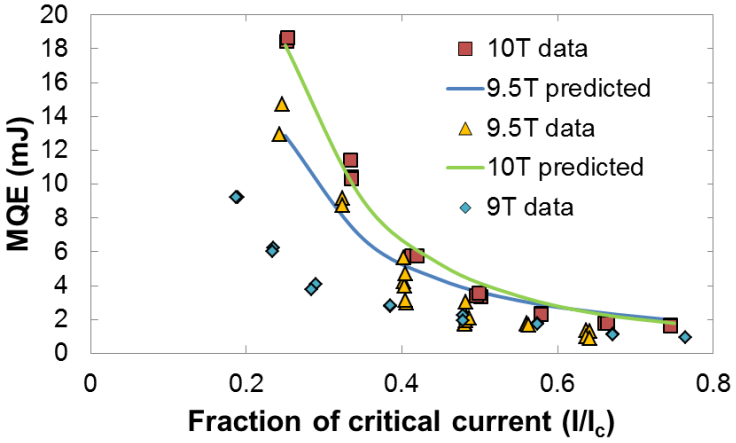

Figure 3.36. The measured data and the curves predicted using the 2D thermal, current model for the MQE at 9.5T and 10T and the data at 9T after all predicted results were divided by 1.55.

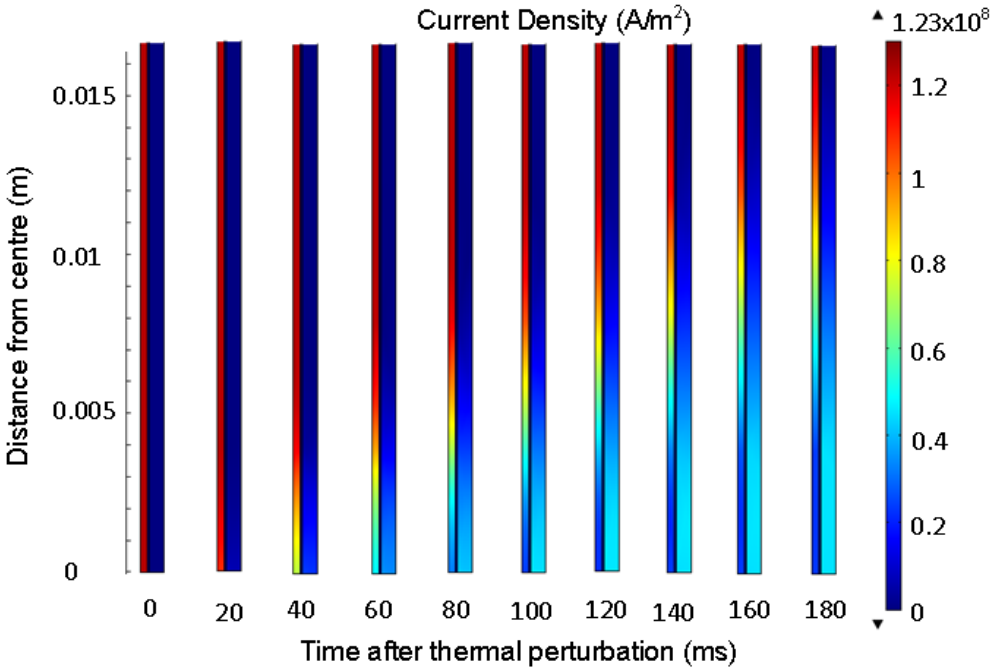

Figure 3.37. Distribution for the current density along the wire (J_y) for the first 180ms after the thermal perturbation large enough to quench the entire wire for 65% of J_c at 9.5T in 20ms time intervals.

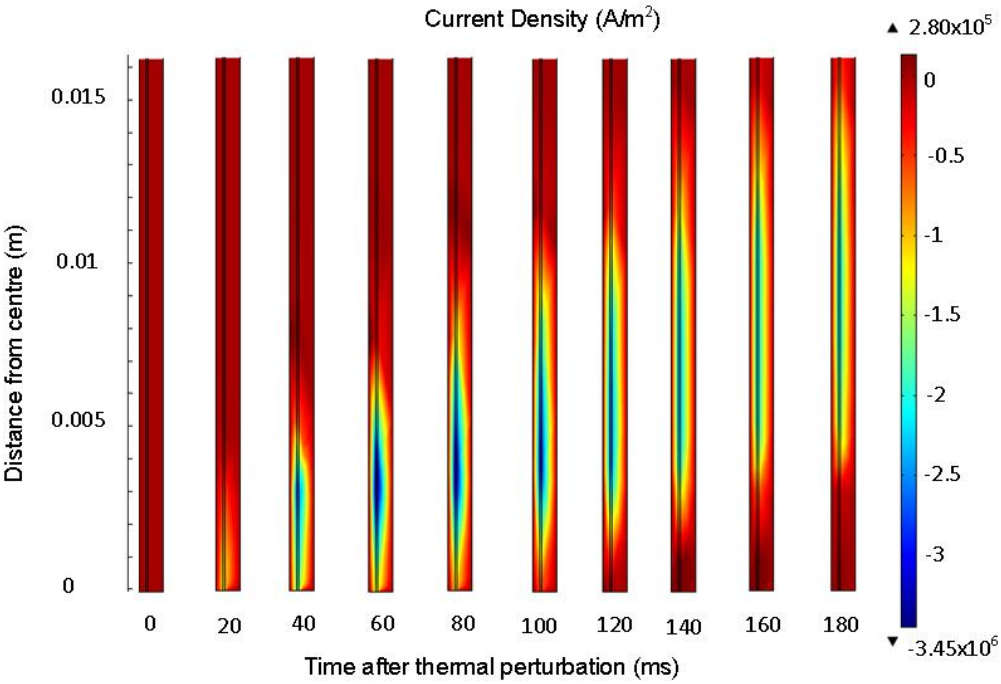

Figure 3.38. Distribution for the current density transverse to the wire (J_x) for the first 180ms after the thermal perturbation large enough to quench the entire wire for 65% of J_c at 9.5T in 20ms time intervals.

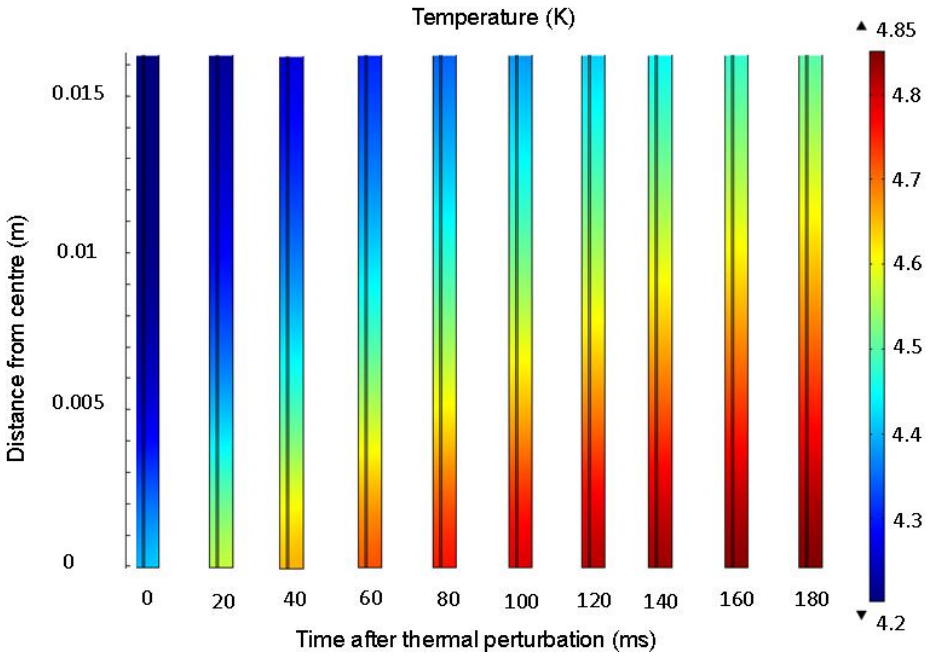

Figure 3.39. Distribution for the temperature of the wire for the first 180ms after the thermal perturbation large enough to quench the entire wire for 65% of J_c at 9.5T in 20ms time intervals.

The only region which lacks accuracy is the high current regime for the 9.5T curve where the predicted values are higher than the measured ones and are very slightly higher than the 10T values for currents over about 60% of the critical current. It is thought that the reason for this is due to the fact that, at those currents, the length of the minimum propagating zone is of the same order of magnitude as the heater length. The exact length of the predicted MPZ is difficult to measure as, as shown in the J_x plot in Figure 3.38, at the front of the normal zone the current transfers back into superconductor over a considerable length. This current transfer length is $\sim 0.8 - 1.0 cm$ long at 65% of the critical current at 9.5T and so it is difficult to know which part of this extended quench front to define as the edge of the quench zone. For now we shall use the arbitrary definition for the edge of the quench zone as being the point where the current drops to the mid-point between the unquenched current density and the quenched current density. Using this definition the MPZ is $\sim 1.2 cm$ long (see section 3.3.4.8) and so, the length of the $2mm$ heater is no longer much smaller than the MPZ. This will be compounded by the fact that, in the model, the copper sheath and the solder layer is between the heater and the superconductor and so these layers will 'smear' the thermal perturbation, increasing the length of superconductor which is heated efficiently by a short heater.

As the length of heated wire will be of a similar length (or indeed even longer) to the MPZ, the dependence of the MQE on the length of the MPZ is weakened and the critical temperature becomes a

more important factor. As the critical temperature is higher for lower fields this forces up the predicted MQE at high currents to be higher at 9.5T than at 10T. Although this cross-over effect wasn't observed in the 9.5T-10T data it is possible that it occurred at about 55% of critical current for the 9T-9.5T. If this is a real effect then it is possible that it would have been observed at a current level higher than could be achieved with the experimental setup. The incorrect prediction for the 9.5T-10T cross-over could be caused by a number of factors including:

- The model geometry and assumptions being too simplistic for example the effect of the heater being outside the sheath, increasing the length of heated superconductor, the temperature independence of i or the geometric assumptions (refinements to these are discussed briefly in section 3.3.4.10).
- Inaccurate material data giving rise to an MPZ which is too short.
- The cracked insulation observed in the experimental setup (as discussed in section 3.3.4.5) changing the cooling conditions for different fields. It is also not clear when the crack occurred and whether it expanded or contracted for different magnetic field intensities and currents. The wire itself would try to expand in the hoop direction due to the magnetic pressure/force.

It is clear that, despite the difficulties of obtaining a solution at 9T and predicting the location of possible curve cross-overs, the model has reached a state where it is able to accurately reproduce a wide variety of complicated superconducting behaviour. The model is also capable of giving a detailed picture of what may be occurring within a wire as it quenches or recovers from a quench.

3.3.4.7 Predicted Effect of Copper Ratio on Wire Stability

As the model has been successfully validated it can be used to make some predictions about the effects of the quantity of copper present in the wire's architecture. The wire's composition was varied in three different ways:

- The amount of copper in the sheath was varied.
- The amount of copper in the insert was varied keeping the amount of NbTi constant.
- The amount of copper in the insert was varied whilst also varying the amount of NbTi so that the insert area remained constant.

The quantity of copper in the sheath was varied from the original amount to no sheath at all. To do this the width of the sheath domain was varied whilst keeping the dimensions of the insert and solder domains constant. The modified geometry was then input into the same trial and error code as used in previous sections to find the MQE values. Figure 3.40 shows curves for how the MQE is predicted to vary with the amount of copper in the sheath at 25% and 65% of the critical current at 9.5T and 10T. The graph does not show the absolute MQE but the reduced MQE normalized against the MQE of the original wire geometry. It shows that, as one might expect, the MQE drops fairly linear with copper fraction, tending to a non-zero remnant MQE typically 10-20% of the original corresponding to the inserts contribution to the wire's stability. It also shows that the MQE at higher currents tends to be less strongly dependant on the amount of copper in the sheath. This is likely due to the fact that, as heat can flow from the hotspot in any direction, the MPZ is not a one dimensional region but a three dimensional one and the higher the current the smaller the size of the MPZ perpendicular to the current. It is possible then that at high currents the size of the transverse MPZ is smaller than the width of the wire and so reducing the size of the wire will have less effect than if the transverse MPZ size was larger than the wire.

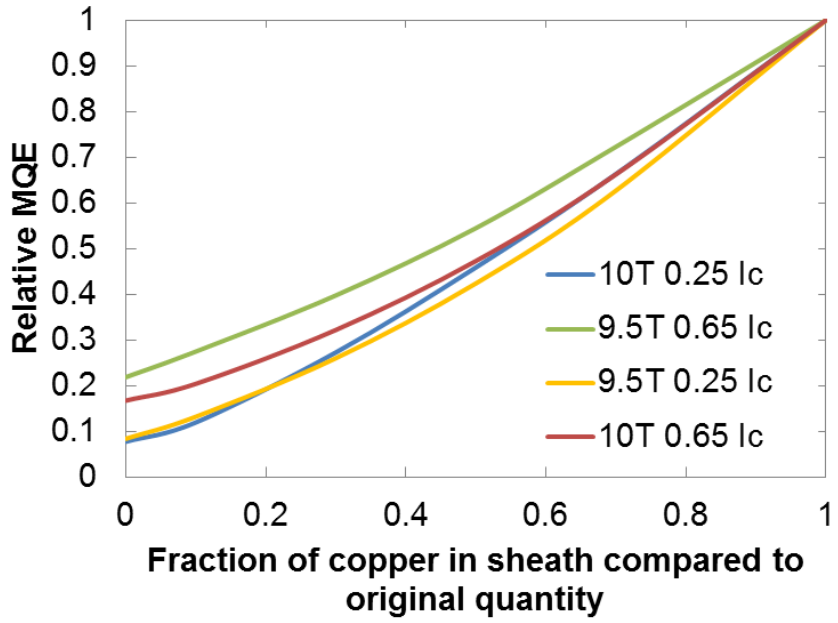

Figure 3.40. The predicted variation of the MQE as a function of the quantity of copper in the sheath at 25% *and* 65% *of* I_c *at 9.5T and 10T.*

To vary the amount of copper on the insert the model had to be varied in two different ways. The first was to change the width of the insert while maintaining the value of the critical current. This was the equivalent of maintaining the amount of NbTi in the wire whilst varying the copper content. The

second method was to keep the width of the insert constant whilst varying the critical current (equivalent to replacing any copper that is removed with extra NbTi). The remaining material properties such as heat capacity, density and thermal conductivity were then all calculated using the fractions method set out in section 3.3.2. The results from these two scenarios are shown in Figure 3.41 where the curves are calculated at 25% and 65% of the original critical current at 9.5T. It is worth noting at this stage that predictions for a copper fraction of less than 0.33 of the original amount for the constant NbTi scenario and 0.5 for the variable NbTi one are not valid and are only included for academic interest. The reason they are not valid is that these values correspond to an NbTi fraction of 0.75 and as the NbTi bundles are cylindrical 0.75 is about the largest fraction attainable before the bundles would deform or merge together. This would then destroy the stability of the insert due to the adiabatic flux jump instability problem introduced in section 3.1.2. The results show that if the NbTi content is constant MQE is fairly tolerant to the amount of copper in the insert. This is likely to be due to the much larger quantity of copper in the sheath which will give the required conditions for stability. The results of the variable quantity of NbTi are more interesting as they show that the MQE could be significantly increased without changing the size of the wire by replacing some of the copper with NbTi. This replacement will significantly increase the critical current of the wire whilst only reducing the thermal and electrical conductivity by a small fraction. This effect is particularly pronounced in the higher current regime where increasing the NbTi fraction to 0.75 could increase the MQE by 25%. This effect offers a method for reducing the size and weight of the wires without sacrificing stability. For example at 9.5T and 65% of critical current replacing half of the copper with NbTi in the insert while simultaneously removing 20% of the copper from the sheath would lead to no net change in the MQE. This would however save $2.4 kg/km$ from the weight of the wire. If we assume that the cost of NbTi is similar to that of copper and the estimate of $45 km$ of wire per MRI scanner this could save Siemens up to £1,400,000 per year.

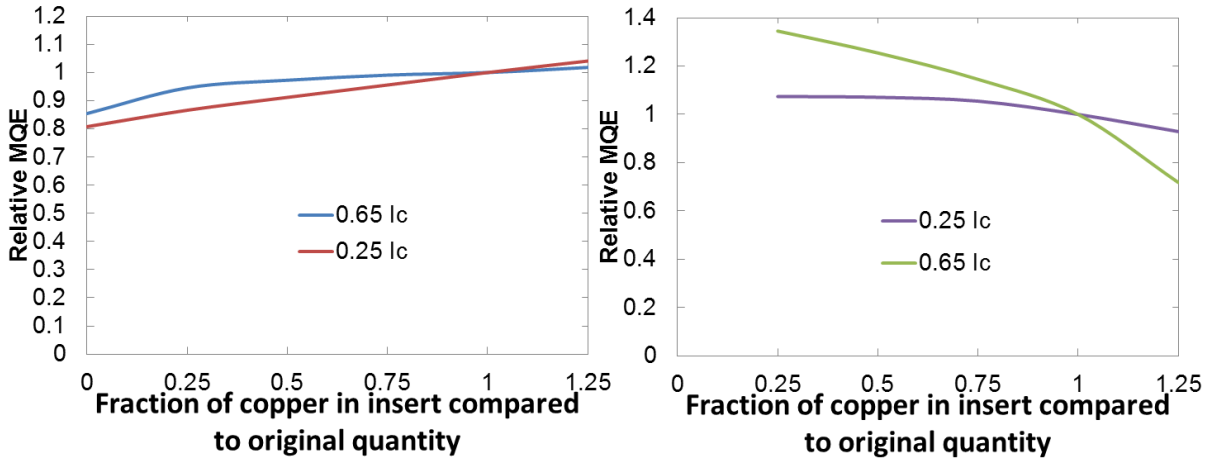

Figure 3.41. The predicted variation of the MQE as a function of the quantity of copper in the insert at 25% and 65% of I_c at 9.5T with a constant quantity of NbTi (left) and a variable quantity of NbTi to maintain a constant insert area (right).

3.3.4.8 Improved wire resistivity function

As mentioned in section 3.3.4.3 the resistivity function used for the superconducting insert was not as accurate as it could have been. A more accurate method for defining the resistivity of the insert is found by considering the current density that will flow through superconducting and copper elements of the insert when an electric field, E, is applied. The current through the superconductor is:

$$J_{sc} = J_c \cdot \left(\frac{E}{E_0}\right)^{\frac{1}{\bar{\imath}}} \qquad 3.83.$$

and through the copper:

$$J_{cop} = \frac{E}{\rho_{cop}} \qquad 3.84.$$

Therefore the total current density, J, is then:

$$J = J_{sc} + J_{cop} = J_c \cdot \left(\frac{E}{E_0}\right)^{\frac{1}{\bar{\imath}}} + \frac{E}{\rho_{cop}} \qquad 3.85.$$

Figure 3.42 shows a graph for how the electric field will vary with current in the insert if the temperature was fixed constant. Also plotted are the traces for a pure superconducting and pure copper region calculated from equation 3.2 and Ohm's law respectively. It shows that in the low current region when $J \leq J_c$ the resistivity of the copper is much higher than the resistivity of the superconductor. Therefore the bulk of the current will be carried by the superconductor and its resistivity will dominate the properties of the wire. When the current passes the critical current the electric field starts to rise nearly linearly with the same gradient which would be expected from a pure copper region where the intercept has been shifted by $\sim J_c$. This is because as the current approaches

the critical value the superconductor becomes saturated and further current carried by the superconductor would cause its resistivity to increase rapidly. Therefore beyond this point it is favourable for the extra current to be carried by the copper region while the superconductor still carries its critical current with the associated lack of dissipation.

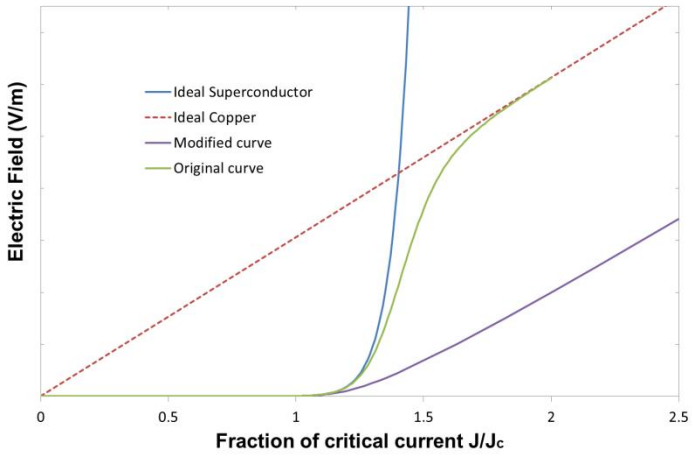

Figure 3.42. *E-J curves for an ideal pure superconductor, copper and the improved electric field curve.*

The effective resistivity function, ρ_{eff}, can be calculated simply using:

$$\rho_{eff} = \frac{E}{J} = \frac{E}{J_{sc} + J_{cop}} = \frac{E}{J_c \cdot \left(\frac{E}{E_0}\right)^{\frac{1}{l}} + \frac{E}{\rho_{cop}}} \qquad 3.86.$$

and is shown in Figure 3.43 along with the resistivity of pure copper and of a pure superconductor. This shows that as the current increases the resistivity tends asymptotically to the copper resistivity without ever reaching it.

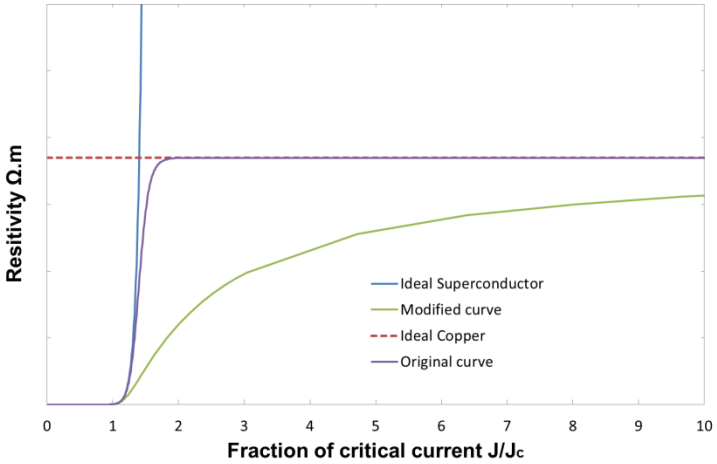

Figure 3.43. *Resistivity as a function of current for an ideal pure superconductor, copper and the improved resistivity curve.*

When the modified curves are compared to the original curves, which are also shown in Figure 3.42 and Figure 3.43 for clarity, the inaccuracy of the original derivation becomes apparent. The original curves give an electric field and resistivity of the insert as being considerably too high which would increase the electrical dissipation predicted. The magnitude of this inaccuracy is reduced when the sheath is also considered. This is because if the insert resistivity is too high it will shunt more current to the low resistivity sheath reducing the dissipation closer to the more accurate level. Figure 3.44 shows the effect of the modification on the current sharing between the insert and the sheath with the data from Figure 3.23 also plotted for ease of comparison. It shows that the original function caused more current to be transferred to the sheath once the critical current had been passed. It does, however, also show that the original and modified functions are almost identical below J_c and become increasingly similar at extremely high multiples of J_c. Therefore this modification will have no effect for regions of the model where the current density is below J_c or where the temperature is greater than T_c (where J/J_c is effectively infinite). It will also have a limited effect as the temperature nears T_c where J_c has been severely reduced.

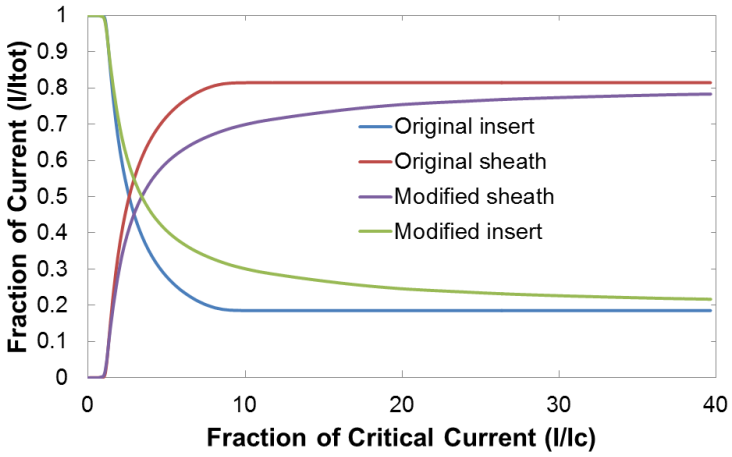

Figure 3.44. Current sharing between the insert and the sheath for a perfectly cooled wire using the original and modified resistivity functions.

To test how the more accurate resistivity function affects the predicted MQE the curves shown in Figure 3.35 were recalculated. The resistivity function for each applied magnetic field was calculated and input into the model as an interpolation function. The model then used equation 3.73 to calculate the dimensionless parameter, θ, at all points in the wire so the value for the resistivity within each element could be calculated from the interpolation function. The results calculated using the modified resistivity, along with the original results, are shown in Figure 3.45. This shows that, as one might expect, as the modified function reduces the resistivity of the insert it will reduce dissipation within

the wire and hence increase the predicted MQE. Although there was an error in the original function difference between the original and modified values is small and is less than 10% of the final calculated values. Therefore, as there is a small error caused by the original resistivity function, any future models should include the improved resistivity function to ensure the maximum possible accuracy.

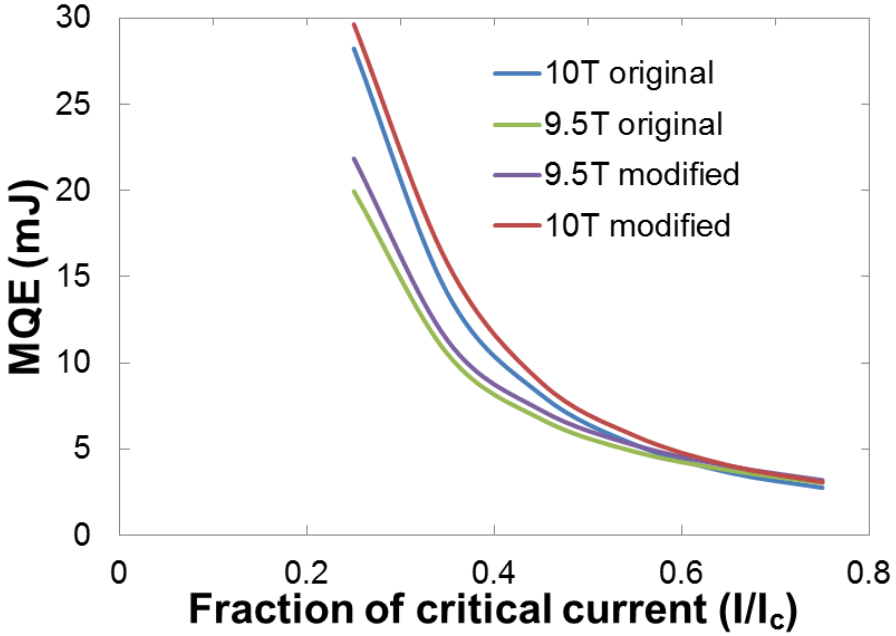

Figure 3.45. The MQE values predicted at 9.5T and 10T using the original and modified resistivity functions.

3.3.4.9 Other Possible Model Uses and Predictions

Along with making predictions about how the amount of copper in the wire may affect its stability the model can predict and model other properties of superconducting wires. Perhaps the most obvious properties are the length of the MPZ and the quench velocity of any superconducting wire. Along with the MPZ we can use the model to calculate estimates of a new parameter which we will call the minimum propagating voltage or MPV. The MPV is the voltage caused by a normal zone the length of the MPZ at a given current. This could be a useful parameter for magnet designers worrying about quench protection [1] as it would give a definite voltage level which could indicate a quenching magnet. Voltages less than the MPV could be caused by hotspots which may recover of their own accord whereas if the voltage exceeds the MPV the magnet is quenching and active quench protection may need to be engaged (although a complication is that multiple hotpots could cause a voltage above the MPV without the magnet quenching). Figure 3.46 shows the predicted MPZ, MPV and quench propagation velocity at 9.5T for the wire tested. The model also makes predictions about how the

quench will propagate along the wire. Also shown in Figure 3.46 is a plot showing the distribution of heat dissipated by the current in the wire at the front of a quench propagating towards the top of the page. From this it is clear that the quench is led by a band of high dissipation in the superconductor before the current transfers into the copper greatly reducing the dissipation within the insert.

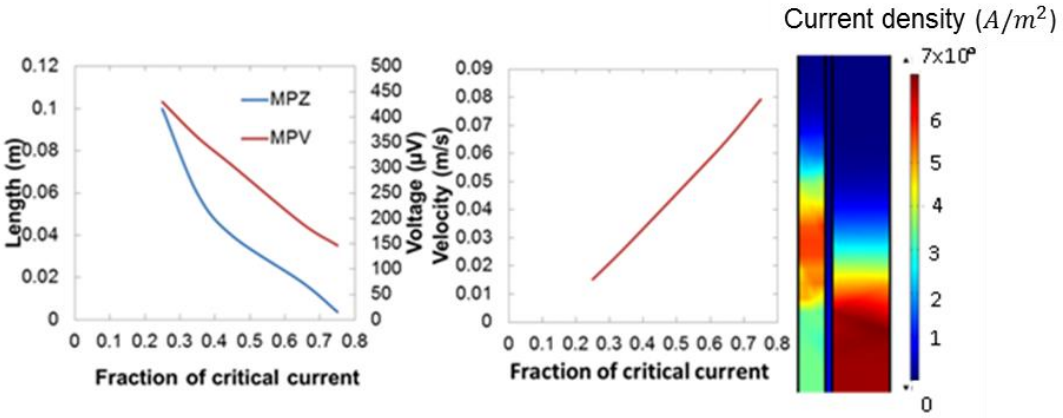

Figure 3.46. Predictions for other quench properties for the wire at 9.5T: Left: MPZ and MPV (minimum propagating voltage). Centre: Quench velocity. Right: Heat dissipation within the wire at the front of a propagation quench.

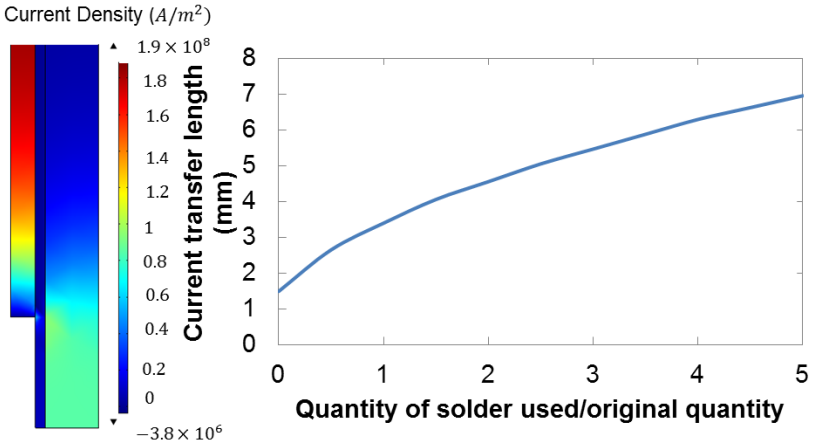

Figure 3.47. Predicted current distribution for current penetrating insert along with the predicted current transfer length as a function of the thickness of the solder layer between the copper sheath and the insert.

As well as a providing predictions of how a quenching wire will behave the model can also be used for analysing other scenarios related to superconducting wires such as how the current will behave as it flows through a section of damaged or degraded wire, or a section with a reduced critical current. An example of this is shown in Figure 3.47 which shows the results of a brief investigation into the current transfer length for a wire with a variable thickness solder layer between the insert and the sheath. For this 2mm of the insert domain was removed from the model but the geometries of the insert and the sheath were otherwise left unchanged. The thickness of the solder layer between them

was then varied between no solder used to a layer 5 times thicker than the original. The current transfer length was predicted to be of the order of 3-4mm long in a well cooled wire.

3.3.4.10 Further Possible Model Improvements

Within the final model used to investigate the thermal stability of the wire there are several simplifications which could be removed to further increase the accuracy of the model. The first is that the index of transition, i, is independent of temperature. This is likely to be a false approximation as i gives an indication of the strength of the flux pinning in the superconductor, the higher i is the stronger the flux pinning. Since flux pinning weakens as the temperature is increased it is likely that i will decrease, tending to 1 as the temperature reaches the critical temperature. Including this effect within the model would be relatively straight forward as the i ratio is already input as a constant function so changing it to a function of temperature would be simple. However there is very little data available in the literature discussing this subject and so a detailed experiment would need to be conducted to measure the exact dependence of i on T to maximize the accuracy of the model.

The next assumption was presented in section 3.3.4.3 where the equations governing the current distribution model were set out. The Maxwell-Faraday equation:

$$\nabla \times \mathbf{E} = -\frac{d\boldsymbol{B}}{dt} \tag{3.87.}$$

was approximated using the assumption that the magnetic field changed slowly with time and so could the right hand side of the equation could be set to zero. In reality this term is non-zero and will lead to magnetic diffusion effects within the wire and so the governing equation for the longitudinal model (equation 3.48) should be refined to:

$$\mu_0 \frac{d\boldsymbol{H}}{dt} + \nabla \cdot \begin{pmatrix} E_y \\ -E_x \end{pmatrix} = 0 \tag{3.88.}$$

To illustrate the effect that magnetic diffusion may have on a model of superconducting wire a model was built to look at the A.C. loss inside three superconducting wires with different filament arrangements. The magnetic diffusion model was altered so that the current was perpendicular to the plane of the 2D model. The required governing equation for this orientation is:

$$\begin{bmatrix}\mu_0 & 0\\ 0 & \mu_0\end{bmatrix}\begin{bmatrix}\frac{dH_x}{dt}\\ \frac{dH_y}{dt}\end{bmatrix}+\nabla\cdot\begin{bmatrix}0 & E_z\\ E_z & 0\end{bmatrix}=0 \qquad 3.89.$$

where H_x and H_y are the in-plane components of the field and E_z is the out of plane electric field component. The current can be introduced by imposing:

$$|\boldsymbol{H}|=\frac{I}{2\pi|r|} \qquad 3.90.$$

on the model's exterior boundaries where $|r|$ is the distance from a point of the boundary to the centre of the current distribution. This was used to model the current and temperature distribution as the current was increased from zero to 80% of the critical current for three different wire configurations: a typical 54 filament wire in channel wire, a typical 35 filament wire in channel wire and a hypothetical 54 filament monolithic wire. All wires had the same cross-sectional area of copper and NbTi and the same superconducting properties ($I_c = 1000A$, $B_{applied} = 1T$ and $i = 25$) and the outer boundary of each wire was held at 4.2K to model a well cooled wire section.

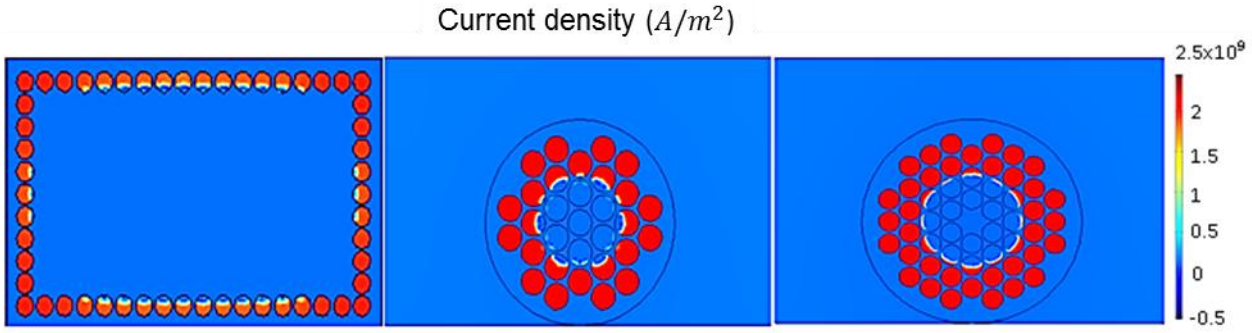

Figure 3.48. Current distributions during a current ramp in a 54 filament monolithic wire (left), a typical 35 filament wire in channel wire (centre) and a typical 54 filament wire in channel wire (right) Note that there are empty filaments in the centre of both wire in channel wires which may be hard to see on printed format.

Figure 3.48 shows the current distribution predicted across the surface of each geometry during the current sweep while Figure 3.49 shows the predicted AC loss per metre of wire and the maximum temperature reached within the wire during the sweep for sweep rates in the range $10 - 50A/s$. The model shows that the monolithic wire has less unused superconductor with a corresponding lower maximum current density and hence has a lower AC loss. Furthermore, as the filaments are close to the cooled surface the maximum temperature (which occurs at the centre of a filament) was much lower than the wire in channel geometries. Naively one might assume that this wire is the most stable

against external thermal perturbations however the, as the filaments are very close to the surface, an external heat source may disturb the current more easily. Of the two wire in channel geometries the 54 filament one will be far more stable. First of all the AC loss is about 30% lower as the current is distributed more evenly resulting in less heat being dissipated into the wire. Secondly, as the filaments are thinner, heat is conducted away from their centres much more efficiently resulting in a maximum temperature which is around half that of the 35 filament geometry. For a well cooled wire with 35 filaments the current would need to be swept at half the rate of a 54 filament wire to achieve the same maximum temperature. If the wires were less well cooled this temperature difference would be even greater requiring a greater reduction in sweep rate to achieve the same maximum temperature.

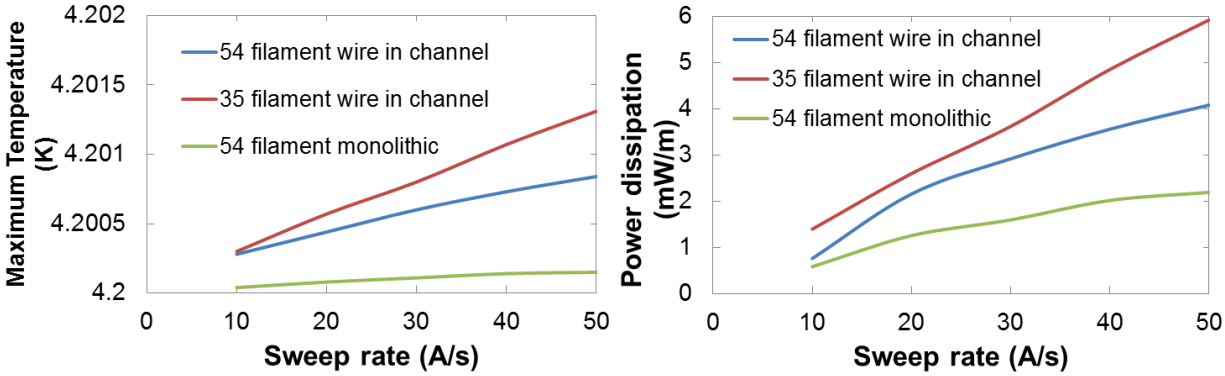

Figure 3.49. The maximum temperature within the wire and the maximum power dissipation per metre of wire for the three wire geometries as the current is swept up to 80% I_c with a variety of sweep rates.

The final major assumption is of course that the wire can be modelled as a 2D object when it has a complicated 3D shape. It would be fairly straight forward to combine the 2D magnetic diffusion cross-section model with the longitudinal model to form a full, detailed, 3D model of the wire. This would require a large amount of processing power and would take a long time to solve but could yield very detailed and useful predictions about the stability of very specific wire architectures.

3.4 Conclusion

In summary this chapter has presented a two-fold investigation into the thermal stability of technical superconductors used in MRI body scanners. An experimental investigation discovered that the current and applied magnetic fields strongly affect the amount of thermal energy required to quench the entire sample. At higher fields the critical current is suppressed and so the energy required to quench the sample for a given fraction of the critical current is increased. At a constant background field the lower the current the more energy is required. After the experiment had been conducted a

project was undertaken to develop a computer model which could accurately replicate the behaviour of the wire observed in the experiment. This model evolved through three generations (a purely thermal 1D model, a purely thermal 2D model and finally a 2D model which calculated both the electromagnetic and thermal properties) with each generation improving the accuracy and predictive power of the model. Improvements to the third generation model were also suggested such that a fourth generation model could be developed to hopefully increase the accuracy further. The final model generation model was used to predict the possible effect that the quantity of copper in the wire may have on the wire's stability and discovered that, dependant on the field that the wire was exposed to and fraction of critical current in the wire, it may be possible to increase the stability of the wire or reduce the weight/dimensions of the wire without affecting the stability. Finally the model was altered slightly to explore what effect that the cross-sectional geometry of the wire may have on the AC losses within the wire during current ramping.

The project was very successful in that, despite an inaccuracy in the resistivity function of the wire's insert, it has given Siemens Magnet Technology (UK) enough information to justify a new series of experiments based on the experimental section of this chapter. Furthermore the development of the models provided possible answers to at least three different problems/questions that the engineers at Siemens Magnet Technology had been unable to solve which were:

- Why some wires would quench more than others during magnet training.
- Why magnets wound with some wires would take longer to settle after current ramping than others.
- The shape of some unusual voltage traces taken during a magnet quench.

References

[1] M. Wilson, Superconducting Magnets, Oxford: Oxford University Press, 1983.

[2] M. Lakrimi, "Private Communication," *Siemens plc Eynsham, Witney, Oxon, OX29 4BP*.

[3] E. W. Collings, Applied superconductivity, metallurgy, and physics of titanium alloys: Vol 1, New York: Plenum Press, 1985.

[4] A. F. Clark and J. W. Ekin, "Defining critical currents," *IEEE Trans. Mag.*, vol. 13, no. 1, pp. 38-40, 1977.

[5] H. Jones and R. G. Jenkins, "Transport Critical Currents," *High-temperature Superconducting Materials Science and Engineering: New Concepts and Technology*, vol. Chapter 6, 1995.

[6] K. Tachikawa, K. Hoh, H. Wada, D. Gould, H. Jones, C. R. Walters, L. F. Goodrich, J. W. Ekin and S. L. Bray, "VAMAS Intercomparison of critical current measurements in Nb3Sn wires," *IEEE Trans. mag.*, vol. 25, no. 2, pp. 2368-2374, 1989.

[7] M. Tinkham, Introduction to superconductivity 2nd edition, New York: McGraw-Hill Book Co., 2004.

[8] M. N. Wilson and R. Wolf, "Calculation of minimum quench energies in Rutherford cables," *IEEE trans. ap. sup.*, vol. 7, no. 2, pp. 950-953, 1997.

[9] "Market data - Commodity Prices," BBC, 2011. [Online]. Available: http://www.bbc.co.uk. [Accessed 2011].

[10] K. Yamada, M. Aoki and Y. Matsui, "Measurement of minimum quench energy in a superconducting winding using a YAG laser," *Cryogenics*, vol. 48, no. 11-12, pp. 518-520, 2008.

[11] G. P. Willering, A. P. Verweij, C. Scheuerlein, A. den Ouden and H. H. J. ten Kate, "Difference in stability between edge and center in a rutherford cable," *IEEE trans. ap. super.*, vol. 18, no. 2, pp. 1253-1256, 2008.

[12] R. G. Mints, A. A. Akhmetov and A. Devred, “Enhanced quench propagation velocity,” *IEEE trans. ap. sup.,* vol. 3, no. 1, pp. 654-657, 1993.

[13] F. Sonnermann and R. Schmidt, “Quench simulations for superconducting elements in the LHC accelerator,” *Cryogenics,* vol. 40, no. 8-10, pp. 519-529, 2000.

[14] W. Pi, Y. Wang, L. Chen and C. Li, “Numerical Study of Current Distribution and Stability of LTS/HTS Hybrid Superconductor,” *IEEE Trans Ap. Super.,* vol. 20, no. 3, pp. 2180-2183, 2010.

[15] G. Volpini, “Quench Propagation in 1-D and 2-D Models of High Current Superconductors,” *Proc. Comsol Conf. Milan,* 2009.

[16] M. S. Lubell, “Empirical scaling formulas for critical current and critical field for commercial NbTi,” *IEEE Trans. Mag.,* vol. 19, no. 3, pp. 754-757, 1983.

[17] A. Stenvall, A. Korpela, J. Lehtonen and R. Mikkonen, “Current transfer length revisited,” *Super. Sci. Tech.,* vol. 20, no. 1, pp. 92-99, 2007.

[18] D. T. Ryan, H. Jones, W. Timms and N. Killoran, “Critical current measurements in the pV/m regime,” *IEEE trans. app. sup.,* vol. 7, no. 2, pp. 1455-1458, 1997.

[19] K. Yoda and M. Morita, “Minimum quench energy measurement of NbTi wires using a small ceramic heater,” *IEEE Trans. Mag.,* vol. 27, no. 2, pp. 2159-2161, 1991.

[20] C. Schmidt, “Simple method to measure the thermal conductivity of technical superconductors, e.g., NbTi,” *Rev. Sci. Inst.,* vol. 50, no. 4, pp. 454-457, 1979.

[21] A. K. Ghosh and W. B. Sampson, “Miniumum quench energies of rutherford cables and single wires,” *IEEE trans. ap. super.,* vol. 7, no. 2, pp. 954-957, 1997.

[22] M. N. Wilson and Y. Iwasa, “Stability of superconductors against localized disturbances of limited magnitude,” *Cryogenics,* vol. 18, no. 1, pp. 17-25, 1978.

[23] F. Rondeaux, P. Bredy and J. M. Rey, “Thermal conductivity measurements of epoxy systems at low temperature.,” *Adv. Cryog. Eng.,* vol. 48, pp. 197-203, 2001.

[24] A. Salazar, “On thermal diffusivity,” *European Journal of Physics,* vol. 24, pp. 351-358, 2003.

[25] Comsol Multiphysics User's Guide version 4.2a, Cambridge: Comsol, 2011.

[26] L. L. J. Isaacs, “Low-Temperature Specific Heat of Gold, Silver, and Copper,” *J. Chem. Phys.,* vol. 43, pp. 307-308, 1965.

[27] V. J. Johnson, A Compendium ofProperties of materials at low temperature (phase 1), National Bureau of Standards, Pergamon Press, 1961.

[28] R. W. Shaw, D. E. Mapother and D. C. Hopkins, “Critical Fields of Superconducting Sn, In, and Ta,” *Phys Rev,* vol. 120, no. 1, pp. 88-91, 1960.

[29] G. Chanin and J. P. Torre, “Critical Field of Superconducting Lead,” *Phys. Rev. B,* vol. 5, no. 11, pp. 4357-4364, 1972.

[30] J. De Launay, R. L. Dolecek and R. T. Webber, “Magnetoresistance of Copper,” *J. Phys. Chem.,* vol. 11, no. Launay J. de, Dolecek R. L. Webber R. T., pp. 37-42, 1959.

[31] D. H. J. Goodall, Cryogenic Data Wall Data Chart, APT Division, Culham Science Centre, Abingdon. UK, 1970.

[32] A. Wiedemann and W. Franz, “Ueber die Warme-Leitungsfahrigkeit der Metalle,” *Ann. Phys. (Lepzig),* vol. 89, pp. 497-531, 1853.

[33] R. K. Fickett, “Properties of Non-Superconducting Technical Solids at Low Temperatures,” in *Proc. 4th Int. Conf. Mag. Tec.*, Ny, 1972.

[34] Stycast 2850FT Technical Data Sheet, Emerson and Cuming, 2001.

[35] C. A. Swenson, “Linear Thermal Expansivity (1.5–300 K) and heat capacity (1.2–90 K) of Stycast 2850FT,” *Rev. Sci. Instrum.,* vol. 68, no. 2, pp. 1312-1315, 1997.

[36] W. H. Keesom and B. Kurrelmeyer, “Specific Heats of Alloys of Nickel with Copper and with Iron from 1.2 to 20K,” *Physica VII,* vol. 10, pp. 1003-1024, 1940.

[37] J. C. Erdmann and J. A. Jahoda, “Thermal Conductivity of Copper-Nickel Alloys at 4.2K,” Boeing Scientific Research Laboratories, Seattle, Washington, 1964.

[38] Introduction to Comsol Multiphysics version 4, Cambridge: Comsol, 2010.

[39] L. Bottura, “A Practical Pit for the Critical SurEace of NbTi,” *IEEE Trans. App. Sup.,* vol. 10, no. 1, pp. 1054-1057, 2000.

[40] B. Colyer, “The Impregnation of Superconducting Windings with Epoxy Resins,” Rutherford Laboratory Report RHEL/R264, Didcot, 1972.

[41] T. C. Cetas, C. R. Tilford and C. A. Swenson, “Specific Heats of Cu, GaAs, GaSb, InAs and InSb from 1 to 30K,” *Phys. Rev,* vol. 174, no. 3, pp. 835-844, 1968.

[42] M. Dixon, F. E. Hoare, T. M. Holden and D. E. Moody, “The low temperature specific heats of some pure metals,” *Proc Roy. Soc. Lon. A Math. and Phys. Sci.,* vol. 285, no. 1403, pp. 561-580, 1965.

[43] C. A. Bryant and P. H. Keesom, “Low-temperature specific heat of indium and tin,” *Phys. Rev,* vol. 123, no. 2, pp. 491-499, 1961.

[44] R. Berman, B. L. Foster and H. M. Rosenberg, “The thermal conductivity of some technical materials at low temperatures,” *J. Appl. Phys.,* vol. 6, pp. 181-183, 1955.

[45] Y. Hariharan, M. P. Janawadkar and T. S. Radhakrishan, “Electrical and thermal conductivity of soft solder at low temperatures,” *Pramana,* vol. 13, no. 2, pp. 117-125, 1979.

[46] K. Seo, M. Morita, S. Nakamura, T. Yamanda and Y. Jizo, “Minimum quench energy measurement for superconducting wires,” *IEEE trans. mag.,* vol. 32, no. 4, pp. 3089-3093, 1996.

[47] C. Schmidt, “Stability tests on the euratom LCT conductor,” *Cryogenics,* vol. 24, no. 11, pp. 653-656, 1984.

4 High Field Pulsed Coil Design

4.1 Introduction

One of the primary goals of this thesis was to investigate the flux trapping properties of bulk high temperature superconductors. The details of flux trapping in the bulk superconductors are explained in detail in the next chapter along with the experimental details. However to complete these experiments a pulsed electromagnetic coil was required. This coil needed to have: as large a sample volume as possible; as long a pulse length; and should achieve as high a field as possible while fulfilling the previous two requirements. There is a history of producing high magnetic fields in the Clarendon and with the Nicholas Kurti Magnetic Field Laboratory (NKMFL) opening in 2002 [1] magnetic fields of up to 65T became available in pulsed electromagnets [2]. Therefore the basic facilities for such a flux trapping project existed within the department. However all of the coils produced to date within the NKMFL were monolithic solenoids with a central bore of 20mm or less. As the samples for the flux trapping experiments were cylinders with diameters of up to 32mm heights of 15mm they were far too large to fit into the bore of the existing coils. Furthermore the existing coils had a very short pulse length with a maximum pulse length of around ~12ms so would be too fast for the envisaged experiment even if the samples could be placed in the field centre. Thus it was decided that a new type of coil would be designed and constructed for the facility. It was decided that the new coil should be a high inductance and variable inductance split pair coil. This would give the long pulse lengths required while the split pair arrangement would allow samples of any size to be placed in the field centre.

4.2 NKMFL

4.2.1 Introduction

The core of the NKMFL is a large, high voltage capacitor bank. The bank itself is split into four roughly equal quarter banks each of which contains ten individual capacitors with a nominal capacitance of $8.16\mu F \pm 10\%$. This gives the operator the option of using a ¼, ½, ¾ or the full capacitor bank. The total bank has a capacitance of 31.93mF which is 2.2% less than the nominal capacitance [2]. As the capacitors have a maximum charge voltage of 7kV and the energy stored in a capacitor is given by:

$$E = \frac{1}{2}CV^2 \qquad 4.1.$$

The total energy available is around 0.8MJ. Figure 4.1 shows a simple circuit diagram of the NKMFL along with the other key components of the system which allow it to provide pulsed currents to an electromagnetic coil.

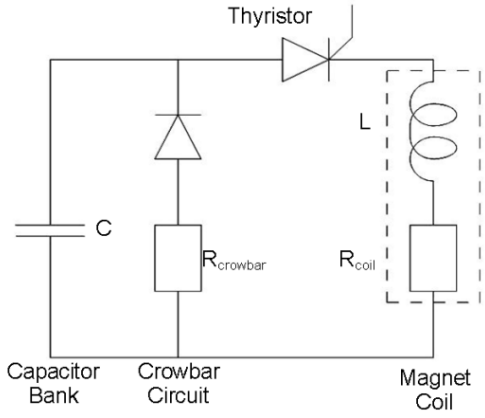

Figure 4.1. A simplified circuit diagram of the NKMFL capacitor bank and associated electronics.

The main components of the pulsed field system are:

- The capacitor bank whose purpose is to store a large amount of energy which can be released in a very short period of time, generating a high current which, in turn, generates high magnetic fields in the coil.
- The thyristor is a semiconductor device with a main through channel and an extra gate input which can act as a bistable switch. They are fully insulating when there is no gate current flowing but become conducting if a current is applied to the gate and will remain fully open until the current passing through it falls below a certain holding current.
- The crowbar circuit which is required as, like a lot of high voltage capacitors, the capacitor bank is uni-axial. This means that the capacitors can only be charged in one direction and if they are charged to too high a voltage in the wrong direction they can be damaged. Therefore the crowbar circuit, which is diode and a resistor in turn, is used to prevent negative voltages from arising on the capacitors. The crowbar resistor also serves a secondary purpose as the value of the resistance will vary the shape of the decay (or tail) portion of the magnetic pulse.
- The magnetic coil itself which is included on most circuit diagrams as an inductor and a resistor in parallel.

4.3 Theory of pulsed coils

4.3.1 Electromagnetics

It is important to know how magnetic fields are generated in a coil before setting about designing an electromagnet. The starting point for any electromagnetic derivation is Maxwell's equations:

$$\nabla \cdot \boldsymbol{E} = \frac{\rho}{\varepsilon_0} \tag{4.2.}$$

$$\nabla \cdot \boldsymbol{B} = 0 \tag{4.3.}$$

$$\nabla \times \boldsymbol{E} = -\frac{\partial \boldsymbol{B}}{\partial t} \tag{4.4.}$$

$$\nabla \times \boldsymbol{B} = \mu_0 \boldsymbol{J} + \mu_0 \varepsilon_0 \frac{\partial \boldsymbol{E}}{\partial t} \tag{4.5.}$$

The equation which is primarily of interest is equation 4.5 which is known as Ampere's law. Ampere's Law simply tells us that a current has an associated magnetic field and that the curl of the magnetic field gives the magnitude and direction of the current density. However before it can be truly useful we need to manipulate it into a form where it can be used to calculate the magnetic field for any given current distribution. For the following derivation the magnetic vector potential $\vec{\boldsymbol{A}}$ is a useful quantity which is defined as:

$$\boldsymbol{B} = \nabla \times \boldsymbol{A} \tag{4.6.}$$

By substituting equation 4.6 into equation 4.5 we can obtain to following:

$$\nabla \times (\nabla \times \boldsymbol{A}) = \nabla(\nabla \cdot \mathbf{A}) - \nabla^2 \mathbf{A} = \mu_0 \boldsymbol{J} + \mu_0 \varepsilon_0 \frac{\partial \boldsymbol{E}}{\partial t} \tag{4.7.}$$

To obtain a full time dependant formation of this equation which can be solved for the magnetic field we must substitute the definition for the magnetic vector potential into Faraday's law (equation 4.4) so we obtain:

$$\nabla \times \boldsymbol{E} = -\frac{\partial(\nabla \times \mathbf{A})}{\partial t}$$

$$\therefore \quad \nabla \times \left(\boldsymbol{E} + \frac{\partial \mathbf{A}}{\partial t} \right) = 0 \tag{4.8.}$$

If we recall the vector identity for a general scalar field, φ:

$$\nabla \times (\nabla \varphi) = 0 \tag{4.9.}$$

Therefore we can rewrite the expression in the parentheses in equation 4.8 by defining a new scalar field as:

$$-\nabla\varphi = \boldsymbol{E} + \frac{\partial \mathbf{A}}{\partial t} \tag{4.10.}$$

The generality of this equation can be shown by using the well-known equation of $\vec{\boldsymbol{J}} = \sigma\vec{\boldsymbol{E}}$. This allows us define the two components of the current in equation 4.10 as:

$$\boldsymbol{J} = \boldsymbol{J_s} + \boldsymbol{J_i} \tag{4.11.}$$

with

$$\boldsymbol{J_s} = -\sigma\nabla\varphi \tag{4.12.}$$

which is the current density applied externally from the plane of interest and:

$$\boldsymbol{J_i} = \sigma\frac{\partial \mathbf{A}}{\partial t} \tag{4.13.}$$

This is the induced current caused by a time varying magnetic field which is also known as eddy currents which will be important later in the chapter. We are now ready to return to Ampere's law and by substituting equation 4.10 into equation 4.5 we can obtain a general equation for the time evolution of the magnetic scalar potential:

$$\nabla \times \nabla \times \mathbf{A} = \mu_0\boldsymbol{J} - \mu_0\varepsilon_0\frac{\partial}{\partial t}\left[\frac{\partial \mathbf{A}}{\partial t} + \nabla\varphi\right]$$

$$\nabla^2\mathbf{A} = -\mu_0\boldsymbol{J} + \nabla(\nabla \cdot \mathbf{A}) + \mu_0\varepsilon_0\frac{\partial \nabla\varphi}{\partial t} + \mu_0\varepsilon_0\frac{\partial^2 \mathbf{A}}{\partial t^2} \tag{4.14.}$$

Equation 4.14 will be of use later in this chapter but for now we will make the stationary or quasi-stationary approximation. This approximation states that the magnetic field is either changing very slowly or is stationary and so any eddy currents are negligible compared to the applied external current density. In this approximation any $^{\partial}/_{\partial t}$ terms become negligible and we will also make use of the Coulomb gauge:

$$\nabla \cdot \mathbf{A} = 0 \tag{4.15.}$$

Therefore equation 4.14 becomes the much simplified:

$$\nabla^2\mathbf{A} = -\mu_0\boldsymbol{J} \tag{4.16.}$$

This is a form of a vectorial Poisson's equation and can be written in unbounded space by Poisson's integral formula with the result [3]:

$$\boldsymbol{B} = \int \frac{\mu_0}{4\pi} \frac{I d\boldsymbol{\ell} \times \boldsymbol{r}}{|r|^3} \qquad 4.17.$$

Where I is the current, $d\boldsymbol{\ell}$ is a unit element in the direction of the current flow and $\boldsymbol{r}$ is the displacement vector or the vector which describes the position of interest with respect to the current. This formula is the famous Biot-Savart law for calculating magnetic fields from current distributions from which we can now start to calculate the magnetic field of magnetic coils.

The simplest coil is a single turn of radius R carrying a current I. We can define the axis of this coil as being parallel to the z-axis so if we want to calculate the on-axis magnetic field for this coil we can ignore the B_x and B_y components of the field as, by symmetry, these field components will be zero. Figure 4.2 shows the geometry and the relevant vectors and quantities needed to solve the on-axis problem. From the figure it is clear that for a position, z, the length of the vector r can be found simply by using Pythagoras:

$$|r| = \sqrt{R^2 + z^2} \qquad 4.18.$$

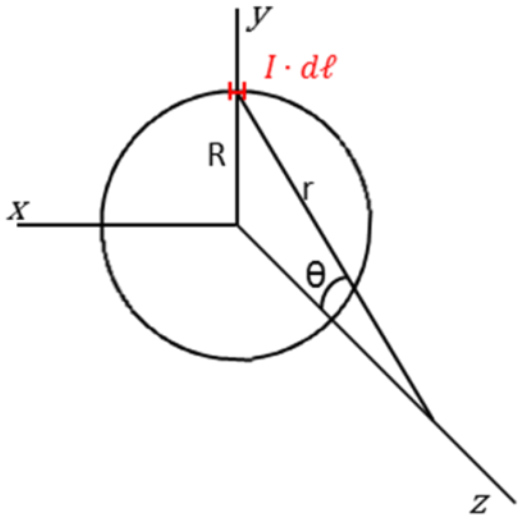

Figure 4.2. Coil geometry and relevant vector quantities for a single turn coil.

This, along with the cross-product of the vectors within the integral of equation 4.17 gives the formula to be integrated:

$$B = \frac{\mu_0 I}{4\pi} \int \frac{R \cdot d\ell}{(R^2 + z^2)^{\frac{3}{2}}} \qquad 4.19.$$

The integral of $d\ell$ simply gives the circumference of the circle and so the final equation for the current from a single turn is:

$$B = \frac{\mu_0 I}{2} \frac{R^2}{(R^2 + z^2)^{3/2}} \quad 4.20.$$

And the field at the centre of the coil where $z = 0$ is:

$$B = \frac{\mu_0 I}{2} \frac{1}{R} \quad 4.21.$$

Using the expression in equation 4.20 we can then start to calculate the fields generated by integrating over the volume of the windings. The simplest multi-turn coil is simply a thin solenoid with one layer of n turns and a length 2b. As we have more than one turn we now need to replace the current value I with a current density. For a thin coil this is defined by the current per unit length, J_L which can be calculated from:

$$J_L = \frac{nI}{2b} \quad 4.22.$$

For such a coil the field at the centre is simply:

$$B = \frac{\mu_0 J_L}{2} \int_{-b}^{b} \frac{R^2}{(R^2 + z^2)^{3/2}} dz \quad 4.23.$$

Which can be integrated using the substitution of $z = R \tan\theta$ to yield the solution:

$$B = \frac{\mu_0 J_L}{2} \left[\frac{z}{\sqrt{R^2 + z^2}} \right]_{-b}^{b} = \frac{\mu_0 J_L b}{\sqrt{R^2 + b^2}} \quad 4.24.$$

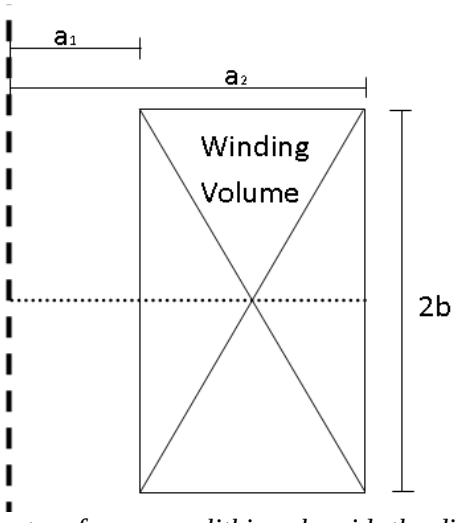

Figure 4.3. The key parameters for a monolithic solenoid; the diagram is drawn such that the dashed line represents the centre of the bore and so is the axis of symmetry.

The next step is to expand the integration so that we can integrate over the thickness of the coil as well as its length. Figure 4.3 shows a diagram of a simple monolithic coil with axial symmetry with the key

geometric properties of the coil marked where a_1 and a_2 are the inner and outer radii of the coil and b is half of its length. For such a coil equation 4.17 becomes:

$$B = \frac{\mu_0 J}{2} \int_{a_1}^{a_2} \int_{-b}^{b} \frac{r^2}{(r^2 + z^2)^{3/2}} dr\, dz \qquad 4.25.$$

with $$J = \frac{nI}{2b(a_2 - a_1)} \qquad 4.26.$$

In this formulation J is now the current per unit area rather than the current per unit length introduced earlier. Equation 4.25 can then be integrated to give [4]:

$$B = \mu_0 J b \ln \frac{\alpha + \sqrt{\alpha^2 + \beta^2}}{1 + \sqrt{1 + \beta^2}} \qquad 4.27.$$

where $$\alpha = \frac{a_2}{a_1} \; and \; \beta = \frac{b}{a_1}$$

As the final coil design is not going to be a simple monolithic solenoid but a split pair there is one more step to be undertaken before we have an analytical equation for calculating the field. For the next step we need to use the fact that magnetic fields are linear fields and can be combined by linear superposition. Thus if we have N coils each producing a magnetic field B_N at a defined point then the total field at that point is simply the sum of all the individual fields:

$$B = \sum_N B_N \qquad 4.28.$$

Thus this gives us two subtly different but entirely complementary methods for calculating the field at the centre of a split pair. The first is to use equation 4.25 but you calculate the field at a position displaced by the distance from the individual coil centre to the centre of the pair. To do this you can either substitute z in the integration or the value of the limits:

Adjusting z $$z \Rightarrow z' \pm \left(b_{gap} + b\right)$$

Or by adjusting the limits $$\pm b \Rightarrow \begin{cases} b_{gap} + 2b \\ b_{gap} \end{cases} \qquad 4.29.$$

Once you have calculated the field for one individual coil then the field of both coils is simply twice the answer.

The other method for calculating the field at the centre of such a coil pair is to first calculate the field at the centre of a monolithic coil with a_1 and a_2 the same as the split pair but with a total length

$L = 4b + 2b_{gap}$. This gives a field value which we will denote B_{long}. We then need to calculate the contribution to B_{long} from the added extra section of the coil which occupies the gap between the two real coils. This extra coil section is shown in Figure 4.4 as the red central coil and we will denote the field produced by this imaginary section as B_{short}. Then finally the total coil of the real pair is simply:

$$B = B_{long} - B_{short} \tag{4.30.}$$

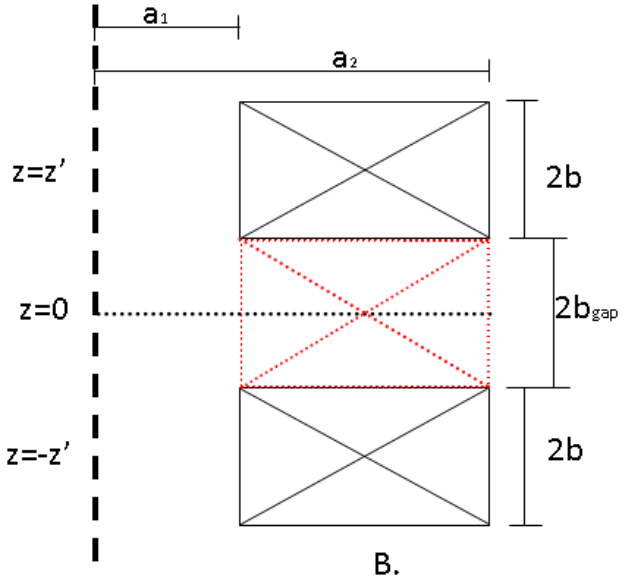

Figure 4.4. Coil cross-section for a split pair coil with axial symmetry around the vertical dashed line. The key coil parameters are shown along with the extra coil marked in red used for the second method of calculating fields from such a coil arrangement.

The full integration of these expressions is given in appendix D but both give the result:

$$B = \frac{\mu_0 J_L}{2}\left\{(2b + b_{gap})\ln\left(\frac{\alpha + \sqrt{{\beta_1}^2 + \alpha^2}}{1 + \sqrt{1 + {\beta_1}^2}}\right) - b_{gap}\ln\left(\frac{\alpha + \sqrt{{\beta_2}^2 + \alpha^2}}{1 + \sqrt{1 + {\beta_2}^2}}\right)\right\} \tag{4.31.}$$

where
$$\beta_1 = \frac{2b + b_{gap}}{a_1} \; and \; \beta_2 = \frac{b_{gap}}{a_1} \tag{4.32.}$$

It is very easy to show that this reduces to equation 4.27 for a coil with total length 4b for $b_{gap} = 0$ as expected as this would just be a normal monolithic solenoid. This rather fearsome looking expression gives some useful guides on how to design a split pulse coil. From inspection it is obvious that to maximise the field from a coil we must maximise the current density in the coil. It is also obvious that the gap size and the inner bore diameter should both be minimized to maximise the field for a fixed current density. The dependence of the field on the parameters a_2 and b is less obvious so a plot of B against α and β with an arbitrary fixed split gap, current density and a_1 is plotted in Figure 4.5.

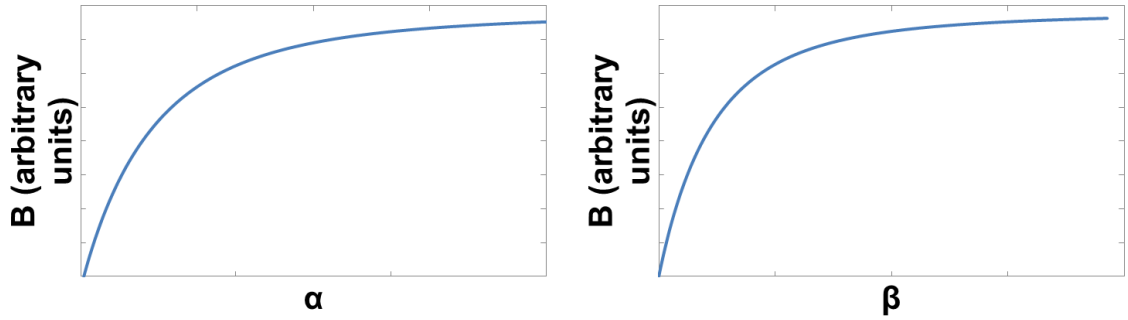

Figure 4.5. Variation of the central peak field of a split pair magnet on the coil parameters α and β for a fixed gap.

It is clear from Figure 4.5 that, for both α and β, the field achievable from a coil increases with the parameter up to a certain point and then the inevitable law of diminishing returns starts and there is little point in further increasing the size of the coil in that dimension. The physical meaning of this is that as you increase the coil size you add Ampere turns to the coil and hence increase the magnetic field but as the coil grows each successive turn moves further away from the centre and so adds less field. Therefore you eventually reach a state where each added turn does not add an appreciable amount to the field and, as we shall see later in this chapter, can actually reduce the maximum field from a pulsed coil.

Another useful value to calculate is the ratio between the field at the centre of one of the individual coils, B_{indiv}, to the field at the centre of the pair, B_{centre}. Although the field at the centre of one individual coil is not the true maximum field (that occurs just inside the winding closest to the bore) it does give a good estimate of the maximum field and is a much simpler quantity to calculate analytically. This ratio then tells us how 'efficiently' the field is being generated at the point where the samples will be placed. It is a useful quantity as, as we shall see in section 4.3.3, higher fields generate higher stresses in the coil and so increase the chances of a coil failure. Therefore to maximise the chances of achieving the highest possible field we want to minimise this ratio so that we do not end up with a coil which generates a very high field in the bore of the individual coils while producing no field in the sample space. The variation of this ratio as a function of α/β for a fixed gap is shown in Figure 4.6 and it is clear from this graph that this ratio is very high for a low α/β but very quickly tends to close to unity. This tells us that to minimise this ratio we need to create a coil which is short (small b) with a large outer diameter (large a_2 and hence α).

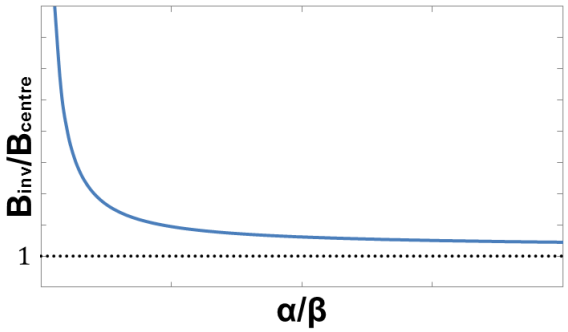

Figure 4.6. Variation of ratio of the field at the centre of one individual coil, B_{indiv}, to the field at the centre of the pair, B_{centre} as a function of α/β for a fixed gap.

The final important aspect to consider from an electromagnetic perspective is the inductance of the magnet. The inductance of a magnet gives a measure of how efficiently a coil will store magnetic energy from a current. To understand what an inductance is and where it comes from we must look at the definition for the total flux passing through a surface:

$$\Phi = \int \boldsymbol{B} \cdot d\boldsymbol{S} \tag{4.33.}$$

But we have seen from earlier equation such as the Biot-Savart law in equation 4.17 that, in the absence of ferrous materials, the total magnetic field is simply proportional to the current and an integral over the geometry of the coil generating the field [5] so we can write:

$$\Phi = LI \tag{4.34.}$$

Where L is the inductance of the coil and is calculated purely from the geometric properties of the coil. From this simple equation it is clear that the inductance gives the total flux passing through a given coil as a function of applied current. To see one of the most important results of this we return to Faraday's law given in equation 4.4 and integrate both sides over a surface bounded by a current loop we get:

$$\int \nabla \times \boldsymbol{E} \,.\, d\boldsymbol{S} = -\int \frac{\partial \boldsymbol{B}}{\partial t} \,.\, d\boldsymbol{S} \tag{4.35.}$$

This expression can easily be rewritten by using the definition of the flux through a surface in equation 4.33 and Stokes' theorem as:

$$\oint E \,.\, d\boldsymbol{\ell} = -\frac{\partial \Phi}{\partial t} = -\frac{\partial (LI)}{\partial t} \tag{4.36.}$$

The integral on the left is simply the voltage in the current loop and, as the inductance is purely a geometric parameter, it will not change with time and so we end up with the equation:

$$V = -L\frac{dI}{dt} \tag{4.37.}$$

This is a fundamental equation for an inductor. It tells us that as we try to vary the current passing through a magnetic coil or inductor we will have to overcome an induced voltage or back electromotive force (back emf). The physical origin of the emf is that to change the current we must change the magnitude of the magnetic field and so must change the total energy stored in the field. Therefore as we are changing the energy we must be doing work and hence a voltage is generated. This also allows us to calculate the energy stored in an inductor by noting that the power dissipation of an electrical current is $P = IV$:

$$W = \int P\,dt = \int IV\,dt = L\int I dI$$

$$W = \frac{1}{2}LI^2 \tag{4.38.}$$

If a second coil is added to the system and a current I_1 in the original coil then some of the magnetic flux generated by the first coil will pass through the second:

$$\Phi_1 = L_{12}I_1 \tag{4.39.}$$

where L_{12} is a geometric factor which is a measure of the coupling from the first coil to the second. Similarly a current I_2 in the second coil will cause a flux to pass through the first coil:

$$\Phi_2 = L_{21}I_2 \tag{4.40.}$$

By energy considerations you can show that [6]:

$$L_{12} = L_{21} = M \tag{4.41.}$$

where M is introduced here as the mutual inductance. If we assume that the two coils are perfectly coupled so that all of the flux generated by one passes through the other then the ration of the fluxes Φ_1 and Φ_2 is simple the ratio of the turns in each coil n_1 and n_2 and so:

$$\frac{\Phi_1}{\Phi_2} = \frac{L_1 I_1}{M I_1} = \frac{n_1}{n_2} \tag{4.42.}$$

And similarly:

$$\frac{\Phi_2}{\Phi_1} = \frac{L_2 I_2}{M I_2} = \frac{n_2}{n_1} \tag{4.43.}$$

Therefore in the limit of perfect coupling the mutual inductance is given by:

$$M = \sqrt{L_1 L_2} \tag{4.44.}$$

However perfect coupling is not realistic and in reality the coupling constant is less than the value given by equation 4.44 so a coupling parameter, k, is introduced. Furthermore in our split pair coil the inductances of the two coils should be identical and so in our system we have a mutual inductance of:

$$M = kL, 0 \leq k \leq 1 \tag{4.45.}$$

Thus the total energy of our systems is now the sum of all of the individual inductances or:

$$L_{tot} = \sum_i L_i = 2L(1 + k) \tag{4.46.}$$

Hence we can obtain an estimate of the total inductance of our coil by calculating the inductance of one of the individual coils. In general this is still a difficult parameter to calculate and so the calculation will be completed using FEA by using the fact that in a linear medium the total amount of energy stored in a magnetic field is given by:

$$W = \frac{1}{2}\int \boldsymbol{B} \cdot \boldsymbol{H}\, dV = \frac{1}{2\mu_0}\int \boldsymbol{B^2}\, dV \tag{4.47.}$$

The inductance can then be calculated by comparison with equation 4.38 to give:

$$L = \frac{1}{\mu_0 I^2}\int \boldsymbol{B^2}\, dV \tag{4.48.}$$

An estimate of the inductance of one coil can however be made by using the formula [7]:

$$L = \frac{31.5 \cdot a^2 \cdot n^2}{6a + 18b + 10(a_2 - a_1)}\mu H \tag{4.49.}$$

where

$$a = \frac{a_2 + a_1}{2}$$

4.3.2 Pulse Evolution

When the thyristor is triggered a current will begin to flow through the circuit and through the coil. Until the current starts to flow through the crowbar circuit i.e. during the rise of the magnetic pulse, the only components in the system which will affect the pulse will be the capacitors, the magnetic coil and any wiring used to connect the two. A magnetic coil has both resistance and an inductance and so is usually modelled as being an inductor and resistor in series. Therefore the system can be modelled

as a simple inductor-capacitor-resistor (or LCR) circuit with three components wired in series as in Figure 4.7. This circuit is an LCR resonator circuit with easily derivable time dependant properties.

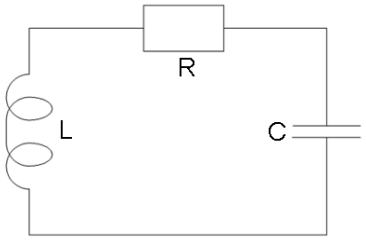

Figure 4.7. A simple circuit diagram for the important components during the rise of the magnetic pulse where R represents the combined resistance of the coil and the systems wiring.

The starting point for an analysis into the time dependant properties of the LCR resonator are the current voltage relations for each component [8]:

Resistor: $$V_R = IR$$

Capacitor: $$V_c = \frac{1}{C}\int I(t)dt \qquad 4.50.$$

Inductor: $$V_L = -L\frac{dI(t)}{dt}$$

It is clear from the diagram the voltage across the capacitor must be equal and opposite to the voltage across both the resistor and inductor:

$$V_C = -(V_L + V_R)$$

$$V_C + V_L + V_R = 0 \qquad 4.51.$$

This then leads to the ordinary differential equation which governs this system:

$$\frac{d^2I}{dt^2} - \frac{R}{L}\frac{dI}{dt} + \frac{1}{LC}I = 0 \qquad 4.52.$$

This has the general solution:

$$I(t) = I_0 e^{-\frac{\alpha}{2}t}\left[A_1 e^{i\omega t} + A_2 e^{-i\omega t}\right] \qquad 4.53.$$

where $$\alpha = \frac{R}{L}$$

and $$\omega = \left(\omega_0^2 - \left(\frac{\alpha}{2}\right)^2\right)^{\frac{1}{2}} \qquad 4.54.$$

$$\omega_0 = \frac{1}{\sqrt{CL}}$$

As the system starts with no current flowing and the capacitors charged to an initial voltage V_0 so the initial conditions of the system are:

$$I(0) = 0 \qquad 4.55.$$

$$V_C(0) = V_L(t) = V_0$$

By taking the real part of equation 4.53 we obtain the equation:

$$Re\big(I(t)\big) = I_0 e^{-\frac{\alpha}{2}t}[A_1 \cos \omega t + A_2 \sin \omega t] \qquad 4.56.$$

Therefore, as the current at time $t = 0$ must be zero, it is immediately obvious that $A_1 = 0$. To find the value of the constant A_2 we need to differentiate equation 4.56 and compare the result to the equation for the inductor in equation set 4.50. Using this method we reach the result:

$$V_L(t) = LI_0A_2 e^{-\frac{\alpha}{2}t}\left[\omega \cos \omega t - \frac{\alpha}{2}\sin \omega t\right] \qquad 4.57.$$

By again setting the time to $t = 0$ we find:

$$I_0A_2 = \frac{V_0}{L\omega} \qquad 4.58.$$

Therefore the current will vary with time during the rise period as:

$$I(t) = \frac{V_0}{L\omega} e^{-\frac{\alpha}{2}t} \sin \omega t \qquad 4.59.$$

Which is a maximum when: $$t_{max} = \frac{1}{\omega}\tan^{-1}\frac{2\omega}{\alpha} \qquad 4.60.$$

And so the maximum current achievable in coil with inductance L from a given capacitor bank charged to V_0 is given by the extended expression:

$$I(t_{max}) = \frac{V_0}{L\omega} e^{-\frac{\alpha}{2\omega}\tan^{-1}\left(\frac{2\omega}{\alpha}\right)} \sin\left(\tan^{-1}\left(\frac{2\omega}{\alpha}\right)\right) \qquad 4.61.$$

Although this expression is fairly complicated if we assume that the resistance is small and so is negligible then we can make the approximation:

$$\omega \cong \omega_0 = \frac{1}{\sqrt{CL}} \qquad 4.62.$$

$$I_{max} \cong V_0 \sqrt{\frac{C}{L}} \quad 4.63.$$

$$t_{max} \cong \frac{\pi}{2}\sqrt{CL} \quad 4.64.$$

The results in equations 4.62 and 4.64 show that to maximise the rise time of the coil we need to maximise the capacitance and inductance. As the capacitor bank is fixed that leaves just the inductance to be maximized. This however has to be balanced with equation 4.63 which shows that for the current in the coil, and hence the maximum attainable field, the inductance needs to be minimized. Therefore any coil designed in going to be a compromise between these two competing aspects of the pulse evolution.

The decay of the pulse is slightly easier to predict as it is simply an inductor in series with a resistor so is simple LR decay. By similar methods to above we can show that the decay will follow the curve given by:

$$I_{decay}(t) = Be^{-\frac{\alpha}{2}t_2} \approx I_{max}e^{-\frac{\alpha}{2}t_2} \quad 4.65.$$

with $$t_2 = t - t_{max}$$

The second part of the expression is only approximately equal to the first as, if it were combined with the first part as it was, this would lead to a discontinuity in dI/dt at t_{max} which is unphysical. A more accurate model gives the transition time from the rise regime to the decay regime when the gradient of the two governing equations is equal rather than at the peak current. Despite this the approximate expression describes the shape of the decay (if not its starting point) accurately as so we can see that longer decay times, and hence total pulse lengths, are obtained by maximizing the inductance and minimizing the resistance of the circuit.

4.3.3 Introduction to Structural Analysis and Electromagnetic stresses

A full description and derivation of the relevant solid mechanics equations is given in the next chapter and so this section will not focus too much on the finer details: the aim of this section is to give the reader a basic understanding of some of the key concepts and properties which will discussed in relation to the forces within a pulsed magnetic coil.

A primary concern when building a high field pulsed electromagnet is the forces and stress within the coil. The actual calculation of the stresses and strains will be completed with FEA but it is useful to

get an understanding of the equations behind the stress/strain analysis and the source of the forces. The primary source of the forces within a coil is the Lorentz force on the current carrying wire. The origin of this force comes from the force on electron with charge, q, moving at a velocity, $\boldsymbol{v}$, in a magnetic field which is given by:

$$\boldsymbol{F} = q(\boldsymbol{B} \times \boldsymbol{v}) \tag{4.66.}$$

Then as a current in a wire is simply the average velocity of the electrons in a material multiplied by the carrier density we find that the force per unit length of wire is simply:

$$\boldsymbol{F} = \boldsymbol{B} \times \boldsymbol{I} \tag{4.67.}$$

The magnetic force and the Lorentz force directions are shown in Figure 4.8 for a monolithic solenoid. It is clear that the field direction is roughly parallel to the bore near the centre and with the azimuthal current the force is directed in the outward radial direction. Near the ends of a coil where the field also has an appreciable radial component the force is partially radial and partially longitudinal towards the centre of the coil.

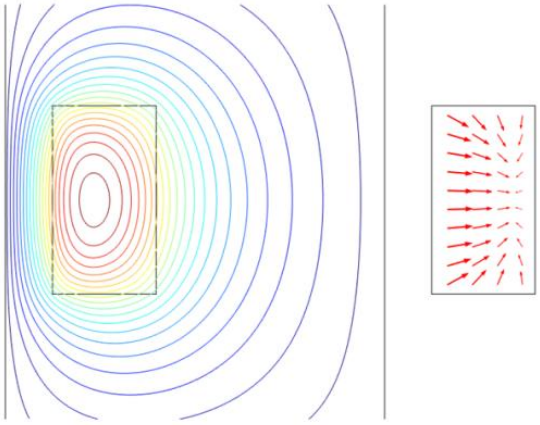

Figure 4.8. Magnetic force lines (left) and the Lorentz force direction (right) on the current in the solenoid for a monolithic solenoid.

As the radial force is the dominate one [9] the simplest case we can consider is a single loop of wire in the coil which doesn't interact with those around it with only a radial force acting on it. In this case the loop will resist the force by a tension within the wire causing a hoop stress of [10] (see chapter 5):

$$\sigma_\theta = \frac{BIr}{A} \tag{4.68.}$$

where r is the radius of the loop and A is the cross sectional area of the wire. If the stress, σ_θ, were relatively small this force would cause an elastic extension or elastic strain, ε, in the wire as dictated by Hooke's law:

$$\sigma = E\varepsilon \qquad 4.69.$$

where E is the modulus of elasticity or the Young's modulus. This relation is linear up to a point known as the yield point or yield stress, σ_Y. Figure 4.9 shows a simple ideal stress strain curve and shows that up to the yield point the relation is linear and after that point the material becomes easier to elongate. Finally, when a certain stress is reached, the material will break. This is known as the failure point and the stress at this break point is often referred to as the ultimate tensile stress or UTS, σ_{UTS}. If a material is stressed to a point below the yield point it will deform elastically in that when the stress is released the material will return to its original length. If the material is stressed beyond its yield point it will deform plastically so after the stress has been removed the material will not return to its original length but will have a permanent strain. Thus, for a simple one dimensional system, we can define the critical stress, σ_c, beyond which the system will either be damaged or destroyed. Whether σ_Y or σ_{UTS} is used will depend entirely on the materials and problem being considered. Thus in our simple one turn coil we can define an engineering limit which our coil will have to remain below if it is to survive multiple pulses:

$$\frac{BIr}{A} < \sigma_c \qquad 4.70.$$

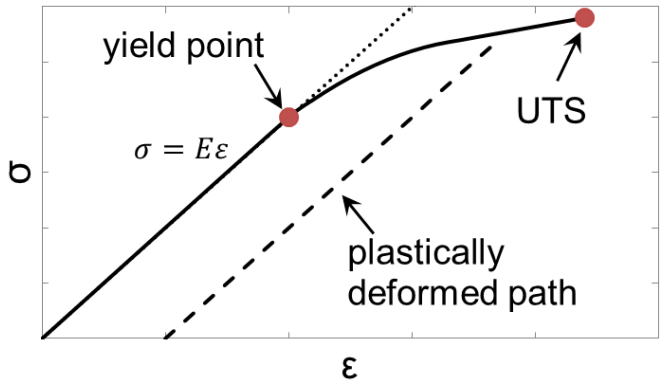

Figure 4.9. A simplified stress/strain graph.

However no loop in the wire is truly independent of its neighbours and the force is only truly radial in the central plane the above approximation is highly inaccurate so to get a more accurate description we must move into a three dimensional environment. For this we must introduce the stress tensor:

$$[\sigma] = \begin{bmatrix} \sigma_{xx} & \sigma_{yx} & \sigma_{zx} \\ \sigma_{xy} & \sigma_{yy} & \sigma_{zy} \\ \sigma_{xz} & \sigma_{yz} & \sigma_{zz} \end{bmatrix} \quad 4.71.$$

The stress tensor describes all of the forces which could act on an infinitesimal cube at a point within the material. The normal stresses denoted by σ_{ii} give the force through the centre of the cube in the direction of the axis. The shear stresses denoted by σ_{ij} give the forces on each surface of the cube and can be looked at as rotational forces around the centre of the cube. For most materials it can be shown that in equilibrium adjacent shear stresses are equal and so $\sigma_{ij} = \sigma_{ji}$ and equation 4.71 can be reduced to just six variable elements [11] and is known as a symmetric tensor.

If we apply a force along the x-axis then in equilibrium the stress in the material will be given by:

$$\frac{\partial \sigma_{xx}}{\partial x} + \frac{\partial \sigma_{xy}}{\partial y} + \frac{\partial \sigma_{xz}}{\partial z} + f_x = 0 \quad 4.72.$$

Or for a general force, $\boldsymbol{f}$**:**

$$\nabla \cdot [\sigma] + \boldsymbol{f} = 0 \quad 4.73.$$

In general the stress tensor can be diagonalized to give the principal stress matrix:

$$[\sigma] = \begin{bmatrix} \sigma_1 & 0 & 0 \\ 0 & \sigma_2 & 0 \\ 0 & 0 & \sigma_3 \end{bmatrix} \quad 4.74.$$

It is clear that the principal stress of a point is the direction in which all of the shear stresses are exactly zero and hence this direction is the known as the principal direction.

In a one dimensional situation the stress caused by a strain is dictated by Hooke's law. However in three dimensions there is an extra effect to consider which is that, in general, when a material is elongated in one dimension it will contract in the other two. The ratio between the elongation in the first direct to the contraction in the other two is known as the Poisson's ratio, υ, of a material. Therefore we need to modify Hooke's law, to include the effects of the Poisson's ratio and so for strains in the x-direction to law becomes [11]:

$$\varepsilon_{xx} = \frac{1}{E}\left[\sigma_{xx} - \upsilon\left(\sigma_{yy} + \sigma_{zz}\right)\right] \quad 4.75.$$

And similarly for the other two axes:

$$\varepsilon_{yy} = \frac{1}{E}\left[\sigma_{yy} - \upsilon(\sigma_{zz} + \sigma_{xx})\right] \quad 4.76.$$

$$\varepsilon_{zz} = \frac{1}{E}\left[\sigma_{zz} - \upsilon\left(\sigma_{xx} + \sigma_{yy}\right)\right] \quad 4.77.$$

In three dimensions we also need a tensor to describe the strain in the material:

$$[\varepsilon] = \begin{bmatrix} \varepsilon_{xx} & \varepsilon_{yx} & \varepsilon_{zx} \\ \varepsilon_{xy} & \varepsilon_{yy} & \varepsilon_{zy} \\ \varepsilon_{xz} & \varepsilon_{yz} & \varepsilon_{zz} \end{bmatrix} \quad 4.78.$$

Here ε_{ii} gives the elongation in the direction of the primary axes. The ε_{ij} components give the change in the angle between the original and deformed axes and in a linear, isotropic, homogeneous material they are related to the shear stress by:

$$\varepsilon_{ij} = \frac{\sigma_{ij}}{G} \quad 4.79.$$

Where G is the shear modulus given by [12]:

$$G = \frac{E}{2(1+\upsilon)} \quad 4.80.$$

We have seen that when we applied a force to a body each point within the material can become distorted but each point will also be subjected to a displacement caused by the distortion of the points around it. For this we must introduce the displacement vector which is clearly related to the strain of the system and in a simple 1-D system is just $u_x = \varepsilon_x x$ or $\varepsilon_x = \frac{du_x}{dx}$. A magnet coil is, however, a 3-D geometry and is typically cylindrical so the displacement vector for this coordinate system is [3]:

$$\varepsilon_{rr} = \frac{\partial u_r}{\partial r},\ \varepsilon_{\phi\phi} = \frac{1}{r}\frac{\partial u_\phi}{\partial \phi} + \frac{u_r}{r}, \varepsilon_{zz} = \frac{\partial u_z}{\partial z} \quad 4.81.$$

And the off-diagonal elements are:

$$\varepsilon_{\phi z} = \frac{1}{r}\frac{\partial u_z}{\partial \phi} + \frac{\partial u_\phi}{\partial z}, \varepsilon_{rz} = \frac{\partial u_r}{\partial z} + \frac{\partial u_z}{\partial r},\ \varepsilon_{r\phi} = \frac{\partial u_\phi}{\partial r} - \frac{\partial u_\phi}{\partial r} + \frac{1}{r}\frac{\partial u_r}{\partial \phi} \quad 4.82.$$

We now have a system of equations which will tell us how a force will stress a body (equation 4.73), how that stress will strain the body (equations 4.75 – 4.79) and how the body will deform and points in the body will move with that strain (equations 4.81 and 4.82). From these equations we can work out how the Lorentz force will affect our coil during a pulse but so far we have only discussed a very simple method for judging whether the coil is likely to fail due to the forces acting upon it. The failure criterion used in this thesis will be the widely [2] [3] [10] [11] used Von Mises Stress, σ_m, so any

magnet designed will reach its strength limits when the Von Mises stress of any part of it passes its failure stress, σ_{cr}. In terms of the principal stresses the Von Mises stress is given by:

$$\sigma_m = \frac{1}{\sqrt{2}}[(\sigma_1 - \sigma_2)^2 + (\sigma_2 - \sigma_3)^2 + (\sigma_3 - \sigma_1)^2]^{\frac{1}{2}} \quad 4.83.$$

A much more detailed description of stress-strain analysis in axially symmetric environments and the behaviour of orthotropic materials will be given in chapter 5 but the detail presented so far should give enough information to understand the concepts discussed in the rest of this section.

4.3.4 Thermal Analysis

One consideration for pulsed magnet design which has yet to be discussed is heating of the coil during the pulse. This can be an important factor as excess heating can cause further stress within the magnet body due to thermal expansion and, if the coil gets too hot, it could lead to charring, burning or damage of the materials from which the coil was constructed. There are two main causes of this heating with the first simply being Joule heating: The second is eddy current heating due to the rapidly changing magnetic field, dB/dt. The eddy current heating is the result of Faraday's law (introduced earlier for induction) but instead of a loop of a conductor we are considering a solid material. If we expose a conductor to a changing magnetic field we will induce current loops in the material in such a direction that the field of those loops will oppose the change in field. This is simply Lenz's law of electromagnetic induction. As the effective frequency, ω, of the pulses in our coil is going to be very low the skin depth, δ, of the copper is going to be very long as given by [13]:

$$\delta = \sqrt{\frac{2}{\mu_0 \sigma \omega}} \quad 4.84.$$

If we use an estimated rise time of 30ms this gives a skin depth of ~15cm which is much greater than the envisaged wire diameter of ~2-3mm so we can ignore the skin depth for any subsequent eddy current calculations. This greatly simplifies the equations and we can approximate the eddy current heating in round wires per unit volume of wire as [14]:

$$P_{ec} = \frac{A}{4\pi\rho(T)}\left(\frac{dB}{dt}\right)^2 \quad 4.85.$$

Where A is the cross-sectional area of the wire, $\rho(T)$ is its resistivity and dB/dt is calculated at each point using FEA. The total heating on the wire by a current pulse is then:

$$P = P_{joule} + P_{ec} \quad 4.86.$$

The flow of any generated heat can then be calculated by using the heat flow equation:

$$\rho_d c_p \frac{dT}{dt} = \nabla \cdot (k \nabla T) + P \quad 4.87.$$

Materials tend to expand when heated and so will induce a thermal strain proportional to the change in temperature:

$$\varepsilon_z = \alpha \Delta T \quad 4.88.$$

where α is the coefficient of thermal expansion. This will cause the greatest problem at the interface between different materials as they have different coefficients of expansion and will be heated at different rates and so will try to expand at different rates. This differential thermal expansion will cause stresses particularly along the join between materials [15] although it has been shown that often in pulsed coils the thermal stresses are much smaller than the electromagnetic ones [2].

4.3.5 Model Details

The FEA model of the pulse coil was built in three main stages with each stage focusing on slightly different analyses of the coil. These stages were:

- Purely electromagnetic analysis to calculate field profiles and coil inductances.
- Coupled electromagnetic and structural analysis to investigate the effects of the Lorentz force on the magnet structure.
- Coupled electromagnetic and thermal analysis to investigate the temperature increase in the coil during a pulse.

To reduce computation time all the models ignored the helical nature of coils and instead modelled them as being axisymmetric so they could be model using the 2-D axial symmetry geometry within Comsol Multiphysics [16]. Furthermore only half of the axisymmetric geometry needs to be modelled as all pulsed coils will have a mirror symmetry plane through the coil mid-plane [2]. A further model which would include all three analysis types could be performed to study the extra thermal stress added by the coil heating during a pulse. However work by Witte [2] on materials with poorer thermal conductivity and with much shorter pulse durations (~10%) showed that the thermal stresses were of the order 10-15% of the electromagnetic ones and that these stresses where primarily induced in the

wire, rather than the reinforcement. Therefore the thermal stresses in this coil should be even smaller and their exclusion will only add a small error to the calculations.

The details of how the physics was input into each model were:

Electromagnetic Model

This used the magnetic fields interface of the ACDC physics module with a stationary, time-independent, solver. This solves for magnetic fields given a current and/or magnetization distribution [17] which does not vary with time. Although this is not strictly accurate the pulse lengths in the desired coil will be long. Therefore transient effects on the current distribution within individual turns will have a negligible effect and do not warrant the greatly increased calculation times required.

Within the model we must define the current in the coil, external boundary conditions and the magnetic permeability of all materials used. As all the materials were linear and non-magnetic the permeability was set to μ_0 over the entire model geometry. The current in the wire was imposed by setting the wire domains to be a Coil Group Domain which simply imposes the condition that the total current in each wire domain is the same. The boundary which demarcated the mirror symmetry plane was set to be a Perfect Magnetic Conductor which imposes the condition:

$$\hat{\boldsymbol{n}} \times \boldsymbol{H} = 0 \qquad 4.89.$$

Where $\hat{\boldsymbol{n}}$ is a unit vector normal to the boundary. This condition forces the components of **H** parallel to the boundary to be zero. This implies that the electric current distribution, and hence magnetic field profile, is identical or each side the boundary and so is the mirror symmetry condition for magnetic fields. The central boundary was left as the default of axial symmetry which is self-explanatory and the final two boundaries were left as magnetic insulation which gives a definite edge to the modelled space.

Once the coil geometry was defined an extra domain was added around the coil to simulate the air around the coil. This domain must be large enough that the spatial extent of the magnetic field was not artificially constrained by the edge of the model. Figure 4.10 shows how having an air domain that is too small compared to the size of the magnetic coil can produce an artificially low inductance value. It is fairly easy to ensure that this artificial constraint is not affecting the calculated results too much by following the simple algorithm:

- Create and run the model with an initial air domain size.
- Integrate the total magnetic energy enclosed in the model volume.
- Increase the air domain size and rerun the model including the magnetic energy integration.
- Repeat until the total magnetic field energy does not increase by more than a set tolerance limit, say 0.1%

Once the field profile had been calculated the inductance of the coil was calculated by using equation 4.48 noting that the result generated by the model must be doubled to take account of the fact that the model will only integrate over the half geometry modelled.

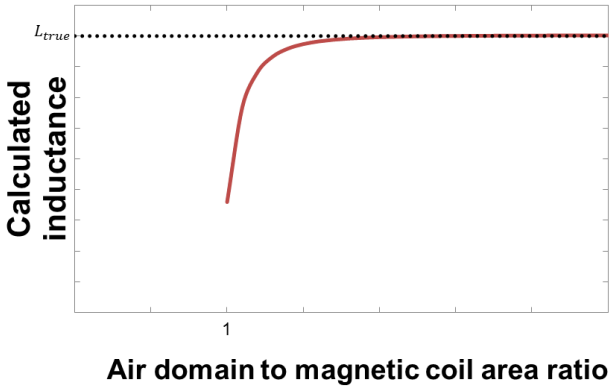

Figure 4.10. Dependence of the calculated inductance on the ratio between the areas of the magnetic coil to the air domain for an arbitrary coil.

Electromagnetic-Structural Model

This model used the magnetic fields interface as before along with the solid mechanics interface within the Structural Mechanics module with a stationary solver. The first stage in this model was to generate a magnetic field profile for the expected peak field as in the last section. Once this profile has been generated the calculated magnetic field profile, $B(r,z)$, can be used to calculate the Lorentz force on each point within the wire domains and is input into the model by applying this force as a body load [18] on all wire domains.

The mirror symmetry plane boundary was set as a roller boundary. This imposes the condition:

$$\boldsymbol{n}.\boldsymbol{u} = 0 \qquad 4.90.$$

This condition forces the displacement vector normal to the boundary to be zero at the boundary. Therefore no point can pass through the boundary but they are free to move parallel to it. This is the symmetry plane as it implies that the material on both sides of the boundary must be behaving in the

same manner. The central boundary was left as axial symmetry as normal and the remaining boundaries of the coil were left as the free displacement so could displace without restrictions in response to the generated stresses.

Once the model had been run the key results to note were the Von Mises stress distribution and peak values along with the strain distribution so that these values could be compared to the failure points of the materials within the coil.

Electromagnetic-Thermal Model

The final model again uses the magnetic fields interface along with the Heat Transfer in Solids interface which is part of the core software package but for the thermal model a transient solver must be used. However, as for the structural mechanics calculations, the starting point was to generate a static magnetic field profile for the expected peak field. It is not necessarily immediately obvious why a static magnetic field profile should be used but the simple reason is that the magnitude of a magnetic field generated by a current is linearly dependant on the applied current. Hence if we know the field profile at one current we know it for every current and so we can greatly reduce the computation time as only the thermal model need be run as a transient model. To further simplify the initial models it was assumed that the insulation around each turn was a perfect insulator as so the wire domains were fully adiabatic. This is not realistic but is the most onerous bounding condition and so we can find a theoretical maximum temperature rise within the wire without having to devote too much time to the properties of the materials around the wire. As we shall see later the temperature rises were, in general, low enough that no further complications were required to ensure that the coil would not overheat.

For the model it was assumed that the pulse was a semi-sinusoidal pulse with a rise time calculated from the modelled inductance and equation 4.60. For a pulse with a rise time of t_{rise} this gives a natural frequency of $\omega = \pi/2t_{rise}$ and so the magnetic field at each point during the pulse is given by:

$$B(r,z) = B_0(r,z) \cdot \sin \omega t \qquad 4.91.$$

And the rate of change of the field is simply:

$$\frac{dB(r,z)}{dt} = \omega B_0(r,z) \cdot \cos \omega t \qquad 4.92.$$

These can be combined with equation 4.86 to give the final power dissipation in the wire domains during the pulse:

$$P = \frac{A}{4\pi\rho(T)}(\omega B_0(r,z)\cdot\cos\omega t)^2 + \rho(T)(J_0\cdot\sin\omega t)^2 \qquad 4.93.$$

where here the resistivity of the wire is a function of temperature.

The validity of this approximate method was tested by recreating a simple model in [2] which used a fully coupled transient model for both the thermal and electromagnetic calculations. The model used a typical geometry for a coil built at the Clarendon and assumed a half-sinusoidal pulse shape with a 5ms rise time and a peak current of 20kA corresponding to a peak field of ~40T. The final minimum and maximum temperatures predicted in the fully transient model were 291K and 213K, respectively. Figure 4.11 shows the predicted temperature distribution for the same coil but using the approximation for the eddy current heating. The final maximum temperatures agree with only 0.05% difference and the minimum temperatures agree within 3%. As this model uses higher fields and faster rise times the eddy current heating will be much severe in this model than in the design for a high inductance and so the approximation will be less accurate than for a longer pulse length coil. Therefore the approximation method was judged to be accurate enough for the required model.

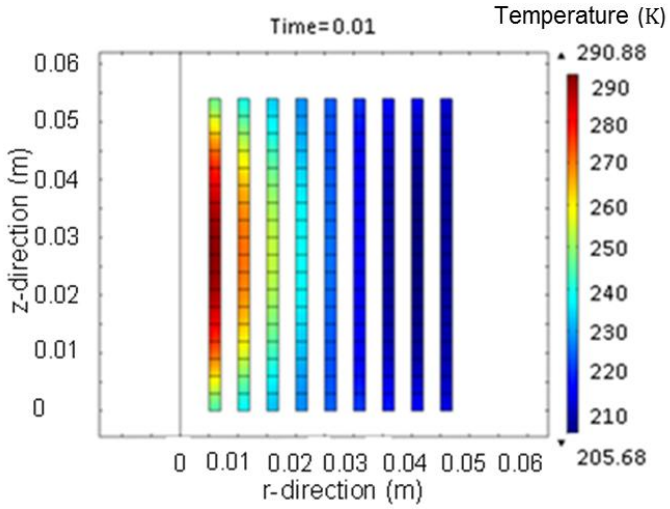

Figure 4.11. The predicted temperature distribution from the eddy current heating approximation for an arbitrary monolithic coil.

4.3.6 Conclusion of Theory

In this section we have derived in some detail the key factors to consider when designing a split pair pulsed electromagnet. In summary these are:

- To increase the pulse length and rise time we must maximise the inductance of the coil and so we must make it as large and with as many turns as possible.
- To increase the maximum current available we must minimise the inductance and resistance.
- To increase the maximum field which can be created we must consider the coil shape factors α and β but increasing them beyond a certain point adds no extra benefit.
- To ensure that the coil does not fail we must reduce the stresses in the conductor as far as possible and part of that involves reducing the peak field to central field ratio. This requires a short, thick coil.

It is obvious that several of these considerations contradict each other so the final design will need to be a compromise to ensure an optimized design.

4.4 Magnet Details

As was specified at the start of this chapter the ideal coil would have in following specifications:

- Have a large enough sample space to encompass a bulk sample 32mm in diameter with the associated cryogenic equipment (the final tail Dewar width was 25mm, for more details see chapter 6).
- Have a variable coil separation.
- Create a field of >15T in the sample volume.
- Have a pulse rise time of >50ms.

As we discussed the theoretical aspects of coil design in the previous section we now have the tools required to discuss the more practical aspects of the design and move onto the construction and testing of the coil.

4.4.1 Design

Any complete design for a pulsed coil must include the superstructure used to hold the coil together along with a method to mount the coil into the apparatus in the NKMFL. Each coil is held in a large Dewar which itself is placed into a pulse module which is used to direct the high current/voltage cabling to the coil and to provide an initial safety barrier in the case of a coil failure. The Dewar is needed as all pulsed coils are cooled in a liquid nitrogen bath which has several benefits; the primary one is that at lower temperatures the resistance of the conductors is greatly reduced (about a factor of 8

for copper from the value at room temperature). This increases the maximum available current while minimizing the temperature increase as the Joule heating is reduced. A secondary benefit is that most materials increase in strength at lower temperatures so the coil can reach higher stresses than it would be able to at room temperature.

4.4.1.1 Materials

Any magnetic coil requires a variety of materials in its construction as it consists of different sections each with different roles. The different parts of a coil that are required are:

- A conductor to carry the current.
- An insulating material around the conductor to prevent shorting between adjacent turns or layers or to the support structure.
- A former to wind the coil on.
- A superstructure to hold the coil together and mount it in the equipment
- Any extra reinforcement required to support the windings.
- A split coil will also require a coil spacer to hold the coils apart during a pulse.

Each of the different parts of the coil will require different materials and with a wide variety of materials available for each section the reasons behind the decision to use specific materials in the coil are as follows (please note that all material data used in the modelling is shown in Appendix E):

<u>Conductor</u>

Perhaps the most important of the coil components is the conductor. The primary requirements are that the material is strong enough to withstand the forces generated by a pulse while having a low resistivity so that the energy lost to Ohmic heating is minimized. There are a wide variety of materials used as conductor from pure metals, macro-composites and micro-composites. An example of a macro-composite which is commonly used in the Clarendon is copper-stainless-steel [19]. This consists of a copper core with a stainless steel jacket thus combining the conductivity of copper with the strength of the stainless steel. There are also a couple of commonly used micro-composites in the form of copper-silver [20] and copper-niobium [21]. As dislocations within a material reduce its strength the premise behind these materials is to form nanoscale structures within the wires which

effectively contain no dislocations and so strengthen the material at the cost of reducing their conductivities [22].

For the purpose of this coil it was decided that soft copper would be the best choice for a number of reasons. The primary reason is that a high inductance coil implies a large number of turns and hence a long length of conductor with a high resistance. Therefore we need a conductor which can be produced in very long lengths with low resistivities so copper is an obvious choice. The other major benefit is cost as soft copper is readily available off the shelf from major producers around the country.

Reinforcement

Copper does however have a major drawback in that it is mechanically weak. At room temperature the UTS of copper is around 220-450MPa [23] compared to ~1GPa for copper-silver [20], 1.3GPa for copper –niobium [24] and up to 1.1GPa for copper-stainless-steel [25]. Due to this structural weakness in the copper extra reinforcement is required to support each layer of copper. There are two different classes of reinforcement commonly used in pulsed magnets. The first is metal (usually austenitic steel) shells heat-shrunk onto the outer layer of windings [26]. As this coil will have many layers steel would be highly impractical. The second is high-tensile fibre reinforcement, making use of the high Young's modulus and UTS of materials such as S-glass fibre, carbon fibre, Kevlar and Zylon. These materials are highly orthotropic in that their properties are highly anisotropic but have at least two orthogonal symmetry planes in which the material properties are independent of the position within this plane. The theory of orthotropic materials will be dealt with in some detail in chapter 5 but for now we will just consider the key properties of Young's modulus along the length of the fibre and the UTS. Table 4.1 shows some typical values for these properties at room temperature for each of the possible materials with typical values for steel as a comparison.

From Table 4.1 it is clear that if the only consideration was the stiffness of the fibre then high tensile carbon fibre would be the obvious choice. If strength was the only consideration then carbon fibre, Zylon or even s-glass would be appropriate. However for a pulsed magnet both stiffness and strength are useful properties. Another consideration is that during a pulse high voltage will develop between turns and so it would be an advantage for the reinforcement to be an insulator to help reduce the

chances of a flashover which will eventually destroy the coil. Thus the best choice of fibre for the split pair pulsed coil will be Zylon as it is insulating while being very stiff and strong.

Property	S-Glass	Carbon Fibre		Zylon	Kevlar	Maraging Steel (grade 300)
		High Tensile	High Strength			
$E \parallel$ (GPa)	85.5	390	240	270	85	190
UTS (GPa)	4.6	2.1	2.5-7	5.8	3.9	2.1
Reference(s)	[27], [28], [29]	[27], [28], [30]		[31]	[32]	[33]

Table 4.1. Key room temperature material properties for a range of possible reinforcement materials.

The values produced for the fibres so far have been for bare, 'virgin', material and so are calculated from the cross-sectional area of the fibres. In a real environment such as in a pulsed magnet these values will never be reached as the fibres will not fill all of the available space. There will be voids which reduce the density of fibres and so reduce the strength of reinforcement. It is standard practice in magnet construction that the fibres are wound into the coil under tension to minimise the voidage [34]. There is a related issue in that as each layer of reinforcement is wound on to the previous it exerts an inward pressure on the layers below which will reduce the pretension until there is no pretension at all and can actually cause the inner layers to buckle. As a stress is applied to the conductor it will strain, re-straining the inner layers of reinforcement until eventually the all of the reinforcement is stressed. At this stage there is little difference between the prestressed and non-prestressed reinforcement [35]. However if the chosen conductor is stiff and brittle the required level of strain may have already degraded or destroyed the conductor but for this coil copper will be used. Therefore the prestress is less important as the copper can strain to a very high degree (>20%) and so the reinforcement will be fully stressed long before there is any risk of conductor damage.

Once the coil has been completed the coil is vacuum impregnated in resin using 10bar overpressure to help drive the resin into the coil [36]. The standard resin used is Araldite CY1300 epoxy resin with hardener HY906 and accelerator DY602. This is favoured due to its long pot life which allows complete evacuation of the coil volume and complete degassing of the resin before impregnation. The purpose of the resin is primarily to provide a glue to hold the coil together but has two secondary purposes. The first is to improve the electrical insulation properties of the reinforcement and secondly to exclude liquid nitrogen from the coil volume. The exclusion of nitrogen is desired as if it was allowed to enter the coil, as the coil heated during the pulse, the nitrogen would rapidly evaporate and

as the expansion factor for nitrogen is 650 [37] (i.e. one liquid litre of nitrogen will produce 650 gaseous litres at the same pressure) this would generate very high pressures which could destroy the coil. Therefore, when we consider the material properties of the reinforcement for the coil, we must include the role of the resin as well; we have a composite material. For the initial modelling most of the material properties of the Zylon was assumed to be the same as was used in [2] as found from [38]. The calculations of the properties assume that the volume fraction of Zylon was 78%. The only difference was that the UTS was assumed to be ~40% lower giving an UTS of 2.4GPa. This is because it is well known that Zylon can be degraded by environmental factors [31], [39]. As the Clarendon's stockpile of Zylon is greater than 5 years old it is likely that its properties are significantly degraded and so a margin for error in the UTS would increase the likelihood of a successful coil design.

Electrical Insulation

For obvious reasons the wire must have an electrically insulating coating. Without this each turn would short to the next turn or a wire may short to any metal in the support structure of the coil. As the wire to be used was standard off the shelf wire it came with an enamel coating. This is a polymer insulator which will typically have a breakdown voltage ~1kV [40] so as adjacent wires, even if they are in intimate contact, would have a breakdown voltage of a couple of thousand volts. This may seem high enough to ensure that no shorts develop within the coil in normal conditions however this does not allow for the fact that the properties of the enamel will degrade with time, exposure to high voltages [41] and possible thermal cycling and conductor movement as well. All of these factors will weaken the dielectric strength increasing the likelihood of coil failure with time. In fact most coils in the Clarendon fail due to the breakdown of the wire insulation [42]. For the split coil it was decided that extra electrical insulation would be beneficial. To this end the wire had layer of s-glass 0.2mm thick braided over the enamel. As the breakdown voltage of s-glass is around $13{,}000V/mm$ [29] (although this figure is likely to increase after the coil has been impregnated with resin) this will increase the dielectric strength of every turn while increasing the separation between adjacent turns. The glass over-braid should also provide a couple of extra benefits in that it will provide a protective casing around the wire to protect the enamel during any conductor movement and, due to its good wetting properties, it should help to wick the resin into the coil volume during impregnation.

Former/Spacer

Every coil constructed requires a former to wind the coil on; it literally gives the coil its shape. Also required in this split pair is a spacer to hold the two coils apart during the pulse as there will be a strong magnetic attraction between them. The material properties required for these two sections are very similar in that they need to be reasonably strong, particularly under compression, they need to be insulating to minimise the risk of shorts and they need to be stable against cracks developing through thermal cycling. The class of materials used in all pulsed coils in the Clarendon is the fabric reinforced composites. The key properties of the two composite materials used in the coil are shown in Table 4.2. For the former, which required a strong material to prevent distortion during winding, 10G/40 was chosen. As the spacers were required to withstand small stresses and only compressive stresses 6F/45 was chosen instead of the 10G/40. This is because although the properties of 10G/40 are better than 6F/45 as it contains glass fibre it is very abrasive to tooling and is much harder to machine.

Property	10/G40	6F/45
Reinforcement fabric material	Glass	Cotton
E (GPa)	18	6.5
UTS (MPa)	355	68
Compressive strength (MPa)	415	290
Dielectric Strength (kV/mm)	~12-17	~10-15
Reference(s)	[43]	[44]

Table 4.2. Key material properties for the two composites used in the split pulsed coil at room temperature.

Superstructure

The superstructure is required to hold the completed coil together and to mount the coil in the pulse module. For this job stainless steel 316L was chosen. It was chosen as it is very strong while having a poor conductivity and is austenitic so is, ideally, non-magnetic and so should not interfere with the produced magnetic fields to any appreciable degree. The one exception is that the hanger plate from which the coil will be suspended which will be made from 6F/45. This is a safety feature so that the steel supporting the coil will be electrically insulated from the rest of the pulsed module. This means that any electrical shorts to the steel plates will not be able to affect anything left on or near the top of the module.

4.4.1.2 Geometry

The starting point to formalizing the geometry is to calculate the inductance required by the minimum rise time. This will then allow us to calculate the maximum current which could be achieved from the capacitor bank for a coil with that inductance. Once we have the operating current range and the target inductance we can then start to perform some calculations on coil geometries before finally testing the structural and thermal properties of the coil to ensure that it will withstand the rigors of generating high magnetic fields.

Using equation 4.64 we can easily obtain an estimate of the required inductance as:

$$L > \frac{1}{C}\left(\frac{2t_{rise}}{\pi}\right)^2 \\ > 32mH \tag{4.94.}$$

Then by using this figure of 32mH and equation 4.63 the current range is given by:

$$I < V_{max}\sqrt{\frac{C}{L}} \\ < 7000A \tag{4.95.}$$

Although this figure is the absolute maximum current that a coil with this inductance it is worth designing a coil which can achieve the desired field with a much smaller current as:

- The coil will have a resistance and so the actual figure will smaller than this simple approximation as given by equation 4.61.
- If possible the coil may have a larger inductance to allow even longer pulse rise time.
- This current will only be available with the capacitor bank fully charged and as this risks damaging the capacitors; using a smaller fraction of the bank energy would reduce this risk.
- The higher the voltage driving the current the greater the chance of shorts developing sooner within the coil.

In the derived equations for how the geometry will affect the properties of the coil there are quite a few free parameters namely; a_1, a_2, b, the initial b_{gap} and n. These are the inner and outer diameter, the half-length of the coil and coil gap and the number of turns in the coil respectively. There is obviously a very large number of ways to combine these which will result in respectable design of coil so it is important to start fixing some of these variables.

The first to be fixed was the inner diameter and the initial coil separation. The initial coil separation was simply the width of the rectangular tail dewar plus 3mm on either side for end-checks of the magnet coils and 1mm on either side to make it possible to insert the dewar into the coil. This gave a figure for b_{gap} of 16.5mm. For a_1 the figure was arrived at as, as shown in Figure 4.5, we want to maximise α and β to increase the achievable field so that requires us to minimise a_1. To balance this it was thought that at some point in the future axial access to the bore may be required and the existing tail dewars had a diameter of up to 20mm so a free access bore of this size could be useful. Finally a wall thickness of 2mm on the tube which would support the inner turns of the coil during winding leads to the value of a_1 used of 12mm.

To maximise the achievable field we need to maximise a_2 and b and to minimise the peak field to central field ratio as shown in Figure 4.6 we need to maximise the ratio of a_2 the b. As both conditions require a_2 to be maximized a figure of ~120mm was decided on as this was the largest diameter coil which could be constructed with the existing equipment at the Clarendon. When the extra reinforcement was added between each layer this allowed 38 layers of 2mm diameter copper wire to be wound. The final stage was then simply to add layers to lengthen the coil until the required inductance level was reached. The final figure for b was 15.6mm corresponding to 13 turns per layer. These dimensions gave a total of 494 turns per coil. Using equation 4.49 this gives the inductance of each coil as $19.1mH$. Thus by equation 4.46 the estimated total inductance range for the magnet is:

$$38.2mH \leq L \leq 76.5mH \qquad 4.96.$$

Therefore, even at a very large separation where the mutual inductance is low, the coil pair will still have a total inductance greater than the required figure. Now that we have a coil geometry and a total number of turns of a set diameter we can estimate the resistance of the coil at 77K. The total length of wire is simply the average diameter of the turns multiplied by the total number of turns or for one coil:

$$\ell_{wire} = \pi n(a_1 + a_2) = 200m \qquad 4.97.$$

As the resistivity of copper at 77K is around $1.99 \times 10^{-9}\Omega m$ [45] this gives the total resistance of both coils as $250m\Omega$.

Now that we have a predicted inductance range and resistance for the coil we can start to estimate the achievable fields. Using equation 4.31 we find that, at the initial separation the coil should produce a magnetic field of $6.24\mathrm{mT/A}$. The maximum current range for a coil of this resistance and inductance

range is 4000-5400A. Finally we can predict that the maximum achievable field and the rise time of this coil will be in the ranges:

$$25T \leq B_{max} \leq 34T$$
$$26.5ms \leq t_{rise} \leq 73.8ms \qquad 4.98.$$

Were the t_{rise} has been calculated using the lowest possible inductance coupled to a quarter of the capacitor bank for the shortest rise time and the maximum inductance couple to the full capacitor bank for the longest rise time.

It is clear that if the design can withstand the magnetic stresses and temperature increase during a pulse that it will exceed the design specifications on all counts.

4.4.1.3 Electromagnetic Properties

The first stage to creating the FEA model is to create a stationary magnetic field profile for the coil design. The general details of the model are set out in section 4.3.5. The final design for split pair coil was to have two identical coils each of outer diameter 115mm. Each coil contained 38 layers with 13 turns in each row. The final design contained 492 turns. The magnetic field profile generated by a magnet current of 2000A as predicted by Comsol is shown in Figure 4.12. It predicts a peak field of 15.3T and a central field of 12.3T giving a central field of $6.13mT/A$. The field to current ratio is lower than the analytical value by just 1.5% but this is likely due to the fact that the model takes into account the actual distribution of the turns within the former area. The predicted inductance of a single coil is $19.73mH$ and the total inductance of the pair at the initial separation is calculated as being $51.7mH$. These values again agree within the analytical predictions to a high degree and give a coupling mutual inductance coupling parameter of $k = 0.31$ at this separation.

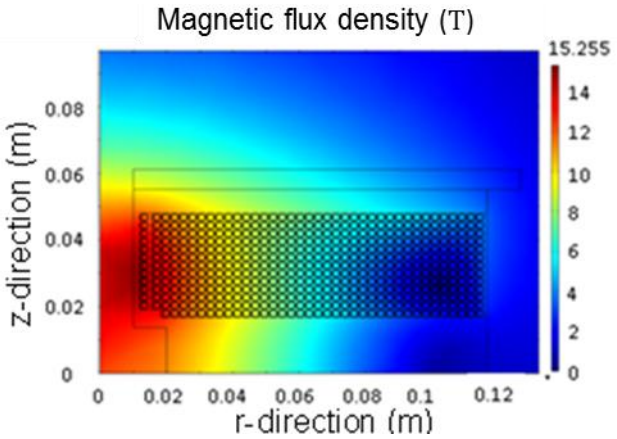

Figure 4.12. Predicted magnetic field profile for half of the axially symmetric geometry.

4.4.1.4 Structural Properties

Within the coil most of the materials can be modelled as being linear elastic materials i.e. that the stresses that will experience will not extend the material past their yield point. This is most applicable to the Zylon as stress-strain curves in the literature [38] show that it behaves linearly up to a point and then it fails so its yield point is the same as its UTS. For the former materials this assumption can also safely be used as if the stress on the former are high enough that they deform plastically the former would rapidly degrade and so the coil should be redesigned. The one exception to the linear assumption is the copper in the wire as it will begin to yield at quite a low stress level and so will transfer more stress to the Zylon than it would were it fully linear. Figure 4.13 shows the stress-strain curves for Zylon [38] and for fully annealed soft copper [46] at 77K. It is clear from these graphs that the Zylon is almost fully linear up to failure whereas the copper is linear until its yield point at around $50MPa$ of stress. For stresses above this point the copper becomes much easier to elongate until it eventually fails at a strain of around 60%. Although this yielding curve is far from linear, for the purposes of the model, it can be approximated as being linear with a Young's modulus of $1.5GPa$. This linear yielding curve is also shown in Figure 4.13. Although this is very inaccurate the fit is a good approximation for strains of up to ~5% and as the Zylon's maximum breaking strain is ~1.5-2% the copper will not enter a regime where the approximation is a bad one without the coil failing.

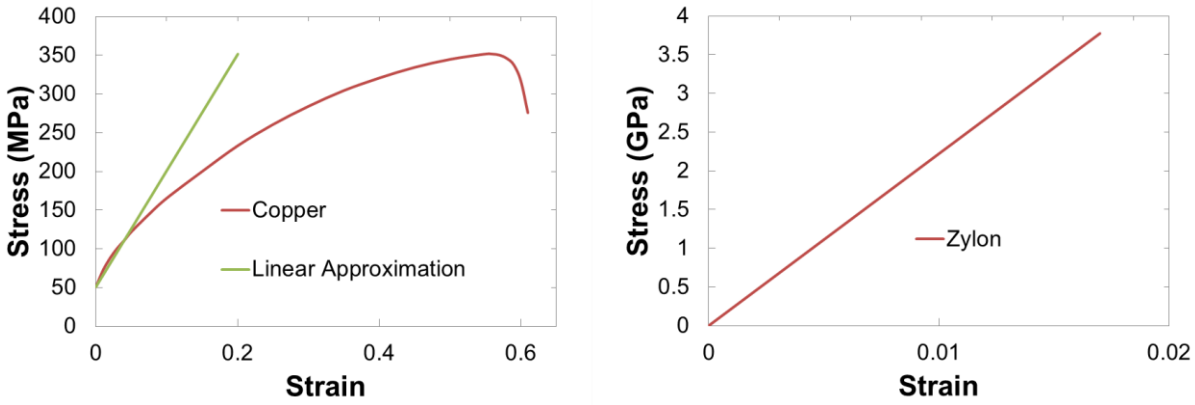

Figure 4.13. Stress-strain curves at 77K for Zylon, copper, and the linear approximation for copper once the material has begun to yield.

Initially the model was run with all materials (including the copper) assumed to be fully linear with no yielding. This was done for a range of applied currents which would give a central field of up to 25T. The model was then re-run using the yielding copper stress-strain curve with the same range of applied currents (the computation time for this calculation was >13hrs). The plot of peak Von Mises' stress in the copper and in the Zylon for both of these models is shown in Figure 4.14. It is clear from this that

if the copper was fully linear then it would reach its breaking stress, destroying the coil at 18T. However as the copper can yield the actual stress on the copper is much lower and the stress on the Zylon is higher reaching 2GPa at 25T. By extrapolating the curve the safe limit UTS of the Zylon would be reached at around 27T.

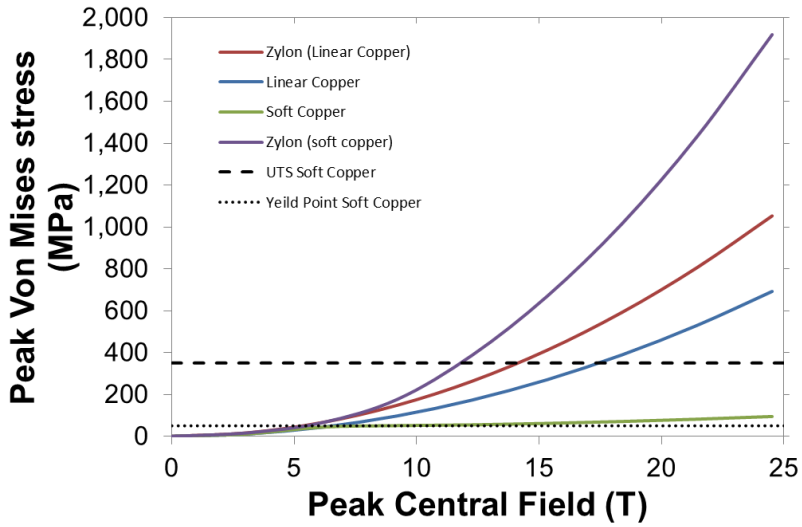

Figure 4.14. The peak Von Mises' stress in the copper and the Zylon as a function of peak central field for soft copper which can yield and for copper which is fully linear so that it cannot yield.

The other major problem is that the stress-strain curve for copper is highly dependent on the history of the wire. Mechanical deformations of the wire can work harden the copper, increasing its Young's modulus and its UTS at the expense of greatly reducing the strain at which the material will break. Conversely, exposure to high temperatures can re-anneal the copper, softening it and reducing its modulus and UTS. To make a wire the copper is first drawn down from a thicker stock of material to the required size. This cold-drawn wire is very hard and is about the limit of how hard pure copper can be. The drawn wire is then heated to temperature of up to 800℃ during the enamelling process which will greatly soften the copper. The copper will then be partially be re-hardened by the overbraiding process and during winding into the coil as both these processes involved bending the wire around radiuses. Finally the copper will be partially re-annealed during the oven baking to cure the resin after impregnation. Therefore it is impossible to know exactly what state the wire will be in when the coil is finally ready to carry a current. A brief experiment was conducted to get an idea of the effects of resin curing on the hardness of the wire and to find the limits of the properties of the copper. To this end a length of 6mm diameter copper wire was cold-drawn down to 2mm. This would harden the copper to the maximum that drawn wire is likely to reach. This wire was then cut into identical lengths and each

length was subjected to a different time/temperature conditions, in line with the standard curing conditions for the resin used [47]. The baking conditions used are shown in Table 4.3. The treated samples were then sent to the Leibniz Institute in Dresden[12] for tensile testing. The results of the testing [48] are also shown in Table 4.3. The results from the wire firing tests show that temperatures as low as $120°C$ will anneal the wire, reducing the yield stress. It also shows that temperatures of at least $160°C$ are required to greatly reduce the yield stress.

Sample	Temperature ($°C$)	Time (hrs)	Young's Modulus (GPa)	Yield Stress (MPa)	UTS (MPa)	Strain at break (%)
A	None	None	130	425	435	2
B	120	10	130	360	385	2.5
C	140	9	110	310	330	7.5
D	160	8	120	120	240	30
E	280	2	80	50	210	40

Table 4.3. Temperature and the time held at that temperature for each sample along with the results of the room temperature stress-strain measurements.

As we do not know the exact hardness of the copper in the coil it is important to define the possible stress-strain range which the coil could occupy. This is bounded by the curves for fully annealed and fully hardened copper and so the model was re-run using the data for the fully hardened copper. The stress-strain curves for the copper and Zylon for both extreme hardnesses of copper are shown in Figure 4.15. In this instance stress on the Zylon is much more important than the stress on the copper as even if the copper is stressed to its UTS it will just yield and strain further, giving more stress to the Zylon. This is even true for fully hardened copper as, although its strain at break is just 2%, the maximum strain increases at lower temperatures and is about 3% at 77K [46]. As the strain at break is just 2.5% for the Zylon it is clear that the Zylon will always fail first. Also marked on Figure 4.15 is the stress region for the Zylon reinforcing copper with an intermediate hardness. This is the region which the stress on the Zylon will occupy. It is clear that for Zylon the lowest stresses are generated by the hardest copper and the highest stresses by the softest copper. However, as explained earlier, the stress on the Zylon will not reach its safe limit until beyond 25T and it is likely that the UTS will not be reached until the applied field is greater than 30T. This information does have a bearing on how the

[12] At this point I must thank Dr Jens Freudenberger for carrying out the tensile tests.

resin is cured; to keep the copper as hard as possible the resin should be cured at as low a temperature as possible and hence it will be cured at $120°C$.

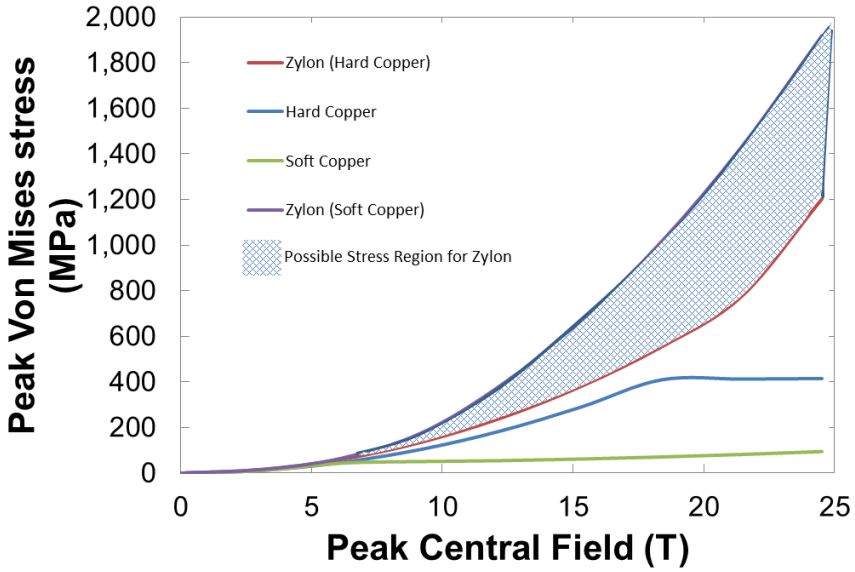

Figure 4.15. The stress-strain curves for Zylon and copper using fully hardened and fully annealed copper and the region in which the actual stress on the Zylon is likely to lie.

It is also clear from Figure 4.15 that the stresses on the copper are low, even at the higher fields, and so, as long as the Zylon does not fail, the copper should never approach its UTS. However somewhere between 6T and 18T (depending on the copper's hardness) the copper will be stressed enough that it will yield, giving rise to plastic deformation. This permanent plastic deformation, although it will not damage the conductor, will cause the radius of each turn to irreversibly increase and so the inductance of the coil will increase slightly as the coil is tested at higher fields.

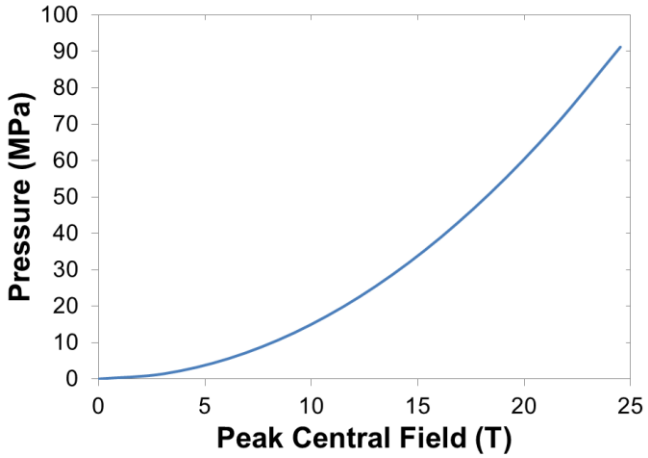

Figure 4.16. The compressive force on the coil spacer as a function of applied field.

The other failure consideration is on the spacer holding the two coils apart could break if the axial compression reaches too high a value. By integrating the z-component of the Lorentz force on all the wire turns a plot for the compressive pressure exerted on the spacer could be created as shown in Figure 4.16. This pressure peaks at just under 100MPa for a 25T pulse which is fairly low compared to the failure compressive stress of the 6F/45 so leaves a large margin for error. This pressure, although low compared to the failure point of the key material, is the equivalent to a 400 tonne mass being placed on the spacer!

4.4.1.5 Thermal Properties

The thermal model, although it will not be used to calculate the extra stresses on the conductor (particularly since the stresses on the conductor were so low) is important to ensure that the coil can be used at the required field levels without overheating. The difficulty here is that it is very hard to state categorically what temperature is too hot for this coil. If the copper is exposed to high temperatures it may anneal and soften, transferring more force to the Zylon but as the worst case scenario, in this respect, is shown in Figure 4.14 this is unlikely to negatively affect the coil performance. Work on the effect of time and temperature on the hardness of copper has shown that temperatures of at least $160°C$ are needed to have a large annealing effect and this temperature was applied for 8hrs so a much higher temperature will be needed to have an effect over a few seconds. Thus the copper wire is unlikely to be the limiting factor in terms of the temperature. The s-glass ($816°C$ annealing point [49]) and Zylon ($200°C$ for ~100hrs to affect strength [31]) both have operating temperatures of well over $200°C$ so again will not be the limiting factor. 10G/40 and 6F/45 both have maximum recommended intermittent operating temperatures of $150°C$ [43] [44] which just leaves the resin. No datasheet could be found for the exact resin/hardener combination used but the datasheet for the same combination with hardener HY905 [47] gives a glass transition temperature of the resin as $109°C$. At this point the resin will soften from its hard, glassy, state to a much softer, rubbery state. This transition could weakly affect the properties the inter-turn insulation either by a reduction of the dielectric strength of the resin or by allowing other insulating components to move. Therefore the maximum safe temperature for the coil will be designated as $110°C$ although, as the resin is not a primary source of inter-turn insulation, the coil could operate at higher temperatures but this may reduce its expected lifetime.

The starting point for the thermal model, as detailed in section 4.3.5, is to consider the insulation around the wire to be a perfect thermal insulator. The other main approximation is that the rise time of the pulse is long enough that the skin effect in the copper can be ignored, as can the distribution of the current across each wire turn.

The model was run for magnetic pulses with two different rise time; 30ms and 60ms as these are approximately equal to the longest and shortest rise times for the coil with the initial separation. The current and hence magnetic field are assumed to have a half-sinusoidal evolution in time.

The key material properties for this model are the specific heat capacity, thermal conductivity and resistivity of copper as functions of temperature. The resistivity of copper is assumed to be linear with temperature as, even at 77K, the dominate resistance will be thermal resistance [37]. Therefore the resistivity of the copper is given by:

$$\rho = \rho_0 \left(1 + \alpha\left(T - T_{ref}\right)\right) \qquad 4.99.$$

Where $T_{ref} = 293K$ is the reference temperature, so in this case is room temperature, the temperature coefficient $\alpha = 0.00393\,{}^{1}/_{K}$ and $\rho_0 = 1.67 \times 10^{-8}\Omega m$ is the resistivity of pure copper at room temperature [50]. The variation of the specific heat capacity was found from [50] [51] and the thermal conductivity was assumed to be independent of temperature with a value of $400\,W/m \cdot K$ [37].

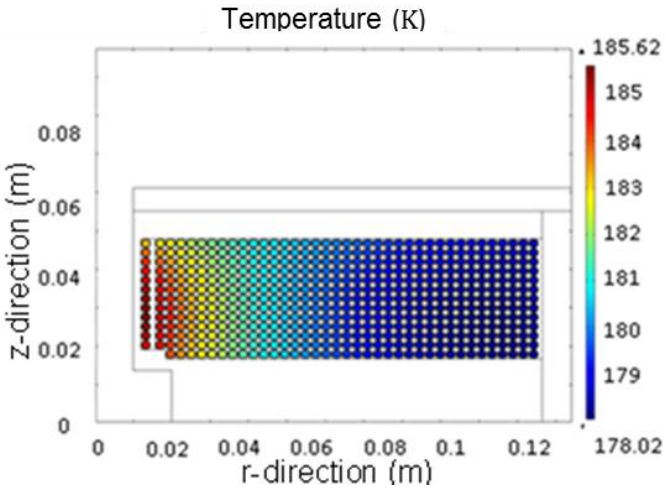

Figure 4.17. Image showing the predicted temperature distribution at the end of a 30ms rise time 25T pulse.

Both rise time models were calculated for peak fields up to 25T. Figure 4.17 shows the temperature distribution across the coil after a 25T peak field 30ms rise time pulse. It clearly shows that the eddy current heating has an effect as the turns towards the centre of the coil have a slightly higher final

temperature. Figure 4.18 shows the evolution of the temperature increase in the coil for 25T pulses with 30ms and 60ms rise times. It shows that difference between the maximum and minimum final temperatures is very low for both pulse lengths and that the primary cause of heating is the Joule heating. In fact eddy current heating accounts for $< 12\%$ of the total temperature increase for a 30ms rise time pulse and for just $2 - 3\%$ of the 60ms one.

By running the model for a range of applied fields we can generate the curves shown in Figure 4.19 which give the final average temperature of the wire as a function of applied field. It shows that for a 30ms rise time pulse that the final temperature should not exceed 180K so should never even approach the safe temperature limit. When looking at the 60ms rise time pulses the picture is not so clear. In the purely adiabatic model the temperature peaks at just 150K for a 15T pulse so the coil should be able to achieve the specification field without difficulty. Problems may occur if the coil is tested to its limits as the temperature peaks at 409K for a 25T pulse, 27K higher than the safe operation temperature. To investigate whether this is likely to cause excessive heating in the resin the model was re-run using realistic data for the materials around the wire. As the thermal conductivity of these materials is very low the heat will not diffuse far during the pulse so the key materials are the Zylon [52] [53], s-glass [54] [55] and pure epoxy [56]. The results from this run are also shown in Figure 4.19 and show that the average temperature of the wire has dropped to 370K. Furthermore the average temperature of the regions with the resin, i.e. the regions which could be degraded by excessive heat, reach an average temperature of just 300K. This shows that, if the pulse is half-sinusoidal, even at the highest field pulses that are likely to be fired the temperature should not reach a temperature where the coil properties will be degraded and certainly will not reach the $200°C$ which would start to degrade the key components of the coil. A note of caution is that the pulse is unlikely to have a true half-sinusoidal evolution as the evolution of the second half of the pulse is solely dictated by the inductance and resistance of the system. As the capacitance will have no effect the pulse will likely have a decay tail which will extend the total length of the pulse. This may cause excessive heating during very high field pulses which will need to be monitored by measuring the coil resistance directly after each pulse.

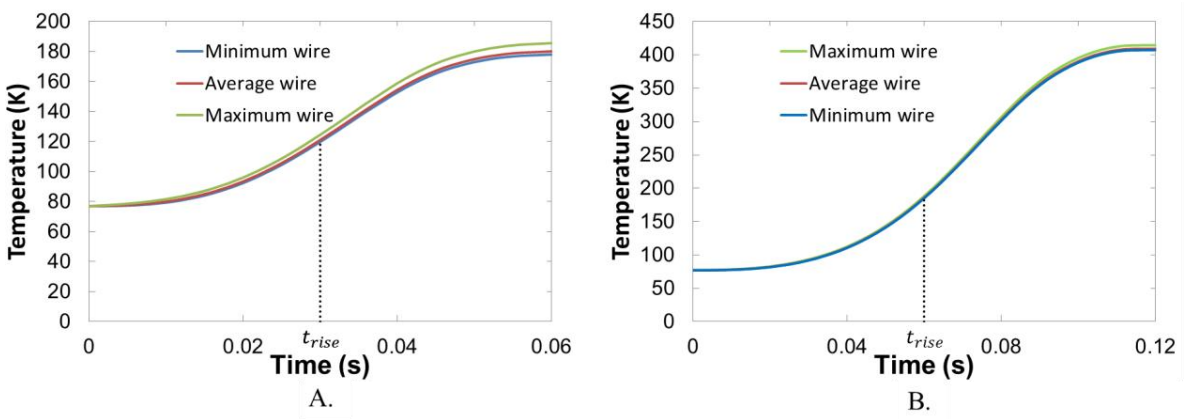

Figure 4.18. *Evolution of the temperature with time for a 25T peak field pulse with a rise time of A: 30ms, B: 60ms.*

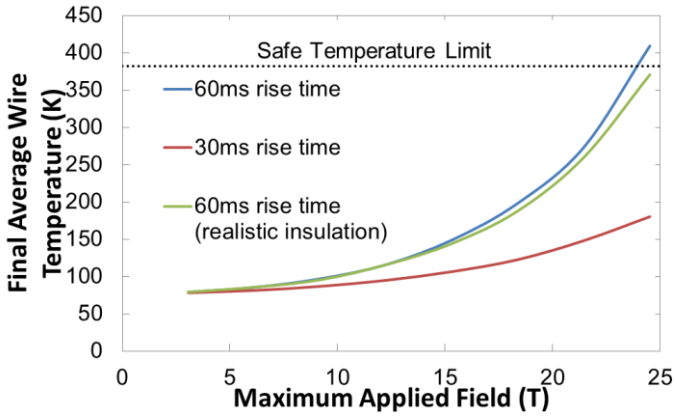

Figure 4.19. *Predicted final average temperature of the wire after a pulse against peak field.*

4.4.1.6 Design and modelling conclusions

The conclusion from the computer modelling is that the coil should be able to produce over 20T without too much difficulty. In fact the structural modelling shows that the coil should be able to produce 25T before the forces generated will start to approach the safety margin however at these fields the coil will start to get very hot during a pulse and this may reduce the expected lifetime of the coil. As the specified required field was 15T it should be able to produce this field for a relatively large number of shots. Before we leave the design it is worth noting that, with any pulsed coil, it is a case of when, and not if, the coil will fail. This is because generating magnetic pulses creates fairly extreme conditions within the coil and, even far from the instantaneous failure conditions, the materials will degrade mechanically through repeated loading and through mechanical creep and fatigue [11]. Furthermore repeated exposure to high voltages will slowly degrade the dielectric strength of the insulation materials and so the coil will eventually develop a short. Therefore any coil will only produce a finite, but unknown, number of pulses within which any and all experimental data must be recorded.

4.4.2 Construction

The first stage of the construction was to build the former and the former mandrel. The former was fabricated by machining each end cheek and the centre tube separately and then gluing all the elements together. The mandrel was required for several reasons: The first is that, as the components of the former are joined by glue over a small area, they are mechanically weak. Therefore the outward pressure that the wire would exert on the end-cheeks during winding would cause them to break from the centre tube. Also, as the end cheeks are thin, they would flex during winding and cause the coil to have a long effective length at the outer turns than at the inner turns. Finally there is nothing on the former which would allow the assembly to be held in the coil winding machine. Both the former and the mandrel have eight radial slots running from near the bore to near the outer edge. These slots were added to aid the vacuum impregnation as without them, for resin to reach the inner turns, it would have to flow through all the layers of the coil but with the slots this distance is greatly reduced.

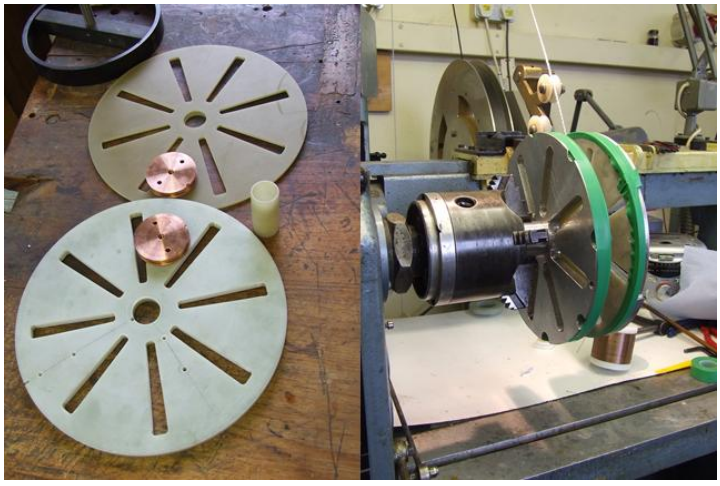

Figure 4.20. *C*onstituent parts of the former and current contacts for one of the coils and the completed former and mandrel on the coil winder both showing the radial slots added to aid coil impregnation.

Before winding of the coil began several smaller spools of Zylon were vacuum impregnated with the resin so that even if the main vacuum impregnation process did not work as planned there would still be an amount of resin in the core of the coil. The vacuum impregnation of the Zylon is a continuous process of drawing Zylon from the primary spool through a resin bath under a partial vacuum and then onto the secondary spools. The secondary spools also make winding the Zylon into the coil much easier as they are much smaller and easier to handle than the primary spool.

Once the former had been assembled and the Zylon had been impregnated the coil was ready to be wound. The first step in winding process involved winding a layer of copper wire into the coil using

the coil winder. Once an entire layer had been laid down the Zylon was wound by hand onto the copper until the total diameter reached that required by the design. During the winding of the Zylon particular attention was paid to applying a tension to the Zylon and to laying Zylon under the turn that would step up onto the next layer as this is where the wire is pressed together most strongly and is an obvious coil failure point. The hand winding of the Zylon is a hugely time consuming process and there was an estimated 15,000 turns of Zylon wound by hand into each coil! Figure 4.21 shows photos of a completed layer of Zylon and copper complete with glass over-braid and also a photo from the end of the coil clearly showing the resin access slots and the layered structure of the coil.

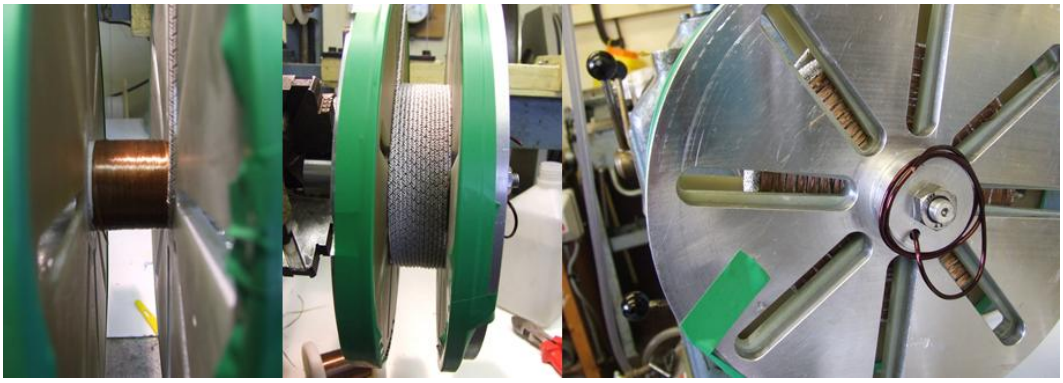

Figure 4.21. Completed layers of Zylon, copper and the end of the coil showing the layered structure.

Once all of the Zylon/copper layers had been wound the coil was vacuum impregnated using 10bar overpressure [36]. The impregnated coil is then baked first in a rotary oven which rotates the coil in a temperature of $\sim 80 - 100°C$ overnight before a final baking at $120°C$ for 8 hours to fully cure the resin. The rotary oven is used so that the resin can thicken and gel so that it will not just flow out of the coil during the final curing process.

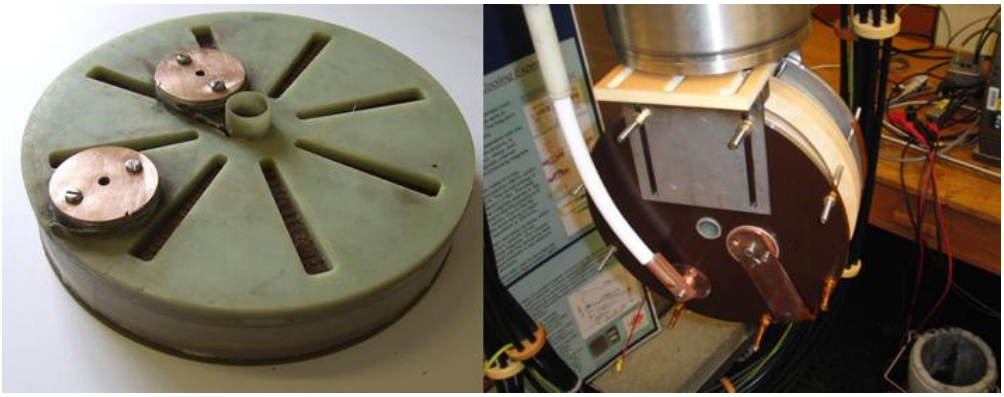

Figure 4.22. Completed coil with wire soldered to current contacts and the completed coil pair mounted on the pulse module with the 6F/45 hanger plate clearly visible.

The final step on an individual coil was to attach the current contacts and to solder the wire to them as shown in Figure 4.22. The contacts were design to maximise the length of wire which could be soldered and hence minimise the contact resistance. The completed coils could then be mounted into the support structure and wired together using an adjustable copper strap. The final assembly mounted in the pulse module is shown in Figure 4.22. A diagram explaining the final geometry set-up is shown in Figure 4.23.

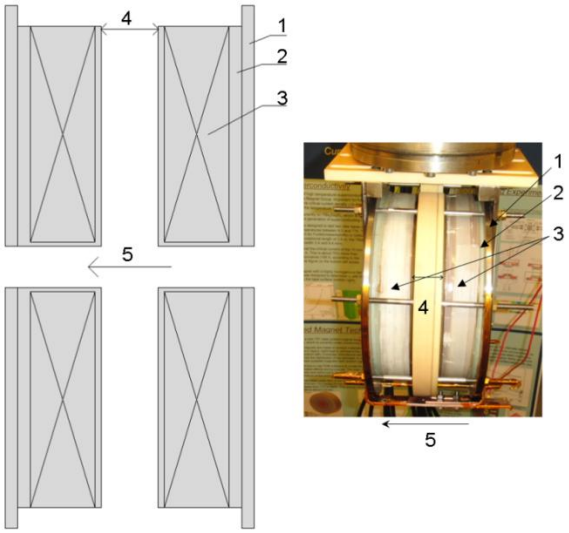

Figure 4.23. Diagram of magnet cross section and photo of completed magnet. 1: Stainless steel mounting plate. 2: Coil former. 3: Winding Volume. 4: Variable split. 5: Bore and field direction.

4.4.3 Preliminary Testing

The first test that was performed upon the coil was to measure the inductance of both individual coils and of the coil pair and to compare these values to the estimated values and the ones calculated using FEA. The inductances were measured using a Wayne-Kerr LCR meter using a frequency of 100Hz as this is the lowest frequency available on the inductance meter and is the frequency closest to the ones at which the coil will operate. Table 4.4 shows these values and shows that the estimated value was just 3.5% off the measured value and the FEA calculated value was just 0.35% off. The estimated value is remarkably close given that it is an approximate formula and the FEA result is even better. In fact the FEA value was closer to the mean measured inductance of the pair than the actual value for either coil. The fact that the FEA value was smaller than the average mean is easily explained as the model only calculates the field in a finite space so will limit slightly the calculated inductance (as explained more fully in section 4.3.5).

	Inductance value (mH) obtained from:		
Coil	Estimated	FEA	Measured
Coil A	19.1	19.73	19.71
Coil B			19.89
Split Pair at Initial Separation (33mm)	38.2-76.4	51.7	52.03

Table 4.4. Estimated, calculated using FEA and measured values of inductance for the individual coils and for the split pair at the initial separation.

Further confidence in the electromagnetic aspects of the FEA model is gained when looking at the variation of inductance of the pair as a function of coil separation. Figure 4.24 shows the calculated curve and measured data points for this inductance variation. It shows that the model is again in very good agreement with measured results with the error increasing slightly as the separation increases with the error being ~1% at zero separation to ~2.4% at the maximum one. This is likely to be due to the fact that as the separation increases so does the fringe field around the coil volume and so the inductance of the coil at a large separation will be limited more be the finite calculation volume than a small separation.

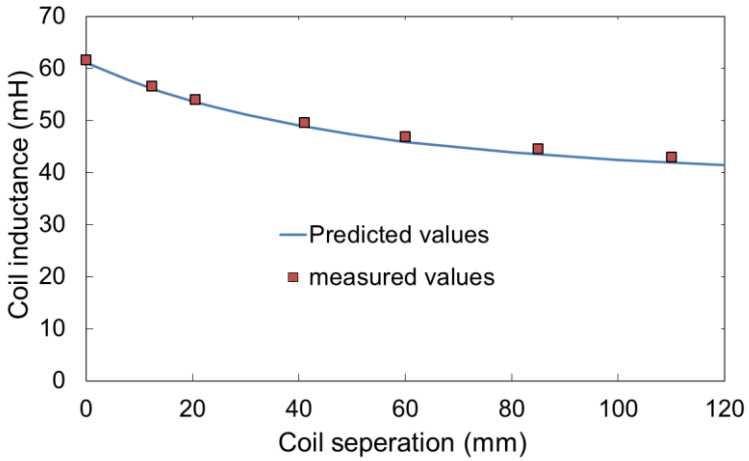

Figure 4.24. Predicted and measured inductance of the split pair as a function of coil separation.

Although the agreement between the calculated and measured inductance values shows that the computer model can predict the electromagnet aspects of the coil accurately the acid test is, of course, to generate some magnetic fields in the coil. The first step is to immerse the coil in a liquid nitrogen bath and wait for it to cool down to 77K. The temperature of the coil is determined via a resistance measurement. Figure 4.25 shows the measured resistance against time for the coil as the Dewar is filled and shows that the total cool down from room temperature is about an hour. The final resistance

is $290m\Omega$ which is close to the estimated value of $250m\Omega$. Any discrepancy is likely to be due to the actual purity of copper used and the fact that the estimated resistance does not take the current leads or the contact resistance of the current contacts into consideration.

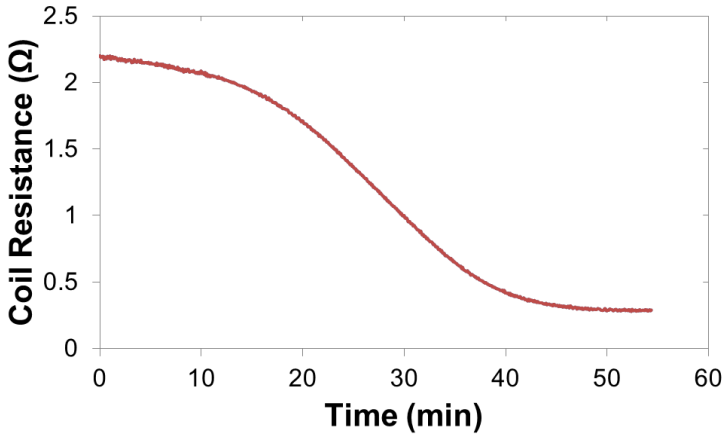

Figure 4.25. Resistance of the coil against time once the coil has been immersed in liquid nitrogen.

Once the coil has fully cooled the capacitor bank is charged and a pulse is fired. After each successful pulse the coil is again allowed to fully cool down to 77K before the next pulse is fired with the magnitude of the pulses increasing with each successive pulse so that, ideally, any faults can be spotted before they occur. The evolution of the field was monitored using two methods; a cryogenic Hall probe and a pick-up coil both placed in the field centre. The Hall probe was a commercially available LHP-NP probe from Arepoc[13]. The hall probe contains a hall chip which is advertised as being linear up to 20T and gives a signal of $21\,mV/T$ with a control current of $100mA$. The pick-up coil was custom made and had a ~32mm diameter with 9 turns of $100\mu m$ diameter wire. The total area of the pick-up coil was $7292mm^2$ and is used to measure changes in magnetic field (not absolute values) via Faraday's law:

$$V = A\frac{dB}{dt} \qquad 4.100.$$

Where A is the area of the coil and B is the average flux density passing through it. Thus the field magnitude can be obtained by numeric integration of the voltage measured across the coil. The signal

[13] AREPOC s.r.o. Iljušinova 4, 85101 Bratislava, SLOVAKIA

from both instruments was recorded at a read rate of $250\,ksamples/s$ using a National Instruments[14] USB-6281 18-bit data logger.

The Hall probe was used in conjunction with a pick-up coil as the two methods are mutually complementary. The Hall probe is good for measuring the absolute field level but may miss very short lived small spikes in field caused by conductor movement or similar within the coil. On the other hand the pick-up coil may give inaccurate readings for very slowly varying fields but will give large signals during a magnetic spike due to the very short time scales of these events.

Figure 4.26 shows the data from both instruments along with the integrated pick-up coil signal showing good agreement between both methods during a pulse. Figure 4.27 shows the peak measured central field against capacitor charge voltage using different fractions of the capacitor. Most of these results (with one notable exception) lie on a straight line as expected from the theoretical equation 4.61. The small variation from the straight line for the ¼ bank data is due to the variation in capacitance between each sub-bank.

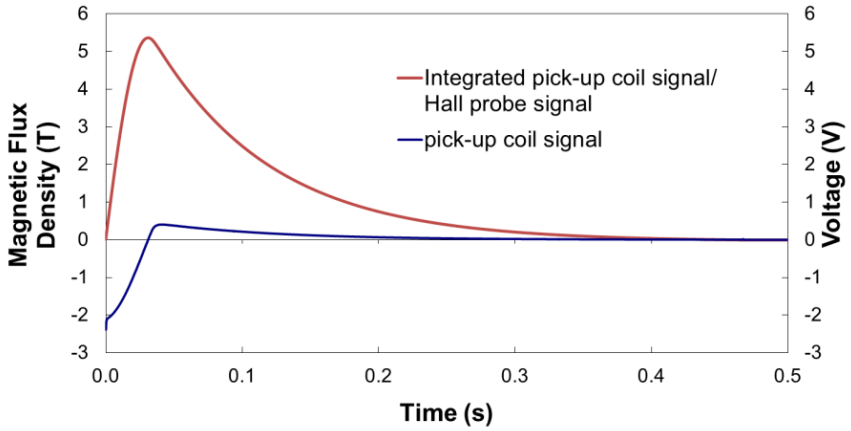

Figure 4.26. Typical signal from the pick-up coil, hall probe and the magnetic flux density found by integrating the pick-up coil signal against time. The red line indicates both the integrated pick-up coil signal and Hall probe signal as they lie directly over one another.

[14] National Instruments Corporation (U.K.) Ltd. Measurement House, Newbury Business Park, London Road, Newbury, Berkshire RG14 2PZ.

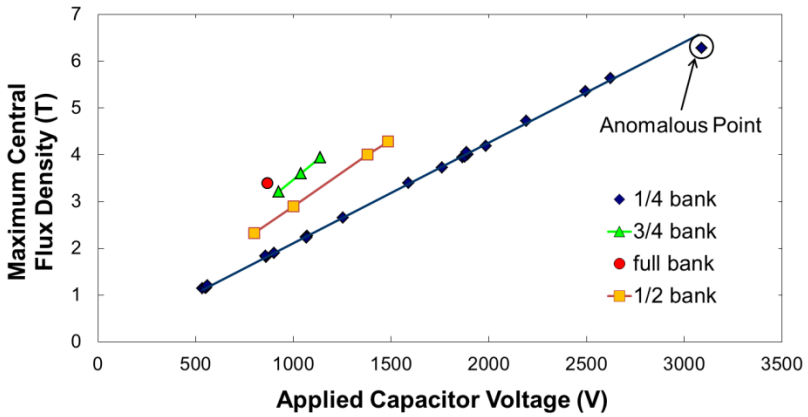

Figure 4.27. *Measured peak central field against capacitor charge voltage for the original coil setup.*

In total 138 pulses were fired with the original coil setup with peak fields of $1.0 - 6.3T$. Pulse number 137 had a peak field of 5.6T and (with hindsight) gave a warning for what happened during pulse number 138. Figure 4.28 shows the pick-up coil trace during this pulse. 15.8ms into the pulse there is distinctive spike in the measured voltage, barely noticeable in the main plot, but very obvious once the plot is enlarged. This spike was a warning that something may be amiss within the coil.

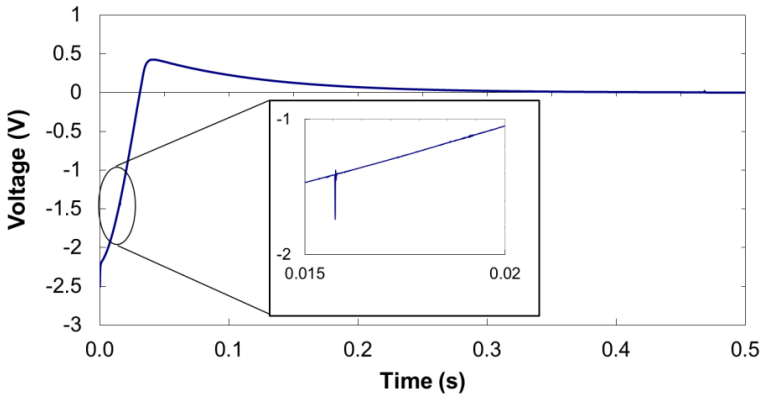

Figure 4.28. *Pick-up coil voltage during pulse number 137 showing the voltage spike 15.8ms into the pulse.*

The one anomalous point on the otherwise straight lines on Figure 4.27 this point was the peak field recorded from pulse number 138 and had a very obvious cause; the coil had failed. Figure 4.29 shows the trace recorded from the pick-up coil during this pulse. After $16.6ms$ the line starts to deviate slightly from a smooth line, after $20.9ms$ this deviation becomes quite large and outright failure of the coil occurs after $22.3ms$ although a partial discharge of the coil continuous despite the failure. Figure 4.30 shows the damage that the coil sustained during the pulse. It is immediately obvious that during the pulse the current contacts for the inner connection had both disconnected from the body of the coil. This caused light damage on one side but on the other this had broken the wire and the capacitors had

continued to discharge by arcing to the remaining wire and to the steel support structure. This had spark-eroded and partially melted the steel plate and had destroyed the wire to well within the end check of the former! A design flaw in the original set-up had been exposed in a very destructive way.

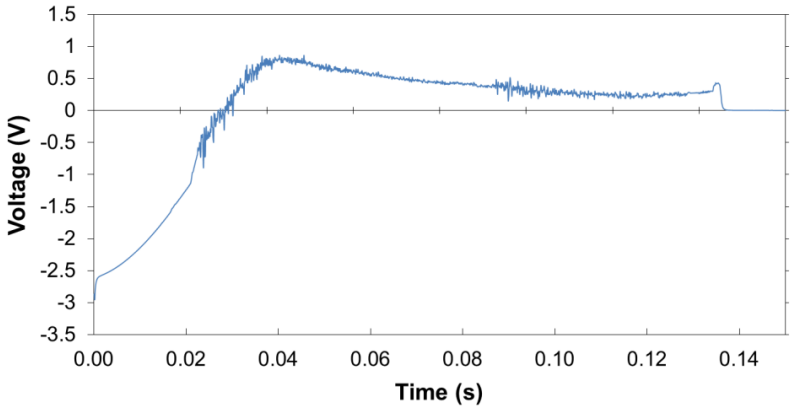

Figure 4.29. *Pick-up voltage against time for pulse number 138; the last pulse fired from the original set-up.*

Figure 4.30. *Damage caused to both sides of the coil pair during pulse 138 and the spark-erosion of the stainless steel plate.*

4.4.4 Failure Analysis

To understand the mechanism which drove the coil to failure we must return to equation 4.10. If we ignore the externally applied current then we are left with the component of the current defined by equation 4.13 which is the induced currents, otherwise known as eddy currents:

$$\boldsymbol{J_i} = \sigma \frac{\partial \mathbf{A}}{\partial t} \qquad 4.101.$$

This tells us that a conductor exposed to a time changing magnetic field will have currents induced in it and, as a consequence of Lenz's law, these currents will be opposed to the change in the magnetic field. As these currents will circulate around within the current contacts, opposing the changing

magnetic field, there will be a Lorentz force exerted on the contacts in a radial and axial direction forcing the contacts away from the body of the coil, as dictated by equation 4.67.

To get an idea of the magnitude of these forces a new FEA model was constructed. As the contacts break the axially symmetry the model must be a 3-D model to fully account for the contact geometry. The only components of the coil that are relevant to this model are the contacts themselves and the winding volume as components with a high resistivity will not affect the field. For simplicity the coil windings are assumed to be of uniform cross-section with a uniform current density. The model must also be fully time dependant as we are only concerned with the transient effects of the changing magnetic field on the contacts. Therefore a half-sinusoidal current pulse which gave a peak field of 6T was applied to the coil domains and the resulting current induced in the contacts and Lorentz force was calculated. Figure 4.31 shows the evolution of the force on the original contacts and it can be seen that the force peaks at around 3000N on the inner contacts (it was much lower but still high at 450N on the outer contacts)! It is unsurprising then that the contacts became disconnected from the body of the coil as they were held by two M4 threads tapped into the 10G/40 glass composite.

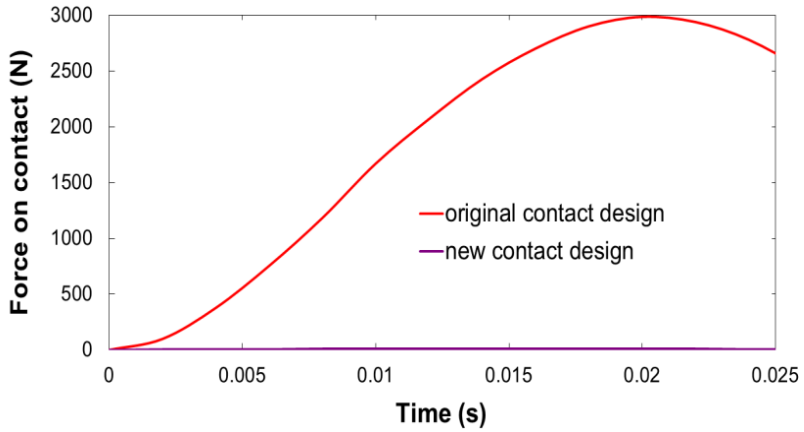

Figure 4.31. Evolution and magnitude of the force on the coil contacts during a 6T 30ms rise-time pulse.

4.4.5 Modified Design

It is clear that when the coil is re-built that the contacts must be re-designed. To reduce the chances of the new coil from failing either the contacts must be secured more strongly to the coil body or the contacts must be designed such that the Lorentz force on them is greatly reduced. As prevention is always better than cure the first step is to reduce the force. The technique for doing this is to minimize the flux linkage in the contacts and so reduce the eddy currents by minimizing the cross-sectional area of the contacts perpendicular to the flux lines. It is clear that the worst possible geometry was a large,

flat disc near to the bore of the coil; exactly the design of contact that failed. The new design for the inner contact consisted of thin rods which could have the wire soldered inside to keep a large contact area. The outer contact design was a thin tombstone shape with a groove around the outside which the wire could be soldered into. The contact was positioned so that it would be edge-on to the applied field so as to have minimal cross-section. The evolution of the force on the new contacts is also shown in Figure 4.31 peaking at just 12N: 250 times lower than the peak on the original design.

The challenge was then to repair the coils. One of the coils was easily repairable as, although the contact had disconnected from the coil body, the wire was largely undamaged; it had just been thinned slightly by spark erosion. The other coil was more challenging as the exposed wire had been destroyed. This coil was repaired by carefully milling through the end-cheek to expose the inner layer of wire below. The first turn was then carefully extracted from the reinforcement and a new 10G/40 cap was made to cover the hole left. This allowed the wire to be jointed to and did not have a measureable difference or the coils inductance or ability to produce magnetic fields.

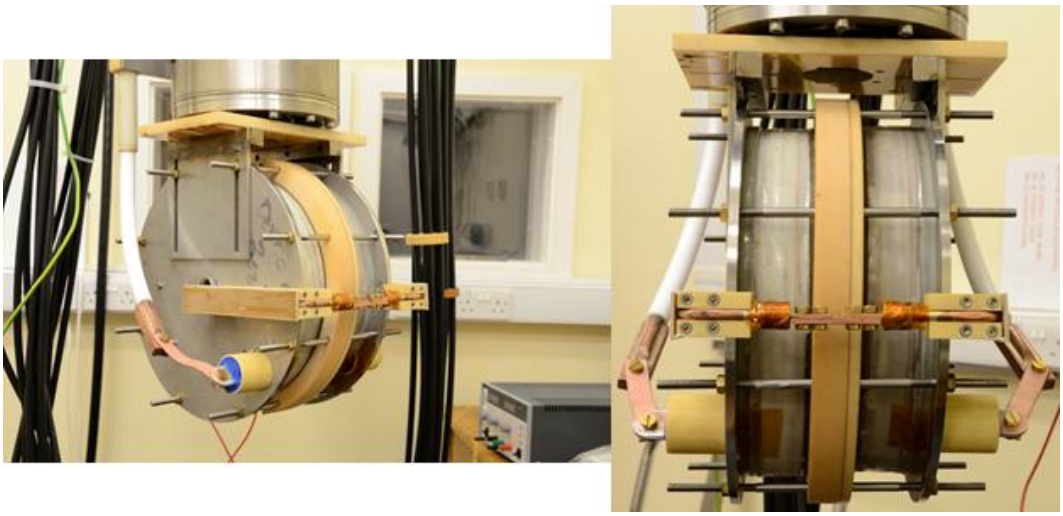

Figure 4.32. The improved coil set-up with the modified contact design.

The new contact designs were soldered onto the wire and were then attached much more firmly to the coil body. The inner contacts were bent round through 6F/45 channels to provide support and electrical insulation and where they passed close to the steel support plates they were potted in Stycast FT2850 to reduce the chances of shorting to the plate occurring again. The outer contacts were simply potted in deep Stycast FT2850 pots to provide mechanical stability and insulation. The completed repaired coil is shown in Figure 4.32 where the new contact designs are clearly visible. The stycast

FT2850 was used as it reasonably conductive (~$0.1 - 1\ W/m \cdot K$) but has excellent dielectric strength (~$14 - 15 kV/mm$ [57])

4.4.6 Second Stage Testing

Once the coil had been repaired and the new contacts had been attached the coil was re-mounted into the pulse module and was tested using exactly the same procedure as in section 4.4.3. Table 4.5 shows the measured characteristics of the coil along with the values predicted during the design stage. The rise time predictions were very accurate: to within 2.2% for a 1/4 bank pulse and 0.8% for the full capacitor bank. It is likely that the accuracy increases with the capacitance used as each capacitor only has a nominal capacitance with a fairly low tolerance on that value. Therefore each of the four 1/4 banks has slightly different capacitance whereas these errors are reduced when more capacitors are used. Furthermore other, small, factors which were not included in the predictions (such as the resistance, inductance and capacitance of the systems wiring) are likely to have a smaller effect as the capacitance becomes larger. The voltage to peak field ratio predicted also proved to be fairly accurate with the 1/4 bank ratio being under by 5.5% and the full bank ration under by 5.1%. These errors are larger than the errors on the rise time as the predicted values do not include system resistance or the increase in resistance due to coil heating during the pulse. Both of these effects will have a small but significant effect on the field achieved from a given voltage. This effect becomes more noticeable as the peak field increases as the coil temperature increases more and so the resistance increases more.

Characteristic	Predicted	Measured
Rise Time (1/4 bank)	30.8 ms	31.5 ms
Rise Time (1/2 bank)	42.8 ms	43.9 ms
Rise Time (3/4 bank)	51.8 ms	52.6 ms
Rise Time (full bank)	59.2 ms	59.7 ms
Voltage-Field Ratio (1/4 bank)	443 V/T	469 V/T
Voltage-Field Ratio (1/2 bank)	326 V/T	357 V/T
Voltage-Field Ratio (3/4 bank)	275 V/T	288 V/T
Voltage-Field Ratio (full bank)	244 V/T	257 V/T

Table 4.5. The predicted and measured rise times and voltage to field ratios for the modified coil.

Figure 4.33 shows as selection of some of the pulses fired from the coil during the course of the testing. The effect of heating reducing the achievable field is apparent when looking at the high field pulses for the full bank. In the end the highest pulse which was successfully completed in the coil had

an amplitude of 19.6T. Unfortunately during a subsequent pulse which was expected to reach 20T the coil failed again, this time on one of the outer current contacts. It appear that the cause of failure was either high voltage breakdown of the wire insulation or that the wire had been damaged slightly where it had been bent into the coil, resulting in a spot with higher resistance which in turn caused excessive local heating. Of these two failure modes the high voltage insulation breakdown seems the most likely. This is because the failure occurred very early in the pulse (after a few ms) when the currents, magnetic fields and temperatures would all still be very low but the voltage would be at its highest value. As the body of the coil was undamaged it appears that the body of the coil was well designed and if the coil was to be re-built or repaired then the same body design could be used with confidence.

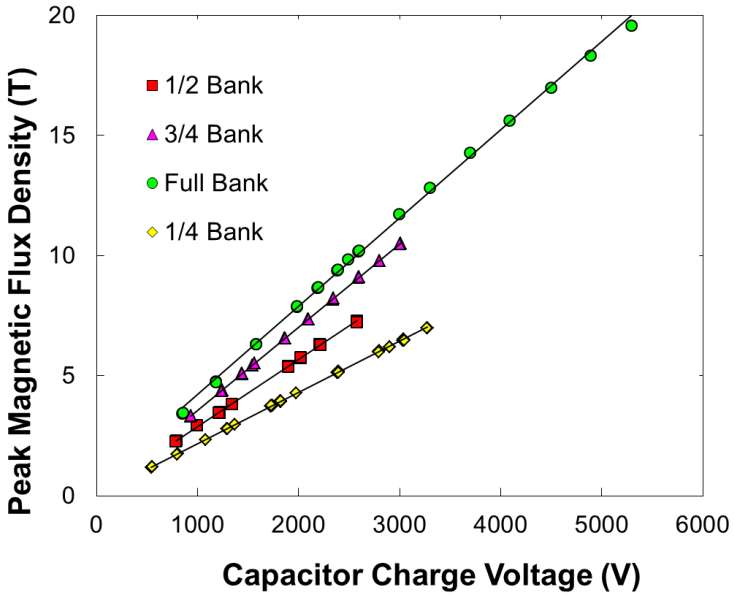

Figure 4.33. Measured peak field against capacitor voltage for the modified coil.

4.5 Conclusion

In summary this chapter has seen the work involved in the conception, design, construction, testing and eventual destruction of a novel high field pulsed coil with a very long pulse length. An analytical method for studying the electromagnetic properties of the coil was detailed before being used to produce an optimized geometry for the coil design which was a horizontal field split pair with a variable inductance. FEA modelling was then used to predict the electromagnetic, thermal and structural properties of the coil. It was predicted that structurally the coil would be capable of producing over 30T and thermally 25-30T. The coil was then constructed by winding a layer of copper which was then reinforced with a layer of Zylon then the completed coil was vacuum impregnated with resin. The testing showed that the electromagnetic predictions had been very accurate ultimately

the coil successfully produced a pulse of nearly 20T before undergoing voltage breakdown at one of the outer current contacts during an attempt at a 20+T pulse.

The coil design proved to be successful as an experiment into flux trapping in high temperature superconductors (chapter 6) was conducted in it before its failure. Furthermore, due to the horizontal field, there was some interest in using the coil for other experiments as an anisotropic sample can easily be rotated in field. Therefore it is possible that a new coil of a similar design may be constructed. Any new coil could use the design of the magnet detailed in this chapter with confidence to up to 20T and probably beyond but extra work should be done on the design of the current contacts to reduce the chances of a similar failure occurring again.

References

[1] H. Witte and H. Jones, “High-field magnet facilities and associated technology at Oxford,” *Physica B: Cond. Mat.*, Vols. 346-347, pp. 663-667, 2004.

[2] H. Witte, Magnet Design using Finite Element Analysis: D.Phil Thesis, Department of Physics, University of Oxford, 2007.

[3] H. E. Knoepfel, Magnetic Fields: A comprehansive Theoretical Treatise for Pratical Use, New York: John Wiley and Sons, Inc., 2000.

[4] B. Montgomery, Solenoid Magnet Design, New York: Wiley-Interscience, 1980.

[5] J. D. Kraus, Ectromagnetics: With Applications 5th edition, London: McGraw-Hill, 1999.

[6] B. I. Bleaney and I. Bleaney, Electricity and Magnetism 3rd edition, Oxford: Oxford University Press, 1989.

[7] H. A. Wheeler, “Simple Inductance Formulas for Radio Coils,” *Proc. IRE*, vol. 16, no. 10, pp. 1398-1400, 1928.

[8] W. J. Duffin, Electricity and Magnetism 4th edition, London: McGraw-Hill, 1990.

[9] R. Gersdorf, F. A. Muller and L. W. Roeland, “Design of High Filed Magnet Coils for Long Pulses,” *Rev. Sci. Intst.*, vol. 36, no. 8, pp. 1100-1109, 1965.

[10] W. D. Pilkey, Formulas for stress, strain, and structural matrices; 2nd edition, New York: Wiley, 2005.

[11] W. C. Young and R. G. Budynas, Roark's Formulas for Stress and Strain 7th edition, London: Mcgraw-Hill, 2002.

[12] R. G. Budynas, Advanced Strength and Applied Stress Analysis 2nd edition, London: McGraw-Hill, 1999.

[13] I. Vagner, B. I. Lembrikov and P. Wyder, Electrodynamics of Magnetoactive Media, London: Springer, 2004.

[14] A. Van den Bossche, V. C. Valchev and S. T. Barudov, “Practical Wide Frequency Approach for Calculating Eddy Current Losses in Transformer Windings,” *IEEE ISIE,* vol. 2, pp. 1070-1074, 2006.

[15] Z. S. Shao, “Mechanical and thermal stresses of a functionally graded circular hollow cylinder with finite length,” *Int. Jour. Press. Ves. and Pip.,* vol. 82, no. 3, pp. 155-163, 2005.

[16] Comsol Ltd, Comsol Multiphysics User's Guide, Cambridge: Comsol Ltd, 2011.

[17] Comsol Ltd, Comsol ACDC Module Users' Guide, Cambridge: Comsol Ltd, 2011.

[18] Comsol Ltd, Structural Mechanics Module User's Guide, Cambridge: Comsol Ltd, 2011.

[19] H. Jones, F. Herlach, J. A. Lee, H. M. Whitworth, A. G. Day, D. J. Jeffery, D. Dew-Hughes and G. Sherratt, “50 tesla pulsed magnets using a copper conductor externally reinforced with stainless steel,” *IEEE Trans. Mag.,* vol. 24, no. 2, pp. 1055-1058, 1988.

[20] Y. Sakai, K. Inoue, T. Asano and H. Maede, “Development of a high strength, high conductivity copper-silver alloy for pulsed magnets,” *IEEE Trans. Mag.,* vol. 28, no. 1, pp. 888-891, 1992.

[21] A. K. Shikov, V. I. Pantsyrnyi, A. E. Vorob'eva, S. V. Sud'ev, N. E. Khlebova, A. K. Silaev and N. A. Belyakov, “Copper-Niobium High-Strength and High-Conductivity Winding Wires for Pulsed Magnets,” *Met. Sci. and Heat Treat.,* vol. 44, no. 11-12, pp. 491-495, 2002.

[22] V. I. Pantsyrnyi, “Status and perspectives for microcomposite winding materials for high field pulsed magnets,” *IEEE Trans. Ap. Sup.,* vol. 12, no. 1, pp. 1189-1194, 2002.

[23] Springer handbook of condensed matter and materials data, Berlin: Springer, 2004.

[24] J. Bevk, J. P. Harbison and J. L. Bell, “Anomalous Increase in Strength of in situ Formed Cu-Nb Multifilamentary Coposites,” *J. Ap. Phys.,* vol. 49, no. 12, pp. 6031-6038, 1978.

[25] J. Freudenberger, A. Gaganov, A. L. Hickman and H. Jones, "Mechanical behaviour of high nitrogen stainless steel reinforced conductor for use in pulsed high field magnets at cryogenic temperature," *Cryogenics*, vol. 43, no. 2, pp. 133-136, 2003.

[26] K. Kindo, "100 T magnet developed in Osaka," *Physica B,* Vols. 284-285, pp. 585-590, 2001.

[27] B. D. Agarwai, L. j. Broutman and K. Chandrashekhara, Analysis and performance of fiber composites., Hoboken, N.J.: John Wiley, 2006.

[28] G. Lubin, Handbook of composites, New York: Van Nostrand Reinhold, 1982.

[29] Agy, "High Strength Glass Fibres: Technical Paper," Agy, Aiken, USA, 2006.

[30] M. R. Etemad, E. Pask and C. B. Besant, "Hoop strength characterization of high strength carbon fibre composites," *Composites,* vol. 23, no. 4, pp. 253-259, 1992.

[31] Toyobo Co. Ltd., "Zylon Technical Datasheet," 2005. [Online]. Available: www.toyobo-global.com. [Accessed 2011].

[32] M. Cheng, W. Chen and T. Weerasooriya, "Mechanical Properties of Kevlar® KM2 Single Fiber," *J. Eng. Mater. Tech.,* vol. 127, no. 2, pp. 197-203, 2005.

[33] H. M. Ledbetter and M. W. Austin, "Elastic constant versus temperature behavior of three hardened maraging steels," *Mat. Sci. and Eng.,* vol. 72, no. 1, pp. 65-69, 1985.

[34] R. P. Walsh and C. A. Swenson, "Mechanical Properties of Zylon/Epoxy Composite at 295K and 77K," *IEEE Trans. Ap. Super.,* vol. 16, no. 2, pp. 1761-1764, 2006.

[35] Y. K. Huang, P. H. Frings and E. Hennes, "Exploding Pressure Vessel Test on Zylon/Epoxy Composite," *Comp. B,* vol. 33, pp. 117-123, 2002.

[36] H. Jones and A. L. Hickman, "Insulation and Impregnation procedures used in Magnet Technology at the Clarendon Laboratory," *IEEE Trans. Ap. Sup,* vol. 10, no. 1, p. 1345, 2000.

[37] D. H. J. Goodall, "Cryogenic Data," Culham Laboratory, Culham, 1970.

[38] Y. K. Huang, P. H. Frings and E. Hennes, “Mechanical Properties of Zylon/epoxy Composite,” *Composites B,* vol. 115, no. 1, p. 109, 2002.

[39] S. V. Hart, “Third status report to the academy general on body armor safety initiative testing and activities,” U.S. Department of Justice, Washington, 2005.

[40] S. U. Haq, S. H. Jayaram and E. A. Cherney, “Evaluation of medium voltage enameled wire exposed to fast repetitive voltage pulses,” *IEEE Trans. Dielec. Elec. Insul.,* vol. 14, no. 1, pp. 194-203, 2007.

[41] S. Grzybowski, C. D. Taylor and S. R. Chalise, “Electrical Degradation Study of Machine Winding Insulation,” *ICHVE 2008,* pp. 321-325, 2008.

[42] H. Jones, “Private communication, Clarendon Laboratory, Parks Road, Oxford, OX1 3PU,” 2011.

[43] “Grade 10G/40 Epoxy Glass Fabric Prouct Data Sheet,” Bay Plastics Ltd, [Online]. Available: www.bayplastics.co.uk. [Accessed 2011].

[44] “Grade 6F/45 Epoxy Cotton Product Data Sheet,” Bay Plastics Ltd, [Online]. Available: www.bayplastics.co.uk. [Accessed 2011].

[45] F. Pawlek and D. Rogalla, “The electrical resistivity of silver, copper, aluminium, and zinc as a function of purity in the range 4–298° K,” *Cryogenics,* vol. 6, no. 1, pp. 14-20, 1966.

[46] Copper Development Association, “Mechanical Properties of Copper and Copper Alloys at Low Temperatures,” [Online]. Available: www.copper.org. [Accessed 2010].

[47] Ciba, Araldite CY1300 Casting Resin System, Ciba Specialty Chemicals Inc., 1998.

[48] J. Freudenberger, Private Communication, Leibniz-Institut fuer Festkoerper- und Werkstoffforschung Dresden, Helmholtzstr. 20 D-01069 Dresden , November 2009.

[49] Agy, Product Information S2-glass yarn, Lyon: Agy, 2004.

[50] J. R. Davis, Copper and copper alloys, USA: ASM International, 2001.

[51] J. W. Ekin, Experimental techniques for low-temperature measurements; cryostat design, material property, and superconductor critical-current testing, Oxford: Oxford University Press, 2006.

[52] H. Fujishiro, M. Ikebe, T. Kashima and A. Yamanaka, "Thermal Conductivity and Diffusivity of High-Strength Polymer Fibers," *Jpn. J. Ap. Phys.*, vol. 36, pp. 5633-5637, 1997.

[53] K. Saito, Y. Takahashi and M. Sorai, "Heat capacity and thermodynamic functions of crystalline poly(p-phenylenebenzobisoxazole), the synthetic polymer with the highest Young's modulus," *J. Poly. Sci. B: Poly. Phys.*, vol. 38, no. 11, pp. 1584-1588, 2000.

[54] R. P. Reed and M. Golda, "Cryogenic properties of filamentary-reinforced composites: an update," *Cryogenics,* vol. 34, no. 11, pp. 909-928, 1994.

[55] J. G. Hust, "Low-temperature thermal conductivity of two fibre-epoxy composites," *Cryogenics,* vol. 15, no. 3, pp. 126-128, 1975.

[56] I. E. Evseeva and S. A. Tanaeve, "Thermophysical properties of epoxy composite materials at low temperatures," *Cryogenics,* vol. 35, no. 4, pp. 277-279, 1994.

[57] "High Voltage Breakdonw of Solid Epoxies at Room Temperature and in Liquid Nitrogen," *An. Rep. Conf. Elec. Insul. and Diel. Phen.*, pp. 542-545, 2002.

[58] P. D. Craig and J. Summerscales, "Poisson's ratios in glass fibre reinforced plastics," *Comp. Struc.*, vol. 9, no. 3, pp. 173-188, 1988.

[59] "Mechanical properties for stainless steels to BS EN 10217-7," British Stainless Steel Association, 2005. [Online]. Available: http://www.bssa.org.uk/topics.php?article=347. [Accessed 2009].

[60] N. J. Saleh, A. A. Abdul Razak, M. A. Tooma and M. E. Aziz, "A study on mechanical properties of epoxy resin cured at constant curing time and temperature with different hardeners," *Eng. and Tech. Jour.*, vol. 29, no. 9, pp. 1804-1818, 2011.

5 Explosive Vessel Testing of High Tensile Fibres

5.1 Introduction

In the previous chapter we saw that one of the most important factors involved in the successful design of a high field pulsed coil is accurate knowledge of the properties of the materials used. The traditional method for obtaining material data is to test short samples in a tensile testing machine. This is a device which applies an ever increasing known load to the sample whilst measuring the strain of the sample. This method works extremely well for isotropic materials such as copper and steel as their properties are invariant with the direction from which they are measured and scale linearly with size. This method also works well for measuring the properties of single high tensile fibres (or small groups of fibres) along the length of the fibres. However these materials are extremely anisotropic and so measuring properties along the length of the fibres will tell you little to nothing about the properties transverse to the fibres. Also high tensile fibres are rarely used individually; they are bundled together and impregnated in a resin to form a composite material. The properties of these depend highly on the density of the fibres in the material so knowing the properties of one fibre does not necessarily tell you how a composite will behave. To further complicate matters when obtaining material data for pulsed coils the fibres are actually used in multilayer composites with the force applied on the fibres perpendicular to the length of the fibre. Therefore what is needed is a method of testing the fibres in an axially symmetric environment at both room and cryogenic temperatures so that bench mark results can be created with which FEA analysis and theory can be compared.

A lot of effort has been made to create tensile testing rigs which can test the fibres in a geometry which can be approximated as a cylindrical geometry [1]. For tests which use a truly cylindrical geometry various methods have been considered over the years all based around forming the fibre to be tested into a cylinder and then creating an internal pressure. This will then induce a hoop stress in the composite and the strain and bursting pressure can easily be measured. As this form of testing is directly relevant to the design of high pressure vessels and pipes a reasonable amount of work has been carried out on glass and carbon fibre [2] [3]. On glass and carbon fibre most of the work has been carried out at room temperature but there has been some limited work carried out at cryogenic temperatures (both liquid nitrogen and hydrogen [4]). It is worth noting that of the limited

experimental data available on composites to date only one paper has been published to date on Zylon tested in this configuration and this was only at room temperature [5].

A common factor in all the methods found in the literature is that they use a liquid as the medium to transmit the pressure to the composite ranging from oil, water and liquid cryogens (N_2 and H_2). The advantages of oil and water are that they are relatively easy to use but are obviously unsuitable for any temperatures below about $0°C$ as the medium will freeze solid. For cryogenic temperatures liquid cryogens have been used but these too have their disadvantages primarily that a different pressurizing system would be required for room and cryogenic temperatures.

A key part of any high pressure testing system is the seal between the sample and the apparatus. A variety of methods have been tried over the years. Some of the older work consisted of manufacturing free standing cylinders of the composite and then potting the ends in a low melting point solder [2]. Another method is again to manufacture a free composite cylinder and then to use rubber O-ring seals pressed against the sample by tapered wedges [3]. Yet another was to use epoxy resin to glue the cylinder into 10G/40 end cheeks [6]. The other main method is to manufacture a cylinder of metal (aluminium [7], steel [4] and copper [5] have all been used). The metal cylinder is then a liner over which the fibre can be wound. Joints can then be formed to the liner by a metal-metal press seals or by soldering/welding.

All of the above sealing methods have their advantages and disadvantages. The use of free standing cylinders with seals formed directly to end cheeks is highly prone to leaks. This is because it is highly dependent on the entire sample and seal being immaculate as any slight imperfection will allow the pressurizing medium to leak through. Furthermore, even if the sample is leak tight at room temperature thermal cracks may appear as the sample is cooled to cryogenic temperatures and some sealing methods such as the O-rings are entirely unsuitable for temperatures below room temperature. Adding a liner will remove the problems of leaking through the composite but sealing problems still remain. Metal-metal press seals will suffer from the same leaking problems as any imperfection will allow the pressurizing medium to escape; a problem which will only get worse as the pressure increases as any clamps holding the seal together will begin to flex. Therefore a liner with a fixed seal, such as soldering or welding, is deemed to be the most robust and dependable but will still depend on careful quality control as the joint is made. A liner will also add the complication that it will take some

of the stress so that the actual stress exerted on the inner wall of the composite will be reduced. This effect needs to be taken into account during any data analysis and needs to be minimized at the design stage.

For this work the pressurizing medium used is helium gas. The use of gas is almost unique in the literature and has the large advantage that only one medium need be used for any temperature above about 5K (the exact minimum temperature would depend on the pressure to which the gas was taken). However, it does mean that extra care needs to be taken when considering the method for sealing the vessel as gas will escape much more easily than a liquid. The actual vessel used will have a copper liner sealed by brazing. Copper will be used for the liner as it is easily annealed so that very large plastic deformations will be achievable and it will contribute very little to the strength of the cylinder.

5.2 Theory

For the vessel it is important to have a theoretical model to compare any measured results to. This is due to the fact that there are not one, but two, different materials affecting the results so having a copper layer will reduce the stress exerted on the fibre. Furthermore, once we have removed the contribution from the copper, we need to be able to determine the actual material data from just the strain measured at the surface of the composite and from the pressure of the helium gas. Although this can and will be achieved by using FEA any results produced will not be useful unless the FEA models can be validated by comparison to an analytical model.

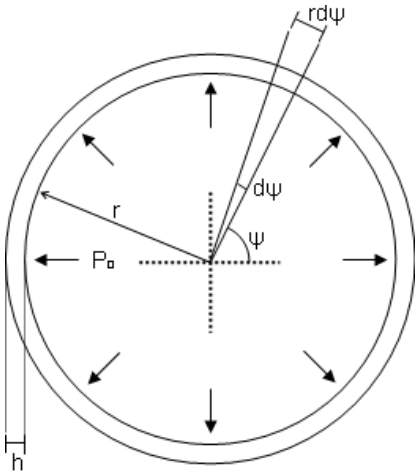

Figure 5.1. A cylindrical thin-walled vessel with an internal pressure.

The starting point for an analytical theoretical model for this axially symmetric system is to consider a cylindrical vessel of infinite length so that end effects play no part. For now we will consider only

'thin' walled vessels. This means that the radius of the vessel is much greater than the thickness of the vessel walls. If we consider a vessel with radius, r, and thickness, h, and apply an internal pressure, P_0, inside the vessel as shown in Figure 5.1 then the force on an infinitesimal section of the vessel will be $P_0 r d\psi$.

By considering the vertical components of the force, $\sin\phi\, P_0 r d\psi$, on half of the cylinder, in equilibrium the force is:

$$F = \int_0^{\frac{\pi}{2}} \sin\psi\, P_0 r d\psi = P_0 r \tag{5.1.}$$

Therefore, as in a thin walled vessel the stress can be assumed to be constant across the thickness, the hoop stress, σ_ϕ, is simply:

$$\sigma_\theta = \frac{P_0 r}{h} \tag{5.2.}$$

as stated in equation 4.68. As has already been mentioned earlier, when a material is stressed it will undergo a strain and elongate. As it elongates in one dimension it will contract in the other dimensions by an amount related to the primary strain by the Poisson's ratio, ν; so a strain ε_1 will cause a strain in the other directions. In a general isotropic system with two dimensions, stresses σ_1 and σ_2 and a Young's modulus, E, the strain will be given by:

$$\varepsilon_1 = \frac{\sigma_1}{E} - \frac{\upsilon\sigma_2}{E} \tag{5.3.}$$

$$\varepsilon_2 = \frac{\sigma_2}{E} - \frac{\upsilon\sigma_1}{E} \tag{5.4.}$$

Rearranging these equations leads to the expressions for the stresses in terms of the strains:

$$\sigma_1 = \frac{(\varepsilon_1 - \upsilon\varepsilon_2)E}{1-\upsilon^2} \tag{5.5.}$$

$$\sigma_2 = \frac{(\varepsilon_2 - \upsilon\varepsilon_1)E}{1-\upsilon^2} \tag{5.6.}$$

However for the vessel that will be designed the most accurate results will be found by considering the stresses in a thick walled vessel. In such a vessel the magnitude of the stresses will vary through the material. For now we will only consider isotropic materials and follow the derivation found in Harvey [8]. Figure 5.2 shows a diagram of such a thick walled vessel and highlights an infinitesimal section

marked by abb'a'. By symmetry the radial stress will vary only with the position r, not in z or ϕ and so if the radial stress at r is σ_r then the stress at position $r + dr$ is simply:

$$\sigma(r + dr) = \sigma_r + \frac{d\sigma_r}{dr} \cdot dr \tag{5.7.}$$

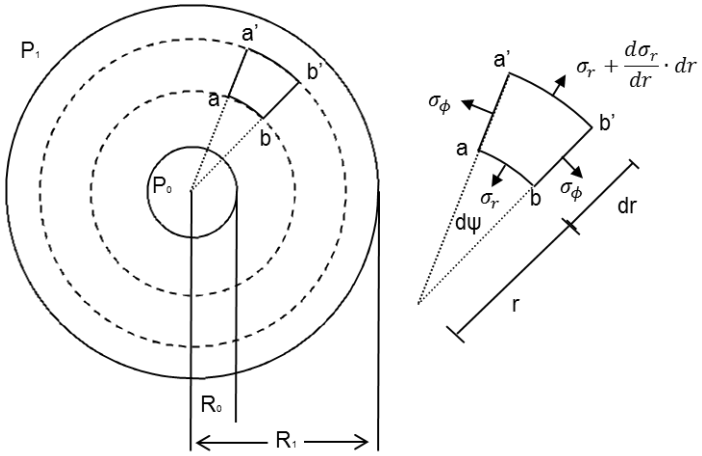

Figure 5.2. An infinitesimal section abb'a' of a thick wall cylinder subject to an internal pressure P_0 and external pressure P_1.

If the section is in equilibrium then the forces must be balanced in the radial direction including the component from the stress in the azimuthal direct which for an sector angle $d\psi$ is simply $\sigma_\phi \sin\psi$. Noting that for small angles $\sin\psi \cong \psi$ and as the force is simply a stress over an area the total forces in the radial direction are:

$$\sigma_r r d\psi + \sigma_\phi dr d\psi - \left(\sigma_r + \frac{d\sigma_r}{dr} \cdot dr\right)(r + dr)d\psi = 0 \tag{5.8.}$$

$$\sigma_\phi - \sigma_r - r\frac{d\sigma_r}{dr} = 0 \tag{5.9.}$$

We know that by applying a force we will cause the material to strain and hence will cause each point of an element to displace. If we let u be the displacement in the radial direct at a distance r then as the magnitude of the displacement will vary with radius (in the same manner as the stress earlier) the displacement at $r + dr$ will be:

$$u(r + dr) = u(r) + \frac{du}{dr} \cdot dr \tag{5.10.}$$

This will lead to a radial strain of the unit cell per unit length of:

$$\varepsilon_r = \frac{u(r + dr) - u(r)}{dr} = \frac{du}{dr} \tag{5.11.}$$

For a displacement of u at r there is a corresponding strain in the azimuthal direction given by:

$$u = \int_0^{\frac{\pi}{2}} \varepsilon_\phi r \cos\psi \, d\psi = \varepsilon_\phi r$$

$$\varepsilon_\phi = \frac{u}{r} \qquad 5.12.$$

These expressions for the strains can now be substituted into equations 5.5 and 5.6 to give the pair of equations:

$$\sigma_r = \frac{E}{1-\upsilon^2} \cdot \left[\frac{du}{dr} + \upsilon \frac{u}{r}\right] \qquad 5.13.$$

$$\sigma_\phi = \frac{E}{1-\upsilon^2} \cdot \left[\frac{u}{r} + \upsilon \frac{du}{dr}\right] \qquad 5.14.$$

By substituting these into equation 5.9 we can obtain the equation for equilibrium in terms of the displacement of the material:

$$\frac{d^2u}{dr^2} + \frac{1}{r}\frac{du}{dr} - \frac{u}{r^2} = 0 \qquad 5.15.$$

This is a Euler equation which has a general solution $u \propto r^n$. Substituting this into equation 5.15 gives the simple solution of $n = \pm 1$. Therefore the general solution is:

$$u = C_1 r + \frac{C_2}{r} \qquad 5.16.$$

Where C_1 and C_2 are constants. By substituting this back into equations 5.13 and 5.14 we get the equations which give the dependence of the stresses on position through the material:

$$\sigma_r = \frac{E}{1-\upsilon^2} \cdot \left[C_1(1+\upsilon) - C_2\frac{(1-\upsilon)}{r^2}\right] \qquad 5.17.$$

$$\sigma_\phi = \frac{E}{1-\upsilon^2} \cdot \left[C_1(1+\upsilon) + C_2\frac{(1-\upsilon)}{r^2}\right] \qquad 5.18.$$

Before this equation can actually be used we must apply some boundary conditions. These are obviously that the radial stress at the inner surface is $-P0$ and the stress at the outer surface is $-P1$ as these are just the applied pressures. Substituting these into equation 5.17 gives a pair of simultaneous equations which can be solved to gain the values of C_1 and C_2:

$$C_1 = \frac{(1-\upsilon)}{E}\left(\frac{R_0^2 P_0 - R_1^2 P_1}{R_1^2 - R_0^2}\right), \qquad C_2 = \frac{(1+\upsilon)}{E}\left(\frac{R_0^2 R_1^2}{R_1^2 - R_0^2}\right)(P_0 - P_1) \qquad 5.19.$$

Finally we can express the stresses through the isotropic material as a function of position with equations which only contain fundamental properties of the cylinder:

$$\sigma_r = \frac{P_0 T_1^2 \left[1 - \left(\frac{R_1}{r}\right)^2\right] - P_1 \left[1 - \left(\frac{R_0}{r}\right)^2\right]}{1 - T_1^2} \quad 5.20.$$

$$\sigma_\phi = \frac{P_0 T_1^2 \left[1 + \left(\frac{R_1}{r}\right)^2\right] - P_1 \left[1 + \left(\frac{R_0}{r}\right)^2\right]}{1 - T_1^2} \quad 5.21.$$

where: $$T_1 = \frac{R_0}{R_1}$$

As governed by the Poisson's ratio this will of course cause one further stress in the direction of the axis of the cylinder given by:

$$\sigma_z = \upsilon(\sigma_r + \sigma_\phi) \quad 5.22.$$

The equations derived so far are only applicable for isotropic materials so will describe the stress distribution in the copper liner but are not adequate to describe the behaviour of the fibre wound layers. This is because, as alluded to earlier, they are orthotropic. Orthotropic materials are a subset of anisotropic materials in that their properties depend entirely on the direction which is being considered but they do have at least two orthogonal symmetry planes. In an isotropic material plane stresses will only cause plane strains and vice-versa shear stresses only cause shear strains. In contrast a fully anisotropic material plane stresses will cause shear strains and shear stresses will cause plane strains. In an orthotropic material, if the stresses are applied perpendicular to one of the symmetry planes then the material will behave isotropically; if it is applied in any other direction it will behave anisotropically. Therefore it is useful when analysing orthotropic materials to work in a coordinate axis such that the principal stress directions lie along the symmetry directions of the material. In the case of a wound cylinder there are three symmetry planes in that the properties will be the same in the axial and radial directions; i.e. perpendicular to the fibres, but will be markedly different in the azimuthal direction. Therefore we must modify the Young's modulus and Poisson's ratio used in equations 5.3 and 5.4 as $E_z = E_r \neq E_\emptyset$ and $\upsilon_{zr} = \nu_{rz}$, $\nu_{\emptyset r} = \nu_{\emptyset z}$. To get an understanding of how this will affect our results we must introduce the stiffness matrix. This is simply the full tensor form of equation 4.69 and we have been using the isotropic form to reach equations such as 5.3 and 5.4. For a

general orthotropic material the strains are expressed by using the inverse of the stiffness matrix: the compliance matrix:

$$\begin{bmatrix} \varepsilon_r \\ \varepsilon_\phi \\ \varepsilon_z \\ \varepsilon_{\phi z} \\ \varepsilon_{zr} \\ \varepsilon_{r\phi} \end{bmatrix} = \begin{bmatrix} \frac{1}{E_r} & -\frac{\upsilon_{\phi r}}{E_\phi} & -\frac{\upsilon_{zr}}{E_z} & 0 & 0 & 0 \\ -\frac{\upsilon_{r\phi}}{E_r} & \frac{1}{E_\phi} & -\frac{\upsilon_{z\phi}}{E_z} & 0 & 0 & 0 \\ -\frac{\upsilon_{rz}}{E_r} & -\frac{\upsilon_{\phi z}}{E_\phi} & \frac{1}{E_z} & 0 & 0 & 0 \\ 0 & 0 & 0 & \frac{1}{2G_{\phi z}} & 0 & 0 \\ 0 & 0 & 0 & 0 & \frac{1}{2G_{zr}} & 0 \\ 0 & 0 & 0 & 0 & 0 & \frac{1}{2G_{r\phi}} \end{bmatrix} \begin{bmatrix} \sigma_r \\ \sigma_\phi \\ \sigma_z \\ \sigma_{\phi z} \\ \sigma_{zr} \\ \sigma_{r\phi} \end{bmatrix} \quad 5.23.$$

For this orthotropic material, as the properties are the same in the r and z directions, the following relations can be used:

$$\frac{\upsilon_{r\phi}}{E_r} = \frac{\upsilon_{\phi r}}{E_\phi};\ \frac{\upsilon_{z\phi}}{E_z} = \frac{\upsilon_{\phi z}}{E_\phi} = \frac{\upsilon_{\phi r}}{E_\phi} \quad 5.24.$$

For the specific orthotropic material of composite cylinders the axial strains are assumed to be small so are set to zero and so the strains of the system are:

$$\varepsilon_r = \frac{\sigma_r}{E_r} - \frac{\upsilon_{\phi r}\sigma_\phi}{E_\phi} - \frac{\upsilon_{zr}\sigma_z}{E_z} = \frac{1}{E_r}\left(\sigma_r - \upsilon_{r\phi}\sigma_\phi - \upsilon_{rz}\sigma_z\right) \quad 5.25.$$

$$\varepsilon_\phi = \frac{\sigma_\phi}{E_\phi} - \frac{\upsilon_{r\phi}\sigma_r}{E_r} - \frac{\upsilon_{z\phi}\sigma_z}{E_z} = \frac{1}{E_\phi}\left(\sigma_\phi - \upsilon_{\phi r}\sigma_r - \upsilon_{\phi r}\sigma_z\right) \quad 5.26.$$

$$\varepsilon_z = \frac{\sigma_z}{E_z} - \frac{\upsilon_{rz}\sigma_r}{E_r} - \frac{\upsilon_{\phi z}\sigma_\phi}{E_\phi} = \sigma_z - \upsilon_{rz}\sigma_r - \upsilon_{r\phi}\sigma_\phi = 0 \quad 5.27.$$

From this stage we can follow the same steps for deriving the dependence on stress with distance as used for the isotropic material. We can rearrange these equations to give the stresses in terms of the strains and then substitute the strains into equations 5.11 and 5.12:

$$\sigma_r = \frac{1 - \upsilon_{r\phi}\upsilon_{\phi r}}{\alpha} \cdot \left[E_r \frac{du}{dr} + \left(\frac{\upsilon_{r\phi} + \upsilon_{r\phi}\upsilon_{rz}}{1 - \upsilon_{r\phi}\upsilon_{\phi r}}\right) E_\phi \frac{u}{r}\right] \quad 5.28.$$

$$\sigma_\phi = \frac{1 - \upsilon_{rz}^2}{\alpha} \cdot \left[E_\phi \frac{u}{r} + \left(\frac{\upsilon_{\phi r} + \upsilon_{\phi r}\upsilon_{rz}}{1 - \upsilon_{rz}^2}\right) E_r \frac{du}{dr}\right] \quad 5.29.$$

$$\alpha = 1 - 2\upsilon_{r\phi}\upsilon_{\phi r} - 2\upsilon_{r\phi}\upsilon_{\phi r}\upsilon_{rz} - \upsilon_{rz}^2$$

These can then be substituted into equation 5.9 to give:

$$E_r \frac{d^2u}{dr^2} + \frac{E_r}{r}\frac{du}{dr} + \left(\frac{1 - \upsilon_{rz}^2}{1 - \upsilon_{r\phi}\upsilon_{\phi r}}\right)\frac{E_\phi}{r^2}u = 0 \qquad 5.30.$$

Like equation 5.15 this is a Euler equation so the solution will again be of the form $u \propto r^n$ but the value of n will not be so neat. Substituting $u = r^n$ into equation 5.30 then dividing through by r^{n-2} yields:

$$E_r n(n-1) + E_r n + \left(\frac{1 - \upsilon_{rz}^2}{1 - \upsilon_{r\phi}\upsilon_{\phi r}}\right)E_\phi = 0$$

$$E_r n^2 + \left(\frac{1 - \upsilon_{rz}^2}{1 - \upsilon_{r\phi}\upsilon_{\phi r}}\right)E_\phi = 0 \qquad 5.31.$$

which can easily be solved for n to give:

$$n = \pm\sqrt{\frac{1 - \upsilon_{rz}^2}{1 - \upsilon_{r\phi}\upsilon_{\phi r}}\frac{E_\phi}{E_r}} \qquad 5.32.$$

Using this the general solution to equation 5.30 is then:

$$u = C_3 r^n + C_4 r^{-n} \qquad 5.33.$$

where the positive solution of equation 5.32 is used. In the same manner as for the isotopic material we can insert this solution back into equations 5.28 and 5.29 and apply relevant boundary conditions. For the isotropic cylinder earlier an external pressure, along with the internal pressure, was applied as any fibre wound on top of the inner cylinder will exert a large inward pressure. However the fibre cylinder will only be surrounded by air which will exert a pressure which is very small to the magnitude of the internal one so for simplicity the external pressure is assumed to be zero. Therefore for a fibre cylinder with an inner radius R_2, an outer radius R_3 and an inner pressure P_2, we arrive at the solution for the variation of the stresses:

$$\sigma_r = \frac{P_2 T_2^{n+1}}{1 - T_2^{2n}}\left[\left(\frac{r}{R_3}\right)^{n-1} - \left(\frac{R_3}{r}\right)^{n+1}\right] \qquad 5.34.$$

$$\sigma_\phi = \frac{P_2 n T_2^{n+1}}{1 - T_2^{2n}}\left[\left(\frac{r}{R_3}\right)^{n-1} + \left(\frac{R_3}{r}\right)^{n+1}\right] \qquad 5.35.$$

where $T_2 = R_2/R_3$. These stresses will cause a stress in the axial direct given by:

$$\sigma_z = \upsilon_{rz}\sigma_r + \upsilon_{r\phi}\sigma_\phi \tag{5.36.}$$

The final stage of the derivation is to match the conditions on the inner, isotropic cylinder, to the outer, orthotropic cylinder. If the outer cylinder is wound tightly onto the inner cylinder then it is immediately obvious that $R_1 = R_2$. It is also clear that the outer pressure on the inner cylinder is the same as the inner pressure of the outer cylinder. The other condition comes from the fact that obviously the inner cylinder cannot pass into the outer cylinder, nor can a gap form between them. Therefore the radial displacement at the interface between the two cylinders must be the same for both cylinders. The boundary conditions are thus:

$$\begin{gathered} P_1 = P_2 \\ u_r^{(1)}(R_1) = u_r^{(2)}(R_1) \end{gathered} \tag{5.37.}$$

where the superscripts (1) and (2) are used to denote the inner and outer cylinder respectively. The radial displacement can be calculated easily as, due to the symmetry of the system, the only direction in which the system can displace is radially. Therefore for the inner cylinder the radial displacement can be calculated by starting from equation 5.12:

$$\begin{gathered} u_r^{(1)} = u^{(1)} = r\varepsilon_\phi = \frac{r}{E}\Big(\sigma_\phi - \upsilon(\sigma_r + \sigma_z)\Big) \\ u_r^{(1)} = \frac{r}{E}\Big(\sigma_\phi^{(1)}(1-\upsilon^2) - \sigma_r^{(1)}\upsilon(1+\upsilon)\Big) \end{gathered} \tag{5.38.}$$

Similarly for the outer cylinder:

$$u_r^{(2)} = \frac{r}{E_\phi}\Big(\sigma_\phi^{(2)}\big(1 - \upsilon_{r\phi}\upsilon_{\phi r}\big) - \sigma_r^{(2)}\upsilon_{\phi r}(1+\upsilon_{rz})\Big) \tag{5.39.}$$

By combining equations 5.37, 5.38 and 5.39 we can calculate the pressure P_1 as:

$$P_1 = \tau P_0 \tag{5.40.}$$

$$\tau = \frac{\dfrac{2T_1^2(1-\upsilon^2)}{E(1-T_1^2)}}{\left\{\dfrac{-\upsilon(1+\upsilon)}{E} + \dfrac{(1-\upsilon^2)(1+T_1^2)}{E(1-T_1^2)} + \dfrac{\upsilon_{\phi r}(1+\upsilon_{rz})}{E_\phi} + \dfrac{n\big(1-\upsilon_{r\phi}\upsilon_{\phi r}\big)(1+T_2^{2n})}{E_\phi(1-T_2^{2n})}\right\}} \tag{5.41.}$$

which is the same as the equation derived in [9]. Therefore by measuring the helium pressure within the inner cylinder we can calculate all of the stresses within the fibre composite and we can measure the strain at the surface of the composite. By combining these we can then obtain the material properties which is the primary aim of this investigation. The one complication is that all of the

equations derived so far have assumed that all of the materials used are perfectly elastic so that the Young's modulus will fully describe the tress/strain relationship. However the copper shell will quickly yield giving a non-linear stress-strain curve, creating a large divergence between the perfect theory and real data. To account for this we will use a similar method to the one presented in [5] which is that as the plastic flow of the copper is considered unidirectional. This is because the strain is negative (i.e. compressive) in the radial direction but is positive (tensile) in the tangential direction. This means that we can approximate the copper as behaving in the same manner as in a linear tensile test where the sample extension is around the circumference of the cylinder. Therefore we can replace the specific Young's modulus (σ/ε) with the differential tangent modulus $(d\sigma/d\varepsilon)$ as extracted from stress-strain data for annealed copper for stresses above the yield point. A further simplification is made by assuming the linear tangent modulus used earlier for the stresses in the magnetic coils with pure soft copper shown in Figure 4.13. To find how the strain varies with the pressure, the pressure is increased in small increments with the initial Young's modulus used to calculate the strain until the total stress reaches the yield point. After this point the linear differential modulus is used and the total strain is calculated by using:

$$\varepsilon_{\phi} = \frac{\left(\sigma - \sigma_{yield}\right)}{E_{Tang}} + \varepsilon_{\phi;\, yield} \qquad 5.42.$$

This method will give an appreciable difference of results between theory and measurement for a bare copper vessel but the error that this gives will be greatly reduced when the fibre is also considered.

To test how the predictions from FEA match theory a simple model was created. The model was simply a 1m long copper cylinder with a layer of Zylon wound over the top where the properties of the Zylon were assumed to be the same as used in Chapter 4 for the coil design. The length chosen was long compared to the modelled diameters of the cylinder (10-30mm) so that effects caused by tension and bending of the cylinder are minimized. By varying the pressure, cylinder radius and the thickness of the two materials the quality of the FEA predictions can be validated. The two simplest scenarios are just copper and just Zylon. The predicted stress strain curves for these situations are shown in Figure 5.3 for internal cylinder pressure of up to $25MPa$ for copper and $200MPa$ for Zylon. Figures 5.3 and 5.4 show the predicted stresses and strains against pressure for these two scenarios. They show that for this low stress regime the theory and the FEA predictions are almost identical differing only slightly for the predicted stress on the copper at the yield pressure. Also shown on the stress/strain

graph for the copper cylinder is the full non-linear stress strain curve for copper. It shows that for just copper the linear yielding prediction is a fairly poor approximation for just copper giving an error of up to 12MPa (corresponding to ~10%) for strains of up to 5%.

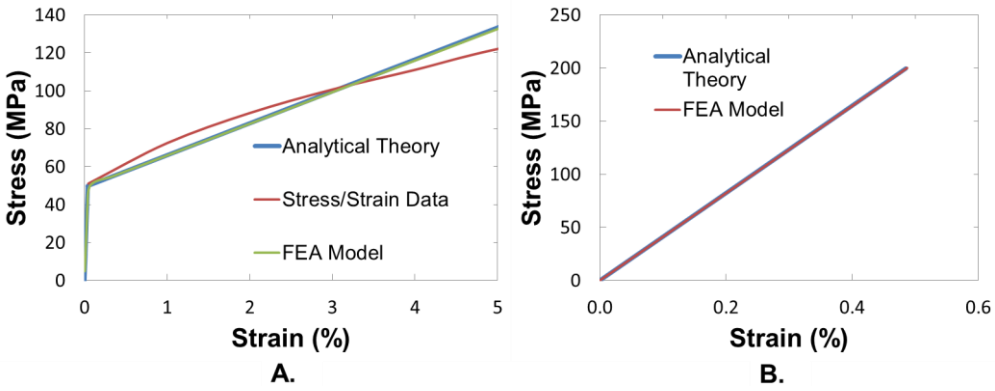

Figure 5.3. Stress/strain curves for an internal cylinder pressure range of A: 0-25MPa (0-250bar) for A pure copper cylinder; B: 0-200MPa (0-2000bar) for a pure Zylon cylinder.

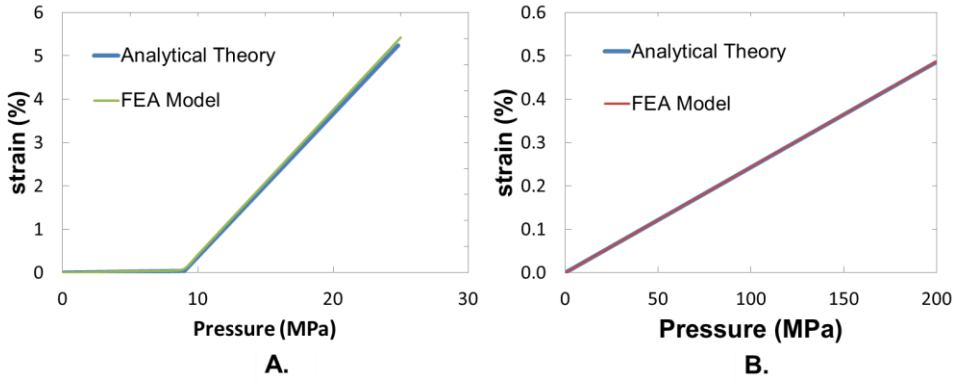

Figure 5.4. Strain/pressure curves for an internal cylinder pressure range of A: 0-25MPa (0-250bar) for A pure copper cylinder; B: 0-200MPa (0-2000bar) for a pure Zylon cylinder.

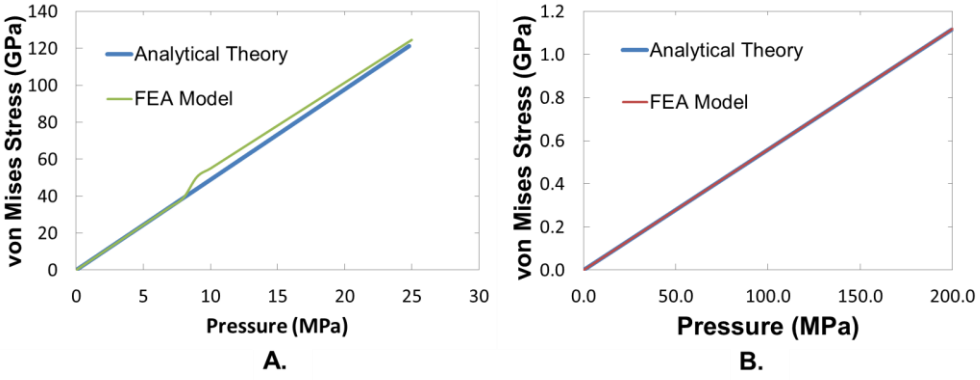

Figure 5.5. Stress/pressure curves for an internal cylinder pressure range of A: 0-25MPa (0-250bar) for A pure copper cylinder; B: 0-200MPa (0-2000bar) for a pure Zylon cylinder.

To test the full theory of coaxially cylinders and the corresponding FEA models various cylinder radii and material thicknesses were tried. Figure 5.6 shows the variation of the azimuthal and axial stresses as a function of position across the two cylinders for a cylinder with an inner radius of 12mm and a 2mm thickness of both copper and Zylon with an internal pressure of 10MPa. It is immediately obvious that for small stresses and strains the theory and the FEA model are in very good agreement; differing only by a maximum of 5% for the axial strain at the interface between the two materials. However when the internal pressure of the cylinder is increased such that the stresses and strains are no longer small the results from the two methods diverge. Figure 5.7 shows the curves for the azimuthal and axial stresses for exactly the same setup as used in Figure 5.6 except that now the internal pressure is 200MPa. The predicted azimuthal stress for both methods still follows a reasonably similar trend but with a differences of up to 100MPa on the predicted stress. In contrast the predicted axial stresses behaved in a very different manner; the two methods cannot even agree on whether the stress at the interface is higher in the Zylon or the copper. Another surprising result from the FEA is that there is a negative hoop stress in the copper at high pressure. This is surprising as in magnets the Lorentz force is applied as a body load, distributed across the entire conductor region, replicated here by the copper liner. Furthermore when considering a magnet it is unusual to consider the stress regime far beyond the yield point of the conductor. The result of this is that the conductor is always under a positive tension. In this case however the loads felt by the copper are surface loads provided by the internal helium gas and the reactionary pressure provided by the Zylon, resulting in a compressive force in the r direction. At low pressures (i.e. at pressures which give a von Mises stress below the yield point of the copper) when the Young's modulus of the copper is high the difference between P_0 and P_1 is large with P_1 being just $4.8MPa$ so less than 50% of P_0. This difference in pressures is enough that the largest stress on the copper is the hoop stress resulting in the positive stresses seen in Figure 5.6. However once the copper has yielded the difference between P_0 and P_1 becomes much smaller; at $200MPa$ P_1 is $172MPa$ or 86% of P_0. The result of this is that the copper acts like it is under compression, not under tension, so by reducing in the r-direction it must expand in the ϕ and z directions inducing the negative hoop and axial stresses seen in Figure 5.7. As the theory does not take this effect into account it becomes inaccurate at higher pressures or lower Young's moduli of the inner material.

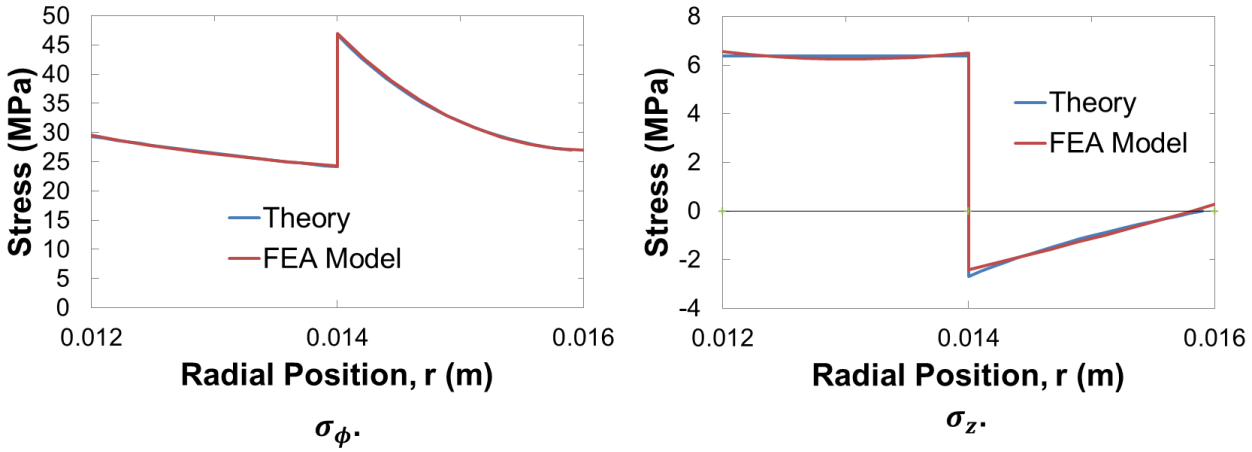

Figure 5.6. Theoretical and modelled variation of two of the principal stresses for a cylinder with a 12mm inner radius, 2mm thick copper and 2mm thick Zylon for an internal pressure of 10MPa (100bar).

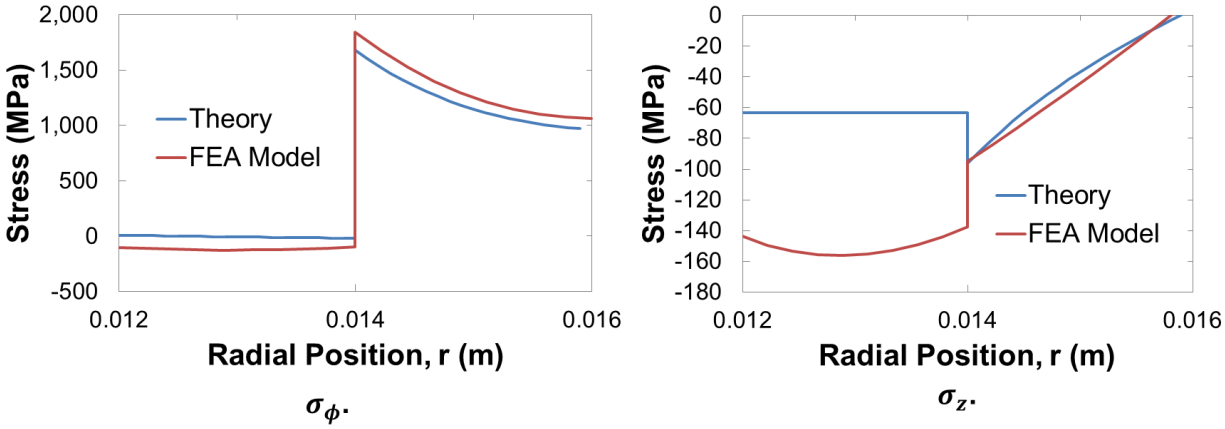

Figure 5.7. Theoretical and modelled variation of two of the principal stresses for a cylinder with a 12mm inner radius, 2mm thick copper and 2mm thick Zylon for an internal pressure of 200MPa (2000bar).

The conclusion of this is that as FEA modelling agrees very well with the analytical theory for small strains, which, as it is an essentially exact solution of the system, we can have confidence in the computed results for other systems. As the stresses increase the theory becomes more and more inaccurate and the results generated by the computer model are trusted to be far more accurate. Due to this, most of the experimental data will be compared to FEA rather than the theory. This also has connotations for [5] as they assumed that the theory was valid for all pressures which appears to be an unsafe assumption especially since the short length of vessel used will compound the errors.

5.2.1 Vessel Design

5.2.1.1 Vessel and Support Details

The most critical component required for this experiment to be successful is the copper vessel. An important factor to consider during the vessel design is that the vessel must have a minimal effect on

the pressure exerted on the test sample whilst being strong enough to be handled during sample preparation without damaging or work hardening the copper (this is easier said than done). It is also important that the failure of the vessel will be repeatable and that it will fail due to failure of the sample rather than through leaking seals or rupture away from the sample. The vessel was first modelled using FEA to try to optimize the design. Once a reasonable design had been created it was decided that the design would be tested bare, without any fibre. This initial test was to ensure that the design would work and that the copper would behave as expected. For the initial test three vessels were prepared and the details of the design, shown in Figure 5.8, used for the copper tests are as follows:

The outside of the vessel was bobbin-shaped with an outer diameter of 45mm for the end cheeks and the winding surface had a smaller diameter and a length of 30mm. This geometry allows fibre to be wound neatly against a flat surface and the thick end cheeks help to maximize the strength of unreinforced cylinder surfaces. The inside of the vessel was bored out from one end so that the bottom of the hole was level with the start of the far end cheek. The purpose of the bored hole was to thin the copper walls under the winding surface to a required thickness. The bored hole had a diameter of 24mm for each of the first three vessels but the winding surface had a diameter of 26mm, 28mm, and 30mm. These diameters corresponded to a wall thickness of 1mm, 2mm and 3mm respectively. This large bored hole forms the basis of the pressurized volume. In the far end a small threaded hole was drilled with very small diameter hole (~1mm) through to the pressurization volume so that the vessel could be attached to the compressor. The next stage of the vessel construction is to seal the open pressurization space with an airtight seal. To this end the start of the large hole was threaded and a corresponding plug was constructed. The thread on the plug was purposely created to be a loose fit in the vessel as the seal is created by filling the thread with hard solder and the loose thread will allow the solder to flow deeper into the joint. The vessel plugs were designed so that they would fill most of the volume within the vessel without sealing the access hole in the far end or touching the outer wall. This is a safety feature as the energy stored in a compressed gas is proportional to its volume and hence by reducing the volume the energy released during a vessel failure is minimised. The final stage was to fire the completed vessels in an oven at 280°C to fully anneal the copper, removing any work-hardening from the machining process. A photo of a completed vessel is shown in Figure 5.11 and a diagram is shown in Figure 5.8.

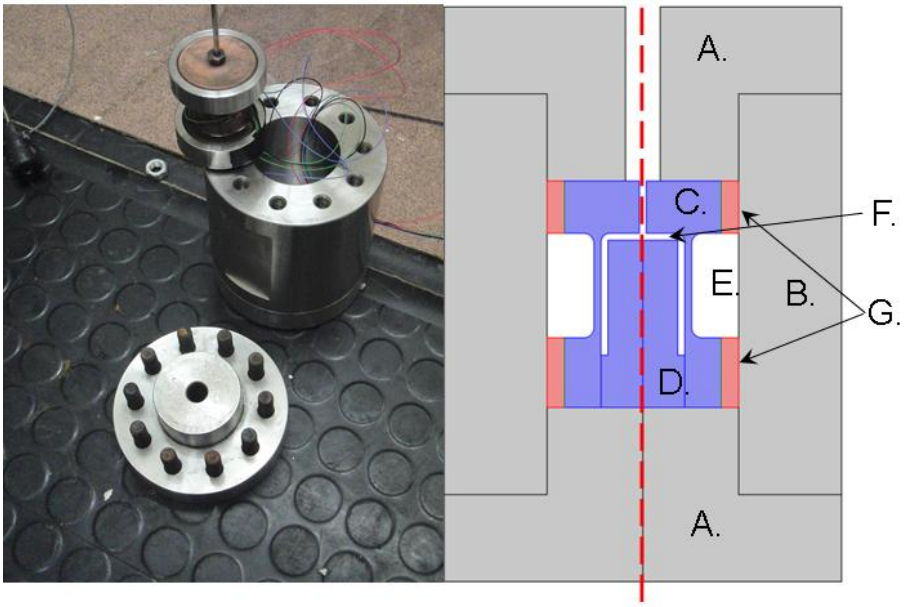

Figure 5.8. The equipment prior to a test and the geometry for the bare copper explosive vessel (shown in blue) and the associated stainless steel support structure (shown in grey) where the red line is the central axial symmetry axis and the components are: A: Stainless steel end-plugs; B: Stainless steel outer cylinder; C: Copper outer vessel; D: Copper vessel plug; E: Sample volume and expansion space; F: Internal volume for pressurised helium; G: Stainless steel vessel support rings.

A subtlety within the design is that all corners where the thin-walled winding surface met the end cheeks at a right-angle were machined to be rounded with a 2.5mm radius. The reason for these rounded corners is shown in Figure 5.9. As the pressure in the vessel builds and the thin walls start to strain, a region of very high stress forms at the top inside corner of the sample wall. If a vessel with square corners is used then the stress at this corner is about three times higher than the stress along the rest of the thin walled-section. Therefore if this design was used it is likely that the vessel would fail by shearing at this point long before the rest of thin walled section reached its UTS. As the desired point of failure is the point of maximum strain, which in this design is the midpoint of the thin-walled section, this squared cornered design is clearly not adequate. By simply rounding the corners this peak stress is greatly reduced to being the same as the stress in the rest of the deformation section. As the model does not take into account the high strain which soft copper can withstand once it has passed its UTS and the stress just above the corner is very low it is likely that when this point passes its UTS the rest of the corner should prevent the failure from spreading. Therefore the likely failure point could be anywhere along the section with the highest strain. The exact failure point is likely to governed more by any defects in the copper than the exact position of greatest stress and strain.

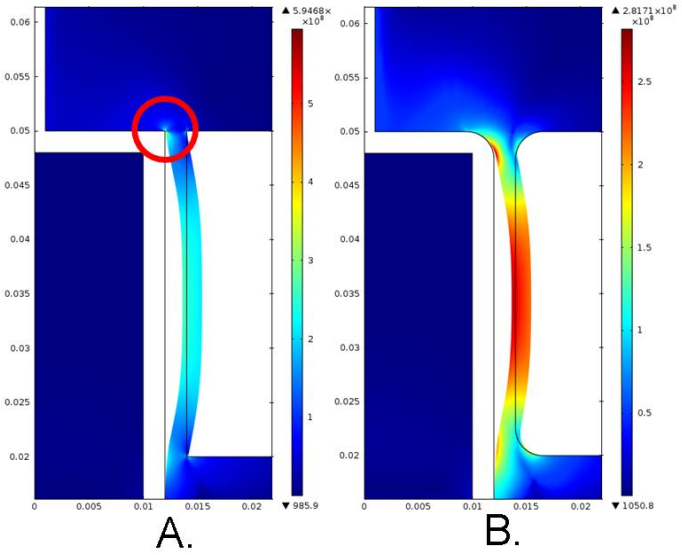

Figure 5.9. The Von Mises stress and total deformation within the bare copper vessel with 2mm thick walls and an internal pressure of 40MPa for A: a vessel with square corners; B: a vessel with rounded corners. The point of peak stress in A. is marked by the red circle.

The desired failure mechanism is through the radial displacement of the thin wall section however the most obvious failure mechanism for the vessel when the high-tensile fibres are added is through elongation of the vessel. The pressure on the top and bottom of the vessel would cause the copper to elongate within the fibre cylinder and failing as one end broke off. To remove this failure mechanism the vessel is placed inside a stainless steel cylinder which then has stainless steel plugs bolted to the ends using ten M10 bolts for each plug. These bolts securing the plugs are fastened finger tight as it would be very easy to generate incredibly high forces, crushing the sample before it can be tested. A secondary advantage of this steel cylinder is that it gives an obvious safety advantage in that any debris produced during a failure should be contained within the nearly sealed chamber (the only access is through a single 4mm hole to allow the escaping pressure out, liquid nitrogen in and to give an access port for instrumentation wiring). Figure 5.8 also shows a photo of the clamp and a vessel ready to be loaded into it. Finally a 5mm thick stainless steel ring is placed around each of the copper end cheeks. These rings were machined to be tight sliding fit around the vessel and also within the external steel cylinder. Their purpose was to prevent radial displacement of the end cheeks which could cause problems in two ways: firstly straining of the end cheeks could cause undesired vessel failures; secondly the vessel will strain plastically during testing, sealing to stiffer materials around it, and so the rings simply make it possible to easily remove the vessel from the cylinder after a run. Once outside the cylinder the rings could easily be removed from the vessel using a fly press and hence be reused for all samples. The geometry of the stainless steel supports is also shown in Figure 5.8.

5.2.1.2 Testing Vessel Design

Once the vessel had been constructed and placed into the support structure it could be pressurised. The vessels are pressurised using an adapted two stage compressor from Harwood Engineering[15]. The compressor is capable of pressurising helium gas up to a staggering 28,000bar! As the vessel was pressurized the azimuthal strain at the centre of the thin walled section was measured using a 5mm long, orange RS Components[16] general purpose strain gauge, usable for strains of up to ~4%. The orange gauge was used as its coefficient of thermal expansion is matched to that of stainless steel which at room temperature is $16.3 \times 10^{-6}/℃$ [10]. This is very close to that of copper which is around $17 \times 10^{-6}/℃$ and so this this gauge should be usable at a range of temperatures. For bare copper at room temperature the gauge was attached using a cyanoacrylate adhesive as recommended in the gauge documentation.

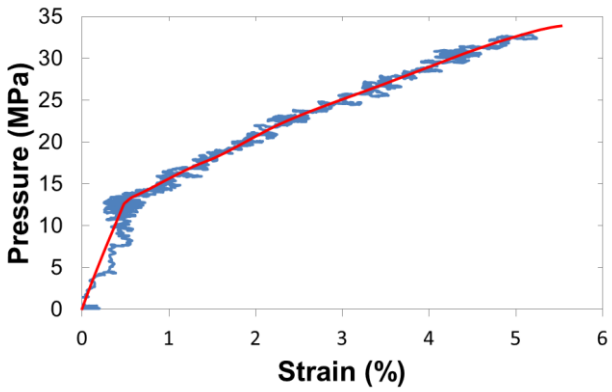

Figure 5.10. Internal gas pressure against strain for the 3mm copper vessel with experimental data and a fitted curve shown.

The resistance of the gauge was measured during each run using a National Instruments[17] USB-6281 18-bit data logger. The strain at the surface can then be calculated from:

$$\varepsilon = \frac{1}{G}\frac{\Delta R}{R_0} \tag{5.43.}$$

Where R_0 is the initial, unstrained, gauge resistance, ΔR is the change is resistance and G is the gauge factor. For the gauge used G at room temperature is $2.1 \pm 1\%$.

[15] Harwood Engineering, 455 South Street, Walpole, Massachusetts, 02081. USA
[16] RS Components Ltd. Birchington Road, Corby, Northants, NN17 9RS, UK
[17] National Instruments Corporation (U.K.) Ltd. Measurement House, Newbury Business Park, London Road, Newbury, Berkshire RG14 2PZ.

A plot of the data produced from the 3mm vessel is shown in Figure 5.10 and the failure and yield pressures for all three of the initial copper vessels is shown in Table 5.1. Also shown in the table is the predicted yield and failure pressures calculated using both the analytical theory and the FEA computer model. For the predicted values a yield stress of 50MPa and a UTS of 350MPa where used. Given that it is such a complicated system and the exact location of the two critical points is very dependent on the uniformity and history of the copper both the model and theory give reasonably accurate predictions. A further complication is the exact definition of the yield point as, fundamentally, this is point at which plastic deformation will start to occur, however in practice the yield point is lower than the point at which the yielding behaviour becomes obviously apparent. This will lead to estimates of yield pressures using the true yield point to be lower than the yield point measured from the turning point of the pressure/strain curve. The agreement is good enough to give confidence that the approximated properties of copper used will only give a very small error in the analysis of the later fibre experiments. This is because, although the relative error is up to 75% for the yield point of the 1mm sample, the absolute error is only a couple of bar and this will be small compared with the total pressure inside a fibre reinforced cylinder. Furthermore the sample had been slightly pre-stressed by over-tightening of the axial clamp which could have altered the material properties from that of fully annealed copper. The one anomalous point is the yield pressure of the 2mm vessel where the actual value is more than twice as great as either predicted value. It is also worth noting that the yield pressure of the 2mm sample is also higher than the yield pressure of the 3mm sample. Although this may seem like there is a large discrepancy here there is a simple explanation: the sample was dropped as it was being placed into support cylinder. This had the effect of twisting the sample which required some slight further machining before it could be fitted into the cylinder. This twisting and machining will have significantly hardened the copper, giving rise to the increased yield pressure.

Parameter	1mm	2mm	3mm
Failure Pressure (MPa)	21.9 (219bar)	49.2 (492bar)	66.4 (664bar)
Yield Pressure (MPa)	6 (60bar)	14 (140bar)	13 (130bar)
Estimated Failure Pressure (MPa)	24	46	66
Estimated Yield Pressure (MPa)	3.4	6.6	9.5
Modelled Failure Pressure (MPa)	27	52	73
Modelled Yield Pressure (MPa)	5.5	7.5	10

Table 5.1. Data measured for the three initial copper vessels along with the predicted values calculated using the theory and computer model.

Figure 5.11. Photos showing a new vessel on the left and the final state of two vessels after completion of a run with the entire 3mm vessel in the centre and a cut-away of the 1mm vessel on the right. The solder filled threads are clearly visible at the bottom of the 1mm vessel.

Despite the impaired quality of the data from the 1mm and 2mm samples it was felt that the initial tests had been successful enough that repeats were unnecessary. The vessels had all strained and failed in the desired manner (irrespective of their treatment before testing) and neither the seal nor the helium capillary attachment had failed or indeed showed any sign of degradation. The initial tests also lead to the decision to use 2mm walled vessels for all of the fibre experiments: 3mm is too strong and would lead to higher pressures being required to reach failure whilst 1mm is too weak and easily damaged during the assembly process.

5.2.2 Results

Before the experiments could begin with fibre the vessel design needed to be finalized as the bare copper vessels were not quite suitable for use with fibre. The reason behind this is simple; as the fibre is so much stronger than the copper any feature on the vessel which resulted in a thinner fibre section would be a weak point which could fail prematurely. Therefore the vessel used for the tests with fibre was almost identical to the 2mm vessel detailed in the previous section. The one minor difference was that the external corners of the sample winding space, which were radiused for the bare copper vessels, were instead sharp right-angles however the inner corner remained radiused. The geometry of the final vessel is shown in Figure 5.12. The creation of the vessels was completed by using a CNC computer controlled machine lathe used to ensure that all of the vessels are as similar as possible.

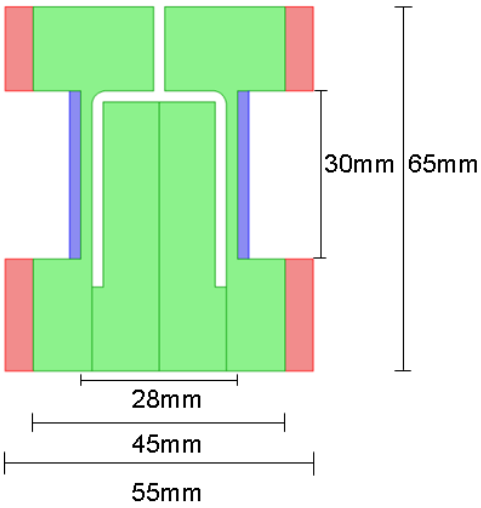

Figure 5.12. Sketch of the final vessel design with the copper vessel (shown in green), steel support rings (shown in red) and the fibre space (shown in blue).

Once the vessels had been completed the fibre to be tested was wet wound directly onto the winding surface. The fibre was wound as accurately as possible to a total thickness of 1mm on all vessels with an error of $\pm 0.05mm$. Strain gauges were attached to the sample by placing them on the surface of the wound fibre and then are captured in place using a couple of turns of s-glass. The glass was used to secure the gauges during the curing process as, as the glass is weaker and less stiff, a couple of turns of glass will have a very limited effect on the measured results. The finished sample vessels then underwent a similar curing process to that used for the pulsed coil in that the sample is placed overnight in the rotary oven at 100℃ to gel the resin before final curing at 160℃ for 8 hours in a conventional oven.

Figure 5.13. A Zylon fibre sample before and after testing.

The prepared sample would then be placed into the clamp and, if cryogenic temperatures were required, the entire clamp assembly would then be placed into an open bucket which could be filled

with liquid nitrogen. The test procedure was then exactly the same as for the bare copper vessels earlier. Figure 5.13 shows a typical fibre vessel which has been prepared for testing and the same vessel after the test.

The first fibre tested was the high modulus Zylon fibre used to reinforce the magnet coil. The fibre comes off the reel as a bundle of many individual filaments. For the fibre used the bundle has a linear density of 996dtex ($1dtex = 1\ g/10km$) which, as the density of the fibre is $1560\ kg/m^3$ [11], gives a bundle diameter of $0.285mm$. The bundles were wound onto the vessel to a layer thickness of 1mm under two different prestresses with tensions of around 15N and 50N which, given the diameter of the bundles will give a prestress in the fibres of around $230MPa$ and $800MPa$. The fibre is prestressed to improve the packing factor of the bundles [12] which should increase both the UTS and the Young's modulus of the composite around the vessel. As a comparison two vessels were prepared with a different high strength fibre known as Dyneema[18] SK75 which, it is claimed, is the strongest fibre in the world by weight [13]. The Dyneema was wound to a thickness of 1mm and was wound with the same tension as the low prestress Zylon of 15N giving a prestress of 100MPa. The sample tests could then be spilt into 5 groups: low and high prestress Zylon at 77K at 300K along with low prestress Dyneema at room temperature. At least two samples were tested in each group to ensure repeatability of the results.

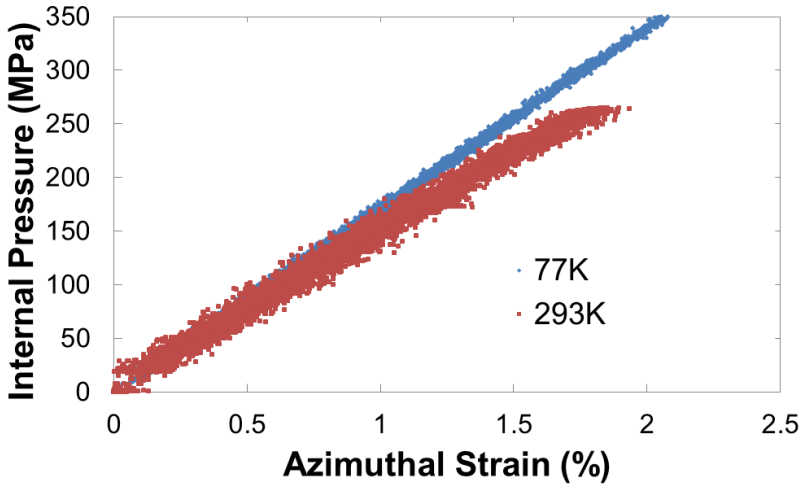

Figure 5.14. The typical measured strain against integral helium pressure for 1mm of Zylon wound with a prestress of 230MPa at room and nitrogen temperature.

Table 5.2 shows the properties of each fibre configuration as calculated by using both the analytical theory and the FEA model while Figure 5.14 shows plots of the data measured during typical runs for

[18] DSM Dyneema B.V. Mauritslaan 49. 6129 EL Urmond. The Netherlands. http://www.dyneema.com/

low prestress Zylon at both room temperature and at 77K. It is immediately clear that by lowering the temperature the Zylon becomes both stiffer and stronger as shown by the increase in the Young's modulus and the increase in the bursting pressure. The effects of increasing the prestress are less clear. As expected from the literature the Young's modulus increases by around 10%, a significant increase. However the effect on the UTS of the composite appears to be opposite to the published material. At room temperature the high prestress vessels failed at a very similar pressure to the low prestress ones but at 77K there was a considerable reduction of 10% in both the bursting pressure and the UTS. The cause of this reduction in strength is not clear but could be caused by a fault or design flaw in the design or winding of the samples. An alternative possibility is that as the prestress has both stressed and strained the fibres before any load is added then less extra force is required to break them; if this is correct it could have connotations for all high field magnet designers. However more data would be needed before any concrete conclusions about the effects of prestress on composite strength could be drawn.

		Analytical Theory		FEA	
Fibre	Failure pressure $(MPa\ (bar))$	Young's Modulus (GPa)	UTS (GPa)	Young's Modulus (GPa)	UTS (GPa)
Zylon $(300K)$					
Low prestress	265 (2650)	190	3.7	170	4
High prestress	260 (2600)	216	3.51	193	4
Zylon $(77K)$					
Low prestress	359 (3590)	220	4.97	194	5.6
High prestress	326 (3260)	240	4.54	216	5.1
Dyneema	203 (2030bar)	89	2.35	74	2.6

Table 5.2. The properties of the composites calculated using the analytical theory and FEA.

A further result of this work is that it has become apparent that the data analysis used in the literature to analyse the results of similar experiments are flawed giving a figure which is roughly 10% too high for the Young's modulus and 10% too low for the UTS and so the published data on the properties of Zylon may be inaccurate.

The experiment has also given credence to the claims that Dyneema is the strongest fibre by weight as, despite the fact the its UTS was $2.6GPa$ as opposed to Zylon's $4GPa$, as its density is just $960kg/m^3$ it is $\sim$3.5% stronger per unit weight of material.

5.2.3 Failure of Zylon Composites

The general model for catastrophic failure of composites stressed to their UTS is that the failure will be initiated within a single fibre or bundle of fibres [14]. As the composite is stressed and approaches its UTS all of the fibres in the composite will be highly stressed. Eventually one fibre will reach its UTS and it will rupture. Once the fibre is ruptured it can no longer support a load and so it will transfer the load that it was carrying to the fibres around it. As these fibres will have been very close to their UTS the increased load due to the failure of their neighbouring fibre will cause them to exceed their UTS and hence, as in an avalanche effect, they in turn will fail. Therefore once a failure has initiated in such a stressed environment, as the fibres are stiff so will not strain much before breaking, such a failure will propagate rapidly and failure will be nearly instantaneous across the composite. Furthermore for the explosive vessel the failure should be initiated in the fibre shell and the copper shell should fail later.

To test the timescales involved in the failure of the vessel and, by extension pulsed coils, a brief extension to the explosive vessel testing was conducted. For this test the Zylon was wound with a prestress of $230MPa$ to a thickness of $0.3mm$. The vessel was then placed between the usual plugs used to constrain the axial deformation of the vessel but instead of the steel outer cylinder being used the plugs were fixed using steel tie-bars. This allowed the vessel to be filmed using a high speed camera recording images at 400 frames per second.

At a pressure of $\sim 1kbar$ the vessel failed. Figure 5.15 shows three screen shots taken from the high speed footage. The first two images are consecutive shots from the camera so are taken just $250\mu s$ apart. The first clearly shows an intact and undamaged Zylon shell. The second image shows that the entire Zylon shell has failed catastrophically. No further movement of the Zylon occurs after this shot indicating that the maximum time scale associated with this type of failure is less than the $250\mu s$ frame rate. Further analysis of the later shots shows a distinctive blurring of the background 11 frames after the initial failure which is highlighted in the red circle in the third shot. This blurring is caused by the ejection of the pressurised gas as the copper shell fails. This shows that the copper shell failed at

least $2.75ms$ later than the Zylon; a considerable timescale given the rapid failure of the Zylon. This occurs as, once the Zylon has ruptured, the copper shell will be stressed far beyond its UTS and so will strain rapidly ballooning out. However the failure of the copper does not occur instantly as it was so heavily annealed that it can undergo a very large strain before breaking and hence some time is required to inflate the copper.

Figure 5.15. Photos showing frames from the high speed footage recording of the failure of 0.3mm of Zylon at 1000bar. The footage shows that the entire Zylon shell fails in less than $250\mu s$ whereas the copper takes almost 3ms to fail after the Zylon has been destroyed.

5.2.4 Conclusion

In this chapter we have seen the work into refining a novel method for testing high strength fibres in cylindrical geometries using highly pressurized helium gas. An analytical theory describing the system was derived and compared with FEA modelling to show its strengths and limitations. The comparison between the FEA and the analytical theory has shown that there may be an error of ~10% in the results given by the theory. Therefore, by extension, there may be a ~10% error in the data presented in the literature which uses the analytical theory to calculate the material properties. A new sample holder and axial clamp was developed which enabled 100% of all samples to be tested successfully. Zylon fibre was tested at low and high winding prestress at room and liquid nitrogen temperatures and Dyneema fibre was tested at low prestress at room temperature only. It showed that Zylon composites become stiffer and stronger at cryogenic temperatures than at room temperature and that, Zylon composites become stiffer and, possibly, weaker when more prestress is used to prepare the sample. The data also supported the claim that Dyneema is the strongest fibre by weight. By filming the failure of a sample using a high speed camera it was shown that the failure of composites in this geometry is nearly instantaneous across the entire structure.

References

[1] R. P. Walsh and C. A. Swenson, “Mechanical Properties of Zylon/Epoxy Composite at 295K and 77K,” *IEEE Trans. Ap. Super.*, vol. 16, no. 2, pp. 1761-1764, 2006.

[2] M. P. Hanson, “Tensile and cyclic fatigue properties of graphite filament-wound pressure vessels at ambient and cryogenic temperatures,” NASA Technical Note D-5354, Washington D.C., 1969.

[3] S. Kobayashi, T. Imai and S. Wakayama, “Burst strength evaluation of the FW-CFRP hybrid composite pipes considering plastic deformation of the liner,” *Composites A,* vol. 38, no. 5, pp. 1344-1353, 2007.

[4] A. R. Simon and R. Alfring, “Properties of Graphite Fibre Composites at Cryogenic temperatures,” Naval Ordinance Laboratory Technical Report, White Oak, USA, 1972.

[5] Y. K. Huang, P. H. Frings and E. Hennes, “Exploding Pressure Vessel Test on Zylon/Epoxy Composite,” *Comp. B,* vol. 33, pp. 117-123, 2002.

[6] N. Bednar and H. Garmestani, “Biaxial testing of high strength carbon fiber composite cylinders for pulsed magnet reinforcement,” *Composites A,* vol. 30, no. 2, pp. 147-152, 1999.

[7] L. Grimes-Ledesma, S. L. Phoenix, H. Beeson, T. Yoder and N. Greene, “Testing of carbon fiber composite overwrapped pressure vessel stress-rupture lifetime,” Jet Propulsion Laboratory Technical Report, Pasadena, 2006.

[8] J. F. Harvey, Theory and Design of Pressure Vessels, London: Chapman and Hall, 1991.

[9] P. M. Wild and G. W. Vickers, “Analysis of filament-wound cylindrical shells under combined centrifugal, pressure and axial loading.,” *Composites A,* vol. 28A, pp. 47-55, 1997.

[10] “Foil Strain Gauges and Accessories,” RS Online Data Library, 1981. [Online]. Available: www.rs-online.com.

[11] Toyobo Co. Ltd., “Zylon Technical Datasheet,” 2005. [Online]. Available: www.toyobo-

global.com. [Accessed 2011].

[12] Y. K. Huang, P. H. Frings and E. Hennes, “Mechanical Properties of Zylon/epoxy Composite,” *Composites B,* vol. 115, no. 1, p. 109, 2002.

[13] Dyneema, “Dyneema datasheet,” 01 Jan 2008. [Online]. Available: http://www.dyneema.com/. [Accessed 2010].

[14] L. Mishnaevsky and P. Brøndsted, “Micromechanical modeling of damage and fracture of unidirectional fiber reinforced composites: A review,” *Computational Materials Science,* vol. 44, no. 4, pp. 1351-1359, 2009.

6 Pulsed Field Magnetization of (re)BCO Bulk Superconductors

6.1 Introduction

In recent years there has been a lot of interest in flux trapping in bulk high temperature superconductors. The main reason behind this is that they have the ability to generate a much higher magnetic energy density than conventional rare earth permanent magnets. The current record for the trapped flux in any sample is over 17T [1] using the field cooling method and is 5.2T using a pulsed magnetic field method [2]. These records compare to around 1.2-1.4T for the conventional magnets [3]. The higher flux density available can improve the performance of a number of devices and so they have a wide range of possible applications including: low-friction levitating bearings [4], magnetic levitation systems [5] [6], high powered motors and generators [7] [8], magnetic water purification systems [9], drug delivery systems [10] and compact high field NMR systems [11].

For these bulks to be utilized in any of these applications they must first be magnetized. The most efficient method for doing this, the method which can and has trapped the largest fields is called the field cooling (FC) method [1]. This involves placing a warm sample (i.e. above its transition temperature) in an external DC magnetic field. The sample is then cooled to the required temperature and the applied field is slowly removed. This allows the applied field to fully penetrate the sample and limits the heating over the sample as the field is removed. The disadvantage of this system is that it requires the sample to be placed inside a magnet which can produce the required field. This can be quite complicated in terms of cryogenics and doesn't allow for 'in-situ magnetization' where the bulks are magnetized once the bulks need to be magnetized within a piece of machinery or equipment. Another method of magnetization is the zero field cooling (ZFC) method [12]. This differs from FC magnetization in that the sample is pre-cooled to the required temperature and the applied field is then increased from zero to the required field before being slowly removed again. This can simplify the cryogenics required as the sample doesn't have to be cooled within a large magnet but in-situ magnetization is still very difficult. For in situ-magnetization the only method which can be used without too much difficulty is pulsed field magnetization (PFM) [13] [14]. This method involves exposing a superconducting bulk to pulsed magnetic fields generated by, what is usually, a copper coil. There has been a lot of research over the past ten or so years into the best way to magnetize the bulks with this method. Over the years several methods have been proposed including multi-pulse magnetization with variations such as 'iteratively magnetizing pulsed field method with reducing amplitude' (IMRA) [15], multi-pulse with stepwise cooling (MPSC) [16] or the modified MPSC (MMPSC) [2]. IMRA involves exposing a bulk to several successive magnetic pulses where each

pulse has a smaller amplitude than the pulse before. This helps to force a bit more flux into the bulk with each successive pulse while reducing the heating effect. MPSC involves applying several pulses to the bulk with the temperature of the bulk reduced between pulses. The final method MMPSC is very similar the MPSC but uses lower field pulses at a higher temperature to partially magnetize the sample then the sample is cooled to its final temperature before two larger pulses are applied. This method initially traps a field around the periphery of the sample and the higher field pulses then drive the flux towards the centre with a reduced heating effect as some flux has already penetrated the sample before the final magnetizing pulses are used [17]. The most effective of these methods appears to be the MMPSC as this method has achieved the record for the highest flux trapped using a pulsed field of 5.2T although no data was presented as to how much flux would have been trapped by a single pulse of the appropriate magnitude [2].

A detailed review of the published literature on PFM and flux trapping revealed many interesting and relevant papers. Of the literature on PFM Fujishiro is one of the more prominent individuals. As well as holding the record for flux trapped using a pulsed field Fujishiro has performed some of the more detailed experiments in recent times. In reference [18] he details the flux trapped at 20K, 30K, 50K and 70K after one and three magnetic pulses of up to 6.3T. At 70K the trapped flux peaks when the applied field is around 4.5T and decreases if the applied field is larger or smaller than that. At the lower temperatures he was unable to determine the location of these peaks as they were above the 6.3T which he had available to him. Ida [19] tested whether a pair of vortex coils was better than a standard solenoid for magnetizing the bulks. A vortex coil is a coil whose bore has a very small diameter when compared to the outer diameter of the coil. For a pair of these coils the sample is placed between the two of them forming a ‘split-pair’ magnet. This has the obvious benefit of being able to fit much larger samples in the magnetic field. Ida also found that it improves the amount of flux which can be trapped by PFM. He theorized that this was because the field in a vortex coil pair is roughly parabolic in shape with a sharp peak in the centre whereas the field is much more uniform in a standard solenoid. The result of this is that with a pair of vortex coils there is less “excess flux penetration around the periphery area”. This then reduces the excess heating in the outer areas of the sample while maintaining full flux penetration in the centre. This reduced heating should reduce the degradation in flux trapping ability caused by the heating of the sample. Chen [20] investigates the effect of the rise time of the magnetic pulse on the flux trapping using 12.5ms, 25ms and 50ms. He showed that a small increase in trapped flux can be achieved by increasing the pulse rise time up to saturation. He also concluded that “it is desirable to optimize pulse widths, pulse shapes (rise/fall times) and peak amplitudes for the selected sample”.

A new paper by Fujishiro [21] details recent developments the modelling of the MMPSC method. The key result from his simulation is that the optimal method of trapping flux is to apply two 6.5T pulses to a sample at 60K followed by two 15T pulses to the sample once it has been cooled to

40K. He goes on to state that the optimum has been found experimentally to be two 4.5T pulses at 45K followed by two 6.7T pulses at 29K as in [2]. However no experimental evidence of a pulse greater than 7T is presented so it is hard to judge whether the values are indeed the optimum ones.

Reference	Applied field range	Temperature range (K)	Rise time of applied field	Cooling method	Sample sizes diameter/length
[2]	4.5T & 6.7T	45K & 30K	13ms	cryocooler	45mm/15mm
[13]	<4.2T	77K + 30-80K	0.8-5ms	LN_2 bath + cryocooler	34mm/14mm
[24]	<5T	77K	1.3+3.6ms	LN_2 bath	34mm/14mm
[18]	2.8-6.3T	20-70K	12ms	cryocooler	45mm/18mm
[19]	<7.7T	77K	5.8ms	LN_2 bath	33mm/24mm 60mm/19mm 24mm/15mm 48mm/19mm
[25]	2.6-5.11T + 3.3-6.3T	70K + 40K	12ms	cryocooler	45mm/18mm
[26]	<6.3T	30-70K	12ms	cryocooler	45mm/15mm
[22]	<28T	55-85K	~3ms	Pumped LN_2 balanced with heater	<1mm
[27]	<7T	40K	10ms	cryocooler	46mm/15mm
[28]	2T & 3.2T	77K	~4ms	LN_2 bath	46mm/15mm
[20]	<3.6T	77K	12.5ms, 25ms, &50ms	LN_2 bath	28mm/10mm
[29]	<1.1T	77K	13-35ms	LN_2 bath	20mm/10mm
[30]	<8T	40K	14ms	cryocooler	36mm diameter
[31]	<2T	77K	7ms	LN_2 bath	46mm/15mm
[23]	<3.3T	77K + 50K-80K	3ms + 30ms	LN_2 bath + cryocooler	30-32mm/ 8mm + 16mm

Table 6.1. Table showing the details found from the literature review for the range of variables which have been investigated for flux trapping experiments on bulk superconductors.

The papers detailed so far are just a few of the papers available and several more relevant papers from around the world are listed in Table 6.1 along with the range of temperatures and magnetic fields used, the method of cooling the samples and the sample sizes. From this table and from the papers detailed above it is clear that, despite the large amount of work that has gone into this area, there are still some areas of pulsed field magnetization which have not been explored or would benefit from further work. There was only one paper, [22], which had investigated the

superconducting properties of bulks above about 8T (with most focussing on pulses of less than 6T) and this paper was not concerned with flux trapping; it was measuring the magnetization curves of the bulks. Further to that the samples used in that experiment were no more than 1mm across, far too small to be useful in bulk applications. As [21] and [13] both hint at the need for a higher field to be applied to the samples some work on the sample in higher fields could be instructive. It is also noted that there has been little to no work done on magnetizing the bulks which are cooled directly by a cryogenic fluid at any temperature other than 77K. The work has usually focused on a LN_2 bath or, for temperatures other than 77K, a cryocooler. The one paper which is different is again [22] which uses pumped solid nitrogen to achieve temperature of 55K but this isn't used to directly cool the sample, it is used as a cold source, balanced with a heater, to achieve the required temperature. This, along with the differences mentioned previously, indicate that it could be beneficial to investigate how flux trapping is affected by temperature when the sample is immersed in pumped LN_2 as, if the samples are immersed in a cryogen, any heat generated will be removed much more efficiently than by conduction through a cold stage to a cryocooler. One final possibility is that although there has been some work on the effect of pulse rise time/shape on flux trapping these have either been at liquid nitrogen temperatures [20], at lower temperatures but with lower fields (<5.5T) and relatively short pulse lengths (<20ms) or, possibly the most detailed paper [23], has documented rise times of 3ms and 30ms at temperatures between 50K-80K. The work in these papers could easily be expanded on by using higher fields and longer pulse lengths.

From the literature survey it was concluded that there the three areas of pulsed field magnetization which could benefit most from development were:

- Investigating the effects of high magnetic fields (>7/8T)
- Investigating the effects of immersion in liquid cryogens at temperatures other than 77K
- Investigating the effect of pulse lengths longer than 30ms at a range of temperatures.

To this end several new pieces of equipment were designed and constructed to allow these regimes to be investigated. The key equipment needed was:

- A new high field pulsed coil that was capable of producing at least 15T with a rise time of at least 30ms and as large a sample space as possible (Chapter 4).
- A Dewar suitable for use with large samples and any magnet constructed (section 6.3.2).
- A manostat gas handling board to control the pressure above any cryogen in the Dewar so that the temperature can be controlled accurately (section 6.3.3).

- A Hall probe array to measure the profile of the magnetic flux across the surface of the sample (section 6.3.1).

6.2 Theory of Flux Trapping

The central principal behind flux trapping is that when any conductor is exposed to a time varying magnetic field there will be eddy currents induced in the material which oppose the change in the magnetic field as governed by Faraday's Law (see section 4.3.1 for more details):

$$\boldsymbol{J_i} = \sigma \frac{\partial \mathbf{A}}{\partial t} \qquad 6.1.$$

The total magnitude of the induced currents is then proportional to the integral of the total change in magnetic field. In a normal, resistive, materials these currents will quickly decay away dissipating their energy as heat in the material and are thus the cause of effects such as eddy current heating. However in a superconductor, up to the critical current, there is effectively no resistance and so any induced currents will remain 'trapped' in the material as long as the material remains cold. If the induced currents are higher than the critical current the trapped current will quickly decay to the critical current. However the decay will stop once the critical value is reached and so there will still be a trapped current. This current, as with any current, will have an associated magnetic field

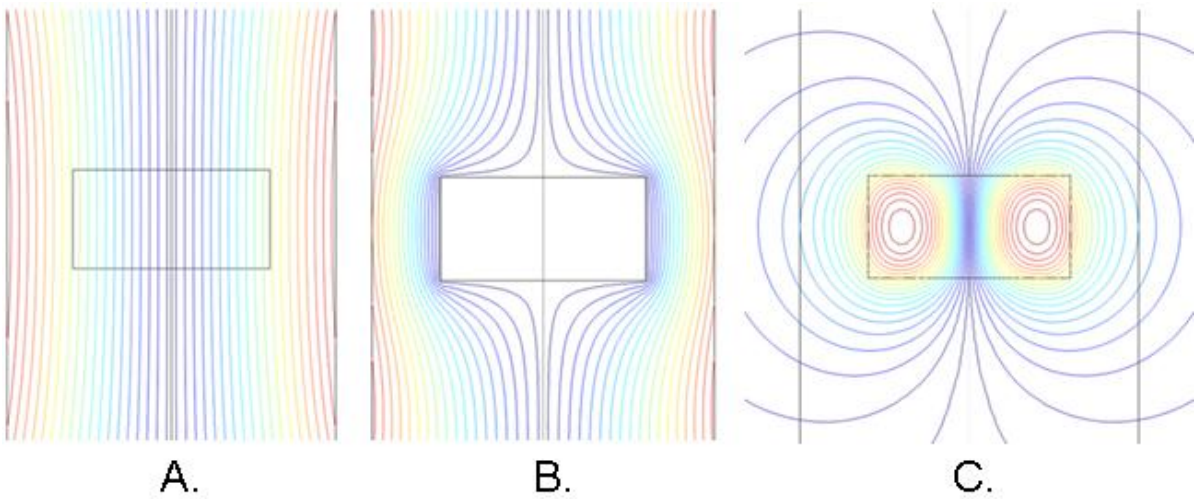

Figure 6.1. The field lines associated with a monolithic coil and bulk high temperature superconductor during flux trapping via the field cooling method. With A: Field applied to a warm sample; B: Sample cooled in field; C: Trapped flux in the bulk once the field has been removed.

To illustrate the effect of flux trapping we will briefly consider a hypothetical experiment based on the field cooling method for trapping flux. The simplest case to consider is a bulk with a cylindrical geometry within the bore of a monolithic solenoid coil and is shown in Figure 6.1. If the magnetic

field produced by the solenoid is applied to the warm bulk then the applied flux will fully penetrate the bulk. Once the sample is cooled the flux will be expelled from the bulk of the sample due to the Meissner effect causing the bulk to act as a perfect diamagnet. Finally as the applied field is removed the currents will be induced in the bulk which will flow in the azimuthal direction around the bulk leaving the bulk with a trapped dipole field.

Although field cooling is the most effective method for magnetizing bulks the method which will be investigated in this chapter will be pulsed field magnetization. It is not immediately obvious why a pulsed magnetic field can be used to trap flux in a bulk. Naively one would expect that as the applied magnetic field at the start and end of a pulse is zero then the total change in magnetic field is zero and so the trapped flux must also be zero. Although this would is true for an idealized (fully annealed and pure) superconductor it is not true for most materials due to flux pinning and the irreversibility line. Flux pinning was discussed in section 1.4.4 and the irreversibility line will be discussed in the next section but essentially they cause the magnetization processes to become hysteretic and so once a flux is trapped in the bulk it can never be fully removed without quenching the sample.

6.2.1 Irreversibility and the Irreversibility Field

The central property which allows the pulsed field magnetization of high temperature superconductors to work is their irreversible or hysteretic response to changing magnetic fields. The behaviour is not, however, hysteretic for all applied fields up to the critical field. It was first observed by Müller [32] who saw that at some field, known as the irreversibility field, B_{irr}, below the critical field where the behaviour would become fully reversible. It was found that the level of B_{irr} varies with temperature and this dependence obeys the empirical relation:

$$B_{irr} = B_{irr}(0)\left(1 - \frac{T}{T_c}\right)^n \qquad 6.2.$$

where n~1.5, although for the specific cuprate superconductor GdBCO which was used for this experiment it has been shown that B_{irr} increases linearly in the temperature range 63K-77K [22].

This change in behaviour from irreversible to reversible is due to the pinning of the fluxons in the superconductor. In an unpinned superconductor any fluxons which penetrate the bulk will be in a ‘liquid’ state in that they are free to move and flow. In such a superconductor any magnetization process is fully reversible as any fluxons which have moved into the bulk are equally free to flow out

the bulk when the applied field is removed. The other consequence of this lack of pinning is that the critical current for any bulk currents is zero as the fluxon movement will cause energy dissipation. For superconductor with pinning there are more states available for the fluxons. For strong flux pinning there are two fluxon states; the solid, fully pinned, lattice and the unpinned fluid state [33]. For the case of weak pinning (defined as being a superconductor where the lattice shear strength is greater than the bulk pinning force) there is a third state between the solid and liquid states. In this phase the fluxons are still ordered in the lattice formation typical of the pinned state but groups of ordered fluxons are free to move; causing dissipation. The case of weak pinning does not need to be considered in any more detail as, in the context of the flux pinning experiment, the behaviour of a bulk will not be affected by whether it is weakly or strongly pinned as B_{irr} is the field at which dissipation due to flux motion can occur. Therefore it is irrelevant as to whether the dissipation is because the fluxons are in the liquid or semi-liquid state and so the inclusion of the third state is an unnecessary complication.

As any magnetization above B_{irr} is fully reversible we can increase the remanent flux trapped in a bulk by applying larger fields only up to a point. Fields applied which are greater than B_{irr} may even reduce the trapped flux due to increased dissipation through flux motion.

6.2.2 Bean Critical State Model

In 1964 Bean published a phenomenological model of flux trapping [34] which sought to predict and explain the hysteretic behaviour. The central assumption of his model was that the current in a superconductor, with a critical current density, J_c, could only take one of three values: $\pm J_c$ or 0. The current will be zero for portions of the superconductor which have never felt a magnetic field and $\pm J_c$, if the superconductor has been exposed to a field with the direction governed by the direction electromotive force generated by the last local change in field.

In the model, when a small external field is applied to the bulk, currents form in the very outer layers which shield the inside of the bulk from the applied field, as predicted by the Meissner effect. As the applied field gets larger the thickness of the layer carrying current increases to shield the diminishing, virgin, centre of the bulk until, eventually, the field will reach such a level that there is the critical current density flowing in all parts of the bulk. Further increases in applied field will not change the profile of the currents or the shape of the field across the bulk but will then increase the field

uniformly across the bulk. The distribution of the field and currents for an increasing applied field up to a magnitude of $2H^*$ is shown in Figure 6.2 where H^* is known as the critical magnetization field.

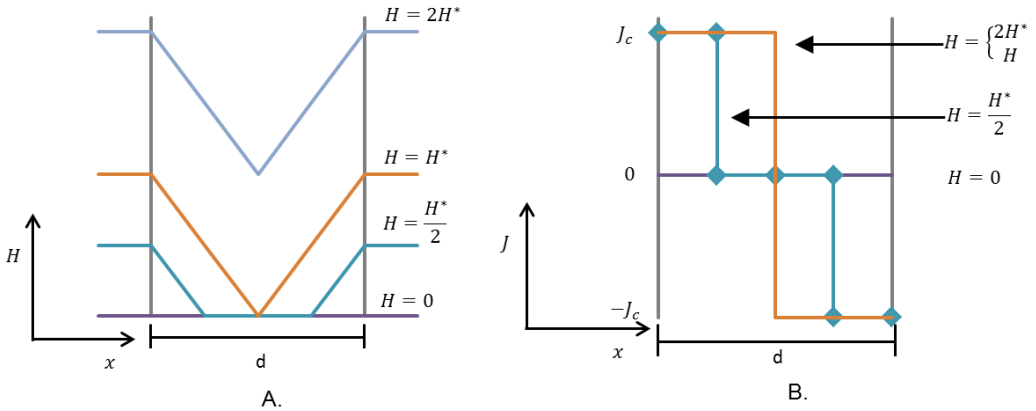

Figure 6.2. A. magnetic field strength and B. current density across a cylindrical sample of diameter d for an increasing applied magnetic field predicted by the simple Bean model.

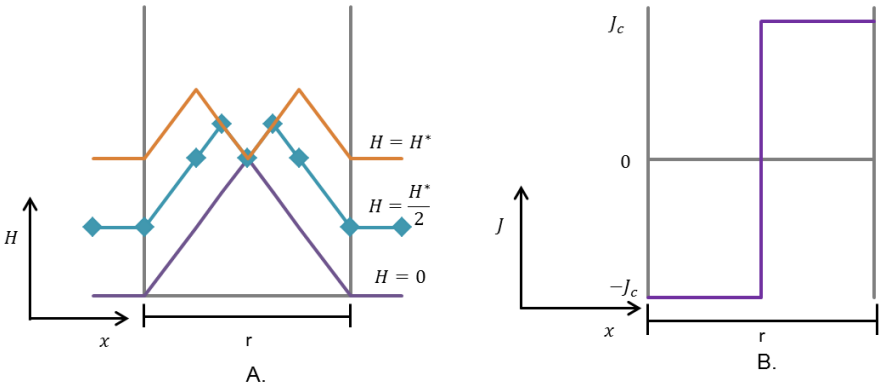

Figure 6.3. A. The magnetic field distribution across a sample of diameter d for a decreasing magnetic field where the initial condition was the same as for an applied field $H = 2H^*$ in Figure 6.2. The final trapped field profile is shown by the purple line. B. The profile of the trapped current after the applied field has been fully removed.

If the applied field is swept down from the $2H^*$ level then the current in the skin of the bulk material reverses direction. As the field is swept further down the reversed current profile spreads through the bulk until, when the applied field reaches zero, the entire current profile will have been reversed from the profile at the peak applied field. This current profile will have an associated field profile which in this simple model will be a perfectly conical shape, known as the Bean cone. The current and field profile for the removal of the applied field is shown in Figure 6.3. Once there is a trapped flux it is impossible to remove it by applying a negative field as this will simply result in the same profile but with a negative field magnitude. This model is hence fully compatible with the magnetization curves. For increasing fields the induced currents will always shield some of the applied field from the centre of the bulk until a certain, magnetizing field level is reached. At this level the magnetization will

remain constant. On the down sweep the trapped currents will give a larger field in the bulk than the applied field until the applied field is removed and the remanent field gives the permanent magnetization.

The model also gives a prediction for the effects of applying a pulsed field with a magnitude that is less than the critical value of $2H^*$. Figure 6.4 shows the trapped flux and current profiles after a magnetic field of H^* has been applied and removed. The result of such an incomplete magnetization process is the distinctive M-shaped profile where the central field is lower than the magnitude of the field around it.

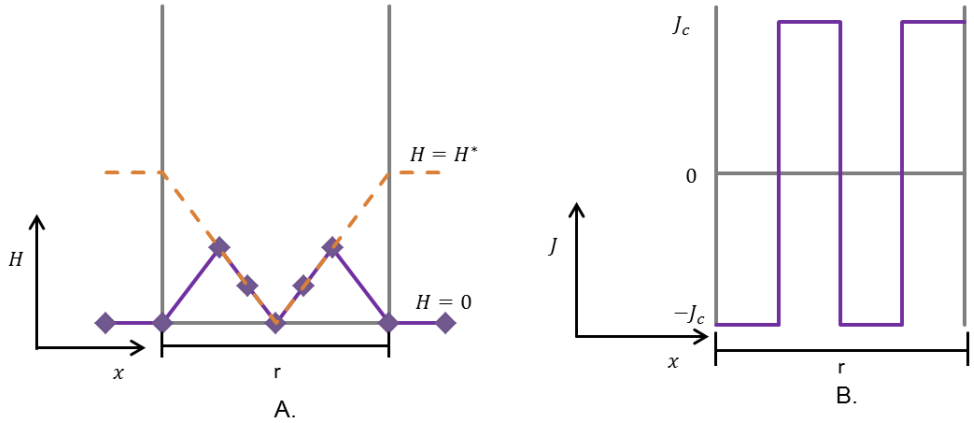

Figure 6.4. A: the 'M-shaped' magnetic field distribution and B: current density profile after and magnetic field of H^* has been applied and removed.

So far in this section the concept of the critical magnetization field has been introduced and has been demonstrated to be the maximum field which can be trapped within a superconducting bulk using a pulsed magnetic field. As there must be the critical current density flowing at all points of the superconductor we can calculate the theoretical magnetizing field using the differential form of Ampere's law:

$$\nabla \times \boldsymbol{H} = \boldsymbol{J} \qquad 6.3.$$

i.e. that the magnitude of the magnetic flux density will vary linearly with the current density. This leads straightforwardly to the magnetizing field for a cylindrical bulk:

$$H^* = J_c r \qquad 6.4.$$

It is immediately obvious that the maximum magnetizing field is dependent on both the critical current density and the size of the sample.

One important modification to this simple theory is to note that so far we have assumed that the critical current density of a superconductor is independent of the applied field. In reality, as demonstrated in section 3.2.6, the critical current density is strongly dependant on the field, reducing as the applied field increases. The result of this is that the current density will be lower at the centre of the bulk than at the centre leading to a flattening of the sharp Bean cone into a smoother one while also reducing the height of the peak. Figure 6.5 shows an example of how this behaviour will change the current and field profile for an typical superconductor with a cylindrical geometry.

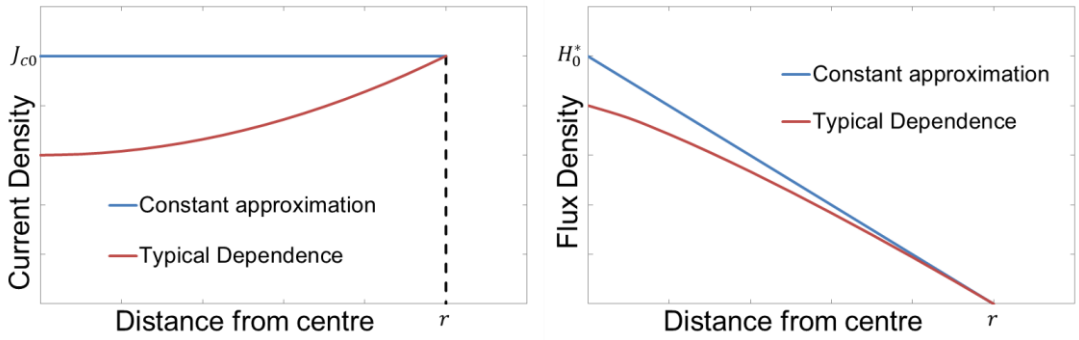

Figure 6.5. The current density and magnetic field profile across an arbitrary cylindrical sample where the critical current is dependent on the field.

6.2.3 Computer Modelling

One of the motivations behind this experiment has been to generate data to aid the development of accurate computer simulations of the pulsed field magnetization of bulk superconductors which is being conducted by Professor Campbell and his students at the University of Cambridge[19]. The most recent of these papers [35] [36] have attempted to model pulsed field magnetization using a modified critical state model calculated using the force-displacement curve of the magnetic flux lines penetrating a high temperature superconductor. The central equation used was proposed by Campbell in 2007 [37] and is:

$$\nabla \times (\nabla \times \boldsymbol{A}) = \mu_0 J_P + k\left[1 - e^{\left(-\left|\frac{(A-A_P)\mu_0 J_c}{kA_r}\right|\right)}\right] \qquad 6.5.$$

where

$$k = \mu_0 J_c sgn(A_P - A) - \mu_0 J_P \qquad 6.6.$$

In this equation A is the magnetic vector potential, A_P and J_P are the peak vector potential and current density, A_r is a constant model fit parameter and the function sgn is to ensure that the force on the field lines is always in the correct direction.

[19] Professor Archie Campbell, University of Cambridge, Department of Engineering, Trumpington Street, Cambridge, CB2 1PZ, UK

Although these models, like the Bean model, assume that the magnitude of the current flowing in the superconductor is either the critical current or zero they encompass the Kim model [38] to describe the dependence of the critical current on applied field:

$$J_c = \frac{J_{c0}}{1 + \frac{B}{B_0}} \tag{6.7.}$$

Where J_{c0} is the critical current density with no applied field and B_0 is an empirical fit parameter taken to 0.37T at 77K. A further refinement is the inclusion of the heat equation so that heating in the bulk during a pulse can be modelled. It was work on this modelling method which showed that fields of up to 15T may be desirable for efficient flux trapping in certain situations [39].

6.2.4 Overview

So far in this chapter we have seen that it is possible to trap a current and hence magnetic field in a superconducting bulk, effectively making powerful, semi-permanent, magnets. To a first approximation the maximum field that can be trapped is dependent on just the size and the critical current density of the bulk and the magnitude of the applied field and so larger bulks at colder temperatures should be able to trap higher fields. From the literature it appears that the most important second order effect is the rise time of the magnetizing pulse; faster rise times will cause higher dissipation in the bulk reducing the total trapped field from a given applied field. The rest of this chapter will be devoted to an experiment which was designed to test these properties in higher applied fields than has ever been published in the literature.

6.3 Experimental Details

The most important piece of equipment for any experiment investigating pulsed field magnetization of bulk superconductors is clearly the magnetic coil. In the previous sections we have seen that larger bulks have a higher maximum attainable trapped field but they also have a larger saturation magnetization field. Therefore, as most applications require the largest field possible it would be most worthwhile to test the largest sample possible which requires a pulsed coil with a large sample volume. Previously we have seen that there are detailed papers which have investigated these properties in pulsed fields of up to 8T with rise times of less than 30ms and another paper which investigate fields of less than 3.6T with a 50ms rise time. Therefore the parameter regions which would benefit most from further investigation would be the longer rise time and higher field regimes.

Furthermore computer modelling has indicated that fields of up to 15T could be useful in certain scenarios. As there is no coil in the Clarendon laboratory with these properties a new coil was designed and constructed. The design and properties of this coil are described in great detail in Chapter 4 but in summary the coil had: a very large sample volume (initial sample space was $28mm \times 55mm$ but this could be enlarged if necessary); a maximum field of 19T; and had a range of rise times which could be varied between 27ms-74ms but at the initial separation the rise times available were: 31.5ms, 43.9ms, 52.6ms and 59.7ms.

Along with the magnetizing coil a flux trapping experiment also requires a means of measuring the applied magnetic field along with the surface field of the superconductor. Furthermore, as the experiment aims to investigate the effects of temperature on flux trapping, some method for regulating and varying the temperature of the superconductor is needed. The method chosen for monitoring the surface magnetic field was a custom built Hall probe array which is described in section 6.3.1. As the experiments were to be conducted in liquid cryogens a tail dewar (detailed in section 6.3.2) would be need to insulate the sample bath from external heat sources while holding the sample within the magnetic field. The temperature of the cryogen within the tail dewar could be varied by controlling the pressure of the gas above the bath by using a manostat gas handling board as detailed in section 6.3.3. The actual temperature of the cryogen will be measured using a standard platinum PT100 resistance thermometer available from RS online[20]. The applied field will be measured by using a secondary pick-up coil mounted on the sample probe away from the sample and the field centre. Although this will not measure the field actually applied to the sample it will only differ from the sample field by a constant multiplier defined by the actual distance from the sample to the pick-up coil. The advantage of moving the pick-up coil out of field centre and away from the sample is that the sample will greatly distort and influence the field around it making accurate measurement of the actual applied central field impossible.

6.3.1 Hall Probe Array

The core method for measuring the magnetic field at the surface of the sample was an array of five Hall chips. An array, rather than just a single probe, was chosen as it would allow the evolution of the magnetic field along with the final trapped field could be measured at various points across the

[20] RS Components Ltd. Birchington Road, Corby, Northants, NN17 9RS, UK. http://uk.rs-online.com/web/

surface, not just the central point, and so the M-shaped profile discussed earlier can be measured. The array was a custom array built in the Clarendon using five Arepoc[21] low sensitivity transverse mounted Hall probes; the same as used earlier when testing the pulsed magnet. These probes were mounted in a straight line in a 10G/40 holder before having their current terminals wired in series to ensure that all probes received the same control current. The array was constructed so that the probes would be as close to the surface of the sample as possible and so that the probe connections would be protected from damage. A series of holes was drilled through the board so that the probes could be wired to the probe contacts whilst lying flat on the sample. A photo of the completed array is shown in Figure 6.6 and the details of the individual probes are given in Table 6.2.

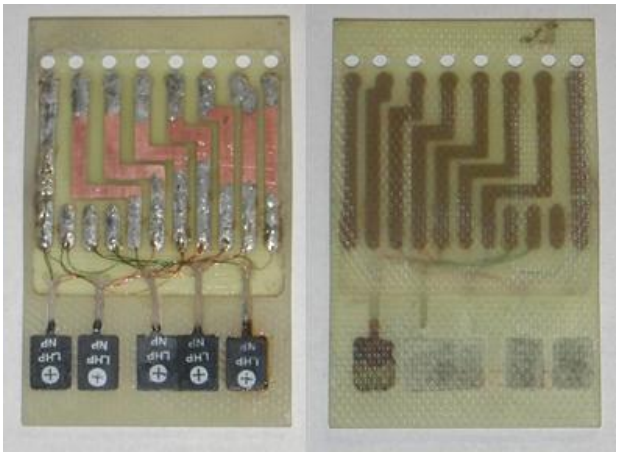

Figure 6.6. The completed Hall probe array. The left hand photo shows side of the array which will face the sample while the right hand photo shows the back of the array board.

Probe	Distance from sample centre (mm)	Sensitivity (mV/T)
1	15	16.9
2	8	41
3	0	28.1
4	5.5	16.3
5	11.6	50.5

Table 6.2. Details of the Hall probe array.

6.3.2 Rectangular cross-section Tail Dewar

As the magnetic coil is immersed in a liquid nitrogen bath if 77K was the only temperature at which the flux trapping was to be investigated then no further equipment would be required beyond the bucket dewar containing the magnet. However as a range of temperatures are to be used a vacuum

[21] AREPOC s.r.o. Iljušinova 4, 85101 Bratislava, SLOVAKIA

insulated dewar is required to insulate the sample bath from its surroundings. A standard piece of equipment used for this purpose in conjunction with magnets is the tail dewar. The standard tail dewar is a vessel which, like any simple dewar, has an inner and an outer vessel separated by a vacuum space. The key difference is that in a tail dewar these vessels have a long thin lower, or tail, section. The thin tails can then easily be inserted into the bore of a magnet coil. The existing tail dewars in the Clarendon had a cylindrical cross-section and the largest ones had a sample space with a diameter of 17.6mm. These are clearly unsuitable for allowing a sample with a diameter of up to 35mm to be cooled to below 77K. Therefore a new, larger, set of tails had to be designed and constructed for the flux trapping experiment. The design of the new tails was unusual in that they had a rectangular, rather than cylindrical cross-section. The reason that the geometry was changed so radically is that the sample has a cylindrical geometry and, as the magnet is a horizontal field split pair, the sample is mounted in the coil with its symmetry axis horizontal. Therefore, when viewed from above the sample will have a rectangular geometry, and the coil separation (and thus the distance between the sample and the coils) can be minimized if the tail dewar is also rectangular as shown in Figure 6.7.

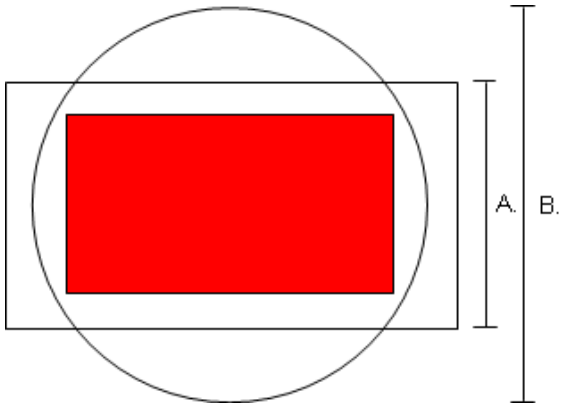

Figure 6.7. For an arbitrary sample (shown in red) the minimum coil separation for a rectangular cross-section tail dewar (A.) is much less than that of a round one (B.).

The drawback of using a rectangular geometry is that the walls of the tails must be strong enough to withstand atmospheric pressure without collapsing or distorting to the extent that the two tails touch, allowing direct thermal conduction between the inner and outer tails. For obvious reasons a round geometry is the strongest and a rectangular geometry is one of the weakest. Therefore the walls of a rectangular tail must be much thicker than those of an equivalent round tail which typically has a wall thickness of ~0.25mm. A simple FEA model showed that for a stainless steel plate with a wall thickness of 1mm and a length of 50mm would flex by ~0.1mm under atmospheric pressure therefore the tail separation must be at least twice this if this thickness were used. The final design featured tails

with 1.2mm wall thickness and the outer tail had a width of 50mm and a breadth of 25mm while the inner tail had a width of 40mm and a breadth of 20mm. This gave a working sample cross-section of 17.6mm by 37.6mm. A photograph and diagram of the tail dewar is shown in Figure 6.8.

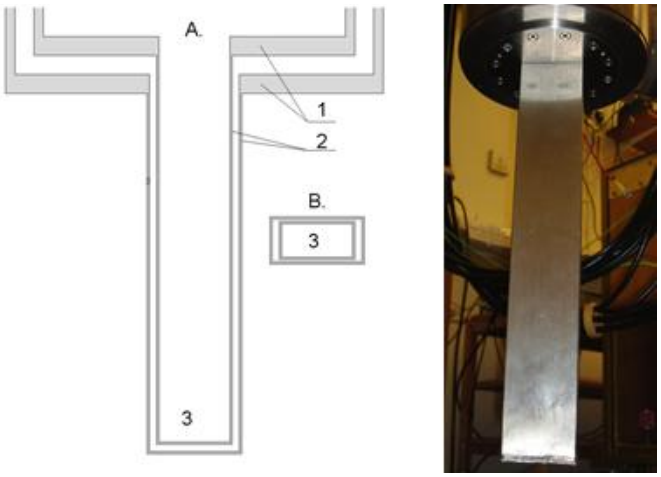

Figure 6.8. A photograph and a diagram of the tail dewar where the details of the diagram are: A. Side view of assembly. B. Plan view of tails. 1. Stainless steel flanges to attach tails to bottom of dewar. 2. Tails separated by vacuum space. 3. Sample space

6.3.3 Manostat

The boiling point of a liquid is a function of the environmental pressure at the surface of the liquid. This fact gives a very simple and convenient method for varying the temperature of the sample cooled by a boiling liquid nitrogen bath as, if the pressure at the surface of the bath is lowered, its boiling point will lower and the entire bath will cool to a reduced temperature. The boiling point of liquid nitrogen at room pressure is 77.35K and the liquid will remain liquid down to the triple point which exists at a pressure of 0.124bar and a temperature of 63.15K [40]. The problem is then how to control the pressure inside the dewar to a high enough accuracy that the nitrogen can be kept at a constant temperature for the duration of an experimental run. The solution to this problem was to build a simple manostat which is a device for automatically regulating a pressure within an enclosure. The central feature of the manostat constructed was a front plate with two ports; one connected to the sample dewar and the other to the pump. A thin (~2mm although a thinner diaphragm could be used for increased accuracy at lower pressures) neoprene diaphragm was then stretched across these two ports and the space behind the diaphragm was connected to a reference volume sealed by a valve through which the pressure in the reference volume could be varied. A simple diagram of this geometry is shown in Figure 6.9. The operation of the manostat is then very simple: if the pressure in the sample dewar is lower than the reference volume pressure then the diaphragm will be pressured against the

pump and sample port, greatly increasing the impedance of the gas flow to the pump. This will greatly reduce the gas flow from the dewar, allowing the pressure to rise. Conversely if the sample dewar pressure is greater than reference pressure then the diaphragm will be moved clear of the ports allowing the pump to freely reduce the pressure in the dewar. It is worth noting that this design of manostat will only work on a 'wet' load as the diaphragm will only vary the impedance of the gas flow, it cannot stop the flow entirely, and so a dry dewar would still be pumped out to a high vacuum, albeit at an increasingly slow rate. A photo of the completed manostat and the associated plumbing is shown in Figure 6.10.

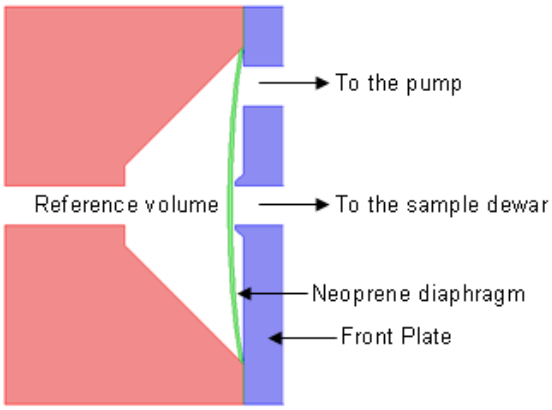

Figure 6.9. Simplified manostat geometry showing the pumping port, sample dewar port, reference volume along with the neoprene diaphragm.

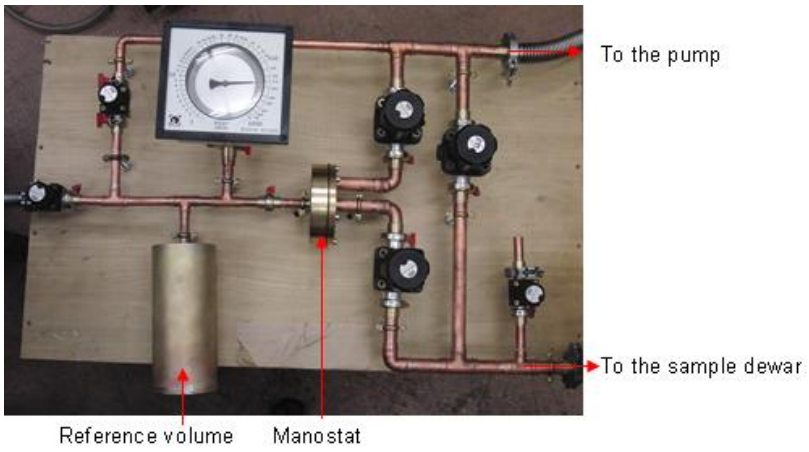

Figure 6.10. The completed manostat and related plumbing.

6.3.4 Bulk Superconducting Sample

The sample used for the flux trapping experiments in this thesis was a high temperature superconductor gadolinium-barium-copper-oxide (GdBCO) prepared and supplied by Professor

Cardwell at the university of Cambridge[22]. The sample was prepared using a standard top-seeded melt-processing method [41]. This method involves grinding the precursor powders until only a single crystal phase is present before being compressed into cylindrical pellets. The pellets are then melted in a furnace and are seeded with a cold-seed to start the crystal growth before the temperature is gradually reduced and the mixture is allowed to re-solidify. This method results in a large single grain crystal. The sample used had a nominal outer diameter of 35mm and a nominal depth of 15mm and is shown in Figure 6.11.

Figure 6.11. The GdBCO single grain sample used in the flux trapping experiments.

6.3.5 Magnet Probe

The final piece of equipment that is required for the flux trapping experiment is a probe which can be inserted into the tail dewar. This probe must hold the sample, the Hall probe array, field pick-up coil and the PT100 in the correct locations within the field during a pulse. As the instrumentation on the probe will be in a partial vacuum the probe must allow electrical contacts to made from inside to outside the dewar whilst maintain a vacuum tight seal. A further requirement is that it must be non-magnetic and have as low an electrical conductivity as possible to minimize eddy currents. To satisfy these requirements the majority of the probe was constructed out of thin-walled stainless steel tubing. To provide the electrical connections two Cryospares - Oxford Instruments[23] ten-pin lead through connectors were attached to the top via a rubber O-ring providing 20 vacuum tight channels. The bottom section was constructed out of 6F/45 grade Tufnol. 6F/45 was used as it is a good insulator and would be exposed to the highest fields this would prevent any complication from interactions between metal and the applied fields. The 6F/45 has the added benefit that it has a low thermal contraction [42] and so would be less likely to damage the sample as it contracts during the cool down process. Finally

[22] Professor David Cardwell, University of Cambridge, Department of Engineering, Trumpington Street, Cambridge, CB2 1PZ, UK

[23] Oxford Instruments Direct, Tubney Woods, Abingdon, Oxfordshire, OX13 5QX. www.cryospares.com/

a sliding Klein flange seal with captive O-rings was fitted to the tube section so that the probe to be raised and lowered within the dewar without breaking the vacuum seal. Photos of the completed and assembled probe are shown in Figure 6.12. It is estimated that the Hall probe array will be situated $\sim 0.2 \pm 0.1mm$ above the surface and $< 1mm$ from the centre of the sample. The large error in positioning from the centre is due to slightly irregular shape of the sample.

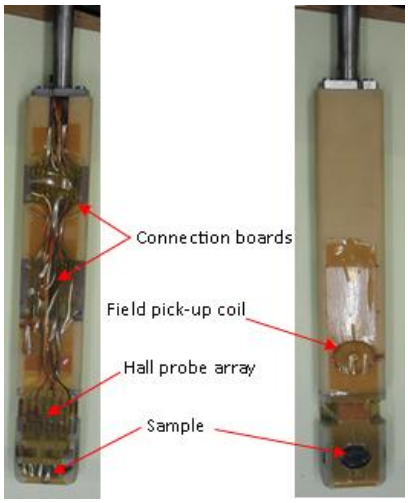

Figure 6.12. A front and rear view of the lower section of the magnet probe.

6.4 Single Pulse Magnetization

The first series of tests performed on the sample was to ascertain what the remanent flux trapped in an initially unmagnetized sample would be when it was exposed to a single magnetic pulse. As previously stated the sample was cooled using liquid nitrogen or liquid helium with the result that the sample was tested at 4.2K and between 63.2K-77.3K.

6.4.1 Procedure

The initial stage of the single pulse experiment was to cool the dewar and sample to the required temperature in the cryogen. Once the sample was in the cryogen it was given ~5mins to cool down fully. The cooled sample was then exposed to a magnetic pulse and the surface magnetic field was measured both during and after the pulse. In the literature the trapped flux is often defined as the remanent flux remaining in the sample 20 minutes after magnetization [43]. However for this experiment the trapped flux is defined as the remanent field after 10 minutes. This was chosen as there is a very large number of possible combinations of applied field and temperature to measure and so by halving the time criterion the experiment could progress much faster. Although this differs from the

literature we will see in section 6.6 that it induces very little error and, if required, the value after 20 minutes could easily be estimated to using the value measured after 10 minutes.

Once the required data had been measured the probe was raised within dewar so that the sample was situated in the neck of the dewar, well above the level of the cryogen. This simple process allowed the sample to warm slowly, removing any trapped field, without exposing the sample to the atmosphere. This gentle warming within the dewar has many advantages such as: it removes the need to re-pressurize the dewar after each pulse; it lowers the thermal shock to the sample which can break through thermal cycling due to its brittle nature; it prevents water vapour from freezing either within the dewar, which could lead to a blockage, or on the sample which could easily degrade it. During the warming process the flux decay was monitored and once all of the flux had been remove the sample was re-immersed in the cryogen ready for the next pulse.

6.4.2 Results

6.4.2.1 Pumped liquid nitrogen

For the single pulse magnetization the key parameter which were measured were the remanent flux 10 minutes after the pulse had been applied and what we will call the M-ratio or M_R. The M-ratio is specific to this thesis and is defined as the ratio between the field at the centre of the bulk to the field 5.5mm from the centre i.e. the ratio of the signal from Hall probe 3 to Hall probe 4 or:

$$M_R = \frac{B_{hp3}}{B_{hp4}} \tag{6.8.}$$

This is a useful quantity as it will give a direct measure of the shape of the trapped flux profile. A value of $M_R < 1$ shows that there has been incomplete magnetization leaving an M-shaped profile, $M_R = 1$ is again incomplete magnetization but with a flat-topped profile and $M_R > 1$ is a Bean cone with near complete or complete magnetization.

The evolution of the surface magnetic flux can be divided into three distinct phases as follows:

- Phase 1 – Flux evolution during the magnetizing pulse.
- Phase 2 – Rapid flux relaxation in the seconds immediately after the pulse.
- Phase 3 – Flux creep regime of trapped flux.

Furthermore the magnitude of the pulse can be in one of three possible flux trapping regimes by comparing it to $2H^*$ and these are the under, over and critical magnetization regimes. These regimes are defined as:

- $B_{applied} < 2\mu_0 H^*$ - under-magnetization regime.
- $B_{applied} = 2\mu_0 H^*$ - critical-magnetization regime.
- $B_{applied} > 2\mu_0 H^*$ - over-magnetization regime.

During the three phases of the magnetization process the flux evolution at the centre of the sample behaves in a very similar manner during under and critical magnetization but behaves in a markedly different manner during over-magnetization.

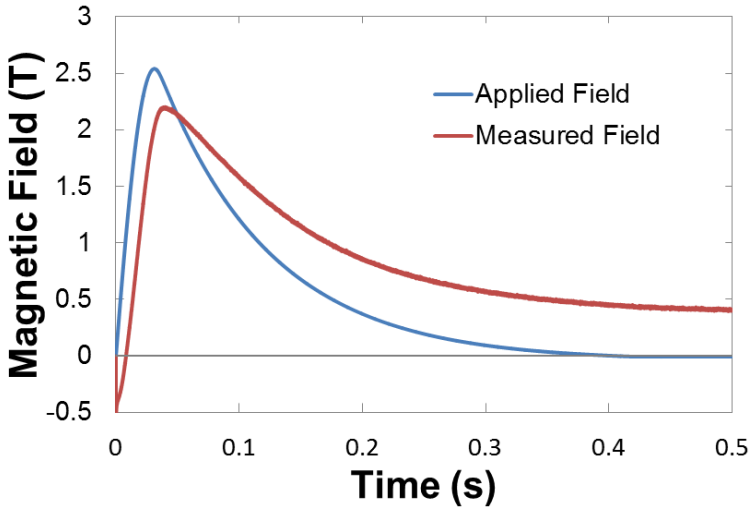

Figure 6.13. Typical curves for the applied magnetic field against the field measured at the surface at the centre of the sample during under-magnetization at 77K.

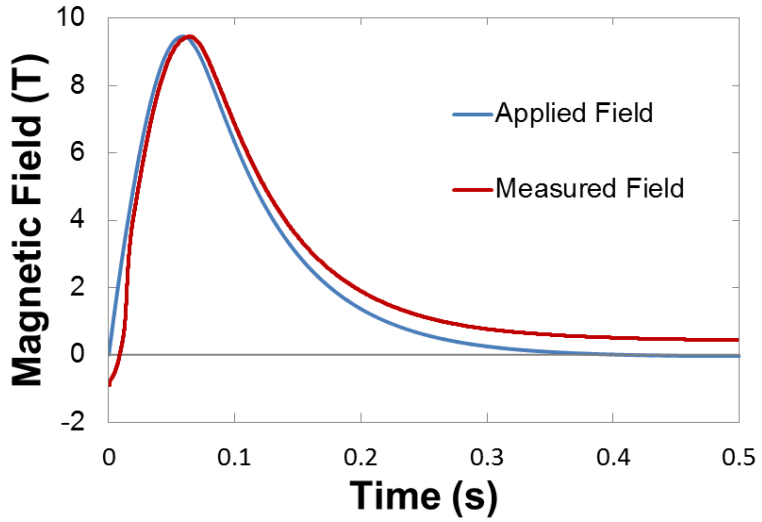

Figure 6.14. Typical curves for the applied magnetic field against the field measured at the surface at the centre of the sample during over-magnetization at 63K.

This difference in behaviour during the pulse becomes most apparent by comparing the evolution of the field measured at the centre of the sample to the applied field. Figure 6.13 shows the trace for the data recorded during a typical under-magnetization pulse while Figure 6.14 shows a typical over-magnetization pulse. The central flux during an under-magnetization is consistently lower than the applied field peaking at a lower magnitude than and ~5-6ms later than the applied field. In the over-magnetization regime the central field begins to evolve in a similar manner to the under-magnetization regime but as the applied field approaches the critical magnetization field the central field increases rapidly to a level just below the applied field. It then remains just below the applied field until the peak where it again peaks 5-6ms after the applied field at about the same magnitude. The central field during a critical magnetization shows the same sharp increase in the central field as the over magnetization case but peaks with a lower maximum than the applied field as in the under-magnetization regime. In all cases, as the applied field falls, the central field becomes the larger field with a large remanent flux remaining when the applied field drops to zero.

The fact that the measured field is lower than the applied field during the rise stage of the pulse is easily explained within the Bean model as the measured field is combination of the applied field and the magnetization, M, of the sample:

$$\mu_0 H_{applied} = B_{measured} - \mu_0 M \qquad 6.9.$$

In the Bean model the bulk of the sample is shielded from the applied field by supercurrents in the outer layers during a field increase. The result of this is that the field within the sample is lower than the applied field and so the magnetization is always negative for an increasing field. Therefore the measured field must always be lower than the applied field as long as there are still currents in the bulk. The sharp increase in the measured flux is harder to explain but it is surmised that it is due to the critical current of the sample being reduced by the higher field and so, as the supercurrents decay, the shielding of the bulk of the sample, and hence the magnetization, is greatly reduced. This effect becomes ever greater as the applied field increases and could be used to gain an estimate of the dependence of the critical current density on applied field. The delay in the peaking of the surface flux is simply caused by the magnetic diffusivity of the sample. As the sample has a very high conductivity it will resist any change in magnetic field and so it takes a finite amount of time for the changing field to diffuse across the sample's surface.

The magnetization of the bulk remains negative for the initial stages of the decay of the applied field but it will increase rapidly as the reverse current are induced until the magnetization becomes positive. At this point the measured central field will be higher than the applied field and will remain so until the sample is quenched.

Immediately after the magnetizing pulse there is a rapid relaxation of the trapped flux. This is likely due to the fact that, unlike the assumptions of the critical state model, currents significantly higher than the critical current are likely to be induced in the sample. These high current levels will then be subject to the dissipative process of flux flow which will cause a temperature increase in the sample. This temperature rise will then, in turn cause a further decay in the trapped currents. However as the trapped currents decay to their critical current level the rate of the decay reduces greatly. Very quickly the sample enters the flux creep regime where thermal fluctuations are the principal cause of the decay. Figure 6.15 shows the decay of the trapped field at the centre of the bulk for a typical under-magnetization pulse. It shows that immediately after the pulse there is clearly rapid flux relaxation as the trapped field reduces by ~15% in just 1.5s. This can be compared to the next 10 minutes where the flux decays by just 5% more and of that 3% of the decay happens in the first minute.

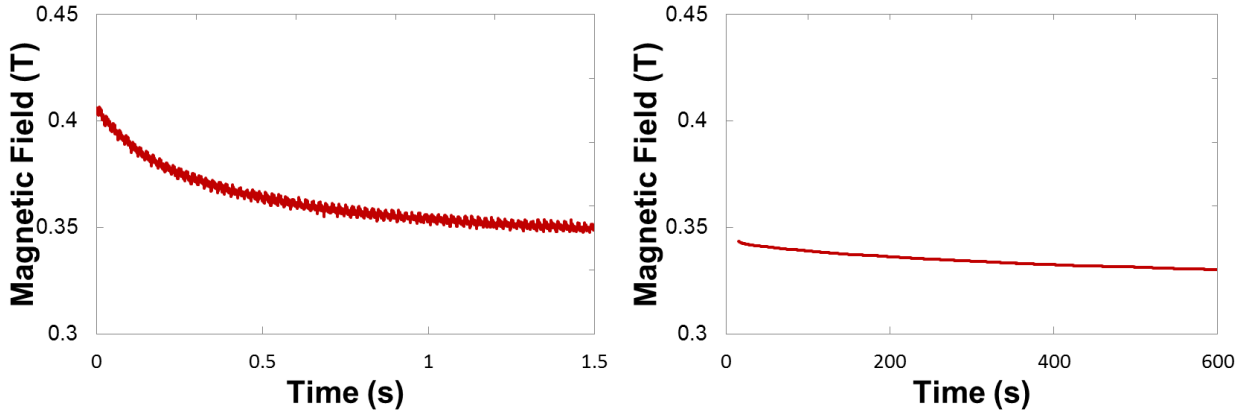

Figure 6.15. The rapid relaxation of the trapped flux immediately after a magnetizing pulse (left) and the decay of the flux due to flux creep for the 10 minutes after the initial flux relaxation period.

A critically magnetized bulk will show very similar decay characteristics as the under-magnetized one however an over-magnetized bulk shows very different behaviour. Although the periphery fields do decay as expected the central flux of an over-magnetized bulk will actually increase slightly after the magnetizing pulse and will continue to do so for a considerable time as shown in Figure 6.16 (see the end of this section and section 6.6 for more details).

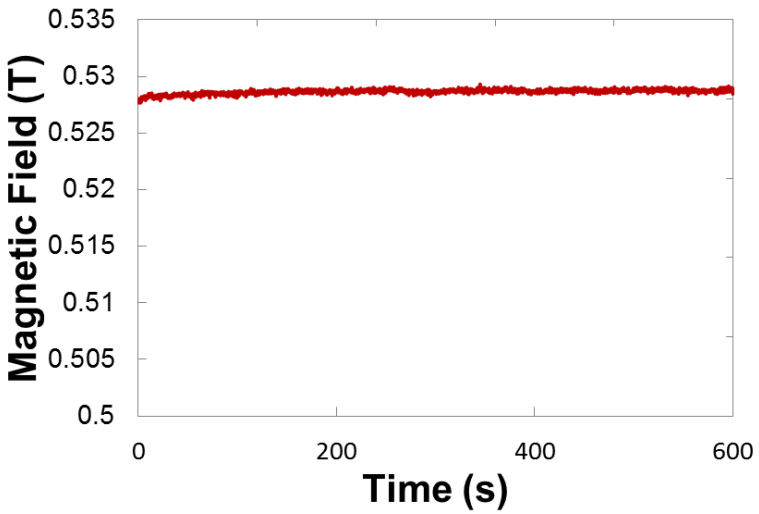

Figure 6.16. *The increase in the central field trapped in an over-magnetized bulk during the 10 minutes after the magnetizing pulse.*

A plot of the variation of the trapped field against applied magnetic field for magnetizing fields of up to 10T at 63.2K is shown in Figure 6.17. It shows that the field that is trapped is very strongly dependant on the magnitude of the applied field and it clearly shows the three regimes defined earlier: 3.5T is the peak and hence is the critical magnetizing field while applied fields in the under and over-magnetizing regimes trap considerably less field. It is also interesting to note that, despite the results found in the literature, the flux trapped has no clear dependence on the rise time of the magnetizing field despite the large range of rise times used in the experiment. The logical explanation to this is that, as this investigation used much longer rise times than those used in the literature (with the exception of [20]), is that the rise times used are slow enough that the heating effect due to the changing magnetic field is small compared to other factors affecting the magnetization process.

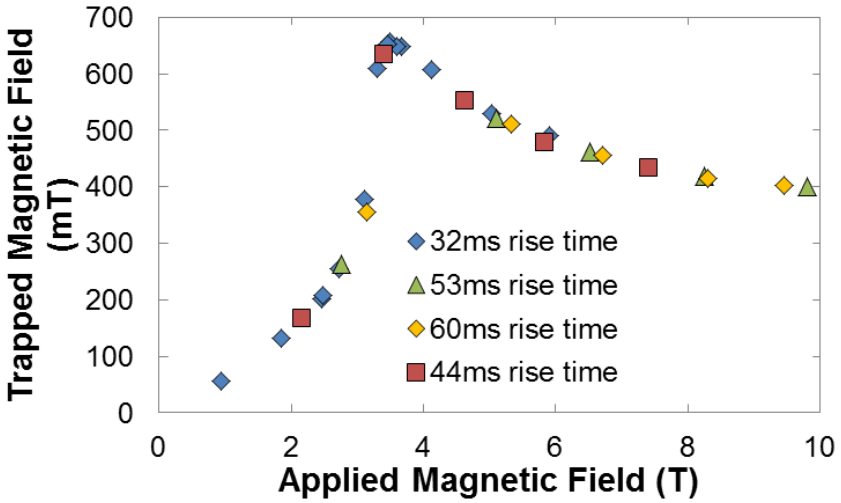

Figure 6.17. *The trapped field as a function of applied field at 63.2K for a range of magnetizing field rise time.*

By utilizing the manostat the temperature the curve shown in Figure 6.17 was measured at 5 temperatures in total, namely: 77.4K, 73.3K, 69.4K, 66.2K and 63.2K. The error on the temperatures is estimated to be ±0.5K due to the fact that the calibration curves available only extend to ~73K [43] and so the temperature was calculated using an extrapolated curve. By combining the curves measured at each temperature the flux trapping surface for the sample as a function of temperature and field can be plotted as shown in Figure 6.18. It is clear from this graph that the basic shape of the curve is the same for all temperatures but that the critical magnetizing field and the peak trapped flux varies considerably. The peak trapped field varied from 320mT at 77.4K up to 660mT at 63.2K and had a linear dependence on temperature following:

$$B_{trapped}(T) = 2260 - 25.3T \qquad 6.10.$$

with a regression factor of 0.999 where $B_{trapped}(T)$ is the trapped field in mT and T is the temperature in kelvin. In this temperature range the critical magnetization field also varied with a range from 2.7T at 77.4K to 3.5T at 63.2K and followed the formula:

$$B^*(T) = -1.2 \times 10^{-3}T^2 + 0.11T + 1.2 \qquad 6.11.$$

with a regression of 0.994 and where $B^*(T)$ is measured in T.

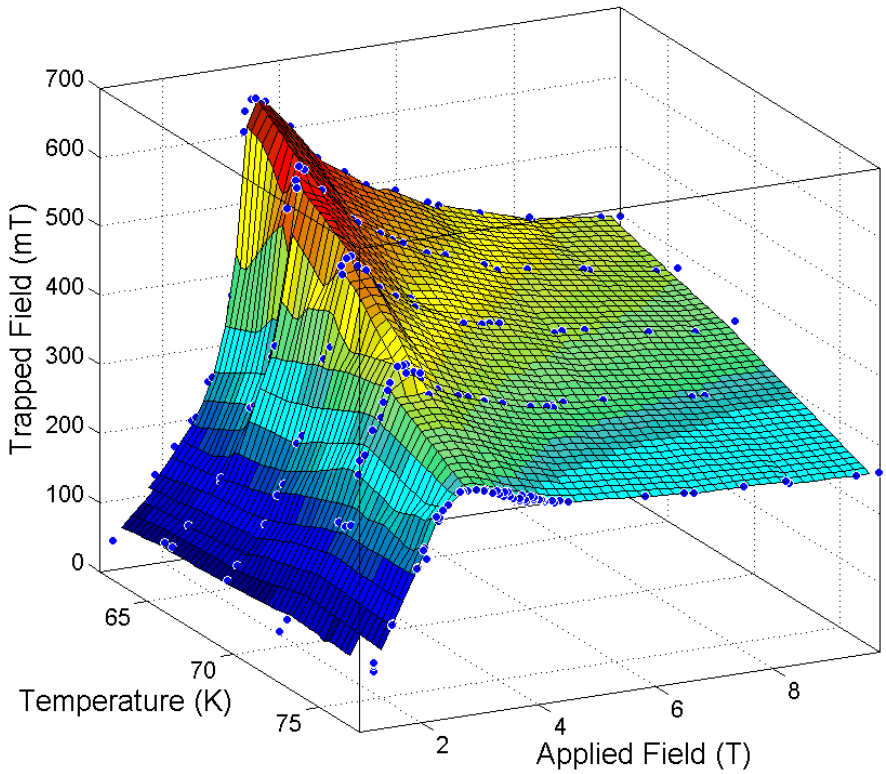

Figure 6.18. The surface showing the flux trapped in the bulk as a function of applied field and temperature.

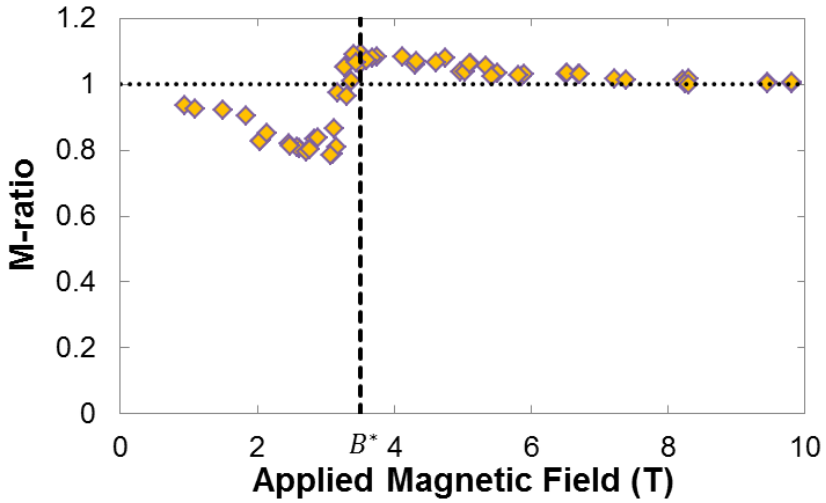

Figure 6.19. The variation of the M-ratio of the sample with applied field at 63.2K.

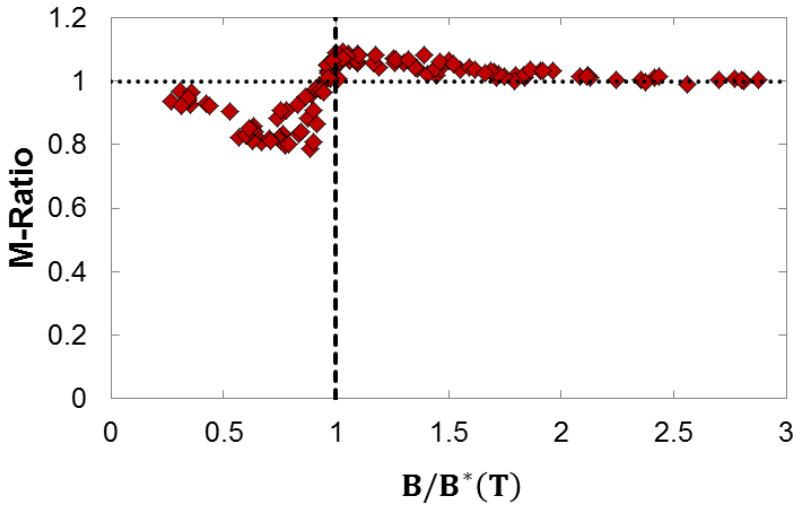

Figure 6.20. The variation of M-ratio against the ratio between the applied field and the critical magnetizing field for all temperatures in liquid nitrogen.

Another interesting parameter to explore is the M-ratio defined in equation 6.8 which, as previously mentioned, gives a measure of the shape of the magnetization profile. Figure 6.19 shows the variation of the M-ratio against magnetizing field at 63.2K while Figure 6.20 shows the M-ratio against applied field normalized by dividing by the critical magnetization field for all temperatures in liquid nitrogen. These figures show that at the critical magnetization field the M-ratio for this sample is about 1.1 and that the ratio is lower for both under and over-magnetization pulses at all magnetic fields. In the under-magnetization regime the M-ratio is significantly below 1 until $B/B^*(T) \geq 0.95$ where it becomes greater than one, quickly reaching the maximum value. In the over-magnetization regime the M-ratio decays from the maximum value as the applied field increases, slowly tending to unity at high values of $B/B^*(T)$. At very small applied fields the M-ratio again tends to 1 but this is likely just an artefact of the small fields trapped, primarily in the periphery of the sample. When this is combined with the

fact that the probes will not be exactly at the surface (they will be ~0.2-0.3mm from the surface) some small value of flux generated by the periphery field will be detected by the central probes. This is supported by the measurements from the outer probes of the array as a typical low field shot with at 73K with $B/B^*(T) = 0.31$ had a central field of just 75mT but the field 12mm from the centre was 105mT.

Although the value of the M-ratio can be greater than or equal to 1 in both the under and over-magnetization regimes the actual shape of the magnetization profile is likely to be different as shown in Figure 6.21. In the under-magnetization, even when the M-ratio is greater than 1, there profile will still have a slight dip in the centre, it is just that the dipped centre is still greater than the field 5.5mm from the centre (it is an artefact of having a large gap between Hall probe sensors). However in the over-magnetization regime the reduction in the M-ratio is caused by a flattening of the entire cone.

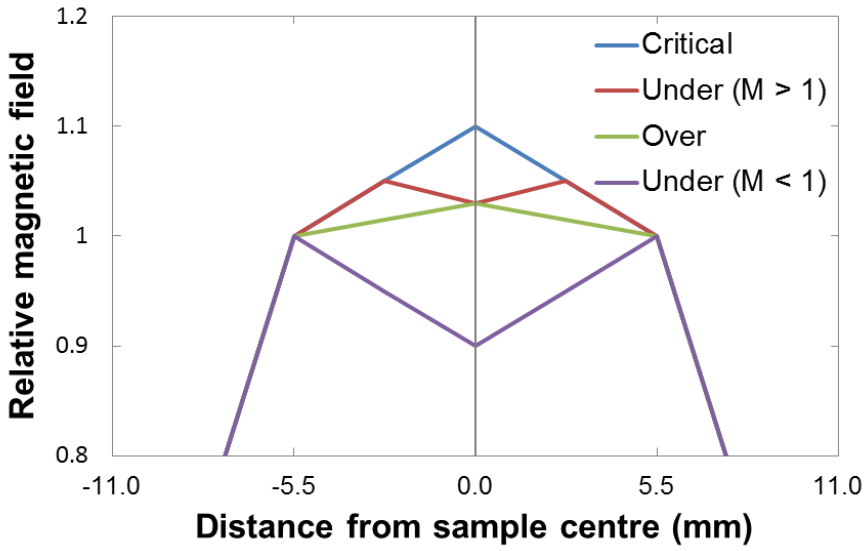

Figure 6.21. *Simplified flux profiles for the different magnetization regimes normalized to the same magnitude.*

The general behaviour of the sample in the under and critical-magnetization regimes is easily explained within the simplistic Bean model with a few simple modifications. The peak of the trapped flux curve is simply the field at which the magnetizing pulse induces the critical current at every point in the sample whereas the reduced field trapped by an under-magnetization due to incomplete penetration of the sample by the magnetizing pulse. The major discrepancy between the model and the data is that the model predicts that a critically magnetized sample should trap about half of the applied field but this is clearly not the case as it traps 11% at 77K and 19% at 63K. The first step to explaining this difference has already been mentioned in section 6.2.2 in that the critical current density of a

superconductor is not independent of applied field but reduces as the applied field increases. As the field in the sample is greater towards the centre the current density must be lower and hence this leads to a rounding, and more importantly here, a reduction in the peak of the trapped flux profile. Another important point to make is that the critical current density is not a step function, with no associated dissipative electric field below that level and a normal state resistivity above it, as assumed in the model. In reality the electric field has a continuous, highly non-linear, dependence on the current density, as explained in section 1.4.5. Therefore the changing magnetic field will induce a current density dependant on the rate of change of the field and the non-linear curve and this current density will cause an electric field and dissipation. This will cause the current to decrease sharply immediately after the magnetizing field is removed until the rate of dissipation becomes negligible with respect to the energy stored in the sample. It is this electrical dissipation which causes the rapid flux relaxation in the seconds after the pulse. The final important factor to consider at this stage is the fact that the electrical dissipation of energy in the sample during and immediately after the pulse must increase the temperature of the sample. This temperature increase will further depress the critical current density causing further dissipation and cause a greater decay in the trapped flux in the sample immediately after the pulse than would occur in a perfectly cooled one. When these three factors: critical current density dependence on applied field; realistic current density/electric field relation; and temperature increase, are all considered the reduction in the maximum trapped flux from the predicted value qualitatively seems to be accounted for although some detailed computer modelling would be needed to back up the hypotheses.

The cause of the reduction in trapped field caused by an over-magnetization pulse is less obvious as, to a first approximation it should not matter if the applied field is higher than the critical magnetization field. This is because although the high field will suppress the initial current distribution, as the field drops from the critical value, it will still induce the critical current density at all points in the sample. The heating of the sample may play a part as the suppression of the critical currents at high fields will cause greater dissipation and greater heating. This extra heating will cause the trapped currents to decay faster and further than the currents induced by a lower field. Furthermore it has been demonstrated in the literature that the heating is greatest towards the centre of the bulk [21]. This should then cause the currents towards the centre of the bulk to decay to a greater extent than the currents at the periphery. Figure 6.22 shows that the ratio between the central flux and the flux

11.6mm from the centre decreases sharply during the first second after magnetization indicating that the central flux does indeed decay at a greater rate. Along with explaining the reduction in trapped field as applied field increases this also would explain the flattening of the Bean cone indicated by the M-ratio at higher fields as this indicates that the currents at the centre of the sample are reduced to a greater extent than currents towards the periphery.

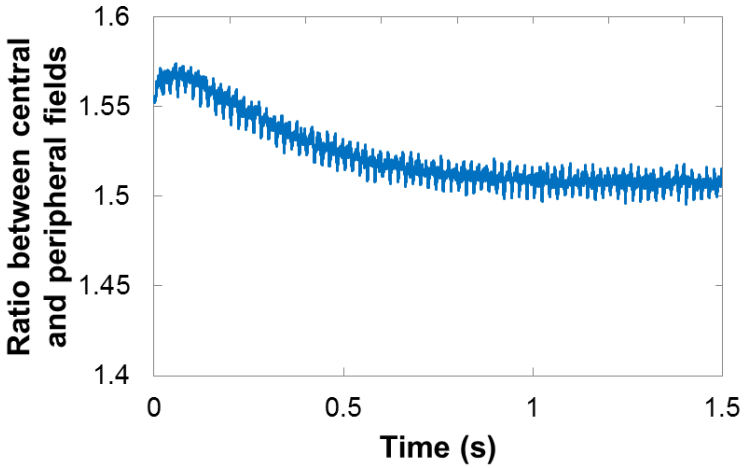

Figure 6.22. The ratio between the central field and the field 11.6mm from the centre of bulk as a function of time after the magnetizing pulse.

The highly uneven distribution of currents within an over-magnetized bulk would also offer a possible explanation to the central flux enhancement demonstrated earlier in this section in Figure 6.16. Once the bulk has fully cooled back down to the coolant temperature the current density would still be greater at the periphery than at the centre. As any current in the bulk will have an associated dissipative electric field this would lead to an uneven distribution of the electric field across the bulk with higher fields at the edge. This could then cause the currents to slowly re-distribute towards the centre of the bulk in an attempt to create a uniform electric field across the bulk thereby increasing or maintaining the central field while the field further from the centre decays as expected. As the bulk will be fully superconducting during this process any re-distribution will be slow due to the very low magnetic diffusivity of the bulk and so would occur over the minutes and hours observed and presented in section 6.6.

6.4.2.2 Liquid helium

Cooling the bulk from liquid nitrogen to liquid helium temperatures will greatly improve the superconducting properties of the bulk. In theory this should greatly enhance the flux trapping by greatly improving critical current density and critical magnetic field. However the low temperature

will also greatly reduce the heat capacity and thermal conductivity of the sample which would make any supercurrents far more vulnerable to the heat generated by a single flux jump event. To ascertain whether the low temperature would improve or destroy the flux trapping abilities of the bulk the single pulse magnetization experiments were repeated at 4.2K. The procedure for the experiment was nearly identical to that used in nitrogen in section 6.4.2.1. The one difference was that, to remove the trapped flux between each run, it proved necessary to add a small heater to help warm the sample to above its critical temperature after it had been removed from the cryogen.

The results of the single pulse magnetization experiment are shown in Figure 6.23. The greatest amount of flux trapped at this temperature with a single pulse was 1.26T with a 4.5T pulse. This is far greater than that achieved at 63K and furthermore it was shown that this trapped flux was very stable as shown in Figure 6.24. This shows that over a 1 hour period there was no measurable decay in a trapped flux of 1.23T and there was certainly no catastrophic flux jump events causing runaway heating and decay of the field. The other defining feature of the trapping characteristics at this reduced temperature was the 'sharpness' of the peak in the trapped flux against applied magnetic field: the flux trapped falls off very quickly on both sides of the peak. This implies that the sample has strong superconducting properties effectively shielding the centre of the bulk if an under-magnetization pulse is applied. It also implies there is a very strong heating effect during the pulse causing the over-magnetization pulses to degrade the current trapped very quickly. It is therefore very important when trapping field at lower temperatures to carefully tune the magnitude of the magnetizing pulse to the optimum value.

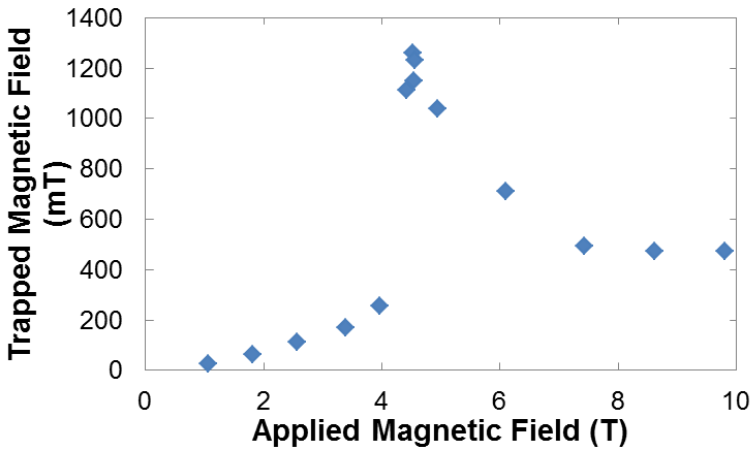

Figure 6.23. *The flux trapped after single magnetization pulses at 4.2K.*

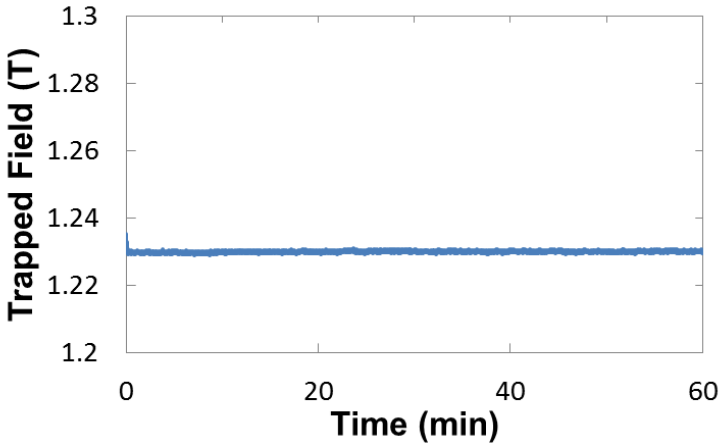

Figure 6.24. The field measured at the centre of the sample for 1 hour after a 4.5T magnetizing pulse.

The use of a multi-pulse magnetizing strategy (see section 6.5 for further details) was also briefly investigated and the most successful at this temperature was to use two 4.5T pulse followed by a 3.5T pulse which successfully increased the flux trapped to 1.4T with no measurably decay in the trapped field during the 10 minutes after the third pulse.

6.5 Multi-pulse Magnetization

It has been shown in the literature [2] [15] [26] that the trapped flux in a bulk can be enhanced by repeatedly exposing the bulk to magnetizing pulses without first removing the trapped field. Therefore it was decided that a brief investigation should be conducted to ascertain whether that is true of the sample used and whether this area would benefit from further work in the future.

6.5.1 Procedure

The majority of the procedure for the multi-pulse experiment was identical to that used in the single pulse experiment described in section 6.4.1. The only key differences were that the sample was not warmed to remove the trapped field after every pulse and that only two liquid nitrogen temperatures (77.4K and 63.2K) were tested. Once the sample and apparatus had been cooled to the required temperature a series of pulses were applied with each pulse being applied 10 minutes after the previous one so that the flux trapped by that pulse could be measured. In general four different combinations of pulses where tried:

- Multiple pulse of the same magnitude.
- Multiple pulses where each pulse was smaller than the previous one.
- Several lower field pulses followed by several medium field pulses.

- A high field pulse followed by several medium field pulse

After each series had been applied the sample was warmed to remove any trapped flux as in the single pulse experiment.

6.5.2 Results

The first multi-pulse test to take place was to expose the sample to 6 repeated pulses of the same magnitude at 77K and 63K. The data for the test at 77K is shown in Figure 6.25. It shows that for the lower field pulses the trapped flux can be significantly improved by the repeated application of the magnetizing pulse with a total increase of 32% being recorded after the sixth pulse. However the amount that each pulse increases the flux decreases with each successive pulse with the second pulse adding 13mT while the sixth adds just 2mT more. This shows that although the flux can be increased at these levels it is unlikely to ever achieve a trapped field of the magnitude achievable from a single higher field pulse. Furthermore the data shows that at this temperature the achievable increase in flux decreases as the magnetizing field increases until, at the critical magnetizing field, no statistically meaningful increase (<0.4%) is measured after the 6 pulses.

It seems likely that the physical reasons behind the enhancement in the trapped flux by using the multi-pulse method is different for the low and high field regimes. In the low field regime the initial pulse will only induce currents in the periphery, resulting in a low trapped field in the centre. However when the second pulse is applied the outer layers are already carrying the critical current density and so they cannot, to a first approximation, have any more current induced in them. Therefore the second pulse will induce the critical current in the layers further into the superconductor, increasing the depth of the currents and hence the central field. This process can be repeated to keep enhancing the flux but, as has been mentioned, the induced currents do decay from the level at which they were originally induced through the dissipative electric field. Therefore the layers which have previously had a current induced will still be able to resist the change in field during a later pulse and so as each successive pulse must penetrate deeper it has less of an effect. This in turn leads to the asymptotic behaviour seen in Figure 6.25. In the high field regime the trapped flux has been suppressed by heating in the sample. As some of this heating is caused by flux flow into the sample during the magnetization the greater the change in the flux in the sample the greater the heating. Therefore if the sample already has a large trapped flux with a current at or near the critical current when a second magnetization pulse is applied

the flux flow and hence the heating will be greatly reduced. There will still be a heating effect caused by the currents decaying to their stable level but the reduction in flux flow heating allows the trapped flux to be increased to a level close to the maximum achievable single pulse field. It appears that the field trapped by the critical magnetizing field cannot be further enhance at this temperature indicating that the flux motion heating is small compared to other effects.

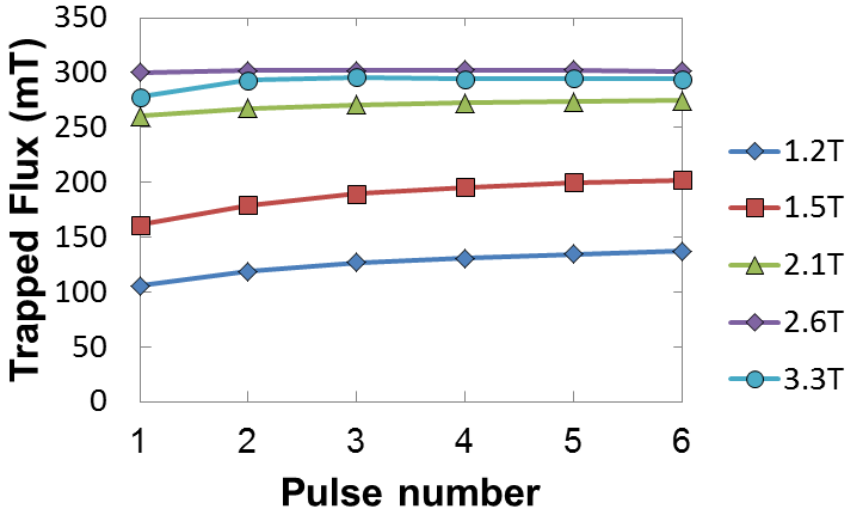

Figure 6.25. *The flux trapped after the application of each pulse using pulses of the same magnitude at 77K for 5 different field levels.*

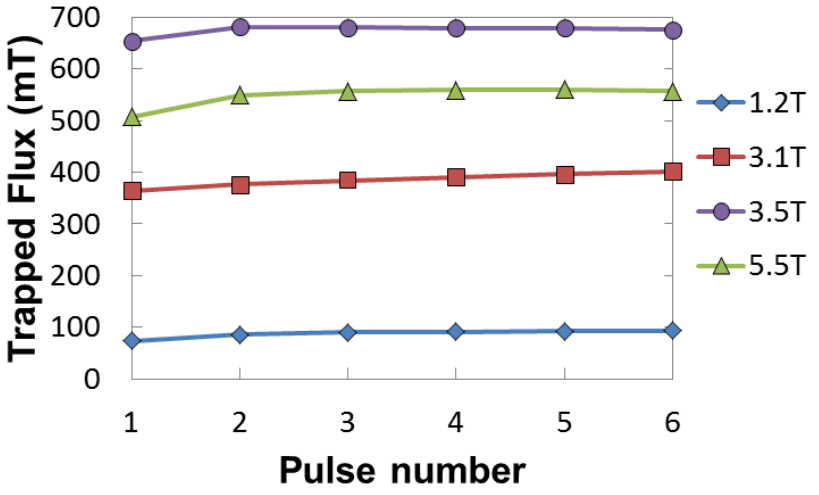

Figure 6.26. *The flux trapped after the application of each pulse using pulses of the same magnitude at 63K for 4 different field levels.*

The data for the repeated pulses of the same magnitude at 63K is shown in Figure 6.26. At this temperature the low field behaviour is very similar to that at 77K in that applying 6 1.2T pulses increases the trapped field by 27% from the field trapped by a single pulse and again the saturation behaviour is seen whereby each pulse adds less flux than the pulse before it. The main difference is that at the critical magnetizing field the second pulse increases the flux by 4% from 650mT to 680mT.

Further pulses do not increase the field any further and may in fact cause a slight decrease (-0.8%) of the total trapped flux. At this lower temperature the critical current will be considerably higher which cause greater heating due to the flux flow into the sample. When this is coupled with the reduced heat capacity, due to reduced temperature, the temperature increase during the magnetization process will be much greater than at 77K. Therefore it is possible that the trapped field at the critical magnetizing field can be increased through similar processes which allow the over-magnetization flux to be enhanced: namely that the pre-trapped flux reduces the flux motion and hence heating, in subsequent pulses.

The next test which was conducted was to expose the bulk to a series of 6 pulses at 63K where each pulse was of a smaller magnitude than the previous one starting with the single pulse critical magnetizing field of 3.5T. The behaviour observed for this method was almost identical to the repeated 3.5T pulses presented in Figure 6.26 but as the later pulses were of a small magnitude they caused a lower reduction of trapped field.

The final test involved exposing the bulk to a series of pulses of differing magnitudes with two distinct regimes tested at 63K. The first was to start with an under-magnetization pulse before increasing the field magnitude to be equal to or just above the critical magnetizing field; a similar technique to the MMPSC used to trap the record field trapped by pulsed field magnetization in [2]. The second was to apply an over-magnetization pulse before reducing the magnitude to the critical magnetizing field; a technique which has not been explored in the literature.

	Magnitude of applied field (T)	
Pulse number	Low to medium field	High to medium field
1	2.8	4.8
2	3.5	4.1
3	3.5	4.1
4	4.2	4.1
5	4.2	4.1
6	4.2	3.5

Table 6.3. The magnitude of the applied pulses in the most successful runs for the high field to medium field and low field to medium field magnetization tests.

Table 6.3 shows the series of pulses used in the most successful run for each of the multi-pulse magnetization techniques. The field trapped after each pulse in each series is shown in Figure 6.27. It

shows that the low to high field pulse advocated in the literature [25] is very successful in increasing the trapped flux resulting in a final flux of 722mT, an increase of 10% above the maximum amount of flux which can be trapped with a single pulse. However it appears that the high to low field pulses are even more successful at improving the trapped flux resulting in a final trapped field of 743mT, an increase of 13%. It is not clear why the over-magnetisation method is more successful but should provide an interesting challenge to consider for future computer models.

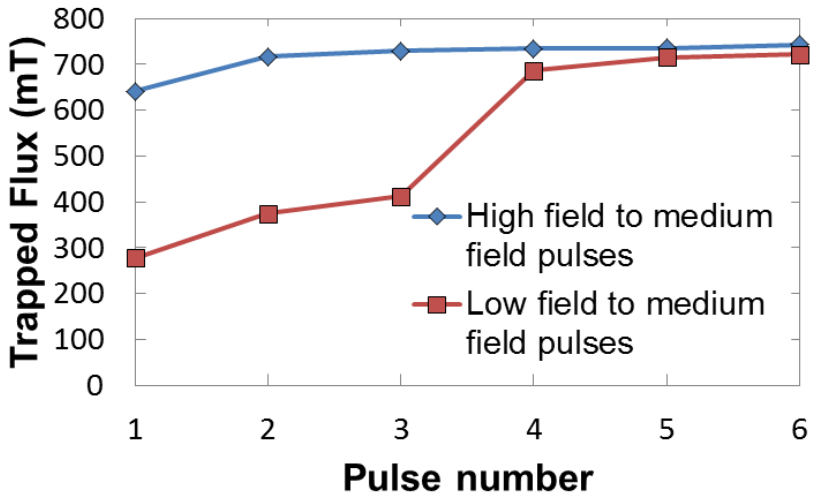

Figure 6.27. The flux trapped after the application of several pulses at 63K with the red data series indicating the application of pulse at 2.8T followed by two pulses at 3.5T before 3 pulses at 4.2T. The blue data series shows the application of a 4.8T pulse followed by 4 4.1T pulses before a final 3.5T pulse.

6.6 Long term trapped flux decay profiles

All envisaged uses of the flux trapped in high temperature superconducting pulses require that the field be trapped for a considerable period of time: it would be of no use if the bulk required remagnetizing too often. As this is an important consideration it was decided that the decay of the flux should be monitored over a much longer period of time than the 10 minutes used to ascertain the value of the trapped flux. The first two scenarios considered were the decay of flux trapped by an under-magnetization pulse and by a critical-magnetization pulse at 63K. The flux trapped by each pulse was monitored for 15 hours after the application of the pulse. Figure 6.28 shows how the flux decays at several points across the sample for each of the two different magnetization regimes. The data shown was recorded at the centre of the bulk as well as 5.5mm and 11.6mm from the centre. The different flux profiles characteristic of the two regimes is clearly visible with the critically magnetized case showing the Bean cone while the under magnetization shows the M-shaped profile. Despite the very different flux profiles it is clear that the flux decays fairly uniformly across the surface of the sample

losing 50mT in the 15 hours for the critically magnetized bulk at 35mT from the under-magnetized one, or a reduction of 7.5% and 13% of the total respectively. These figures can only be used as an estimate of the rate of flux decay at this temperature as the temperature increased by ~1-1.5K over the course of each run, possibly increasing the rate of decay in both cases.

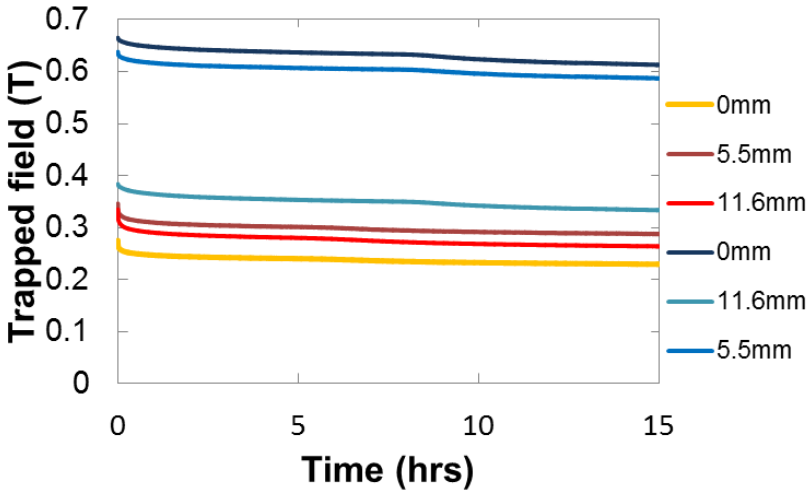

Figure 6.28. The decay of the flux at 63K trapped by a 2.7T under-magnetizing pulse (shown in the red colours) and a 3.5T critically-magnetizing pulse (shown in blue colours) across the surface of the sample (distance are from the centre of the sample) recorded for 15hours.

It has been shown earlier in Figure 6.16 the flux at the centre of an over-magnetized bulk can behave very differently to the flux trapped by the other two regimes. Rather than decaying the central flux actually increases during the first 10 minutes after the magnetization while the periphery fields decay as expected. As this behaviour, for obvious reasons, cannot continue indefinitely, it was decided that the evolution of the central flux should be monitored for as long as practicably possible. A single 5.6T pulse was used to magnetize the bulk at 63K and it was then monitored until the liquid nitrogen keeping it cold evaporated. Due to the simplicity of the cryogenics used the liquid nitrogen could not be refilled without temporarily warming the environment. This resulted in the bulk being monitored continuously for a period of just over 33 hours and the resulting trace is shown in Figure 6.29. Also shown in Figure 6.29 is the temperature of the nitrogen bath recorded by the PT100. It shows that over the first 14 hours the field increased very slowly with a total increase of 2mT or 0.4% of the original trapped flux. The flux then drops slightly before, after the 33 hour period, the flux is the still 0.5mT higher the original value. The field in the periphery again decayed as expected and as seen in the under and critical magnetization cases. The temperature is shown to be reasonably constant throughout the run rising by $\sim 1K$ after 9 hours before cooling again by $\sim 1K$ after 23 hours. As there is no

corresponding change in the measured flux during these two temperature steps it is safe to assume that, to a first approximation, these temperature fluctuations had no effect on the trapped flux. It is possible that part of this behaviour is caused by a slow drift in the calibration of part of the measuring equipment but it is clear that, in this regime, there is no significant change in flux (<0.1% for the period between 15hours and 33hours). As stated in section 6.4.2.1, it is thought that this is caused by an uneven distribution of the electric field within the sample causing the current to migrate slowly towards the centre, maintaining the central field at the expense of the field in the periphery.

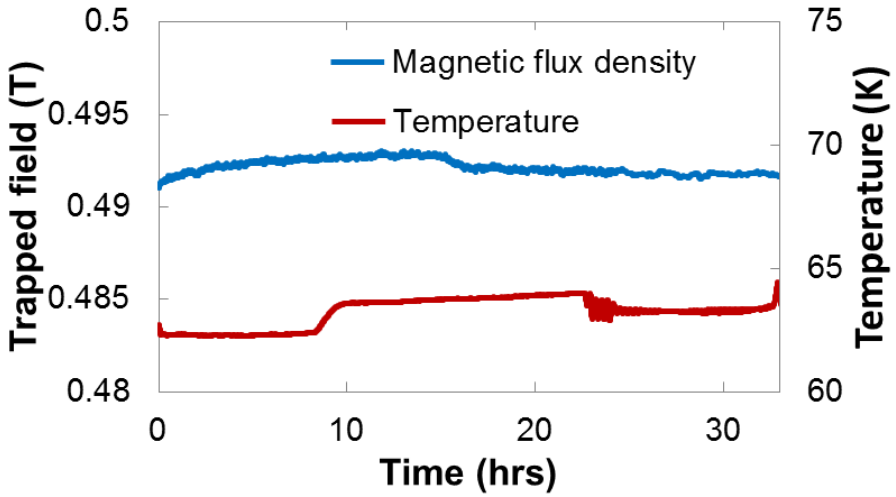

Figure 6.29. The evolution of the flux at the centre of the bulk trapped by a 5.6T over-magnetization pulse and the temperature of the nitrogen bath for 33 hours after the pulse.

6.7 Conclusion

In this chapter we have seen presented an experiment to investigate the flux trapping properties of a high temperature superconducting bulk at a range of temperatures and applied magnetizing fields. For this experiment various pieces of equipment had to be designed and constructed including a high field pulsed magnet (see chapter 4 for details), a rectangular cross-section tail dewar, a manostat pumping board and a Hall probe array. It was found that the lower the temperature the greater the field that could be trapped increasing from 320mT at 77K to 1.4T at 4.2K for the sample tested. Furthermore at each temperature there was critical magnetizing field which would trap the greatest amount of flux from a single pulse ranging from 2.7T at 77K to 4.5T at 4.2K for the sample tested. Although the flux trapped showed a strong dependence on the magnitude of the applied field no dependence on the rise time could be measured. It was also shown that the total flux trapped could be enhanced by using a multiple magnetizing pulses but this was only effective at lower temperatures. At 77K the flux could

only be enhanced by <0.4% but it could be enhanced by ~13% at 63K and ~11% at 4.2K. It also showed that magnetizing by using over magnetization pulses before applying a couple of pulses around the critical magnetization field may be more effective than applying low field pulses before critical field pulses, as is recommended in the literature. The decay of the trapped flux was also studied and it was found that in liquid nitrogen the trapped field will decay slowly with time but an over-magnetized bulk will have a central field which can be stable for many hours. However in liquid helium there is no measureable decay of the trapped flux even after 1hr.

The aim of this experiment was generate detailed data on how the superconducting bulks would behave in different magnetizing scenarios. As the sample was tested at a wide range of applied fields, temperatures and magnetizing field rise times this aim was fulfilled. It is hoped that any future efforts in creating computer models of pulsed field magnetized bulks will use this work to check the accuracy of model's results and so the data may help to create detailed and accurate FEA models.

References

[1] M. Tomita and M. Murakami, “High-temperature superconductor bulk magnets that can trap magnetic fields of over 17 tesla at 29K,” *Nature,* vol. 421, no. 6922, pp. 517-520, 2003.

[2] H. Fujishiro, T. Tateiwa, A. Fujiwara, T. Oka and H. Hayashi, “Higher trapped field over 5 T on HTSC bulk by modified pulse field magnetizing,” *Physica C: Super.,* Vols. 445-448, pp. 334-338, 2006.

[3] J. F. Herbst and J. J. Croat, “Neodymium-iron-boron permanent magnets,” *Journal of Magnetism and Magnetic Materials,* vol. 100, no. 1-3, pp. 57-78, 1991.

[4] A. Patel and B. A. Glowacki, “New fully superconducting bearing concept using the difference in irreversibility field of two superconducting components,” *Super. Sci. Tech.,* vol. 24, no. 1, p. 015009, 2011.

[5] Y. Sanagawa, H. Ueda, M. Tsuda, A. Ishiyama, S. Kohayashi and S. Haseyama, “Characteristics of lift and restoring force in HTS bulk-Application to two-dimensional maglev transporter,” *IEEE Trans. Ap. Super.,* vol. 11, no. 1, pp. 1797-1800, 2001.

[6] S. Fukui, R. Sato, J. Ogawa, T. Oka, M. Yamaguchi, T. Sato, S. Miyazaki, T. Sasahara, T. Tamaki, S. Nishiwaki and Y. Yuki, “Study on application of magnetic levitation utilizing HTS bulks to spin processors for photo mask production,” *Physica C: Super.,* Vols. 463-465, pp. 1289-1292, 2007.

[7] P. J. Masson and C. A. Luongo, “High power density superconducting motor for all-electric aircraft propulsion,” *IEEE trans. ap. super.,* vol. 15, no. 2, pp. 2226-2229, 2005.

[8] H. Ohsaki, M. Sekino, T. Suzuki and Y. Terao, “Design study of wind turbine generators using superconducting coils and bulks,” *ICCEP proc. IEEE,* pp. 479-484, 2009.

[9] T. Oka, H. Kanayama, S. Fukui, J. Ogawa, T. Sato, M. Ooizumi, T. Terasawa, Y. Itoh and R. Yabuno, “Application of HTS bulk magnet system to the magnetic separation techniques for water purification,” *Physica C: Super.,* vol. 468, no. 15-20, pp. 2128-2132, 2008.

[10] T. Terada, S. Fukui, F. Mishima, Y. Akiyama, Y. Izumi and S. Nishijima, "Development of magnetic drug delivery system using HTS bulk magnet," *Physica C: Super.*, vol. 468, no. 15-20, pp. 2133-2136, 2008.

[11] S. B. Kim, M. Imai, R. Takano, J. H. Joo and S. Hahn, "Study on Optimized Configuration of Stacked HTS Bulk Annuli for Compact NMR Application," *IEEE trans. ap. super.*, vol. 21, no. 3 Part 2, pp. 2080-2083, 2011.

[12] T. Oka, K. Yokoyama, H. Fujishiro and K. Noto, "Temperature rise in melt-textured large grain superconducting bulk magnets during their magnetizing operations," *Physica C: Super.*, Vols. 460-462, no. 2, pp. 748-749, 2007.

[13] U. Mizutani, T. Oka, Y. Itoh, Y. Yanagi, M. Yoshikawa and H. Ikuta, "Pulsed-field magnetization applied to high-Tc superconductors," *Ap. Super.*, vol. 6, no. 2-5, pp. 235-246, 1998.

[14] H. Fujishiro, T. Naito and M. Oyama, "Mechanism of magnetic flux trapping on superconducting bulk magnetized by pulsed field using a vortex-type coil," *Super. Sci. Tech.*, vol. 24, no. 7, p. 075015, 2011.

[15] T. Oka, H. Seki, J. Ogawa, S. Fukui and T. Sato, "Performance of Trapped Magnetic Field in Superconducting Bulk Magnets Activated by Pulsed Field Magnetization," *IEEE trans. ap. super.*, vol. 21, no. 3 Part 3, pp. 3356-3359, 2011.

[16] K. Yokoyama, T. Oka and K. Noto, "Evaluation of Pulsed-Field Magnetization on a Superconducting Bulk Magnet System Using a 13 K Refrigerator," *IEEE trans. ap. super.*, vol. 21, no. 3 Part 2, pp. 1657-1660, 2011.

[17] H. Fujishiro, Y. Kimaura, M. Izumi, S. Nariki and I. Hirabayashi, "Possible explanation for trapped field enhancement on REBaCuO bulk by modified multi-pulse technique with stepwise cooling (MMPSC)," *Mat. Sci. and Eng. B,* vol. 151, no. 1, pp. 95-100, 2008.

[18] H. Fujishiro, T. Hiyama, T. Miura, T. Naito and S. Nariki, "Pulsed Field Magnetization for

GdBaCuO Bulk With Stronger Pinning Characteristics," *IEEE Trans. Ap. Super.,* vol. 19, no. 3, pp. 3545-3548, 2009.

[19] T. Ida, H. Matsuzaki, Y. Akita, M. Izumi, H. Sugimoto, Y. Hondou, Y. Kimura, N. Sakai, S. Nariki, I. Hirabayashi, M. Miki, M. Muralami and M. Kitano, "Magnetization properties for Gd–Ba–Cu–O bulk superconductors with a couple of pulsed-field vortex-type coils," *Physica C,* Vols. 412-414 Part 1, pp. 638-645, 2004.

[20] L. Chen, Y. S. Cha, H. Claus, H. Zheng, B. W. Veal and F. Z. Peng, "Optimization of Pulsed-Current Profile for Magnetizing High Tc Bulk YBCO Superconductors," *IEEE Trans Plasma Sci.,* vol. 34, no. 5, pp. 1702-1708, 2006.

[21] H. Fujishiro, T. Naito and M. Oyama, "Simulation of flux dynamics in a superconducting bulk magnetized by multi-pulse technique," *Physica C,* vol. 471, no. 21-22, pp. 889-892, 2011.

[22] T. Kono, M. Muralidhar, K. Nakao, N. Sakai, M. Murakami and N. Koshizuka, "Magnetization measurement of (Nd, Eu, Gd)Ba2Cu3Oy having very high irreversibility fields in pulsed high magnetic fields," *Physica C,* Vols. 412-414 Part 1, pp. 699-704, 2004.

[23] M. Sander, U. Sutter, M. Adam and M. Klaser, "Comparison of pulsed magnetization processes for HTS bulk parts," *Super. Sci. Tech.,* vol. 15, no. 5, pp. 748-753, 2002.

[24] Y. Itoh, Y. Yanagi and U. Mizutani, "Flux motion during pulsed field magnetization in YBaCuO superconducting bulk magnet," *Journal Applied Physics,* vol. 82, no. 11, pp. 5600-5611, 1997.

[25] H. Fujishiro, T. Hiyama, T. Tateiwa, Y. Yanagi and T. Oka, "Importance of initial "M-shaped" trapped field profile in a two-stage pulse field magnetization (MMPSC) method," *Physica C,* Vols. 463-465, pp. 394-397, 2007.

[26] H. Fujishiro, T. Hiyama, T. Naito, Y. Yanagi and Y. Itoh, "Enhancement of trapped field and total trapped flux on GdBaCuO bulk by the MMPSC+IMRA method," *Super. Sci. Tech.,* vol. 22, no. 9, p. 095006, 2009.

[27] K. Yokoyama, M. Kaneyama, T. Oka, H. Fujishiro and K. Noto, “Temperature measurement of RE123 bulk superconductors on magnetizing process,” *Physica C*, Vols. 412-414 Part 1, pp. 688-694, 2004.

[28] R. Shirashi, K. Fujiyama and H. Ohsaki, “Microscopic magnetic flux motion in Y-Ba-Cu-O bulk superconductor during pulsed field magnetization,” *IEEE Trans. Ap. Super.*, vol. 15, no. 2, pp. 3153-3156, 2005.

[29] T. Ishigohka, H. Ichikawa, A. Nimoniya and H. Kamijo, “Flux trapping characteristics of YBCO bulks using pulse magnetization,” *IEEE Trans. Ap. Super.*, vol. 11, no. 1, pp. 1980-1983, 2001.

[30] M. Tokuyama, Y. Yanagi and H. Ikuta, “Local measurement of the pulsed field magnetization process of melt-processed bulk superconductor,” *Physica C*, Vols. 463-465, pp. 405-409, 2007.

[31] R. Shiraishi and H. Ohsaki, “Multipoint Measurements of Transient Flux Motion on Bulk Superconductor During Pulsed Field Magnetization,” *IEEE Trans Ap. Super.*, vol. 17, no. 2, pp. 3664-3667, 2007.

[32] K. A. Müller, M. Takashige and J. G. Bednorz, “Flux trapping and superconductive glass state in La2CuO4-y:Ba,” *Phys. Rev. Let.*, vol. 58, no. 11, pp. 1143-1146, 1987.

[33] T. Matsushita, “On the origin of the irreversibilityline in superconductors Depinning or melting of fluxoids,” *Physica C*, vol. 214, no. 1-2, pp. 100-106, 1993.

[34] C. P. Bean, “Magnetization of high-field superconductors,” *Rev. Modern Phys.*, vol. 36, no. 1, pp. 31-39, 1964.

[35] Z. Xu, R. Lewin, A. M. Campbell, D. A. Cardwell and H. Jones, “Theoretical simulation studies of pulsed field magnetisation of (RE)BCO bulk superconductors,” *J. Phys.: Conf. Ser.*, vol. 234, no. 1, p. 012049, 2010.

[36] Z. Xu, R. Lewin, A. M. Campbell, D. A. Cardwell and H. Jones, “Simulation studies on the magnetization of (RE)BCO bulk superconductors using various split-coil arrangements,” *Sup.*

Sci. Tech., vol. 25, no. 2, p. 025016, 2012.

[37] A. M. Campbell, "A new method of determining the critical state in superconductors," *Super. Sci. Tech.,* vol. 20, no. 3, pp. 292-295, 2007.

[38] Y. B. Kim, C. F. Hempstead and A. R. Strnad, "Critical Persistent Currents in Hard Superconductors," *Phys. Rev. Let.,* vol. 9, no. 7, pp. 306-309, 1962.

[39] A. M. Campbell, "Private Communication," *University of Cambridge, Department of Engineering, Trumpington Street, Cambridge, CB2 1PZ, UK.*

[40] W. H. Keesom and A. Bijl, "Determination of the vapour pressures of liquid nitrogen below one atmosphere, and of solid nitrogen: The boilingpoint and triple point of nitrogen," *Physica,* vol. 4, no. 4, pp. 305-310, 1937.

[41] Y. Shi, N. Han Babu, K. Lida and D. A. Cardwell, "Superconducting properties of Gd-Ba-Cu-O single grains processed from a new, Ba-rich precursor compound," *J. Phys.: Conf. Ser.,* vol. 97, p. 012250, 2008.

[42] "Grade 6F/45 Epoxy Cotton Product Data Sheet," Bay Plastics Ltd, [Online]. Available: www.bayplastics.co.uk. [Accessed 2011].

[43] D. A. Cardwell, M. Murakami, M. Zeisberger, W. Gawalek, R. Gonzalez-Arrabel, M. Eisterer, H. W. Weber, G. Fuchs, G. Krabbes, G. Leenders, H. Freyhardt, X. Chaud, R. Tournier and N. Hari Babu, "Round robin measurements of the flux trapping properties of melt processed Sm–Ba–Cu–O bulk superconductors," *Physica C: Super.,* Vols. 412-412, no. 1, pp. 623-632, 2004.

[44] T. Matsushita, A. Matsuda and K. Yanagi, "Irreversibility line and flux pinning properties in high-temperature superconductors," *Physica C,* vol. 213, no. 3-4, pp. 477-482, 1993.

[45] Temtrol Technologies, "RTD conversion chart," [Online]. Available: http://www.temtrol.com.au/useful-information.html. [Accessed 2010].

Appendix A – Circuit diagram for pulse generator

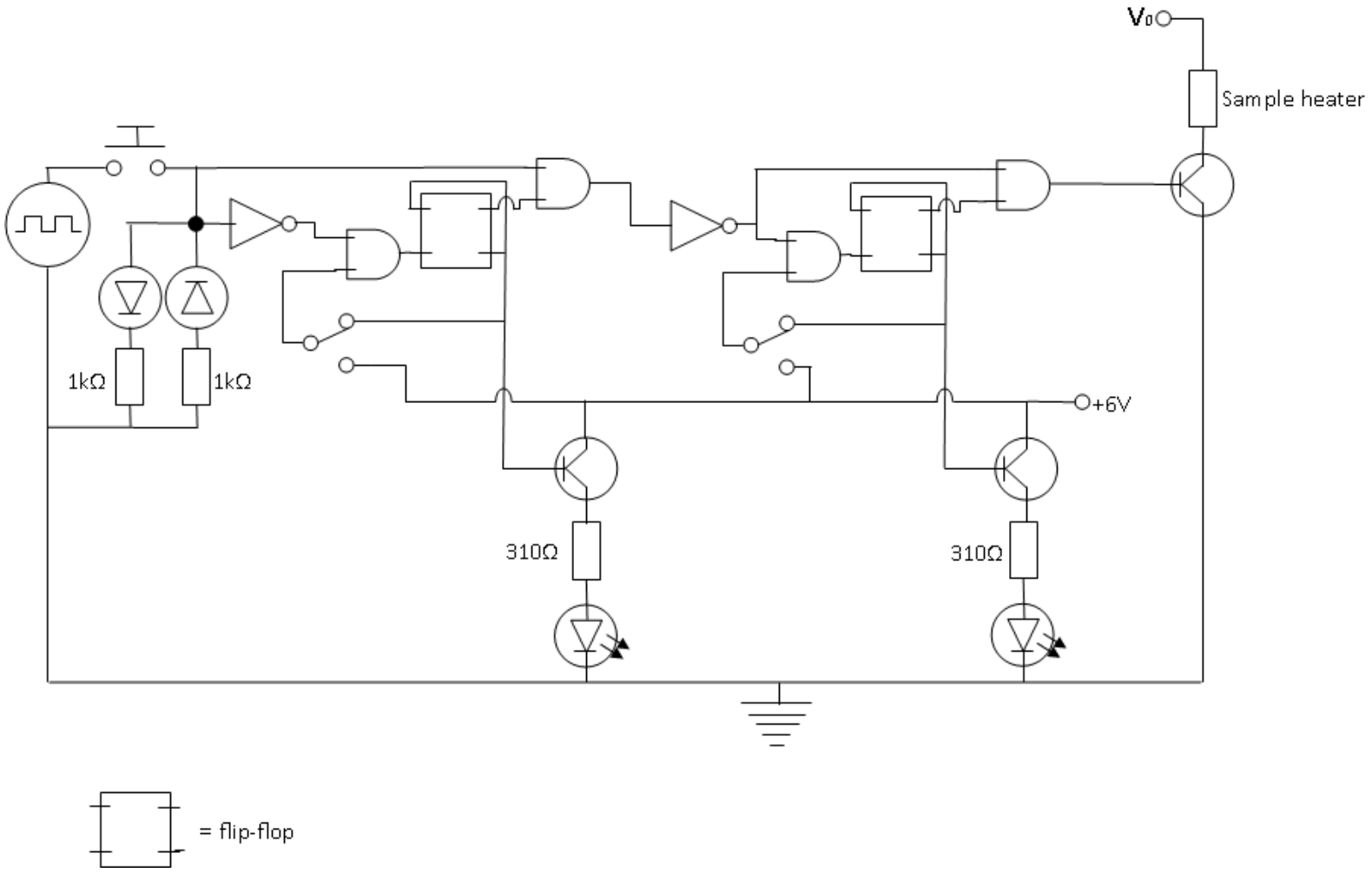

Appendix B – Material Properties used in MQE Modelling

Material	Density (kg/m^3)	SHC $(J/(kg \cdot K))$	Resistivity (4.2K) (Ωm)	Thermal Conductivity $W/(m \cdot K)$	RRR	References (found in chapter 3)
Copper	8933	$10.97 \times 10^{-3}T + 0.7632 \times 10^{-3}T^3$	1.85×10^{-10}	$\sim 100 - 400$	80	[27] [42] [43] [28] [32]
NbTi	6200	$5.16 \times 10^{-2}T + 7.36 \times 10^{-3}T^3\ T \leq T_c$ $0.145T + 2.3 \times 10^{-3}T^3\ T > T_c$	6.5×10^{-7}	0.1	N/A	[1] [2] [22]
SnPb (72:28)	8478	$-6.53 \times 10^{-2}T + 1.05 \times 10^{-2}T^3$	0.3×10^{-8}	$9.82 \times 10^{-3}T^3 - 5.26 \times 10^{-1}T^2 + 10.3T - 17.6$	N/A	[43] [44] [45] [46]
Constantan (55:45 Cu:Ni)	8900	$0.113T + 5.59 \times 10^{-4}T^3$	N/A	$0.298T$	N/A	[37] [38]
Stycast 2850FT	2300	$1 \times 10^{-2}T + 2 \times 10^{-3}T^3$	N/A	$9.5 \times 10^{-3}T^{1.2}$	N/A	[24] [35] [36]

Appendix C – Wire parameters

Dimensions of wire tested:

Width (mm)	Breadth (mm)	Copper area (mm^2)	NbTi area (mm^2)	Solder area (mm^2)	Insert copper to superconductor ratio
1.91	1.142	1.6267	0.3017	0.1649	1

Dimensions for the wire used in FEA model:

Width (mm)	Insert width (mm)	Copper sheath width (mm)	Solder width (mm)	Insert copper to superconductor ratio
0.763	0.1285	0.5642	0.07022	1

Appendix D - Magnetic Field Integrations

Thin Monolithic Coil

The initial integral is:

$$B = \frac{\mu_0 J_L}{2} \int_{-b}^{b} \frac{R^2}{(R^2 + z^2)^{\frac{3}{2}}} dz \quad \text{A1.}$$

$$z = R \tan\theta$$

$$dz = R(1 + \tan^2\theta) d\theta \quad \text{A2.}$$

Then by using the trigonometric identity:

$$1 + \tan^2\theta = \sec^2\theta \quad \text{A3.}$$

Equation A1 can be rewritten as:

$$B = \frac{\mu_0 J_L}{2} \int_{z=-b}^{z=b} \frac{R^2}{(R^2 + R^2\tan^2\theta)^{\frac{3}{2}}} R(1 + \tan^2\theta) d\theta \quad \text{A4.}$$

$$= \frac{\mu_0 J_L}{2} \int_{z=-b}^{z=b} \frac{R^3}{(R^2\sec^2\theta)^{\frac{3}{2}}} \sec^2\theta \, d\theta \quad \text{A5.}$$

$$= \frac{\mu_0 J_L}{2} \int_{z=-b}^{z=b} \frac{1}{\sec\theta} d\theta \quad \text{A6.}$$

$$= \frac{\mu_0 J_L}{2} \int_{z=-b}^{z=b} \cos\theta \, d\theta \quad \text{A7.}$$

$$B = \frac{\mu_0 J_L}{2} [\sin\theta]_{z=-b}^{z=b} \quad \text{A8.}$$

But if we recall equation A2 then we can draw a triangle with sides of length z and R and a hypotenuse $\sqrt{z^2 + R^2}$ and so:

$$\sin\theta = \frac{z}{\sqrt{z^2 + R^2}} \quad \text{A9.}$$

And we reach the final answer of:

$$B = \frac{\mu_0 J_L}{2} \left[\frac{z}{\sqrt{z^2 + R^2}} \right]_{-b}^{b} \quad \text{A10.}$$

$$B = \frac{\mu_0 J_L b}{\sqrt{R^2 + b^2}} \quad \text{A11.}$$

Field at Centre of Thick Monolithic Coil

The initial integral is:

$$B = \frac{\mu_0 J}{2} \int_{a_1}^{a_2} \int_{-b}^{b} \frac{r^2}{(r^2 + z^2)^{\frac{3}{2}}} dr\, dz \quad \text{A12.}$$

For simplicity of presentation we will ignore the limits for the next few steps before reintroducing them later. We can first integrate the dz integral holding r constant using the method show in the first section which gives the second stage integral:

$$B = \mu_0 J \int \frac{b}{\sqrt{b^2 + r^2}} dr \quad \text{A13.}$$

This time we need to make a similar substitution as earlier given A2:

$$r = b \tan\theta$$
$$dr = b(1 + \tan^2\theta) d\theta \quad \text{A14.}$$

and by using the trigonometric identity in equation A3 we can write:

$$B = \mu_0 J \int \frac{b}{\sqrt{b^2 + b^2 \tan^2\theta}} b \sec^2\theta\, d\theta \quad \text{A15.}$$

$$= \mu_0 J \int \frac{b^2 \sec^2\theta}{b \sec\theta} d\theta \quad \text{A16.}$$

$$= \mu_0 J \int b \sec\theta\, d\theta \quad \text{A17.}$$

At first glance the expression in equation A17 is no better than the expression that we started with. To integrate this expression we must multiply by $\frac{\sec\theta + \tan\theta}{\sec\theta + \tan\theta}$ and use the substitution:

$$u = \sec\theta + \tan\theta$$
$$du = (\sec\theta \tan\theta + \sec^2\theta) d\theta \quad \text{A18.}$$

Therefore:

$$B = \mu_0 J \int b \sec\theta \frac{\sec\theta + \tan\theta}{\sec\theta + \tan\theta}\, d\theta \quad \text{A19.}$$

$$= \mu_0 J \int b \frac{\sec^2\theta + \sec\theta\tan\theta}{\sec\theta + \tan\theta}\, d\theta \quad \text{A20.}$$

$$= \mu_0 J \int b \frac{du}{u} \quad \text{A21.}$$

$$B = \mu_0 J \mathrm{b} \cdot \ln u = \frac{\mu_0 J}{2} \mathrm{b} \cdot \ln(\sec\theta + \tan\theta) \quad \text{A22.}$$

We know from our original substitution that $r = z\tan\theta$ and by returning to the triangle from earlier we can write:

$$\sec\theta = \frac{\sqrt{b^2 + r^2}}{b}$$

$$\tan\theta = \frac{r}{b} \quad \text{A23.}$$

$$B = \mu_0 J b \ln\left(\frac{r}{b} + \frac{\sqrt{b^2 + r^2}}{b}\right) \quad \text{A24.}$$

And so we can finally re-introduce our limits to obtain the solution:

$$B = \mu_0 J \left[b \ln\left(\frac{r}{b} + \frac{\sqrt{b^2 + r^2}}{b}\right)\right]_{r=a_1}^{r=a_2} \quad \text{A25.}$$

$$B = \mu_0 J b \left\{\ln\left(\frac{a_2}{b} + \frac{\sqrt{b^2 + {a_2}^2}}{b}\right) - \ln\left(\frac{a_1}{b} + \frac{\sqrt{b^2 + {a_1}^2}}{b}\right)\right\} \quad \text{A26.}$$

$$B = \mu_0 J b \ln\left(\frac{a_2 + \sqrt{b^2 + {a_2}^2}}{a_1 + \sqrt{b^2 + {a_1}^2}}\right) \quad \text{A27.}$$

Which can be expressed as:

$$B = \mu_0 J b \ln\frac{\alpha + \sqrt{\alpha^2 + \beta^2}}{1 + \sqrt{1 + \beta^2}} \quad \text{A28.}$$

where $$\alpha = \frac{a_2}{a_1}, \beta = \frac{b}{a_1} \quad \text{A29.}$$

Field at Centre of Split Pair Coil

Method 1 - Calculate the field from one displaced coil the double the result

As shown above the field from one coil is found by integrating equation A12 about the centre of the coil which is defined as being $z = 0$. In the split pair the centre of each coil is at $z = \pm(b + b_{gap})$ and so the field at $z = 0$ from one coil is:

$$B = \frac{\mu_0 J}{2} \int_{a_1}^{a_2} \int_{b_{gap}}^{2b+b_{gap}} \frac{r^2}{(r^2 + z^2)^{\frac{3}{2}}} dr\, dz \qquad \text{A30.}$$

$$B = \frac{\mu_0 J}{2} \int_{a_1}^{a_2} \left\{ \frac{2b + b_{gap}}{\sqrt{(2b + b_{gap})^2 + r^2}} - \frac{b_{gap}}{\sqrt{{b_{gap}}^2 + r^2}} \right\} dr \qquad \text{A31.}$$

Which can be integrated by the same method as used for equation A13 to reach:

$$B = \frac{\mu_0 J_L}{2} \left\{ (2b + b_{gap}) \ln \left(\frac{a_2 + \sqrt{(2b + b_{gap})^2 + {a_2}^2}}{a_1 + \sqrt{(2b + b_{gap})^2 + {a_1}^2}} \right) - b_{gap} \ln \left(\frac{a_2 + \sqrt{{b_{gap}}^2 + {a_2}^2}}{a_1 + \sqrt{{b_{gap}}^2 + {a_1}^2}} \right) \right\} \qquad \text{A32.}$$

Or $$B = \frac{\mu_0 J_L}{2} a_1 \left\{ \beta_1 \ln \left(\frac{\alpha + \sqrt{{\beta_1}^2 + \alpha^2}}{1 + \sqrt{1 + {\beta_1}^2}} \right) - \beta_2 \ln \left(\frac{\alpha + \sqrt{{\beta_2}^2 + \alpha^2}}{1 + \sqrt{1 + {\beta_2}^2}} \right) \right\} \qquad \text{A33.}$$

Where $$\alpha = \frac{a_2}{a_1}, \beta_1 = \frac{2b + b_{gap}}{a_1}, \beta_2 = \frac{b_{gap}}{a_1} \qquad \text{A34.}$$

Now using linear superposition of fields the field from two such coils is then simply:

$$B = \mu_0 J_L a_1 \left\{ \beta_1 \ln \left(\frac{\alpha + \sqrt{{\beta_1}^2 + \alpha^2}}{1 + \sqrt{1 + {\beta_1}^2}} \right) - \beta_2 \ln \left(\frac{\alpha + \sqrt{{\beta_2}^2 + \alpha^2}}{1 + \sqrt{1 + {\beta_2}^2}} \right) \right\} \qquad \text{A35.}$$

<u>Method 2 – Calculate the field form a long coil, then a short coil and finally subtract the two</u>

An alternative method is to calculate the field from a monolithic coil with total length $L = 4b + 2b_{gap}$ so:

$$B_{long} = \frac{\mu_0 J}{2} \int_{a_1}^{a_2} \int_{-(2b+b_{gap})}^{2b+b_{gap}} \frac{r^2}{(r^2+z^2)^{\frac{3}{2}}} dr\, dz \quad \text{A36.}$$

$$B_{long} = \mu_0 J_L (2b + b_{gap}) \ln\left(\frac{a_2 + \sqrt{(2b+b_{gap})^2 + {a_2}^2}}{a_1 + \sqrt{(2b+b_{gap})^2 + {a_1}^2}} \right) \quad \text{A37.}$$

We then need to calculate the contribution from the part of this coil which occupies the gap space which is given by:

$$B_{short} = \frac{\mu_0 J}{2} \int_{a_1}^{a_2} \int_{-b_{gap}}^{b_{gap}} \frac{r^2}{(r^2+z^2)^{\frac{3}{2}}} dr\, dz \quad \text{A38.}$$

$$B_{short} = \mu_0 J_L b_{gap} \ln\left(\frac{a_2 + \sqrt{{b_{gap}}^2 + {a_2}^2}}{a_1 + \sqrt{{b_{gap}}^2 + {a_1}^2}} \right) \quad \text{A39.}$$

Then the final field is again calculated from a linear superposition of the fields:

$$B = B_{long} - B_{short} \quad \text{A40.}$$

This gives an equation which is exactly the same as equation A35 as expected.

Appendix E - Material Properties used in magnet design

Electrical/Thermal Properties

Material	Thermal Conductivity $(W/m \cdot K)$	Electrical Resistivity $(\Omega m \times 10^{-8})$	Specific Heat Capacity $(J/kg \cdot K)$	Density (kg/m^3)	Reference(s) (Found in Chapter 4)
Copper	400	$1.68\big(1 + 0.00393(T - 293)\big)$	$834 - 4007 \cdot \log T + 4066 \cdot (\log T)^2 - 1463 \cdot (\log T)^3 + 179.7 \cdot (\log T)^4$ -	8700	[37] [50] [51]
Zylon/epoxy composite	$\perp 8.3 \times 10^{-5}(T - 77) + 0.002$, $\parallel 3.94 \times 10^{-4}(T - 77) + 0.015$		$3.2152 \cdot T - 1.8732$	1500	[31] [52] [53]
S-Glass/epoxy composite	$\perp 0.237$, $\parallel 0.6$		0.2 (77K) 0.85 (300K)	2000	[54] [55]
Epoxy	0.15		$0.005T$	1160	[47] [56]

Mechanical

Material	Young's Modulus (GPa)	Poisson's ratio	Tangent Modulus (GPa)	Shear Modulus (GPa)	Density (kg/m^3)	UTS (GPa)	Ultimate Compressive Strength (MPa)	Reference(s) (Found in Chapter 4)
Soft Copper	90	0.33	1.5		8700	0.46		[46] [48]
Hard Copper	130	0.33	0.5		8700	0.350		[46] [48]
Zylon/epoxy composite	$\perp$ 2.7, $\parallel$ 222	$v_{\varphi,z}$ 0.35, $v_{r,\varphi}$ 0.004, $v_{r,z}$0.6		4.5	1500	4-5.2		[35] [38] Chapter 5
S2 glass/epoxy composite	$\perp$ 16, $\parallel$ 65	$v_{\varphi,z}$ 0.33, $v_{r,\varphi}$ 0.087		7	2000	2	800	[54] [29] [58]
10G/40	18	0.35				0.355	415	[43]
6F/45	6.5	0.35				0.068	290	[44]
Stainless steel (316L)	190	0.35				0.7		[59]
Resin	1.5	0.35				0.02-0.04		[60]